TECHNISCHE UNIVERSITÄT MÜNCHEN
FAKULTÄT FÜR CHEMIE
LEHRSTUHL FÜR ORGANISCHE CHEMIE II

Molecular target elucidation of vioprolide A in human cancer cells

and

-omics insights into the ClpXP machinery of *Staphylococcus aureus*

Volker Christian Reinhard Kirsch

Vollständiger Abdruck der von der Fakultät für Chemie der Technischen Universität München zur Erlangung des akademischen Grades eines

DOKTORS DER NATURWISSENSCHAFTEN (Dr. rer. nat.)

genehmigten Dissertation.

Vorsitzender:		Prof. Dr. Michael Groll
Prüfer der Dissertation:	1.	Prof. Dr. Stephan A. Sieber
	2.	apl. Prof. Dr. Wolfgang Eisenreich

Die Dissertation wurde am 08.01.2020 bei der Technischen Universität München eingereicht und durch die Fakultät für Chemie am 06.02.2020 angenommen.

“If I have seen further, it is by standing on the shoulder of giants”

Isaac Newton, 1675

Meiner Familie

Danksagung

An dieser Stelle möchte ich mich herzlich bei Prof. Dr. Stephan A. Sieber, nicht nur für die spannende, abwechslungsreiche und interessante Themenstellung bedanken, sondern auch für die Möglichkeit meine Projekte mit der größtmöglichen wissenschaftlichen und technischen Freiheit durchführen zu dürfen. Vielen Dank Stephan für die Möglichkeiten mein Fachwissen im Bereich Metabolomics und Proteomics mit der Teilnahme an vielen Konferenzen und Workshops zu erweitern, dein großes Interesse an meinen Projekten, die zahlreichen intensiven Gespräche und Anregungen sowie das in mich gelegte Vertrauen deinerseits.

Ein großer Dank geht an die Mitglieder der Prüfungskommission für die Bewertung meiner Arbeit. Herzlich bedanken möchte ich mich bei Christina Orgler, Christian Fetzer, Carolin Gleissner, Martin Pfanzelt und Ines Hübner für eure Zeit die ihr euch für mich genommen habt um meine Arbeit zu korrigieren, eure tollen Anmerkungen sowie das Austreiben des einen oder anderen Fehlerteufelchens!

Des Weiteren möchte ich mich bei Frau Prof. Dr. Angelika M. Vollmar für die zahlreichen Diskussionen und Ideen während des Vioprolid Projektes bedanken. Unsere Zusammenarbeit hat mir sehr viel Spaß gemacht. Vielen Dank Frau Prof. Vollmar, dass Sie mir zusammen mit Stephan mir damals die Teilnahme an dem Workshop in London ermöglicht haben. Durch die Teilnahme an diesem Kurs wurden mir viele Projekte erst ermöglicht.

Ein ganz herzlicher Dank geht an Christina Orgler. Liebe Christina, vielen Dank für die tolle Kooperation die wir die letzten Jahre zusammen hatten! Es hat unglaublich viel Spaß gemacht mit dir unser Vio Thema zu bearbeiten. Klasse war, wie wir uns immer aufeinander verlassen konnten und uns gegenseitig unterstützt und ermutigt haben wenns auch mal nicht so lief. Unsere Zusammenarbeit war für mich wirklich eines der Highlights der Doktorarbeit!

Liebe Mona Wolff, Katja Bäuml und Katja Gliesche, vielen vielen Dank für euren Einsatz, eure Unterstützung und Hilfe jeden Tag im Labor! Ohne euch würde gar nichts im Labor laufen und wir alle wissen eure Arbeit täglich sehr zu schätzen!

Ganz herzlich bedanken möchte ich mich auch bei meiner ehemaligen Sitznachbarin Anja Fux! Vielen Dank für die großartige Zeit! Wir hatten nicht nur viele gute und intensive

Diskussionen über die jeweiligen Projekte sondern auch jede Menge Spaß im täglichen Laboralltag!

Lieber Martin, vielen Dank für unsere Gespräche rund um die Musik! Es war eine tolle Abwechslung im Labor und ich freue mich schon aufs gemeinsame Musizieren! Liebe Caro, vielen Dank für die gemeinsame Zeit im Sport, auf der Wiesn oder beim Tollwood mit dem einen oder anderen Glühwein! Es war sau lustig und ich hoffe es folgen noch viele mehr!

Ganz herzlich danken möchte ich auch meinen weiteren Kollegen aus Lab D für die tolle Atmosphäre bei uns im Labor. Ines, Robert, Till, Katja, Markus und Max. Auch wenn unser Musikgeschmack sehr auseinander driftet, und die gemeinsame Labplaylist zu erstellen eine gewisse Herausforderung darstellte, so hat die Stimmung bei uns im Labor doch auch so immer gepasst! Jeder Tag mit euch hat sehr viel Spaß gemacht und es war wirklich toll wie wir uns tagtäglich mit Rat und Tat zur Seite gestanden haben! Vielen Dank euch dafür!

Herzlichen Dank an die „alte Garde“ unseres Arbeitskreises! Wie ihr mich damals aufgenommen habt, als ich zur Masterarbeit kam, sowie eure Bereitschaft eure Erfahrungen und Tricks mit mir zu teilen, haben mir sehr viel geholfen! Lieber Jürgen und Johannes, vielen Dank für alles was ich bei euch als „Padawan“ in mehreren Praktika lernen durfte! Vielen Dank Philipp für die vielen Diskussionen, die Mittagessen auch mal nach 11 Uhr sowie die gemeinsamen Champions League Abende. Nachdem Liverpool aber immer verliert wenn ich zuschaue fürchte ich wird’s bald Bier ohne Champions League ;). Lieber Wolfgang und Christian, auch wenn eure Ratschläge beim gemeinsamen Zocken bei mir nicht so recht Früchte tragen wollten (ich habs echt versucht) habe ich es sehr genossen, und bin euch auch für eure Tipps und Anleitungen (danke für die Einführung ins Klonieren Christian) im Labor sehr dankbar! Liebe Frani, vielen Dank dass du mich damals mit auf dein Projekt genommen und mir vieles im S2 beigebracht hast! Lieber Max, danke für deine Einführung in Metabolomics! Danke Meghan für deine Einführung in Proteomics und die Begleitung meiner ersten Schritte darin. Vielen Dank Matthias für die Diskussionen bezüglich Bioinformatik und Datenanalyse. Des Weiteren möchte ich mich bei Mathias Hackl (an die Momente wo wir wegen dir beim Fussball weinend vor Lachen am Boden lagen, denke ich immer gern ☺), Weining Zhao, Vadim Korotkkov, Markus Lakemeyer, Igor Pavlovic, Lena Kunold und Annabelle Hoegl für die tolle Zeit bedanken!

Natürlich geht auch ein sehr großer Dank an den gesamten Arbeitskreis! Egal obs Fußball spielen, unsere gemeinsamen Kleinwalsertalbesuche, Grillen, Abende in der Kaffeeküche

oder spontante Gespräche auf dem Gang oder beim täglichen Essen in der Mensa waren, es war immer toll euch als Kollegen zu haben! Vielen Dank Ines, Thesi, Robert, Anja, Caro, Martin, Didi, Till, Barbara, Thomas, Patta, Kyu, Jonas, Dori, Ramona, Pavel, Christina, Angela, Jan, Konstantin, Katja G., Katja B., Mona, Zani, Seppi, Lisa, Christian, Mathias, Frani und Stephan H. (vielen Dank Dottore für die vielen Diskussionen und deine Tipps) für die gemeinsame Zeit und eure Bereitschaft jeden jederzeit mit Rat und Tat zu unterstützen. Eure Hilfsbereitschaft und unser Zusammenhalt hat die Zeit erst so schön gemacht wie sie war, und mich immer gerne ins Labor kommen lassen! Danke euch!

Ganz herzlich möchte ich mich auch bei Sarah-Madeleine Gabler, Juri Kannheiser und Florian Simon für die jahrelange sehr enge Freundschaft bedanken! Ich freue mich sehr euch schon so lange meine Freunde nennen zu dürfen und eure Unterstützung in den letzten Jahren hat mir sehr geholfen!

Mein allergrößter Dank geht an meine Familie für eure große Unterstützung! Danke dir Mias für die Hilfe mit R! Das wir das damals miteinander durchgegangen sind hat mir wirklich sehr geholfen, und bei zukünftigen Informatikfragen werde ich dich weiterhin mit meinen Fragen löchern. Mama und Papa euch kann ich gar nicht genug danken für eure großartige Unterstützung in all den Jahren. Angefangen vom ersten Chemiekasten bis zum Studium habt ihr mich immer unterstützt und gefördert! Euer großes Interesse an dem, was ich den ganzen Tag so treibe hat oft dazu geführt, dass ich euch bis ins Detail erklären musste, wie manche Geräte oder biologische Prozesse funktionieren. Auch wenn das nach einer langen Woche manchmal etwas fordernd war, hat es mich immer sehr gefreut, dass ihr euch so dafür interessiert was ich mache!

Und zum Schluss möchte ich dir Hannah ganz besonders danken! Vielen vielen Dank für deine jahrelange liebevolle Unterstützung, deine aufbauenden Worte, wenn es mal nicht so lief und deinen Rückhalt!

1. Molecular target elucidation of vioprolide A in human cancer cells

2. -omics insights into the ClpXP machinery of *Staphylococcus aureus*

3. Experimental part

Introductory Remarks

This doctoral dissertation was accomplished between March 2015 and December 2019 under the supervision of Prof. Dr. Stephan A. Sieber at the Chair of Organic Chemistry II of the Technische Universität München

Parts of this thesis have been published in:

Volker C. Kirsch*, Christina Orgler*, Simone Braig, Irmela Jeremias, David Auerbach, Rolf Müller, Angelika M. Vollmar, Stephan A. Sieber, *The cytotoxic natural product vioprolide A targets nuelcolar protein 14, which is essential for ribosome biogenesis*, Angew. Chem. Int. Ed., **2019**, doi: 10.1002/anie.201911158

Publications not highlighted in this thesis:

Pavel Kielkowski, Isabel Buchsbaum, Volker C. Kirsch, Nina C. Bach, Silvia Capello, Micha Drukker, Stephan A. Sieber, *FICD activity and AMPylation remodelling modulate human neurogenesis*, Nature Communications, accepted; bioRxiv, doi: 10.1101/787929

Anja Fux, Martin Pfanzelt, Volker C. Kirsch, Annabelle Hoegl, Stephan A. Sieber, *Customizing Functionalized Cofactor Mimics to Study the Human Pyridoxal 5'-Phosphate-Binding Proteome*, Cell Chemical Biology, **2019**, 26, *10*, 1461-1468.

Annabelle Hoegl, Matthew B. Nodwell, Volker C. Kirsch, Nina C. Bach, Martin Pfanzelt, Matthias Stahl, Sabine Schneider, Stephan A. Sieber, *Mining the cellular inventory of pyridoxal phosphate-dependent enzymes with functionalized cofactor mimics*, Nature Chemistry, **2018**, 10, 1234-1245.

Franzsika A. Mandl*, Volker C. Kirsch*, Ilke Ugur, Elena Kunold, Jan Vomacka, Christian Fetzer, Sabine Schneider, Klaus Richter, Thilo M. Fuchs, Iris Antes, Stephan A. Sieber, *Natural-Product-Inspired Aminoepoxybenzoquinones Kill Members of the Gram-Negative Pathogen Salmonella by attenuating Cellular Stress Response*, Angew. Chem. Int. Ed., **2016**, 55, *47*, 14852-14857.

* Authors contributed equally to this work.

Summary

Natural products are a particular rich source for lead structure identification in drug development due to their manifold composition and often complex stereochemistry. In consequence, numerous natural products, *e.g.* taxol and penicillin, turned into successful drugs today and greatly improved the life of patients. Yet new drugs and modes of action are needed in pharmaceutical research. In order to decipher the molecular targets and modes of action of compounds with promising biological activities, MS-based proteomics techniques, *e.g.* Activity-based protein profiling (ABPP) and thermal proteome profiling (TPP) are frequently applied.

The peptolides vioprolide A-D (VioA-D) were isolated in 1996 from *Cystobacter violaceus*. However, besides their general antifungal and potent cytotoxic activities detailed modes of action studies are so far not reported. Inspired by their bioactivity and unique structural composition their antiproliferative activities were determined in different cancer cell lines. VioA, the most potent member of this compound class was subjected to further, detailed biochemical characterization experiments, revealing striking activity against acute lymphoblastic leukemia (ALL) cell lines Jurkat and CEM. Additionally, a selective apoptosis induction in patient derived ALL cells in comparison to healthy peripheral blood mononuclear cells (PBMCs) could be identified for VioA. Inspired by these findings, target identification experiments were conducted to identify the protein targets of VioA in Jurkat cancer cell line.

Initial target identification experiments were conducted using Affinity based protein profiling (A*f*BPP). Therefore, VioA was furnished with a photocrosslinker moiety resulting in probe VioA-P. Despite potent bioactivity, mass spectrometry (MS) based target identification experiments with probe VioA-P remained inconclusive, and potential reasons therefore are discussed.

In consequence, *in situ* thermal proteome profiling (TPP) was applied as modification-free target identification method, revealing nucleolar protein 14 (NOP14) and U2 snRNP-associated SURP motif-containing (U2SURP) as potential targets of VioA. Whereas U2SURP could not be confirmed as target in subsequent validation experiments, NOP14 was validated as target of VioA using multiple biochemical and proteomics-based experiments. NOP14 is part of the small subunit (SSU) processome, and is reported to posess an essential fuction in ribosome biogenesis. Validation experiments showed, that VioA treatment leads to selective disruption of the interaction between NOP14 to one of

its binding partners within the SSU processome, namely ribosomal RNA small subunit methyltransferase NEP1 (EMG1). In contrast, interaction to another interaction partner within this complex Nucleolar complex protein 4 homolog (NOC4L) remains intact. Even though these findings indicate a unique mode of action exhibited by VioA, further validation experiments are required to link the loss of interaction to the antiproliferative and apoptosis inducing activities of this natural product.

The ClpXP machinery depicts a major proteolytic complex with reported regulating role in expression of virulence factors in the human pathogen *S. aureus*. Detailed studies on the global influence on gene expression of ClpP and ClpX using genetic mutants have been reported in literature.

Here, an unbiased evaluation of the effects of ClpP and ClpX on protein translation have been carried out. By comparing expression levels of two genetic deletion mutants, namely *S. aureus ΔclpP* and *S. aureus ΔclpX* as well as active site point mutant strain *S. aureus* S98A relatively to the parental strain *S. aureus* NCTC 8325, altered proteins and pathways could be identified using a MS-based whole proteome analysis. Proteins and protein clusters depending on the sole presence of ClpP regardless of its functional activity were identified in comparison between a ClpP deletion mutant *vs*. a S98A ClpP point mutant. In addition to the evaluation of altered intracellular proteins, a MS-based secretome analysis was carried out to identify altered levels of secreted virulence factors and membrane-bound proteins.

Unbiased proteomics experiments were complemented with initial untargeted metabolomics studies to reveal metabolites influenced by ClpP and ClpX. Even though preliminary results of the metabolomics study could be linked to altered pathways in the whole proteome analysis further experiments are obligatory to validate these findings.

Zusammenfassung

Naturstoffe sind stellen eine reichhaltige Quelle für die Identifikation von Leitstrukturen in der Medikamentenentwicklung, aufgrund ihrer vielfältigen Zusammensetzung und oft komplexen Stereochemie dar. Viele Naturstoffe, wie zum Beispiel Taxol und Penicillin entwickelten sich zu erfolgreichen Arzneimitteln, die das Leben von Patienten wesentlich verbesserten. Nichts desto trotz werden neue Medikamente und Wirkmechanismen in der pharmazeutischen Forschung benötigt. Häufig werden zur Identifizierung der Angriffsziele und Wirkmechanismen von Molekülen mit vielverspechenden biologischen Aktivitäten massenspektrometrie-basierte Methoden, wie z.B. Aktivitäts-basiertes Protein Profiling (ABPP) und Thermisches Protein Profiling (TPP) verwendet.

Die Peptidolide Vioprolid A-D (VioA-D) wurden erstmals 1996 aus dem Bakterium *Cystobacter violaceus* isoliert. Obwohl ihre breite antifugalen und potente zytotoxischen Aktivitäten bekannt sind, wurden noch keine detaillierten Studien zu ihren Wirkmechanismen veröffentlicht. Aufgrund ihrer Bioaktivität und der einzigartigen chemischen Struktur wurden die antiproliferativen Eigenschaften der Vioprolide A-D in verschiedenen Krebszelllinien evaluiert. VioA, das potenteste Mitglied der Familie wurde für weitere eingehende Studien verwendet und zeigte auffallend potente Aktivitäten gegen die akuten lymphoblastischen Leukämiezelllinien Jurkat und CEM. Des weiteren wurde eine selektive Apoptoseinduktion in ALL Patientenkrebszellen im Vergleich zu gesunden mononukleären Zellen des peripheren Blutes festgestellt. Aufgrund dieser Ergebnisse wurden Zielproteinidentifizierungsexperimente durchgeführt um die Angriffziele von VioA in Jurkat Krebszellen zu identifizieren.

Erste Zielproteinidentifizierungsexperimente wurden mittel Affinitäts-basiertem Protein Profiling (A*f*BPP) durchgeführt. Hierfür wurde VioA mit einem Photokreuzvernetzer modifiziert, und dadurch die Sonde VioA-P synthetisiert. Obwohl die Sonde vergleichbare Bioaktivitäten wie der ursprüngliche Naturstoff aufwies, konnte kein eindeutiges Angriffziel mittels massenspektrometrie-gestützen Zielproteinidentifikationsexperimente identifiziert werden. Potentielle Gründe hierfür wurden in dieser Arbeit diskutiert.

Aufgrund dessen wurden ein Thermisches *in situ* Protein Profiling (TPP) als derivatisierungsfreie Methode durchgeführt. Dadurch wurden das nukleoläre Protein 14 (NOP14) sowie U2 snRNP-associated SURP motif-containing Protein (U2SURP) als potentielle Angriffsziele von VioA identifiziert. U2SURP konnte nicht als Zielprotein von VioA validiert werden. NOP14 hingegen wurde als Zielprotein von VioA mittels diverser

biochemischen und Massenspektrometrie-gestützten Experimente validiert. NOP14 ist Bestandteil des small subunit (SSU) processome, und nimmt eine essentielle Rolle in der Ribosom Biogenese ein. Validierungsexperimente zeigten, dass VioA Behandlung zu einer selektiven Störung der Interaktion zwischen NOP14 und einem seiner Bindungspartner, Ribosomale RNA Methyltransferase NEP1 (EMG1), innerhalb des SSU Processome. Im Gegensatz dazu, wurde die Bindung zum Nucleolar Complex Protein 4 Homolog (NOC4L) nicht durch die Behandlung beeinträchtigt. Obwohl diese Ergebnisse auf einen einzigartigen Wirkmechanismus hinweisen, sind weitere Experimente nötig um den Interaktionsverlust zwischen NOP14 und EMG1 mit den antiproliferativen und Apoptose induzierenden Aktivitäten dieses Naturstoffs in Verbindung zu bringen.

Der ClpXP Komplex stellt einen der wichtigsten proteolytischen Komplexe in *Staphylococcus aureus* dar, und wird mit der Regulation von Virulenzfakatoren in Verbindung gebracht. Detaillierte Studien zum Einfluss von ClpP und ClpX auf die globale Genexpression in *S. aureus* mittels genetischer Mutanten wurde mehrfach in der Literatur beschreiben.

Im Rahmen dieser Arbeit wurde der generelle Effekt von ClpP und ClpPX auf die Proteintranslation durchgeführt. Durch den Vergleich der Proteinexpression zweier genetischer Deletionsmutanten (*S. aureus ΔclpP* and *S. aureus ΔclpX*), sowie einer inaktiven ClpP Punktmutante (*S. aureus* S98A ClpP) mit dem Wildtyp *S. aureus* NCTC 8325 lieferte Einblicke in dysregulierte Proteine und Proteinnetzwerke. Des Weiteren, wurden Proteine und Proteinnetzwerke die allein von der Präsenz von ClpP, unabhängig der funktionellen Aktivität durch einen direkten Vergleich der *clpP* Deletions- und der S98A Punktmutante identifiziert. Zusätlich zur Analyse der intrazellulären Proteine wurde eine MS-basierte Sekretomanalyse durchgeführt und dabei dysregulierte sekretierte Virulenzfaktoren und membrangebundene Proteine identifiziert.

Die Proteomikexperimente wurden durch die Durchführung von ersten ungerichteten Metabolomik Studien um den Einfluss von ClpP und ClpX auf das Metabolom zu untersuchen erweitert. Obwohl die vorläufigen Ergenisse mit dysregulierten Stoffwechselwegen in Verbindung gebracht wurden konnten sind weitere Experimente von Nöten um dies zu bestätigen.

Chapter I - Molecular target elucidation of vioprolide A in human cancer cells

The following chapter is based upon work published in Kirsch, V.C., Orgler, C., Braig, S., Jeremias, I., Auerbach, D., Müller, R., Vollmar, A..M. and Sieber, S..A. (2019), The cytotoxic natural product vioprolide A targets nucleolar protein 14 essential for ribosome biogenesis. Angew. Chem. Int. Ed.. Accepted Author Manuscript. doi:10.1002/anie.201911158.

Note: Cell viability assays, immunostaining and immunoblotting experiments as well as nuclear run on assays and XCELLigence experiments were carried out by Christina Orgler in the laboratory of Prof. Dr. Angelika M. Vollmar at Ludwig-Maximilian Universität München.

1. Molecular target elucidation of vioprolide A in human cancer cells

1.1. Introduction

1.1.1. Natural products – taking advantage of nature's tool box

1.1.1.1. Natural products in anticancer therapy

According to the world health organization (WHO), cancer is one of the preeminent causes of death with approximately 18.1 million new cases and 9.6 million fatalities in 2018 worldwide.[1] The severity of this burden of health is further illustrated by the fact, that cancer replaced cardio-vascular diseases as leading cause of death in high-income countries in the age cohort of 35-70.[2] However, cancer as severe disease is not restricted to high-income country but is a global health issue, being one of the leading causes of death in low-income countries.[1] However, due to improvements in diagnostic techniques (*e.g.* identification of biomarkers) and therapeutic options (*e.g.* selective chemotherapeutic agents, immunotherapy), cancer survival rates are increasing.[3-5]

Traditionally, nonspecific chemotherapy [*e.g.* using *cis*-platin, 5-fluorouracil (5-FU), taxol] has been standard treatment for different types of cancer for decades. However, as a result of to their non-specific mode of action targeting cell division in general (*e.g.* DNA-replication) these treatments entailed a broad range of adverse effects.[6,7] The introduction of targeted chemotherapy, *e.g.* axitinib and sorafenib for the medication of renal cell carcinoma, significantly improved treatment results and cancer therapy.[8] Compounds optimized for specific molecular and cancer relevant targets led to increased survival rates and reduced side effects, hence making chemotherapy more tolerable for patients.[9] However, based on occurring resistances against applied drugs and the highly complex and diverse appearance of cancerous diseases, cancer therapy is in need of new molecular targets as well as therapeutic agents with novel modes of action.[10,11]

A particular fruitful source of new chemotherapeutic agents are natural products, repeatedly derived from bacteria, fungi, plants and marine sources. These bioactive secondary metabolites are frequently characterized by their unique and structural highly diverse scaffolds, often furnished with complex stereochemistry. Their diverse chemical space makes them a vulnerable source for drug discovery.[12,13]

A great number of FDA-approved drugs (approx. 50%) are natural products or related derivatives, underlining their impact on drug discovery and lead structure identification.[14,15] Examples of natural products being successfully applied in cancer therapy are amongst others taxol and actinomycin D (ActD). However, due to several drawbacks as hindered synthetic accessibility and low extraction rates from the organisms of origin, pharmaceutical industry preferred synthetic libraries for high-throughput screens in lead identification in the last decades. Despite the expectations, success rates of synthetic libraries were limited over the last years as the chemical space these molecules is limited. With new methods evolving and industry becoming aware of the benefits of natural products over synthetic compounds, these molecules experience a resurgence in drug discovery.[13]

1.1.1.2. Myxobacteria – a fruitful source for bioactive natural products

Myxobacteria are δ-proteobacteria, which can be found globally spread from tropical rain forests, over the entire European continent to areas with extreme climatic conditions, *e.g.* in arctic and desert soils.[16] Myxobacteria originally attracted interest in microbiology research as they have unique features distinguishing them from other bacteria.[17,18]

These gram-negative rod-shaped bacteria live in swarm colonies and move by gliding and creeping over surfaces. Due to a sophisticated communication system they are capable of moving their swarm into a certain direction and even hunt together with individual cells taking over certain tasks. A second unique characteristic of myxobacteria is their capability of forming spore-containing fruiting bodies under hostile conditions. Triggered by starvation, extreme temperatures or acidic pH conditions swarming myxobacteria undergo cooperative and individual morphogenesis. This conversion leads to the formation of characteristic fruiting bodies with part of the myxobacterial population undergoing individual morphogenesis into myxospores. The transition into spores enables the swarm to survive conditions such as heat, dryness and UV radiation. Once living conditions improve, the spores are able to initiate the establishment of a new swarm.[16,19]

Besides these unique characteristics, myxobacteria are also known for having a comparatively large genome (9-16 Mb) among the bacterial kingdom with an exceptional high percentage encoding gene clusters for the production of secondary metabolites.[20,21] This genetic wealth presumably enables myxobacteria to produce a great variety of secondary metabolites they secrete into an extracellular matrix and functions as a defense mechanism against enemies.[22,23] These secreted bioactive natural products often bear great structural variety and unique scaffolds with several molecular skeletons exclusively found in myxobacteria.[23]

Over 600 compounds with promising antibacterial, antiviral, antifungal and cytotoxic activities were reported to date, making myxobacteria a particular comprehensive source for bioactive natural products for lead structure identification in drug development.[18,24,25]

For some of these cytotoxic substances, the respective mode of actions could already be deciphered, and numerous cytotoxic myxobacterial natural products target the cytoskeleton by for example either stabilizing (*e.g.* epothilone B[26,27]) or destabilizing (*e.g.* tubulysin[28-30]) actin polymers.[23] However, also other targets in cancer cells are addressed by cytotoxic secondary metabolites such as V-ATPase (archazolides[31,32]), the proteasome

(argyrines[33,34]) and protein biosynthesis (gephyronic acid[35-38]) in general. But myxobacterial natural products do not solely address proteinogenic targets, as *e.g.* saframycin Mxl[39] exerts its potency by targeting DNA.[18] (Figure 1)

The importance of cytotoxic substances of myxobacterial origin for anticancer drug development is further emphasized by the fact, that a synthetic derivative of epothilone (Ixabepilone®) received FDA approval for the application against an aggressive form of breast cancer.[40]

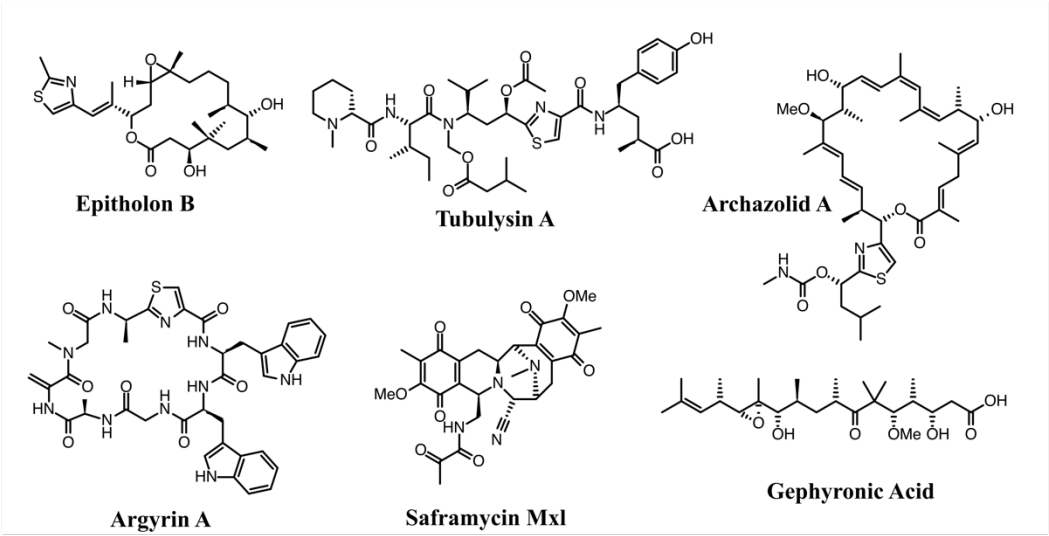

Figure 1: Selected bioactive secondary myxobacterial natural products.[18]

However, the modes of action of the majority of the so far discovered myxobacterial compounds remain elusive. The group includes amongst other the vioprolides A-D.[18]

1.1.1.3. The vioprolides A-D

Vioprolides A-D, reported from *Cystobacter violaceus* Cb vi35 in 1996[41], are cyclic peptolides consisting of eight amino acids and glyceric acid. Their biosynthetic assembly has been deciphered recently.[42,43] The vioprolides are reported to exhibit potent cytotoxic and antifungal activities but lack antibacterial properties.[18,41] Whereas the majority of structural motifs in this compound class is conserved, the class members only differ in ring sizes of both aza heterocycles located at the western and northern part of the molecule (Figure 2). Vioprolide A and C bear a 4-methylazetidinecarboxylic acid (MAZ) structural moiety in the northern part of the molecule (indicated in red, Figure 2). Interestingly, this represents a structural motif so far unreported in natural products.[42] In vioprolide B and D, this MAZ moiety is replaced by L-proline (indicated in red). The heterocycle in the western part of these natural products class either consist of L-proline or L-homoproline (indicated in blue).

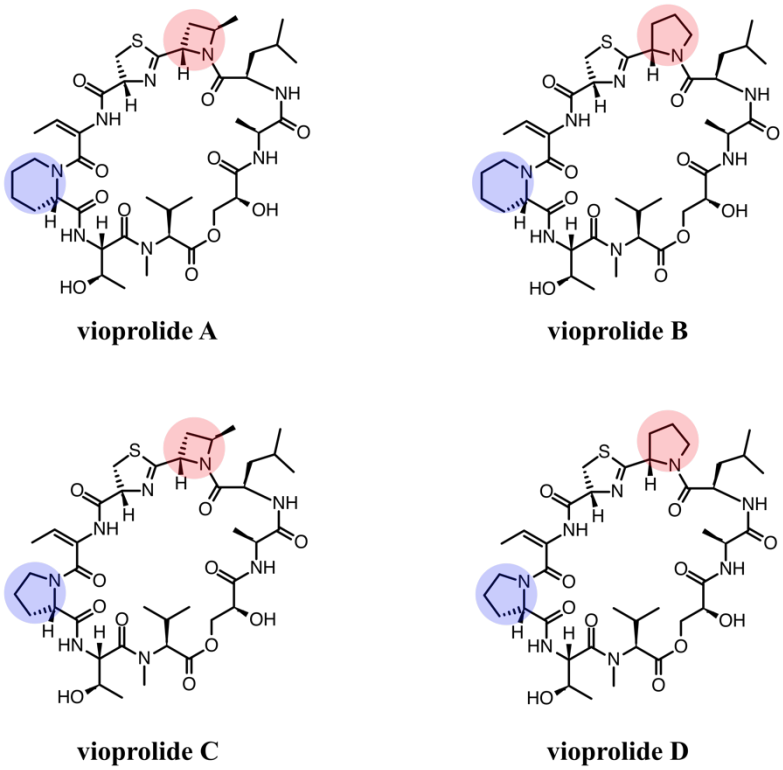

Figure 2: Structures of vioprolides A-D. Structural differences between class members indicated in blue and red.[41]

The deviation in ring sizes is reported to exhibit a dramatic effect on bioactivity. Whereas vioprolide D is reported to exhibit the most potent anti-fungal potency, it is the least active

of the four derivatives against mammalian cells. *Vice versa*, vioprolide A – the most cytotoxic derivative – shows the poorest activity towards fungi.[41]

In contrast to the detailed studies about their biosynthesis, knowledge about their biological activity was limited to the above mentioned general potent antifungal and anti-cancer activities in the nanomolar range. One recently published study revealed an immunomodulatory effect of the vioprolides by functioning as an activator of IL-1β maturation and inducer of intrinsic apoptosis in primary murine macrophages.[44] Additionally, an interference with DNA-replication has been postulated lately.[45] However, the molecular mode of action leading to the potent cytotoxic activity of the vioprolides has not been deciphered so far.

1.1.2. Deciphering new targets in cancer therapy – the nucleolus and ribosome biogenesis

1.1.2.1. The nucleolus and ribosome biogenesis

Cells are in consistent need of freshly synthesized proteins, synthesized by ribosomes, for cellular growth or to replace proteins which exceeded their life span. These macromolecular machines are essential for protein biosynthesis in cells and consist of a small ribosomal subunit (40S) and a large ribosomal subunit (60S), each fulfilling distinct operations during protein biosynthesis. The 40S subunit, consisting of 18S rRNA and 33 ribosomal proteins (RPs), unravels and reads mRNA (messenger RNA). The 60S subunit, consisting of 5S, 5.8S and 28S rRNA and 47 RPs, is responsible for peptide bond formation and subsequent quality control of synthesized peptides.[46] Ribosomes are produced in a process termed ribosome biogenesis, with most of the steps carried out in the nucleolus.

The nucleolus is a sub-nuclear compartment in most eukaryotic cells, initially described in the first half of the 19th century.[47] Even though not encapsulated within a membrane, the nucleolus depicts a highly dense structure in the nucleus, mainly consisting of rDNA (ribosomal DNA), rRNA (ribosomal RNA), histones and proteins involved in ribosome biogenesis, *e.g.* RNA polymerase I (Pol I).[48,49] Yet consisting of a definite structure, Nucleoli are highly dynamic and assemble and disassemble in a cell cycle dependent manner. They are built up in G1 phase in proximity to nucleolar organizer regions (NORs), regions of rDNA repeat units encoding for rRNA, at acrocentric chromosomes.[50]

Only recently is known that the nucleolus takes over crucial tasks within the cell, *e.g.* DNA replication and repair as well as cell cycle control. However, its unique feature is its key task as main locus of ribosome biogenesis, being responsible for rRNA transcription and maturation as well as assembling the ribosome. Ribosome biogenesis is initiated by the transcription of the 47S pre-rRNA from rDNA by RNA polymerase I (Pol I). This 47S pre-rRNA, together with ribosomal proteins (RPs) - transcribed by Pol II and reimported after their maturation into the nucleolus – and the 5S rRNA transcribed by Pol III are assembled to form the 90S processome. Further maturation of the 90S processome, including processing of the 47S pre-rRNA to 18S, 5.8S and 28S rRNAs, leads to the generation of the pre small ribosomal subunit (pre-40S) and pre large ribosomal subunit (pre-60S). Additional separated maturation steps lead to 40S and 60S subunits, shuttled to

the cytoplasm, where they are assembled to the functional ribonucleoprotein complex for protein biosynthesis after final maturation steps (Figure 3).[50-53]

The entire construction process of ribosomes depicts a highly complex procedure, illustrated by the need of an arranged interplay of three RNA polymerases, over 200 ribosome assembly factors as well as 80 small nucleolar RNAs (snoRNAs).[54]

Ribosome biogenesis represents a great effort for eukaryotic cells. More than 80% of synthesized RNA in mammalian cells are rRNAs and each cell contains between 5 and 10 million copies of ribosomes. These molecular machines have to be synthesized and structurally controlled in an augmented amount during the process of cell proliferation and division making ribosome biogenesis a highly energy-intensive process within the cell.[46,54-56] As discussed above, ribosome biogenesis is of fundamental importance for protein synthesis and depicts a highly sensitive and dynamic mechanism just recently known as being tightly linked to biological processes, *e.g.* cell growth and division.

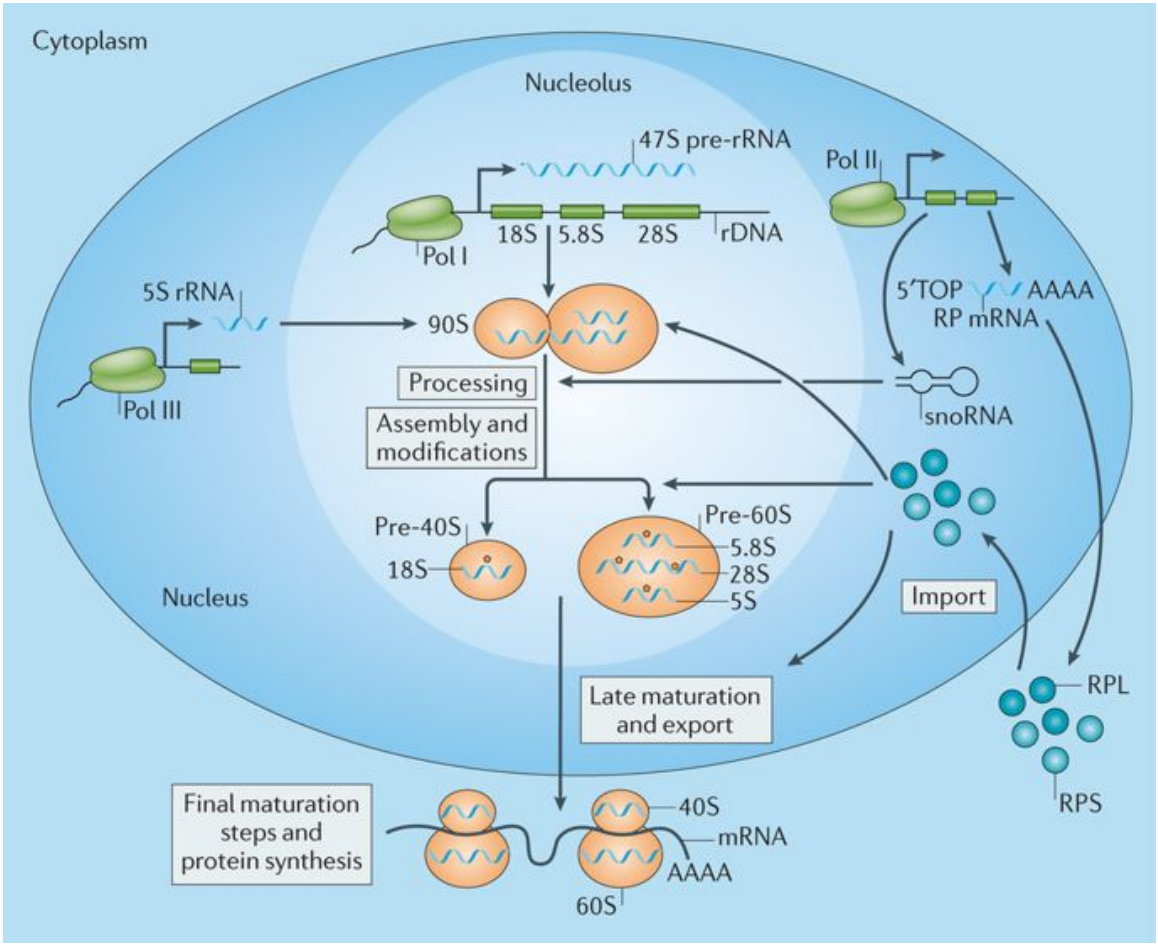

Figure 3: Schematic overview ribosome biogenesis. Figure adapted from Pelletier *et al.*[46] Reprinted with permission.

1.1.2.2. Ribosome biogenesis in cancer

Cancer cells are characterized by their rapid non-regulated growth and proliferation, accompanied with elevated protein biosynthesis, therefore requiring an upregulated ribosome biosynthesis. The connection between enlarged nucleoli and malignant growth has been linked decades ago. Later it was deciphered that augmented nucleoli size is derived from an elevated rDNA transcription and thus elevated ribosome biosynthesis.[57] Dysregulated ribosome biogenesis in cancer is often based on two general modes: hyperactivated ribosome biogenesis or qualitative changes in ribosome biogenesis, which were reviewed in detail previously.[46]

Transcription of rRNA by Pol I and Pol III is considered as the rate limiting step in ribosome biogenesis, and thereby tightly controlled by diverse surveillance pathways and proteins, with some of them known to have crucial roles in cancer development. Pol I transcription is controlled - and in terms of cancer overactivated - amongst others by proto-oncogenic MYC[58-60] leading to enhanced ribosome biogenesis. Downregulation is initiated for example by tumor suppressing signaling pathways including p53 and retinoblastoma protein (pRb).[46,61]

However, dysregulation of ribosome biogenesis is not restricted to altered rRNA synthesis but can, as mentioned above, also be hampered by arising rRNA mutations and non-tangible control mechanisms leading to the synthesis of impaired ribosomes. These defective ribosomes can lack individual ribosomal proteins or contain mutations within these proteins leading to defective translation patterns.[46]

1.1.2.3. The nucleolus and ribosome biogenesis – targets for cancer therapy

With increasing knowledge in ribosome biogenesis and its nestling between biological pathways with crucial impact on cell proliferation and potential cancer development, ribosome biogenesis and its location, the nucleolus, recently gained more attention as potential drug targets.[53,62,63]

Even though compounds specifically targeting ribosome biogenesis are still rare, it has been shown that some FDA-approved drugs, known to target DNA (*e.g.* ActD, 5-FU, cis-platin), partly also interfere with rRNA transcription at different stages, *e.g.* initial transcription or subsequent processing steps. However, their contribution on the inhibition of ribosome biogenesis is not determined yet.[62,64] ActD was actually shown to exclusively inhibit rRNA transcription at low concentrations, as the compound has a binding preference for GC rich DNA sections, which are present in an augmented manner in rDNA repeat units. Numerous other molecules have been shown to interfere with rRNA transcription and have been reviewed recently.[64,65]

As mentioned above, cancer cells have an elevated rRNA transcription *via* Pol I in common. Thereby, the selective disruption of Pol I is regarded as an emerging target in cancer therapy and selective Pol I inhibitors are under development. Pol I inhibitors are considered as less genotoxic, therefore causing selective damage to cancer cells while affecting healthy cells significantly less.[66] One of the first published specific inhibitors for Pol I is CX-5461. It could be shown, that these Pol I inhibitors selectively inhibited rDNA transcription without interfering with DNA, RNA and protein synthesis thereby selectively triggering p53 dependent apoptosis in B-lymphoma cells while healthy B cells remain unaffected.[67,68]

The reduced genotoxicity on the one hand, and potent activity towards cancer cells on the other hand, makes RNA polymerase I interfering compounds a promising strategy for anticancer therapy development.[53,68] Multiple inhibitors are known to interfere with ribosome biogenesis at early stages of the biological process, *e.g.* on the level of rRNA transcription (*e.g.* CX-5461), during rRNA processing steps (*e.g.* natural product haemanthamine), or as functional inhibitors of mature ribosomes (*e.g.* haemanthamine, and natural products homoharringtonine). However, no inhibitor is known to-date for the steps of ribosome assembly and ribosome export, which presumably also evokes from a limited knowledge about these processes, which are far more understood in yeast.[53]

1.1.3. Locks and keys – strategies to identify drug-target engagements

Technical advancements in the last decades entailed the development of diverse techniques in drug discovery, applicable to target deconvolution and mode of action studies of bioactive compounds derived from phenotypic screens. Techniques to study drug-target interactions regularly used are amongst others genomics (*e.g.* gene expression microarrays and cDNA microarrays)[69,70], chemical genetics (*e.g.* yeast-three hybrid system)[71,72] and proteomics[73]. While genomics has been already used for decades, proteomics entered the field as complementary technology in the early 2000s.[74,75] Especially improvements in resolution, sensitivity and speed of tandem mass spectrometers [mostly time-of-flight (TOF) and orbitrap mass spectrometers], ionization techniques [(electron spray ionization (ESI) and matrix-assisted laser disruption/ionization (MALDI)] as well as increased separation resolution of liquid chromatography systems enabled proteomics to contribute effectively to the drug discovery process.[76,77] Proteomics today is applied in multiple stages during the drug discovery process such as biomarker identification, protein expression profiling and target identification.[77]

Chemical proteomics (also termed chemoproteomics) is a sub-category of proteomics focusing on the effects bioactive small molecules exert on proteome level, thereby aiding to unravel the respective modes of action by target identification and identifying affected pathways.[78-80] Whereas techniques like whole proteome analysis and analysis of post-translational modifications, are utilized for the unbiased discovery of compound-induced altered expression levels of a set of proteins, more compound-centric approaches are employed for ligand-target binding event studies. Here, the affinity of small bioactive molecules towards their respective targets is identified and quantified. These techniques have proven to be particular useful to identify proteinogenic targets of first-in class drugs and bioactive natural products derived from phenotypic screens.[79] In addition, this technique is also applied for the identification of additional targets of approved drugs, in order to deconvolute the reason of their adverse effects.[81,82]

Two principal categories for the deconvolution of ligand-target binding events are distinguished in chemical proteomics: first, so called direct methods for target identification, *e.g.* activity-based protein profiling (ABPP) and affinity-based protein profiling (A*f*BPP) and second, protein stability-based methods (also known as capture-free

methods), *e.g.* thermal proteome profiling (TPP), drug affinity responsive target stability (DARTS)[83] and stability of proteins from rate of oxidation (SPROX).[79,80]

1.1.3.1. Activity- and Affinity based proteomics

First examples of ABPP target identification experiments were published in the 1990s by *Powers* and *Walker*. By exploiting isocoumarin derived probes and peptidyl phosphonate ester probes, *Powers et al.* were able to study and isolate serine proteases in human cancer cells.[84,85] *Walker et al.* identified cathepsin b-like enzymes in cancer cells by utilizing a biotinylated dipeptide probe.[86] The methodology was further developed and termed activity-based protein profiling by *Cravatt et al*.[87,88] and *Bogyo et al*.[89-91]

Activity- and affinity based proteomics methods are aimed at the identification of proteinogenic binding partners (also referred to as targets) of molecules under study against a complex biological background (*e.g.* cell lysates or living cells). These methods are based on the principle, that bioactive molecules bind selectively and with high affinity to their respective targets in a covalent or non-covalent manner. Coercively furnished with a tag moiety, these molecules are subsequently termed activity-based probes (ABPs). Depending on the functionality of the applied tag, bound enzymes can be visualized or purified.[87,92]

ABPP uses chemical probes bearing a reactive group (also termed warhead), designed to covalently trap nucleophilic residues in the active sites of specific enzyme classes (*e.g.* kinases, cysteine proteases, serine hydrolases, phosphatases).[88,93] However, as numerous enzymes are expressed as zymogenes, their activity in the cell is regulated by post-translational modifications.[89]

Therefore, technologies focusing solely on protein expression levels rather than on the respective activity state, can only deliver rough estimations on disease-related enzyme activities.[87] In contrast, labelling patterns of ABPP probes are independent of protein expression levels as these probes are designed to exclusively bind to active enzymes. Thereby, these chemical tools enable the elucidation of a disease-related overactivation or impaired activity of an entire enzyme class.[94] Unlike other technologies, ABPP is able to monitor enzyme activity for specific enzymes but also of entire sub-classes of enzymes, the technology can contribute in a complementary manner to the drug discovery process, by providing an in-depth insight into disease specific enzyme dysregulation.

But the use of ABPP is not restricted to the monitoring of disease-related dysregulation of enzyme activities. Over the last decade, natural product derived probes have been successfully applied to decipher the targets of these natural products and elucidate their modes of action, thereby providing new therapeutic opportunities for drug discovery.[95]

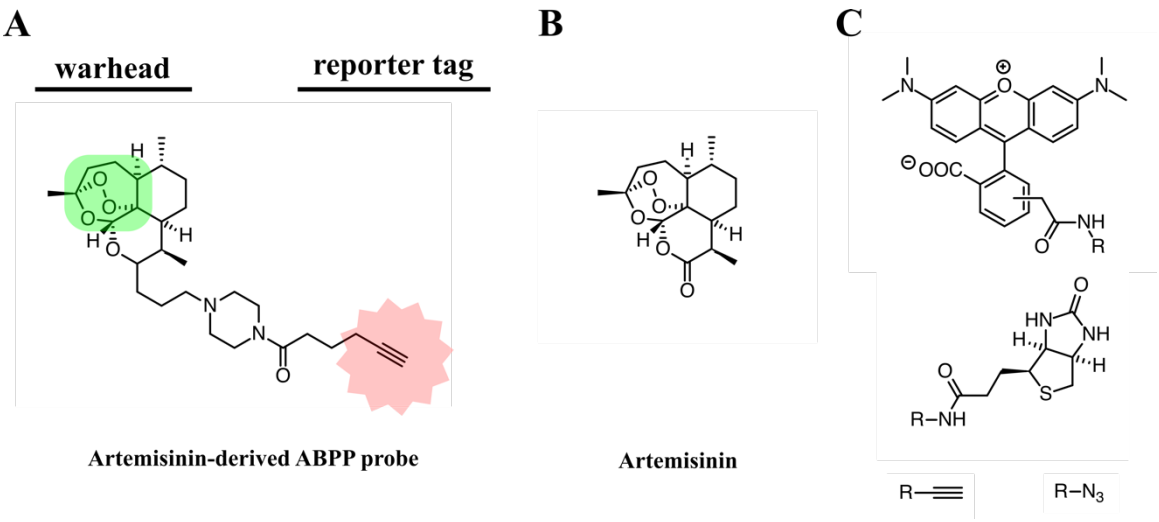

Figure 4: A) Natural product Artemisinin based ABPP probe[96] with warhead highlighted in green and tag (here terminal alkyne) highlighted in red. **B)** Artemisinin natural product[96] **C)** Frequently used reporter tags from top to bottom: rhodamine fluorescence dye, biotin, and analytical handles terminal alkyne and azide.[88]

As lined out above, ABPP probes consist of an electrophilic group (also called warhead), *e.g.* general electrophilic moieties such as fluorophosphonates, enones and epoxyketones, vinylsulfones. In a more complex setting an entire natural product bearing an electrophilic reactive group can function as a warhead template, as depicted here on the example of an artemisinin derived probe (Figure 4A, Parent compound Figure 4B).[87,96-98]

A second important part of the probe is a reporter tag for visualization or enrichment of labeled proteins (Figure 4A and B). A wide array of reporter tags can be found in literature applied in ABPP experiments, *e.g.* radioactive labels[99], biotin, fluorescent dyes as well as analytical handles (*e.g.* terminal alkynes or azides).[87] These analytical handles can react selectively in a bioorthogonal copper-catalyzed Huisgen's azide-alkyne cycloaddition (also referred to as "click-chemistry") with reporter tags containing a terminal azide or alkyne respectively against a complex biological background.[100-102] The biggest advantage of the concept of click chemistry is its broad applicability in various matrices (*e.g.* water, cell lysates and even blood serum), wide pH and temperature ranges and therefore has matured to a frequently utilized tool in ABPP experiments.[103]

However, copper catalyzed click chemistry is not the only biorthogonal ligation reaction used to connect the analytical handle of the probe with a reporter moiety. Staudinger ligation[104] and strain-promoted click reaction[105,106] are also widely applied in

ABPP experiments, thereby enabling an application of ABPP in *in vivo* settings as the utilization of toxic copper(I) is circumvented.[107-110] The development of these 'clickable' handles, and the so called two-step labelling[111], depicted a great improvement as the required modification of compounds in probe synthesis was minimized. Whereas the effect is limited if probes are applied to cell lysates (*in vitro*), sterically less demanding azide or alkyne handles have greatly improved cell permeability of probes for *in situ* ABPP experiments in live cells. Most importantly, this optimized workflow enables the design of chemical probes structurally as close as possible to the parent compound, thereby minimizing the alteration in bioactivity.[91] Often, warhead and tag are linked to each other *via* a spacer, which is often used to modulate parameters such as cell permeability and solubility of the ABPP probe.[94]

However, numerous enzyme classes, *e.g.* metalloproteases, methyltransferases or histone deacetylases, do not contain a catalytically nucleophilic moiety in their active site (*e.g.* cysteines and serines), which could be covalently trapped by electrophilic chemical probes and a wide range of inhibitors and natural products exist depicting their potency via a non-covalent mechanism. As covalent attachment of the respective probe to corresponding proteinogenic targets is vital for disruptive downstream workflow steps, these probes have to be additionally furnished with a photoreactive group (*e.g.* benzophenones, aryl azides, diazirines, 2-aryl-5-carboxytetrazoles, diazo groups)[112,113] additionally to the analytical handle. Upon irradiation at specific wavelengths these photocrosslinker enable a durable covalent linkage of the non-covalently binding ligand to the target protein. These probes are termed affinity-based probes (A*f*BPs) and the boarders between affinity-based protein profiling (A*f*BPP) and activity-based profiling become blurred.[97]

Photoreactive groups

Among the mentioned photocrosslinking moieties, diazirines, benzophenones and aryl azides are the most frequently applied in photoaffinity labelling (PAL)[111]. Upon UV-irradiation, these groups form highly reactive intermediates thereby inserting non-specifically into any non-reactive C-H bond in close proximity.

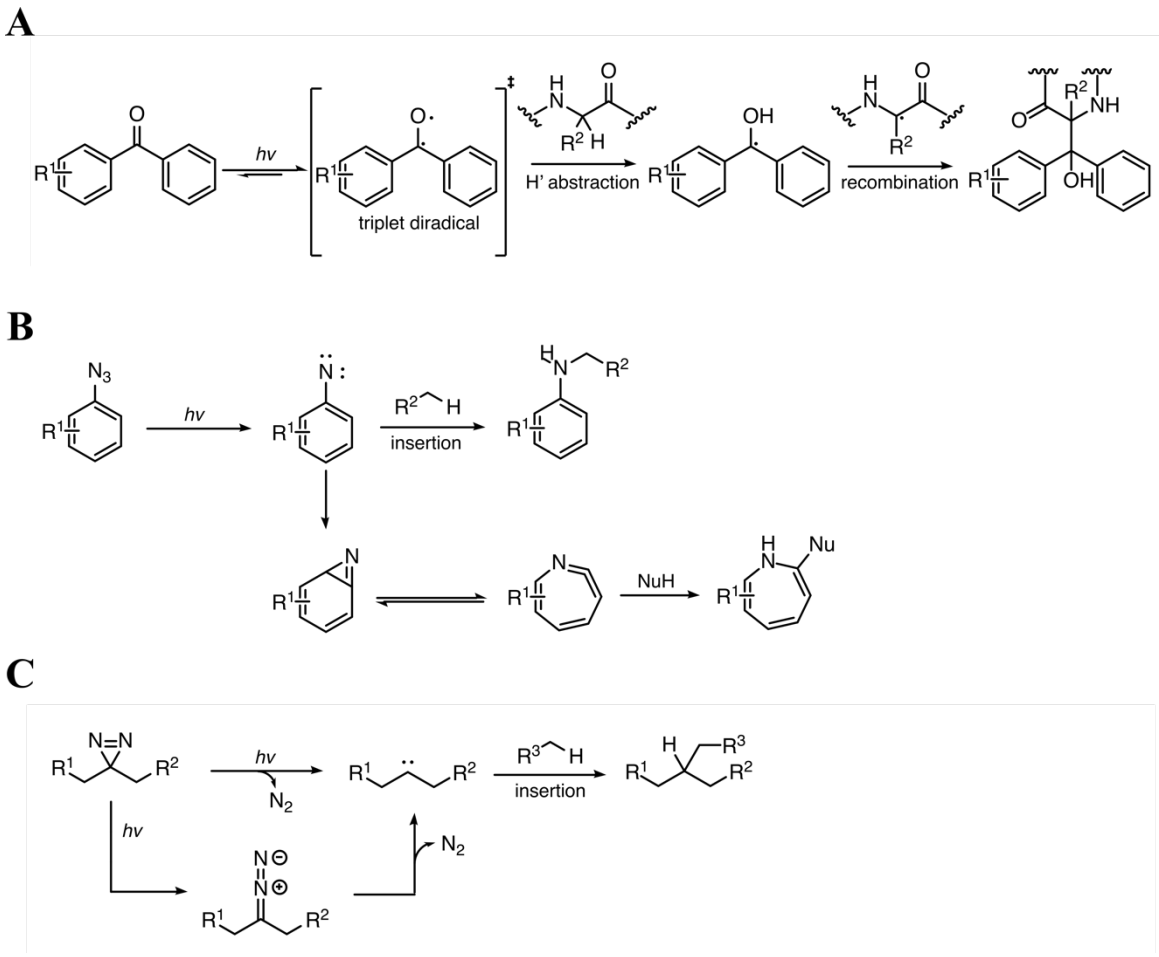

Scheme 1 Commonly applied photocrosslinking moieties and their respective mechanisms upon UV irradiation, exemplarily shown for insertions into C-H bonds. **A)** benzophenones **B)** aryl azides and **C)** diaziriens exemplarily shown for alkyl diazirines.[111]

Whereas all of these moieties have proven to be stable under prevalent synthetic conditions (acidic and basic conditions, thermal), they differ significantly in size, excitation wavelength, potential side reactions and half-life of the activated species.[111] A preferable photocrosslinking moiety is not affecting overall structure of the parent compound in a significant way. In addition, the activated species is solely present for a minimum of time, thereby reducing unspecific binding. Also, the required excitation wavelength is high enough to prevent biological matrix to suffer damage while UV irradiation.

Among the most widely used photocrosslinking moieties, the group of benzophenones depict the sterically most demanding structures. Due to the bulkiness, the integration of this photoreactive group can greatly deviate the structure of the parent compound, thus potentially leading to a significant change in bioactivity. Additionally, the reversible triplet diradical formation upon UV irradiation is stable for a relatively long time before relaxing back into its ground-state if no interaction partner is found. Therefore, unspecific binding events are very likely. The advantage is that the required activation wavelength (350-365 nm) is relatively long.[111]

Less sterically demanding than benzophenones are the aryl azides. Structural perturbation is reduced to a minimum if they are used to substitute for arylic moieties in parent compounds, *e.g.* phenylalanine and adenosines. Upon UV irradiation highly reactive and short living singlet nitrenes are formed by the release of molecular nitrogen. The singlet nitrene can insert into C-H bonds in its proximity, thereby establishing a covalent bond. Same product formation is valid for triplet nitrenes, which can be obtained from singlet nitrenes via intersystem crossing. However, singlet nitrenes can also react by a second mechanism. Upon rearrangement singlet nitrenes can form benzazirines, leading to dihydroazepine in an adjacent rearrangement step. These intermediates are able to react as electrophiles with nucleophiles in proximity. Besides their fast reaction rate and minimal perturbations in parental molecular structure, aryl azides also have diverse disadvantage which cannot be neglected in probe design. Frist, the wavelength needed to generate reactive singlet nitrenes is very short and energetic (< 300 nm) Second, due to multiple reaction pathways of singlet nitrenes, crosslinking efficiency is comparatively low (< 30%).[111]

Introduced for photolabeling in 1973[114] by *Smith* and *Knowles*, diazirines depict a minimal, non-bulky structural perturbation when incorporated into the parental structure in probe design. An additional advantage is their absorption maximum wavelength (360 – 380 nm) is well above the critical wavelength of 300 nm for biological matrices. Upon irradiation of diazirines, a singlet carbene is formed by the release of molecular nitrogen, which can insert into C-H bonds but also O-H and N-H bonds. However, additionally to the formation of a singlet carbene, diazirines can react to the corresponding diazoisomer to a significant extent (>30%). These diazosisomers in turn can also form singlet carbenes under irradiation. However, this process is relatively slow and can be quenched by surrounding water molecules thereby decreasing crosslinking efficiency.[111,112] Due to their minimal size, diazirines can be found in various applications. Besides their frequent use in AfBPP probes, diazirines are also applied for studies of protein-protein interactions.[115]

Workflow of ABPP and A*f*BPP experiments

In ABPP or A*f*BPP experiments for the identification of cellular proteinogenic targets of a compound of interest, cells are incubated with a compound derived chemical probe equipped with a terminal alkyne and, in case of an expected non-covalent binding mode, with an additional photocrosslinking moiety. After incubation with a photoprobe, cells are exposed to UV irradiation to ensure covalent linkage of the photoprobe to the targets, followed by cell lysis. For visualization of labeled proteins, cell lysates are supplemented with a fluorophore containing a terminal azide, covalently attached to the protein bound probes in a subsequent click reaction. Labeled proteins are further separated using sodium dodecyl sulfate polyacrylamide gel electrophoresis (SDS-PAGE) and visualized by fluorescence scanning being compared against vehicle treated cells, in order to distinguish probe dependent labelling from background labelling (Figure 5A).

For enrichment analysis of labeled proteins using mass spectrometry, the workflow step after cell lysis is modified. Instead of utilizing a fluorophore, a terminal azide containing biotin tag is covalently attached to the probe bound to the protein in a click reaction. Taking advantage of the strong avidin-biotin affinity using avidin coated agarose beads, probe tagged proteins can be selectively enriched against the background of the entire complex cellular proteome. Proteins bound to the beads are enzymatically digested in solution using *e.g.* trypsin or chymotrypsin, and subsequently analysed using LC-MS/MS. In order to identify unspecific binding of proteins to the avidin coated beads, the same workflow is carried out with vehicle treated samples (Figure 5B). Numerous isotopic label-based techniques for the quantification of identified peptides have been developed such as metabolic labelling using SILAC (stable isotope labelling by amino acids in cell culture)[116] and multiplexed chemical labelling methods, *e.g.* Dimethyl labelling[117], iTRAQ labels (isobaric tags for relative and absolute quantification)[118] and TMT (tandem mass tag) labels[119]. Besides these label-based techniques, label-free methods[120] are also frequently used in ABPP and other MS-based proteomics experiments[121-124], due to a further optimization of data analysis tools *e.g.* MaxQuant[125,126] However, each of these quantification techniques has its advantages and disadvantages as reviewed recently[127], and the choice of the applied technique has to be adjusted to the experimental setup.

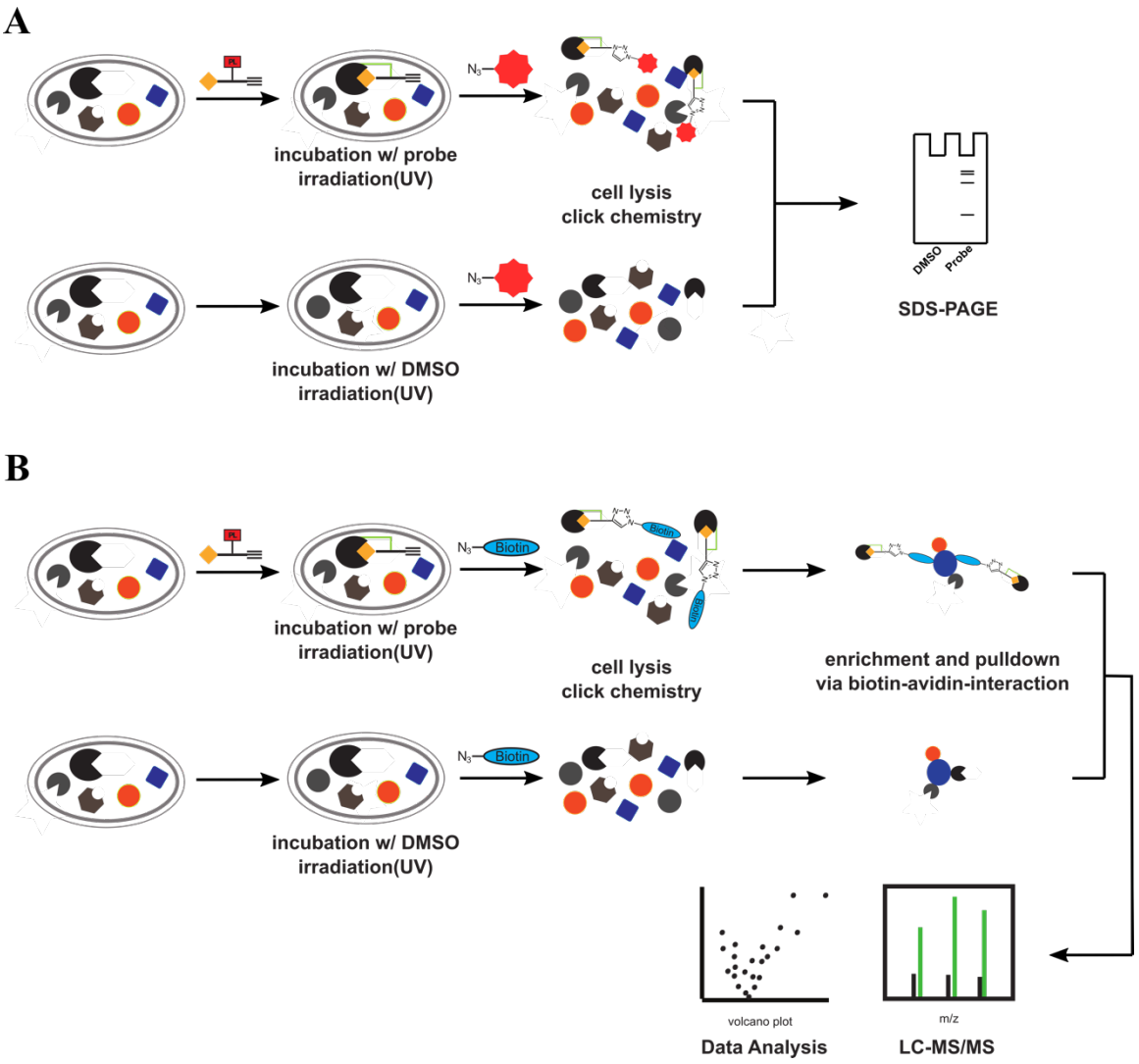

Figure 5: Workflow of AfBPP experiments. A) Gel-based labeling applying fluorescence dyes for visualization of probe labeled protein using SDS-PAGE analysis. Cells are incubated with probe, furnished with a photocrosslinking moiety (PL), or DMSO respectively. Subsequently, labeled cells are subjected to UV-irradiation to ensure covalent linkage (green) to dedicated targets. Finally, cells are lysed and protein-bound probe linked to a fluorescent dye (red) equipped with a terminal azide handle in a click chemistry reaction. Subsequently, proteins are separated using SDS-PAGE and probe-tagged proteins visualized using fluorescence scanning. **B)** Preparative labeling with biotin tags (blue) for enrichment of probe-labeled proteins using avidin beads, subsequent tryptic digest and analysis of resulting peptides *via* LC-MS/MS. Enriched proteins in probe-treated samples relatively to DMSO control are identified in subsequent data analysis steps.

1.1.3.2 Thermal proteome profiling (TPP)

As already discussed, ABPP and A*f*BPP technologies have proven to be highly benificial for the identification of disease specific overactivation or impaired activity of certain enzyme classes as well as target identification. However, the main drawback of these discussed affinity-based methods is the requirement of analytical handles and, in case of photoprobes, additional photoreactive groups. Depending on the size of the modification, structural changes can have great impact on the bioactivity of the probe, originating from a lower affinity towards the original targets of the parent compound. Moreover, even though bioactivity might not drop significantly, the required derivatization might lead to a complete loss of interaction with the respective target, resulting in false-negative target identification. In addition, some molecules, which are synthetically not accessible yet (*e.g.* natural products with no published total synthesis) cannot be transferred into chemical probes easily.

However, the main advantage of capture-free methods, *e.g.* thermal proteome profiling (TPP), is the possibility to apply bioactive molecules directly to target discovery without time-consuming prior derivatization. Consequently, this method is especially valuable for target identification of complex natural products and reversible inhibitors.

Thermal proteome profiling is based upon the thermal shift assay (TSA). In TSA experiments, stabilizing or destabilizing effects on protein folding caused by applied ligands (*e.g.* small molecules) are monitored. Exposed to heat, proteins tend to unfold irreversibly and aggregate. The specific temperature, at which thermally induced unfolding occurs is termed unfolding temperature T_m, also known as melting temperature. The effect on protein stability caused by the applied ligands is also expressed in altered thermostability of protein folding, thereby shifting the melting temperature (Figure 6A).[128] In drug discovery, thermal shift assays with purified proteins of interest have been used for decades in hit identification.[129-133]

As a consequence of the restricted application of thermal shift assay experiments to purified proteins, *Molina et al.* developed the cellular thermal shift assay (CETSA).[134] With this technique in hand, ligand-target engagement studies were no longer restricted to purified proteins, but could also be monitored in live cells *via* western blot analyis. Monitoring ligand-target engagement in live cells depicts several advantages over tracking this interaction under *in vitro* conditions with purified proteins. First, some drugs solely exert their bioactivity after a previous metabolic activation step (referred to as prodrugs).

Second, numerous proteins rely on a functional interplay with other proteins for proper function and structure, which can only be found in intact cells. Third, protein concentration varies greatly over several magnitudes in cells. Therefore, application of the drug to live cells can also reflect on selectivity towards the target at actual cellular concentration levels. Due to its advantage to monitor drug-target engagement in live cells and tissue, the method found wide application in drug discovery.[135]

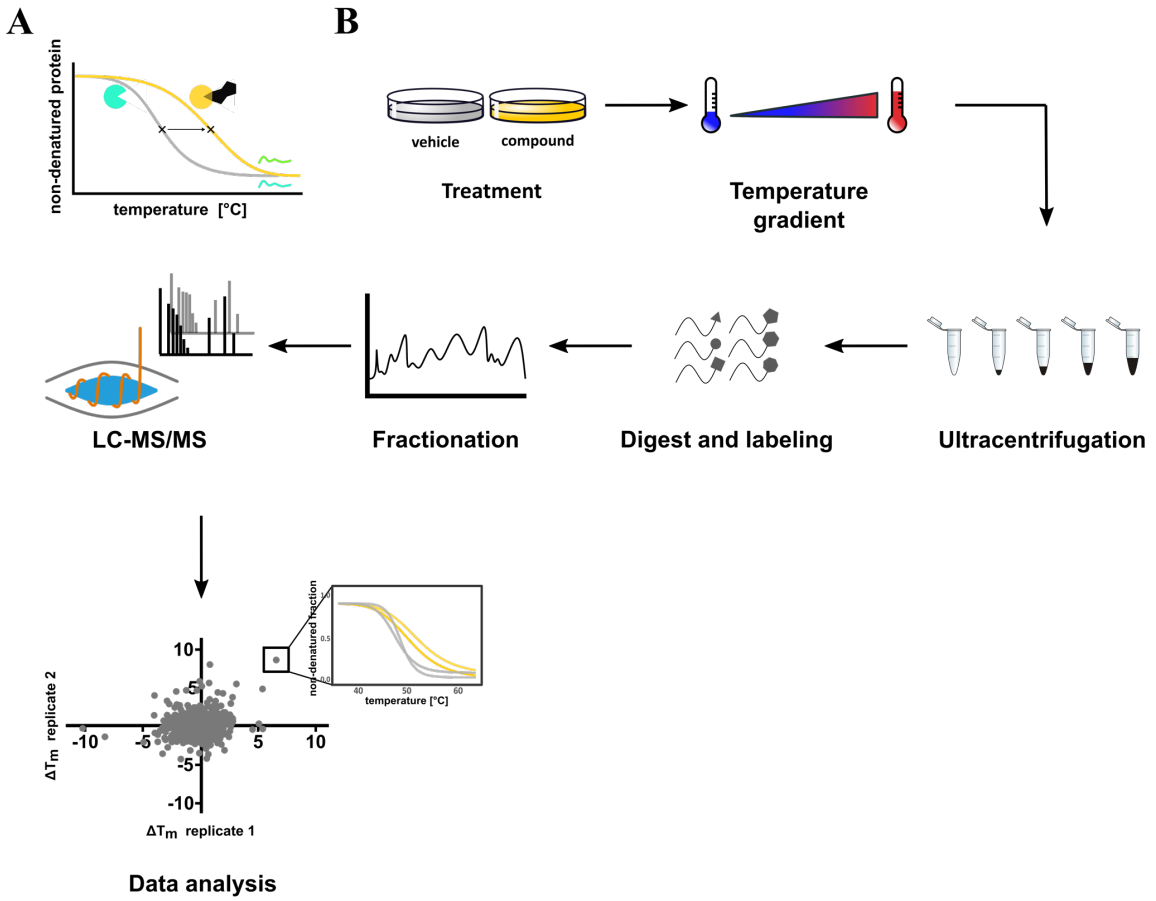

Figure 6 A) Principle of Thermal Shift Assay. Compound binding leads to stabilization (exemplarily shown here) or destabilization of the targeted protein, resulting in an altered melting curve and consequently a deviated melting point (indicated as asterisks **B)** Schematic workflow of a thermal proteome profiling experiment. Intact cells or cell lysates are treated with compound or vehicle, respectively. Subsequently, samples are distributed into aliquots and heated to a range of temperatures. Samples are cleared from aggregated proteins by ultracentrifugation and proteins in the supernatant digested, resulting peptides labeled using TMT tags, combined and subjected to fractionation. Samples are analyzed *via* LC-MS/MS and melting curve fitting, melting point determination and target identification accomplished during data analysis.

In 2014 *Savtizki et al.* reported the combination of CETSA with multiplexed quantitative mass spectrometry, which was termed thermal proteome profiling (TPP), also known as MS-CETSA.[136] By the substitution of the western blot readout with mass spectrometry, an unbiased proteome-wide monitoring of altered thermal stability of protein upon compound treatment in live cells was enabled. Rather than being narrowed down to study target engagement effects for one protein, drug stabilizing effects of several thousand proteins at the same time was enabled. Comparable to the original CETSA approach, live cells are

incubated with compound or vehicle, respectively. Afterwards, each vehicle or compound treated sample is distributed into aliquots, and incubated at different temperatures typically ranging from 37 - 67°C for human cells. Depending on their thermal stability and consequently their melting points, proteins denature and precipitate within the cells. Using ultracentrifugation, the aggregated proteins are separated from residual soluble proteins, which are subsequently tryptically digested. The step-wise thermal dependent loss of proteins in the supernatant is used for melting curve recording. For subsequent quantification, tryptic peptides are labeled with multiplexed isobaric tandem mass tag labels (TMT) using one unique label per temperature for all conditions, and ultimately pooled to one sample per condition. To spring this sample complexity, samples are fractionated using either HILIC or reversed-phase at high pH column chromatography and subsequent LC-MS/MS and data analysis (Figure 6B).[136-138] Peptide identification and reporter ion quantification can be performed using, *e.g.* MaxQuant[125,139,140] or Mascot[141].TPP R package is used for subsequent melting curve fitting as well as melting temperature calculation.[128,137]

This methodology to track drug-target engagement in a unbiased manner was permitted by the introduction of the neutron-encoded isobaric TMT labels.[119] These labels have the same overall mass, ensuring a coelution of the same peptide labeled with different TMT-labels from the LC-column. However, under subsequent fragmentation in the mass spectrometer, reporter ions of different distinct masses with an adjacent difference of 6 mDa are released, which are used for the simultaneous quantification of the same peptide across multiple samples, *e.g.* different temperature stages as applied in TPP experiments.[128]

But TPP is not restricted to the application in thermal response experiments (TPP-TR). Concentration range experiments (TPP-CCR), varying compound concentration at a fixed temperature, are also widely applied in order to compare the affinity of a ligand towards several protein targets *via* concentration dependent stabilization. The initial protocol[136,137] was restricted to soluble proteins, but could be further improved by the incorporation of membrane proteins[138], followed by a merge of TPP-TR and TPP-CCR experiments to the 2D-TPP method[82].

TPP can be applied to distinguish between actual binding partners (termed “direct targets” in the original publication[136]) of the compound under study and downstream affected proteins of the actual targets (so-called “indirect targets”). Whereas - in theory - experiments with live cells should uncover direct-targets as well as indirect targets, experiments in cell lysates should solely reveal direct targets, therefore enabling the

differentiation between these. However, several circumstances might hinder the comparison of *in vitro* and *in situ* experiments. First, protein concentrations in cells can greatly differ from concentrations in cell lysates suffering from dilution while lysis. Therefore, the proportion of compound to target might not correspond to real conditions in the cell. As an example, a low abundance protein targeted by the compound in the cell is stabilized in *in situ* experiments in a detectable manner, but might be too diluted in *in vitro* experiments for a measurable effect. Second, cell lysis can lead to the disruption of protein-protein interactions. If compounds exert their effect by interfering into the intersection of these proteinogenic binding partners, thereby disrupting the protein complex, the effect would not be detectable in *in vitro* experiments as direct target.

However, as all target deconvolution strategies also thermal proteome profiling has its shortcomings in target discovery and mode of action analysis. Compounds binding to their respective targets have to cause a measurable and significant stabilizing or destabilizing effect, which is not always given due to multiple reasons.[128]

1.2. Results and discussion

1.2.1 Effects of vioprolides on proliferation and apoptosis

As mentioned in Chapter 1.1.3., the vioprolides are reported to exhibit potent cytotoxic activity towards cancer cells in the initial publication. However, as no exact values were reported, the half maximal inhibitory concentrations (IC_{50}) of all four class members were elucidated in a cell titer blue assay. The acute lymphoblastic leukemia (ALL) cell line Jurkat, an immortalized line of human T lymphocytes, was incubated for 72 hours with varying concentrations of vioprolide A-D. Structurally, the vioprolides solely differ in the ring size of the N-heterocycles in the northern and western part of the molecule. **VioA** and **VioC** share the same moiety in the northern part, while differing from each other by the ring size of the N-heterocycle in the western part. In line therewith, **VioB** and **VioD** also share the same moiety in the northern part, but differ in ring size in the western part of the molecule as **VioA** and **VioC** (Figure 7A).

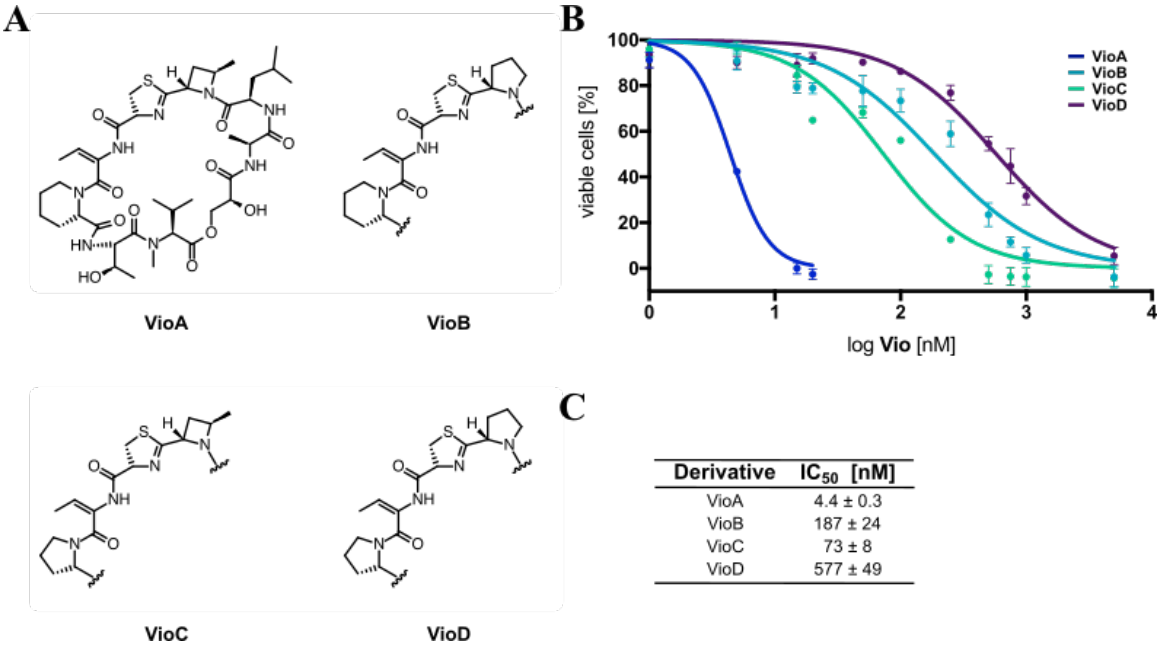

Derivative	IC_{50} [nM]
VioA	4.4 ± 0.3
VioB	187 ± 24
VioC	73 ± 8
VioD	577 ± 49

Figure 7 Analysis of the antiproliferative effects of the vioprolides in Jurkat cancer cell line. **A)** Structure of vioprolide A and northwestern parts of vioprolide B, C and D (**VioA-D**). **B)** Dose-response curves of Jurkat cells treated with varying concentrations of VioA-D for 72 h in a cell titer citer blue (CTB) assay. DMSO treated cells served as negative control **C)** Corresponding IC_{50} values representing mean ± SEM of three independent biological experiments, carried out in technical triplicates. Data was generated and plotted by Christina Orgler.

In general, all four class members exhibit a potent activity in the nanomolar range (Figure 7B and C). In line with the initial publication, a significant difference in bioactivity among

the compound class was observed, with **VioA** displaying the most potent antiproliferative activity (IC_{50} = 4.4 nM) and **VioD** the showing the lowest (IC_{50} = 577 nM).

VioA and **VioC** as most potent derivatives bear a 4-methylazetidine (MAZ) moiety in the northern part of their scaffolds in common. Their elevated activity in comparison to **VioB** and **VioD** seems to stem from this structural element. **VioA** and **VioC** differ in ring size of the N-heterocycle in the western part of the molecule solely by a methylene group (L-proline vs L-homoproline). In terms of bioactivity, a six membered ring (L-homoproline) seems to be more favorable than a five membered ring (L-proline), as activity drops by factor 16 by this slight modification. The diminished bioactivity caused by the reduced ring size of the N-heterocycle is also reflected in the difference in bioactivity between **VioB** and **VioD**.

Based on these findings, it can be concluded that the northwestern part of the vioprolides is essential for binding to the respective targets, and small perturbations in composition of the N-heterocycles lead to a significant drop in potency.

In conclusion, **VioA** is the most potent derivative and thus, the combination of 4-methylazetidine moiety in the northern part with L-homoproline in the western part displays the most favorable combination of N-heterocyclic moieties present in this compound class. Therefore, **VioA** was selected for further studies as it represents the most potent member of this natural product class.

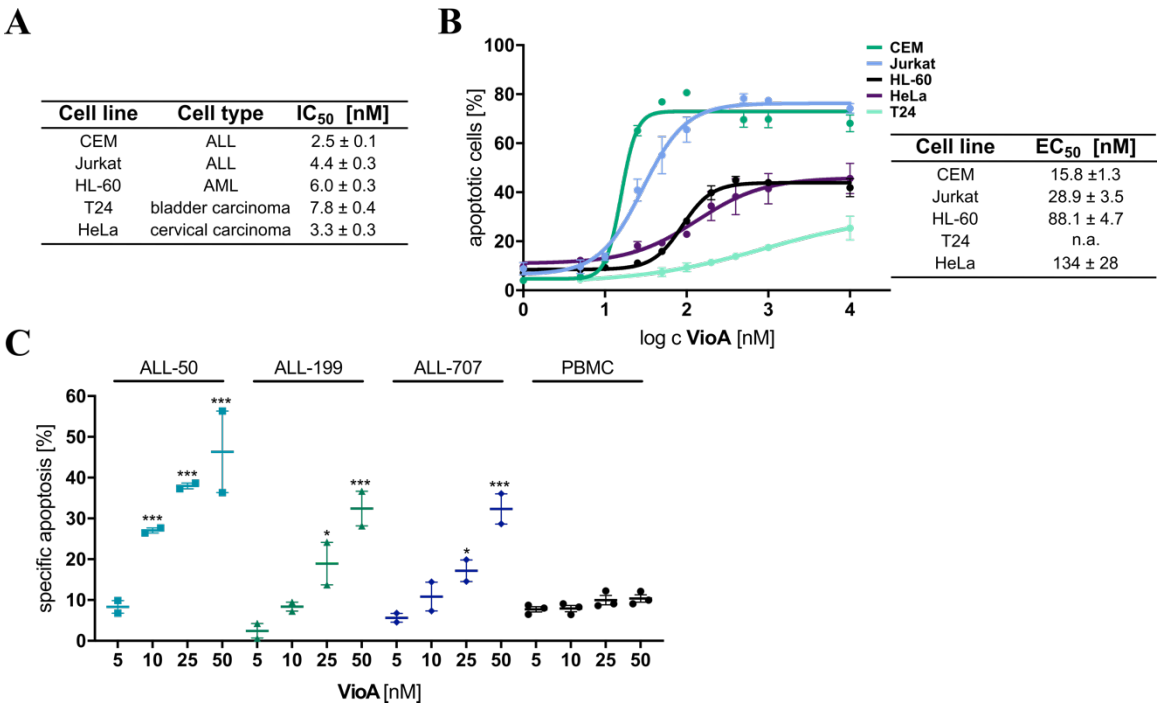

Figure 8: Anticancer effects of **VioA**. **A)** Inhibition of proliferation after 72 h was analyzed in a cell titer blue assay (suspension cell lines) or by using crystal violet staining (adherent cell lines). Corresponding IC_{50} values were calculated using three independent experiments, each performed in triplicates. **B)** Apoptosis of various cancer cell lines treated with VioA (24 h). Percentage of apoptotic cells and corresponding EC_{50} values were calculated using propidium iodide (PI)

staining and flow cytometry. Data points represent the mean ± SEM of three independent experiments performed in triplicates. **C)** ALL PDX cells and PBMCs treated with VioA for 24 h. Percentage of apoptotic cells was determined by flow cytometry and specific apoptosis calculated in comparison to DMSO treated cells. Data points represent independent experiments ± SEM and were performed in triplicates (PDX cells n = 2; PBMCs = 3), one-way ANOVA Dunnett's test, * P<0.033, *** P<0.001. Experiments were carried out and data plotted by Christina Orgler.

Next, the evaluation of the antiproliferative effect of **VioA** was extended to different cancer cell lines to determine if **VioA** selectively inhibits proliferation in a certain type of cancer cell line or shows a broad antiproliferative effect across different cell lines. Therefore, antiproliferative effects of **VioA** in CEM, a second ALL cell line, the acute myeloid leukemia (AML) cell line HL-60, the bladder carcinoma cell line T24, and the cervical cancer cell line HeLa were determined. As resulting IC_{50} values for all tested cell lines were in the single-digit nanomolar range, it can be concluded, that **VioA** exhibits a general potent antiproliferative effect on cancer cells of different origin (Figure 8A).

In order to analyze, whether decreased cell growth induced by **VioA** stems additionally from **VioA** triggered apoptosis, a dose-dependent apoptosis assay was performed to determine the half maximal effective concentration (EC_{50}) of **VioA**. Therefore, cells were treated with **VioA** in various concentrations for 24 hours, and subsequently stained with propidium iodide (PI) and analyzed by flow cytometry to determine the percentage of apoptotic cells and corresponding EC_{50} values.

Whereas **VioA** diminished proliferation in all tested cell lines at comparable concentrations a cell type dependent significant difference was observed in apoptosis induction (Figure 8B). Both ALL cell lines showed to be more sensitive to apoptosis induction via **VioA** than other cell lines tested as VioA exhibited a comparable low EC_{50} value in CEM and Jurkat (15.8 nM and 23.8 nM), in comparison to AML cell line HL-60 (88.1 nM), HeLa (134 nM) and T24 cell line. Of note, apoptosis was barely induced in T24 cells, hence an EC_{50} was not calculable for this cell line. Additionally, at highest applied concentrations, both ALL cell lines displayed a considerably higher apoptosis rate (80% for CEM and Jurkat) than other tested cell lines (40% for HeLa and HL-60).

To further evaluate the bioactivity of **VioA** in ALL cells, **VioA** was tested in ALL patient derived xenograft (PDX) cells (origin of PDX cells see appendix). ALL samples from three different patients were treated with **VioA** in various concentrations for 24 h and subsequently analyzed by flow cytometry. Healthy Peripheral blood mononuclear cells (PBMCs) served as control. Whereas patient derived cells displayed an elevated dose-dependent apoptosis rate, healthy cells barely responded to **VioA** treatment at highest applied concentrations (Figure 8C). This selectivity of **VioA** towards apoptosis induction in cancer cells over healthy cells demonstrates the putative therapeutic relevance of **VioA**.

1.2.2. Target identification of VioA in Jurkat cells

1.2.2.1. Target identification using Affinity-based protein profiling

1.2.2.1.1. Design and synthesis of vioprolide A derived photoprobe

In order to elucidate the proteinogenic targets of **VioA** *via* A*f*BPP, a modification of the natural product with a terminal alkyne is mandatory. The question if a photocrosslinking moiety is additionally needed in probe design is usually answered with the presence or absence of electrophilic warheads in the natural compound scaffold.

The scaffold of **VioA** is equipped with an *E*-dehydrobutyrine moiety, which has been shown to contribute to the cytotoxic activity in other natural products.[142] Even though a covalent binding mode *via* this moiety is possible, a non-covalent binding mode cannot be excluded. Therefore, an additional photocrosslinking moiety incorporated into the natural product derived probe was regarded as favorable.

Due to the already mentioned synthetical inaccessibility of the vioprolides, photocrosslinking moiety and terminal alkyne have to be incorporated into the parental structure retrospectively in a semi-synthetic approach without perturbing the natural products scaffold in a significant way. The most accessible locations in the peptolide structure for synthetic derivatization reactions are the nucleophilic secondary alcohol groups of glyceric acid and threonine (Scheme 2).

The so-called "minimalist linkers" as reported by *Yao et al*[143] depict a small perturbation of parental compounds, as a photoreactive group and an analytical handle are added simultaneously.

These crosslinkers contain a terminal alkyne and a diazirine moiety as photocrosslinking moiety, assembled in a short C7-alkyl chain, additionally furnished with a functional group (either carboxylic acid, primary amine, iodide or primary alcohol) for the synthetic attachment to a bioactive molecule *via* coupling reactions (Scheme 2, example for carboxylic acid as functional group). These minimalist diazirine photocrosslinkers have been applied successfully for the derivatization of bioactive molecules for affinity based protein profiling.[143-147]

In order to prevent hydrolysis by cellular esterases[148], etherification of **VioA** with the photocrosslinker in a WILLIAMSON ether synthesis would display the preferred probe synthesis approach.

However, the reactions tested with **VioA** led to complete decomposition of the natural product or no reaction at all (data not shown), when attempting to deprotonate alcohols of **VioA** with sodium hydride and other bases, prior to reaction with the iodide derivative of the photocrosslinker.

Therefore, even though prone to stability issues, an esterification of **VioA** with the carboxylic acid derivative of the minimalist photocrosslinker leading to the respective vioprolide A probe (**VioA-P**) was chosen.

In line with the procedure of *Yao et al.*[143] and *Kleiner et al.*[145] alcohol was oxidized via JONES oxidation[149] and subsequently applied for the derivatization of **VioA** using STEGLICH esterification[150], as this reaction is known to be favorable to modify sterically demanding alcohol groups.

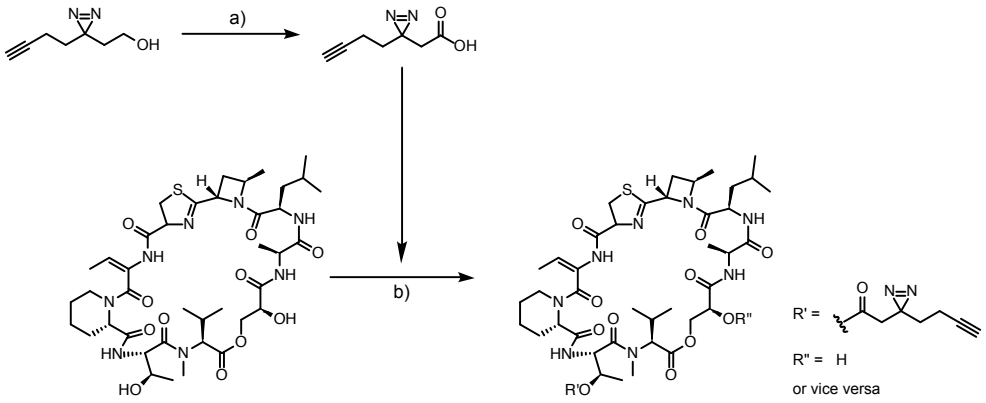

Scheme 2: Synthesis of **VioA-P**. a) Jones oxidation of 2-(3-But-3-ynyl-3H-diazirin-3-yl)-ethanol. Jones reagent, acetone 0 °C, 2 h, 79%. b) Esterification of VioA with resulting 2-(3-(but-eyn-1-yl)-3H-diazirin-3-yl)acetic acid. DMAP, DCC, dichloromethane, 0 °C, 4h, then r.t., overnight, 30%.

Theoretically, both alcohols should be prone to derivatization *via* STEGLICH esterification, however the threonine side chain hydroxy group is potentially more nucleophilic due to larger electron density. However, glyceric acid alcohol is sterically less hindered. In order to identify the esterificated alcohol, 1D and 2D NMR spectra were recorded (see Appendix for 1D spectra), but unfortunately the site of derivatization could not be elucidated due to the complexity of the spectra. In addition, performed MS fragmentation studies conducted to compare MS/MS fragments of **VioA** and **VioA-P** (spectra see appendix) to decipher altered fragments and thereby the site of derivatization, remained inconclusive. However, LC-MS analysis revealed one single UV and MS peak in a C18 chromatographic separation run (see Appendix) indicating selective product formation.

1.2.2.1.2. Biological evaluation of vioprolide A derived probe VioA-P

Prior to gel- and MS-based A*f*BPP experiments, **VioA-P** was tested in a cell titer blue assay for its antiproliferative capacity in Jurkat cells. In order to evaluate the influence on bioactivity of the derivatization with the minimalist photocrosslinker, parental compound **VioA** was utilized as control. Cells were treated with **VioA** or **VioA-P** respectively in a panel of concentrations for 72 hours and compared to DMSO treated cells.

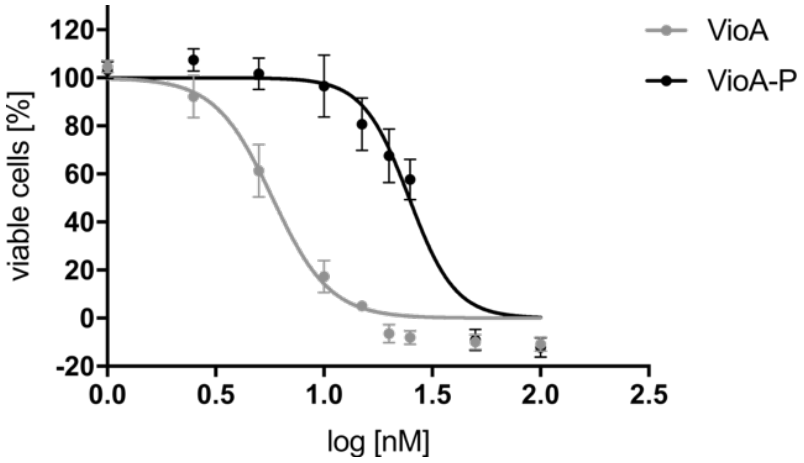

Compound	IC_{50} [nM]
VioA	5.8 ± 0.4
VioA-P	24.7 ± 1.7

Figure 9: Inhibition of proliferation of Jurkat cancer cells treated with VioA or VioA-P for 72 h. Number of viable cells and corresponding IC_{50} values were determined by cell titer blue assay and normalized towards DMSO control. Data points represent the mean ± SEM of three independent experiments performed in triplicates. Experiment was carried out by Christina Orgler.

In accordance with previous experiments **VioA** exhibited an IC_{50} in the low nanomolar range (5.8 nM). Interestingly, the antiproliferative potency **VioA-P** (IC_{50} = 24.7 nM) solely dropped by 4-fold, thus leading to the assumption that the derivatization did not affect the biological activity of the parental compound in a significant manner.

1.2.2.1.3. Analytical gel-based AfBPP experiments

Even though gel-based analytical A*f*BPP experiments cannot provide the in-depth target identification MS-based A*f*BPP approaches are capable of, analytical experiments can still serve important information on the labeling behavior of the probe under study. Information which can be accessed from analytical experiments and utilized in adjacent preparative labelin experiments include cell permeability of the probe, required concentrations for sufficient labeling and revised UV-irradiation durations.

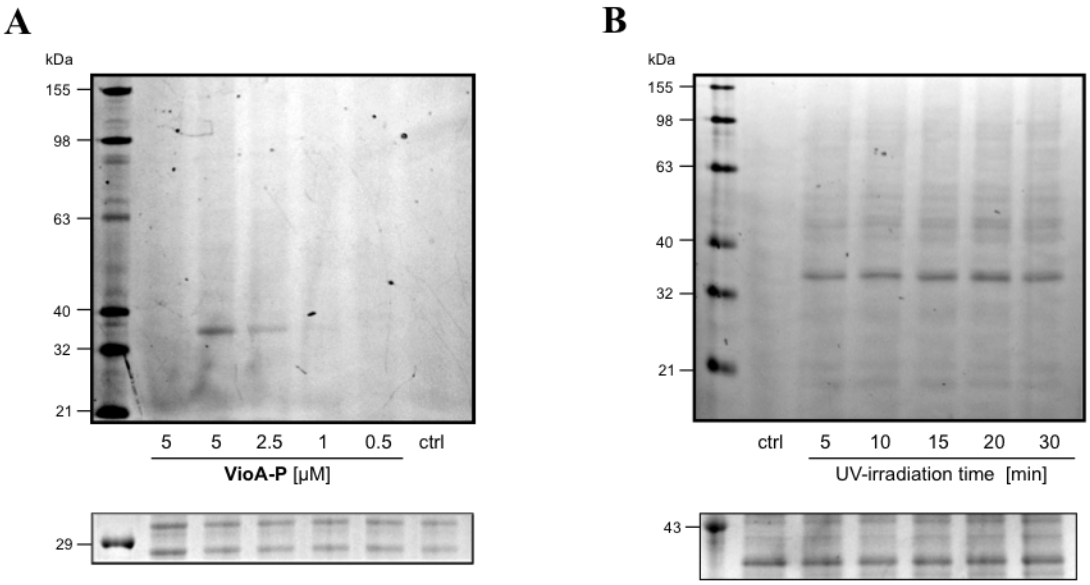

Figure 10: *In situ* analytical A*f*BPP labelling with **VioA-P**. **A)** Fluorescent scan of labelling in Jurkat cells (0-5 µM, incubation for 1 h, irradiation for 30 min, 4 °C). DMSO treated samples served as control (ctrl). Gel was coomassie-stained after fluorescent scan to check for equal sample load (lower part of the picture). **B)** Labelling in HeLa cells (5 µM, incubation for 1 h, irradiation time for 5-30 min, 4 °C), DMSO treated samples served as control (irradiation time for 30 min, 4 °C). Gel was coomassie-stained after fluorescent scan to check for equal sample load (lower part of the picture).

For analytical labeling experiments, Jurkat cancer cells were incubated (37 °C, 1 h) with **VioA-P** in a range of concentrations or DMSO, respectively. Due to the high toxicity of the probe a maximum concentration of 5 µM was chosen and considered as tolerable for a short time period. Subsequently, cells were irradiated with UV light (λ = 365 nm, 30 min, 4 °C) to ensure covalent linkage of the probe to the respective target proteins. A non-irradiated probe treated control was incorporated into the experiment to identify UV-irradiation independent covalent binding events. DMSO control (ctrl) was used to identify unspecific binding events of the fluorescence dye to proteins. Following the irradiation step, cells were washed with phosphate buffered saline (PBS) to remove excess of probe, lysed in a detergent-based buffer and resulting cell lysates were supplemented with

rhodamine azide for subsequent click reaction and labeled proteins separated using SDS-PAGE.

VioA-P bound proteins were visualized by fluorescent scanning (Figure 10A). Coomassie staining of resulting SDS gel was carried out to check for equal protein load for each sample. Even at highest applied concentration (5 µM) the labeling pattern of **VioA-P** solely displayed one prominent band in the range of 40 to 32 kDa. As this concentration-dependent labeled band is not visible in the non-irradiated sample it can be assumed, that **VioA-P** predominantly binds via a non-covalent binding mode to its most prominent protein targets.

The labeling pattern of the probe is rather unusual as photoprobes equipped with a diazirine normally display numerous labeled bands at comparable concentrations, *e.g.* originating from background binding. Therefore, the selective labeling of **VioA-P** could on the one hand speak for an indeed highly selective labeling behavior of the probe, or on the other hand for a low abundancy of the proteins targeted by **VioA-P** being insufficiently abundant to be visualized *via* fluorescent scan.

In order to investigate if the selective labeling of **VioA-P** is cell type specific, or is observable across different cell lines, labeling with the probe was repeated in the solid cancer cell line HeLa (Figure 10B). Here, cells were treated with a single concentration (5 µM) or DMSO respectively and varied duration of UV-irradiation. The scope of the conducted deviation in irradiation duration was to determine if the initial duration of 30 min already leads to UV-dependent damage to probe labeled proteins. If this would be the case, the labeling pattern of different applied excitation durations should time-dependently differ. Therefore, excitation wavelengths of 5, 10, 15, 20 and 30 min were utilized. The experiment was conducted in line with the analytical A*f*BPP experiment in Jurkat cells, except the mentioned deviation in UV-irradiation duration.

Comparable to the labeling in Jurkat cells, the labeling pattern in HeLa cells is conditioned by a prominent band in the range of 40 to 32 kDa. However, in contrast to labeling in Jurkat cells, a ladder of bands is additionally visible in the range of 63 to 40 kDa. An explanation for these additional bands could be a difference in protein amount in HeLa and Jurkat samples. Potentially, these additional bands could have also been detected in this cell line by increasing the cell amount per sample in the labeling experiment.

Interestingly, the labeling pattern in HeLa cells appears to be independent from the irradiation duration to a certain extent, as it did not change significantly across the variably irradiated samples. This observation led to the assumption that labeling events of **VioA-P**

probe largely do not suffer from long irradiation durations, and reversely indicates that already short irradiation times (5 min) are sufficient to ensure maximal crosslink efficiency, at least from a visual perspective.

1.2.2.1.4. MS-based target identification using AfBPP

As analytical A*f*BPP experiments have proven that **VioA-P** is cell permeable and capable of labeling proteinogenic targets at low micromolar concentrations, the probe was applied to in-depth target identification experiments using mass spectrometry based label-free quantitative proteomics experiments.

Lined out in the previous chapter, distinct labeled bands were visualized in analytical experiments starting at 1 µM and became more apparent at highest applied concentrations (5 µM). As MS-driven A*f*BPP experiments are significantly more sensitive than analytical experiments, proteinogenic targets are still detectable and quantifiable at concentrations which are insufficient to generate visible bands in gel-based experiments. To determine optimal labeling concentrations for target elucidation, a panel of **VioA-P** concentrations (0.5 to 2 µM) was applied.

For target identification, Jurkat cells were incubated with **VioA-P** at varying concentrations (0.5 – 2 µM) or DMSO, respectively (37 °C, 5% CO_2, 1 h) in three independent replicates per condition. Incubation step was followed by UV-irradiation to ensure covalent attachment of the probe to the respective targets (30 min, 4 °C). Subsequently, cells were washed to remove excess of probe, cells lysed using a detergent-based lysis buffer and protein amount aligned across all samples. For simultaneous visualization and enrichment of probe modified proteins, cell lysates were supplemented with trifunctional linker containing a fluorescent dye and a biotin tag. Cooper (I)-mediated click reaction was followed by protein target enrichment using avidin coated agarose beads. Enriched proteins were tryptically digested, analyzed by LC-MS/MS and resulting raw data preprocessed using MaxQuant.[125,126,139,140] Perseus was utilized for subsequent data analysis.[151] Detected proteins were statistically evaluated in a two-sample student's *t*-test by comparing protein intensities of **VioA-P** treated samples with DMSO control group respectively, resulting in enrichment ratios [$\log_2$(intensity **VioA-P**/DMSO)] and confidence levels (*p*-value). Proteins meeting threshold criteria [$\log_2$(enrichment) > 1, p-value < 0.05] were considered as potential hits (Figure 11A-C). Additionally an aliquot of the enriched proteins was utilized for SDS-PAGE analysis (Figure 11D). Faint bands were detected for the two highest applied concentrations (1 and 2 µM). Besides background labeling, typical for photocrosslinkers (a band between 40 and 32 kDa) is visible, in line with analytical experiments. However, the overall low labeling intensity indicated a compromised labeling efficiency of the utilized probe.

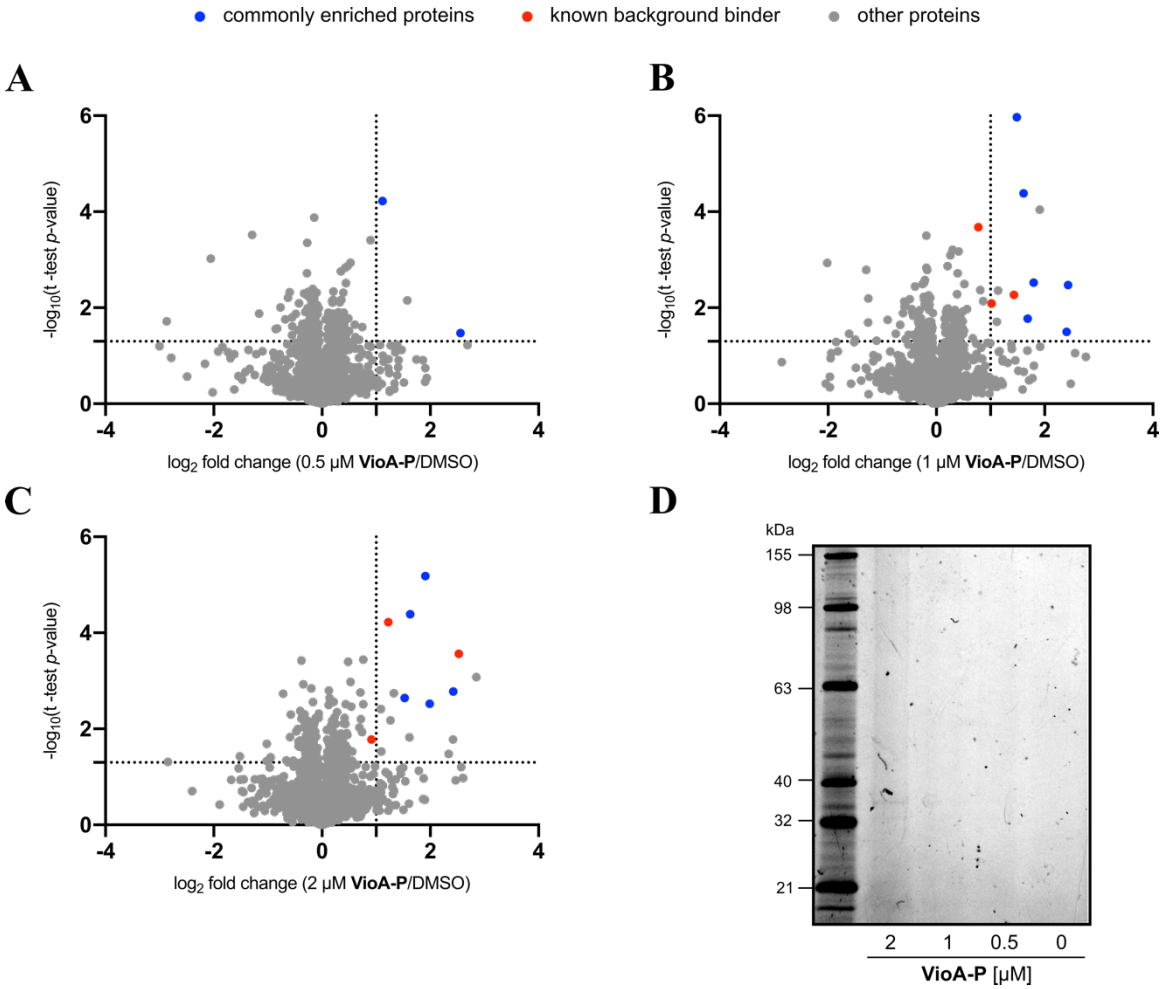

Figure 11: Quantitative proteome enrichment analysis of **VioA-P** treated Jurkat cells. Volcano plots of *in situ* label-free A*f*BPP epxeriments with **A)** 0.5 µM **B)** 1 µM and **C)** 2 µM **VioA-P** treated Jurkat cells compared to DMSO treated cells (n=3). Thresholds for target hit identification (log_2 enrichment > 1, $-log_{10}$ (*t*-test *p*-value) are indicated as dotted lines. Known photocrosslinker are indicated as red dots. Proteins, enriched in more than one concentration labeling are indicated in blue. Remaining proteins are labeled in grey. **D)** Fluorescence scan of SDS-PAGE gel of enriched samples.

The volcano plot of 0.5 µM **VioA-P** (Figure 11A) did not reveal any clear hits even though the applied concentration corresponds to a multiple of the determined IC_{50} concentration (20 fold higher) in the proliferation assay and therefore should in theory be sufficient for proper target binding. The volcano plots of increased concentrations (Figure 11B and 11C) showed significantly more proteins enriched with known background binders[145] included (indicated in red in plots and tables). Numerous proteins were enriched in multiple concentrations (indicated in blue in plots and tables), however, a concentration dependent tendency in enrichment could not be detected. This was also the case for CAAX prenyl protease 1 homolog (ZMPSTE24) representing the only protein enriched across all applied concentrations.

However, no clear target(s) stood out of other enriched proteins and therefore, target identification results of the MS-driven A*f*BPP experiments remained inconclusive.

Table 1: Significantly enriched proteins (log_2 enrichment > 1, $-log_{10}$ *t*-test *p*-value > 1.3) in A*f*BPP experiment with 0.5 µM **VioA-P** compared to DMSO. Blue proteins indicate protein hits observed enriched using multiple concentrations of **VioA-P**.

Log_2 enrichment	$-log_{10}$ (t-test p-value)	Gene name	Protein name	MW [kDa]
2.56	1.47	C14orf1	Probable ergosterol biosynthetic protein 2B	15.8
1.58	2.15	NACC1	Nucleolus accumbens-associated protein 1	57.3
1.12	4.22	ZMPSTE24	CAAX prenyl protease 1 homolog	58.8

Table 2: Significantly enriched proteins (log_2 enrichment > 1, $-log_{10}$ *t*-test *p*-value > 1.3) in A*f*BPP experiment with 1 µM **VioA-P** compared to DMSO. Blue proteins indicate protein hits observed enriched using multiple concentrations of **VioA-P**. Red proteins indicate known photocrosslinker background binders.[145]

Log_2 enrichment	-log10 (t-test p-value)	Gene name	Protein name	MW [kDa]
2.43	2.47	SET	Protein SET	33.5
2.41	2.15	C14orf1	Probable ergosterol biosynthetic protein 2B	15.8
1.91	4.22	SLC12A7	Solute carrier family 12 member 7	119.1
1.80	2.52	CALU	Calumenin	37.1
1.68	1.77	PLD3	Phospholipase D3	54.7
1.61	4.38	ZMPSTE24	CAAX prenyl protease 1 homolog	58.8
1.48	5.97	CD3E	T-cell surface glycoprotein CD3 epsilon chain	23.1
1.43	2.27	CSTD	Cathepsin D	44.6
1.14	2.36	COMT	Catechol O-methyltransferase	29.5
1.12	1.71	RAD23A/B	UV excision repair protein RAD23 homolog A/B	39.6
1.02	2.09	HMXO2	Heme oxygenase 2	36.0
0.78	3.68	VDAC1	Voltage-dependent anion-selective channel protein 1	30.8

Table 3: Significantly enriched proteins (log_2 enrichment > 1, $-log_{10}$ *t*-test *p*-value > 1.3) in A*f*BPP experiment with 2 µM **VioA-P** compared to DMSO. Blue proteins indicate protein hits observed enriched using multiple concentrations of **VioA-P**. Red proteins indicate known photocrosslinker background binders.[145]

Log_2 enrichment	-log10 (t-test p-value)	Gene name	Protein name	MW [kDa]
2.85	3.07	CD3G	T-cell surface glycoprotein CD3 gamma chain	20.5
2.52	3.56	CTSD	Cathepsin D	44.6
2.42	2.78	SET	Protein SET	33.5
2.42	1.78	GOPC	Golgi-associated PDZ and coiled-coil motif-containing protein	50.5
2.34	1.48	SLC25A20	Mitochondrial carnitine/acylcarnitine carrier protein	32.9
1.99	2.52	PLD3	Phospholipase D3	54.7
1.91	5.18	CD3E	T-cell surface glycoprotein CD3 epsilon chain	23.1
1.63	4.39	ZMPSTE24	CAAX prenyl protease 1 homolog	58.8
1.62	1.82	TIMM17B	Mitochondrial import inner membrane translocase subunit Tim17-B	18.3
1.53	2.64	CALU	Calumenin	37.1
1.33	2.74	SCCPDH	Saccharopine dehydrogenase-like oxidoreductase	47.2
1.26	2.18	DNAJB6	DnaJ homolog subfamily B member 6	36.1
1.23	4.22	VDAC1	Voltage-dependent anion-selective channel protein 1	30.8
1.10	1.53	CYB5B	Cytochrome b5 type B	16.7
1.09	2.41	HM13	Minor histocompatibility antigen H13	41.5
0.92	1.78	HMXO2	Heme oxygenase 2	36.0

1.2.2.1.5. Assessment of the metabolic stability of VioA-P

Given the inconclusive target identification results in cancer cells questions arose why **VioA-P** showed low labeling efficiency in analytical but also MS-driven experiments. Three reasons for the poor enrichment results have been considered:

i) Applied concentrations were too low to sufficiently enrich molecular targets.

Due to the potent biological activity in the nanomolar range, the increase of labeling concentration did not seem feasible, as the applied concentration already represented a multiple (20x) of the determined IC_{50} concentration. Ideally, labeling concentrations are in the same range as determined IC_{50} values or at maximum up to 10 fold higher. Exceeding the bioactive concentration too far might lead to unspecific labeling leading to ambiguous target identification, which are not in correlation with the biological activity of the probe.

ii) Synthetic modification with the minimal photocrosslinker either hinders probe-target interactions, thereby impeding enrichment of the respective targets or diminishes cell permeability of the probe.

Derivatizing **VioA** with the minimalist photocrosslinker could lead to an impaired interaction between the natural product and the dedicated targets. The secondary alcohol might function as a hydrogen bond donor during target engagement. By replacing this functional group with an alkyl chain, thereby significantly decreasing the compounds hydrophilicity, might have a critical effect on target interactions. Diminished cell permeability of the molecule due to added hydrophobicity by the attached linker can be excluded to a certain extent, as most of the enriched proteins are located in the cytoplasm or the nucleus. Enrichment of these proteins presupposes cell permeability of the probe.

iii) Ester bond linkage between **VioA** and minimalist photocrosslinker exhibits insufficient metabolic stability.

The ester bond linking **VioA** to the minimalist photocrosslinker might be cleaved in cells by *e.g.* esterases consequently hindering a successful enrichment of respective targets. Hydrolyzation reactions catalyzed by cellular esterases, leading to prodrug activation and/or compound detoxification are common in drug metabolism.[148]

As the two first-mentioned propositions are ambitious to verify, the metabolic stability of **VioA-P** was investigated in order to elucidate if an impaired stability of the probe might be responsible for inconclusive target identification results.

Therefore, the metabolic stability of **VioA-P** was determined in Jurkat cell lysate. **VioA-P** was incubated with cell lysate (37 °C, 400 rpm) in three independent replicates and an aliquot retrieved at certain time points (0, 1, 2, 4, 6, 8 and 24 hours). Proteins in the samples were precipitated with MeCN (-20 °C, 1 h), followed by a centrifugation step. The resulting supernatant was dried *in vacuo* and dried samples reconstituted in 50:50 H_2O:MeCN. LC-MS was utilized to relatively quantify remaining **VioA-P** and potentially generated **VioA** using a single ion monitoring (SIM) method. Raw files were processed using Xcalibur™ and intensities plotted over time (Figure 12A and B). Indeed, a time-dependent decrease in signal intensity for **VioA-P** was observed (Figure 12A) accompanied by a time-dependent increase in signal intensity for **VioA** (Figure 12B). These findings indicate that hydrolysis of the probe under loss of the minimalist photocrosslinker moiety occurs in a time-dependent manner.

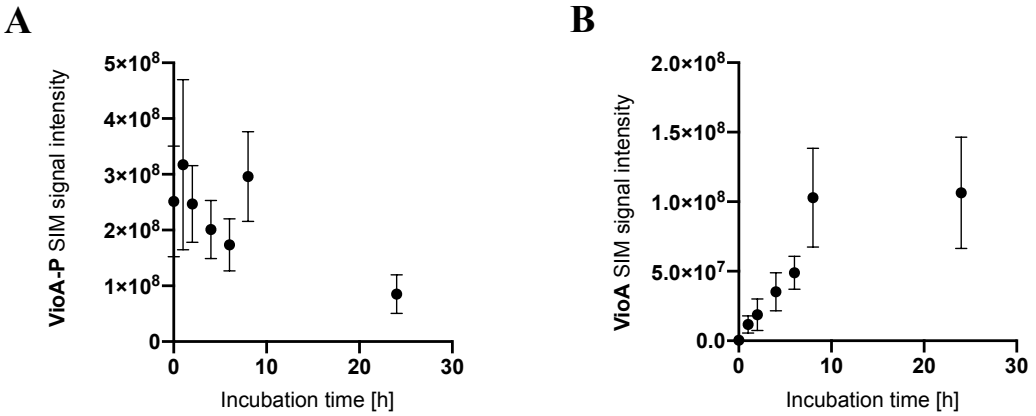

Figure 12: Time dependent metabolic stability of **VioA-P** in Jurkat cancer cell lysate. **VioA-P** was incubated with Jurkat cell lysate, and aliquots sampled at indicated time points. Metabolic reactions were quenched by the addition of cold MeCN. Subsequently, samples were analyzed via LC-MS in SIM mode targeting molecules of interest (**VioA-P** and **VioA**). **A)** Analysis revealed a time-dependent decrease of **VioA-P** with **B)** a concurrent time-dependent increase of **VioA** signal intensity indicating time-dependent hydrolysis of the probe. Data points represent the mean ± SEM of three independent experiments.

In retroperspective, the time-dependent hydrolysis of the probe might explain its potency close to the bioactivity of the parent compound in antiproliferative assays. Assuming that remaining **VioA-P** further hydrolyzes beyond the covered 24 h in the metabolic

degradation assay, it is very likely that a major part of the bioactivity of the probe stems from the generated **VioA** after 72 h readout.

Even though, the hydrolysis is not significantly progressed after the utilized incubation time (1 h) cell lysates experiments, the picture could be different in A*f*BPP experiments with living cells. In intact cells, esterases – deactivated by cell lysis in cell lysates – could still be active, thus leading to a faster hydrolysis rate in living cells in comparison to cell lysate.

In conclusion, the results of the metabolic degradation assay indicate that **VioA-P** is not suitable for the target identification of **VioA** in A*f*BPP experiments.

1.2.2.1.6. Design of next generation VioA probes

Given the restricted options in **VioA-P** probe semi-synthesis, an esterification of **VioA** with the minimalist photocrosslinker moiety depicted the only applicable possibility for the design of the first generation of **VioA** based A*f*BPP probes.

A developed total synthesis for vioprolides would open doors for a new set of next generation probes, as required terminal alkyne and a photocrosslinking moiety (preferable diazirine) could be incorporated directly into the structure, consequently altering the scaffold in a non-significant way.

Even though other methods were used for target identification of **VioA** in cancer cells (shown in the following chapter), new generations of A*f*BPP probes still depict a highly useful tool to study drug-target interactions in detail. One particular field ABPP probes are of great use are MS-based binding site studies. Here, the peptide of target proteins interacting with the probe are identified and can thereby deepen the knowledge of the mode of action of the compound under study. Binding site studies have been successfully applied to mode of action analysis in human cancer cells, as well as bacteria.[108,121]

For the next generation of **VioA** derived probes, four scaffolds are suggested, however there are more options which can be considered eventually (Figure 13). As the bioactivity of the vioprolides heavily depends on the composition of the north-western part of the molecules, derivatizations at this part are demanding. However, an incorporation of a photo crosslinking moiety at this position would have the advantage to covalently trap the interacting peptide of the respective target. The higher the distance of the photocrosslinking moiety to the northwestern part of the molecule, the higher the chance to identify false positive binding sites. However, eligible positions for the installation of a diazirine moiety in this part of the molecule are limited. One obvious option would be the exchange of L-homoproline or L-proline to photo-proline (Figure 13; probes **1** and **3**). This commercially available building block could be easily implemented in a total synthesis approach. Even though depicting a small deviation in structure, differences in bioactivity between **VioA** and **VioC** show how sensitive this positions is to modifications. Therefore, the installation of a diazirine here might lead to loss of bioactivity.

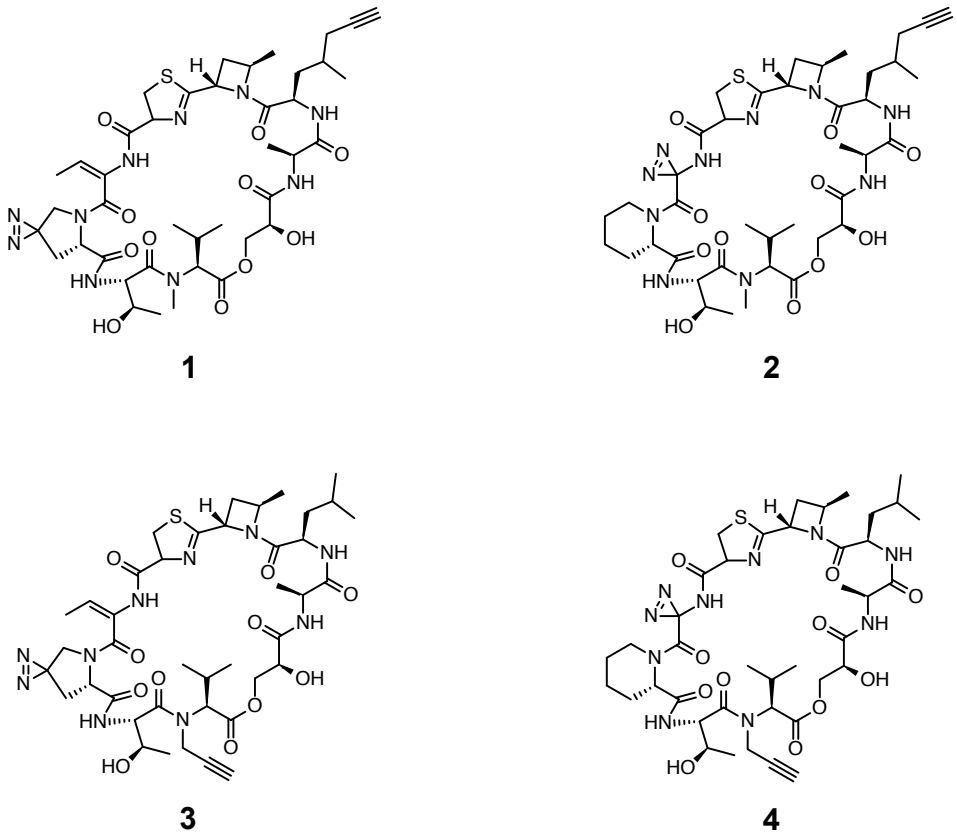

Figure 13: Suggestions for next generation **VioA** ABPP probes.

Another option would be the modification at the site of the *(E)*-dehydrobutyrine building block (Figure 13, probes **2** and **4**). This modification would enable the installation of a diazirine moiety without affecting the N-heterocycles. However, as discussed before, a contribution of the *(E)*-dehydrobutyrine moiety to the bioactivity of the vioprolides *via* a covalent binding mode cannot be excluded. As a consequence, the replacement of this moiety by a diazirine photocrosslinker could also perturb the potency of the probes. In case of the terminal alkyne handle, numerous positions are prone to modification. Valine in the southern part of the molecule already holds a methylation on the nitrogen, thereby an alkylation with a terminal alkyne at this position might be tolerable in terms of bioactivity. A derivatization of the leucine building block (Figure 13 probes **1** and **2**) might be feasible without diminishing bioactivity significantly.

1.2.2.2 Target identification using thermal proteome profiling (TPP)

Due to outlined reasons, modification-based target identification approaches appeared non-feasible in the case of the vioprolides. Therefore, thermal proteome profiling as modification-free method was applied in live cells to uncover the molecular interaction partners of **VioA** following a previously published procedure.[137]

Thermal proteome profiling experiments require elevated, yet for the incubation time tolerable, concentrations of the compound to ensure saturation of the respective target proteins. This saturation is necessary, as measurable melting point shifts of the targets might otherwise not achieved. Therefore, a 10-fold IC_{50} (150 nM, IC_{50} = 15 nM as analyzed by MTT assay for 24 h incubation time, data not shown) as well as further elevated concentrations of 1 µM were applied in two different experiments.

Living cells were incubated with **VioA** or DMSO, respectively (37 °C, 1 h), and checked for viability afterwards using trypan blue staining. Subsequently, cells were washed with PBS to remove excess of **VioA**, resuspended in PBS and distributed into aliquots, followed by exposure to a range of temperatures between 37 °C to 67 °C. Cells were lysed in the following step, soluble proteins isolated by ultracentrifugation, tryptically digested, labeled using isobaric TMT labels and finally combined to one pooled sample per condition. In order to decrease sample complexity for LC-MS/MS analysis, pooled samples were subjected to hydrophilic-interaction liquid chromatography (HILIC). Resulting raw files were preprocessed using MaxQuant[140] and thermal response curve fitting as well as melting point calculations carried out using the published TPP R package (Figure 14A).[138]

Obtained data was analyzed and filtered according to criteria listed in experimental section and compound induced T_m shifts determined from two biological replicates of **VioA** vs DMSO treatment (separately for each applied concentration) visualized in a scatterplot (Figure 14B for 1 µM treatment; see appendix for scatter plot for 150 nM treatment in comparison to DMSO).

Proteins of interest are dysregulated in both replicates to the same extent, resulting in a location ideally on the x = y line in the scatter plot. In case of 150 nM **VioA** treatment, the scatter plot revealed no isolated clear targets.

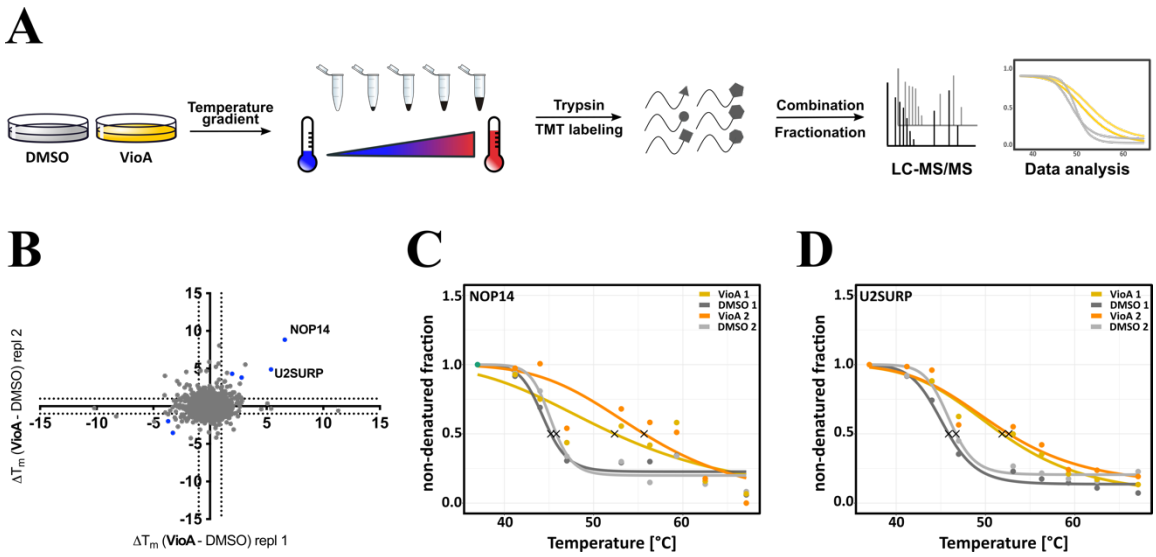

Figure 14: Target identification of **VioA** in Jurkat cells using *in situ* thermal proteome profiling. **A)** Schematic workflow of TPP experiment. Jurkat cells were treated with 1 µM **VioA** or DMSO respectively for 1 h. Next, samples were distributed into 9 aliquots per condition and incubated at temperatures ranging from 37 °C to 67 °C. Following incubation at different temperatures, samples were centrifuged and the proteins in the supernantant tryptically digested, TMT-labeled and combined to one sample per conditions prior to HILIC fractionation. Finally, samples were analyzed by LC-MS. **B)** Scatter plot of T_m shifts determined from two biological replicates of **VioA** vs DMSO treatment. Melting point shifts passing all significance criteria (see experimental section) are indicated in blue. Thermal response curves and calculated melting points (asterisks) of **VioA** treated (orange) and DMSO (grey) treated cells for **C)** NOP14 and **D)** U2SURP.

Whereas *in situ* TPP experiments using 150 nM revealed no demarcated proteins in the scatter plot, results for experiments with a final concentration of 1 µM were more explicit.

In this experiment, 67 proteins displayed a minimal temperature shift of 1°C in both biological replicates. Six of these proteins (Figure 14B, blue dots, melting curves of remaining hits see Appendix) passed all additional filtering criteria required to flag proteins as hits. Two of these six proteins displayed a particular high stabilization upon **VioA** treatment, namely nucleolar protein 14 (NOP14) (scatter plot Figure 14A; melting curves Figure 14C) and U2 snRNP-associated SURP motif-containing protein (U2SURP) (scatter plot Figure 14B, melting curves Figure 14D), which are both located in the nucleolus.

U2SURP, together with four other small nuclear ribonucleoprotein particles (U1, U3, U5 and U6) and numerous non-snRNP proteins, form the catalytically active center of the spliceosome.[152]

NOP14, the protein showing the highest stabilization upon **VioA**-treatment, is of central importance in ribosome biogenesis, in detail playing a significant role in 40S ribosome subunit formation and export, as well as maturation of 18S rRNA.[153]

Table 4: Calculated *p*-value, slope and curve fit for protein targets of vioprolide A in Jurkat cells determined by *in situ* thermal proteome profiling. Proteins listed met all filter criteria.[82,137] CEP170 met all significance criteria in one replicate but was just outside the threshold for significance in the other. Cut-off criteria for: *p*-value < 0.05 in one replicate, < 0.1 in the second replicate. R2 fit > 0.8, min. slope < -0.06.

T_m shift repl 1/2 [°C]	p-value adj. repl 1/2	R2 curve fit (VioA1/DMSO1/VioA2/DMSO2)	Min. slope VioA vs DMSO repl. 1/2	Gene name	Protein name
6.61/ 8.85	6.5E-07/9.32E-14	0.81/0.94/0.84/0.95	-0.10/-0.10	NOP14	Nucleolar protein 14
25.39/4.89	5.18E-03/2.91E-02	0.99/0.99/0.95/0.99	-0.08/-0.09	U2SURP	U2 snRNP-associated SURP motif-containing protein
3.13/5.55	3.13E-01/4.00E-05	0.98/0.99/0.99/0.99	-0.09/-0.11	CEP170	Centrosomal protein of 170 kDa
1.96/4.31	4.93E-02/3.48E-03	0.99/0.98/0.99/1.00	-0.18/-0.13	CDKN2AIP	CDKN2A-interacting protein
2.79/3.82	6.63E-03/1.2E-03	0.82/0.96/0.99/0.84	-1.29/-0.14	POLR3A	DNA-directed RNA polymerase subunit
-3.70/-2.00	3-32E-02/1.55E-01	0.99/0.98/0.96/1.00	-0.13/-0.19	RGS14	Regulator of G-protein signaling 14
-3.27/-3.53	9.03E-02/8.61E-02	0.99/0.93/0.92/0.98	-0.12/-0.09	SNX8	Sorting nexin-8

As splicing and ribosome biogenesis depict essential cellular processes, a dysregulation of both of these pathways *via* **VioA** would explain the cytotoxic properties of the natural compound, and therefore these proteins been selected for further target validation studies.

Remarkably, the majority of identified hits are localized in the nucleus, suggesting **VioA** to have a preference for the nucleolus as site of action. Additionally, with DNA-directed RNA polymerase subunit (POLR3A), a subunit of RNA polymerase III[154], a second protein of essential importance in the ribosome biogenesis process is affected by **VioA**.

1.2.3. Target validation of vioprolide A

1.2.3.1 Validation of U2SURP as target of vioprolide A

As U2SURP was revealed as being highly stabilized by **VioA** in *in situ* TPP experiments, target validation experiments were conducted to investigate inhibitory effects of **VioA** on U2SURP. Therefore, a dual luciferase splicing reporter gene assay was carried out. The assay is based on a modified firefly luciferase gene, furnished with chimeric B-globin/immunoglobulin intron (Luc-I) in the open reading frame (ORF). In case of impaired splicing activity, occurring stop codons lead to translation of an abridged, inactive version of the luciferase, which lacks enzymatic activity. As a positive control, an intron-less luciferase control reporter gene (Luc) is employed. Cells are co-transfected with renilla luciferase control reporter for 24 h and the firefly/renilla luciferase activity is compared relatively.[155]

After transfection of HeLa cells with renilla luciferase and Luc-I or Luc for 24 h, respectively, cells were treated with **VioA** or DMSO. Cells incubated with Isoginkgetin (ISO), a known inhibitor of pre-mRNA splicing, served as positive control.
Splicing activity was not diminished by **VioA**, as the activity of Luc-I here was comparable to activity of DMSO treated cells. In addition, the activity of firefly luciferase translated from Luc-I reporter gene corresponded to the activity of the intron-less variant Luc. As no diminished splicing activity caused by **VioA** treatment was observed, U2SURP was excluded as potential target.

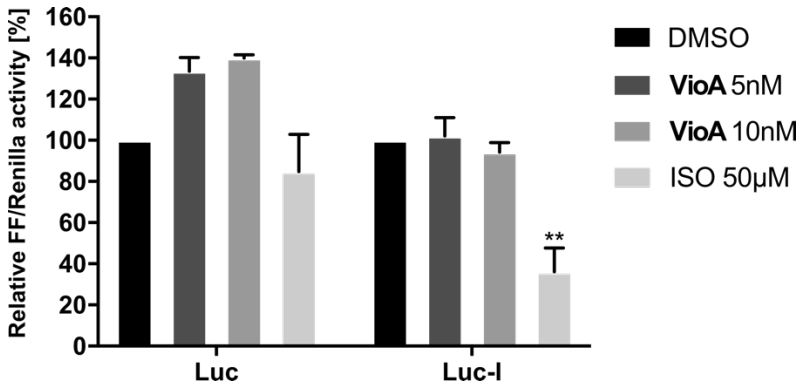

Figure 15: Splicing Dual Luciferase Reportergene Assay Relative expression of the luciferase reporters in HeLa cells. HeLa cells were transfected either with Luc or Luc-I firefly luciferase reporters and co-transfected with renilla luciferase control reporter for 24 h with FUGENE HD reagent according to manufacturer's protocol. After transfection, cells were treated with VioA or the pre-mRNA splicing inhibitor Isoginkgetin (ISO) for 24 h. Luciferase activity was measured using Dual Luciferase Assay Kit (Promega) according to manufacturer's protocol. Relative firefly/renilla luciferase activity was calculated and values were normalized towards untreated control. Bars represent the mean ± SEM of three independent experiments performed in duplicate, one-way ANOVA, Dunnett's test, , ** $P<0.002$. Experiments were carried out and analyzed by Christina Orgler.

1.2.3.2. Target validation of nucleolar protein 14 (NOP14)

1.2.3.2.1. The role of NOP 14 in ribosome biogenesis

Apart from its contribution to several diseases[156,157], knowledge about NOP14 is quite limited. Structural and functional investigations carried out so far concentrated on *Saccharomyces cerevisiae* as eukaryotic model organism. However, as its structure and the structure of its interaction partners are highly conserved[153], most of the conclusions drawn in literature might also be valid for human homologues.

NOP14 captures a significant role in 40S ribosome biogenesis and the maturation of 18S RNA. In detail, NOP14 depicts an essential protein in the initial phase of ribosome biogenesis – the formation of the small subunit (SSU) processome. This 2.2 MDa ribonucleoprotein complex is required for the maturation of the 40S subunit in eukaryotic cells.[158] Within this complex, NOP14 is located in close proximity to nucleolar complex protein 4 homolog (NOC4L) and ribosomal RNA small subunit methyltransferase NEP1 (EMG1) (Figure 16). All three proteins are structurally highly conserved among eukaryotes. As resolved by cryo-EM structures of the SSU processome of *Saccharomyces cerevisiae*, NOP14 and NOC4L are structurally winded into each other, while EMG1 is located on top of NOP14 in the SSU processome complex.[159]

EMG1 exhibits a catalytic activity, methylating pseudouridine at a distinct position in 18S rRNA.[160], however, this activity is not essential for ribosome biogenesis but its physical interplay with other proteins within the SSU processome.[161] Besides, a point mutation of EMG1 has recently been shown to cause the Bowen-Conradi syndrome (BCS), a genetic disorder leading to early infant death.[161,162] NOP14 and NOC4L do not exhibit catalytic activity but possess an essential scaffold function in the SSU processome.[163]

Detailed studies on the interactions between NOP14 and EMG1 as well as NOC4L were carried out with the respective yeast homologues. NOP14 and NOC4L, showing a concentrated occurrence in the nucleolus, were shown to form a stable heterodimer, and NOC4L deficiency led to cellular distribution of NOP14. Additionally, it was shown, that an intact NOP14-NOC4L heterodimer is crucial for maturation and nuclear export of 40S preribosomes.[164]

Studies focusing on the interaction between EMG1 and NOP14 in yeast revealed that while EMG1 can be found throughout the cell, an unperturbed interaction with NOP14 is necessary for its nuclear localization. NOP14 depleted cells showed unaltered expression levels of EMG1, but a nearly complete absence of the protein in the nucleus. Additionally,

the study uncovered that physical interaction of NOP14 and EMG1 is essential for 18S rRNA processing and pre-40S generation. Furthermore, binding site studies with NOP14 and EMG1 revealed a specific domain in NOP14 being responsible for interaction with EMG1.[153]

In summary, the physical unperturbed interplay of NOP14 with both interaction partners was shown to be of essential importance for ribosome biogenesis, in particular 18S rRNA maturation and 40S assembly export. Whereas NOP14 is required for nuclear localization of EMG1, NOC4L is in turn required for nucleolar localization of NOP14.

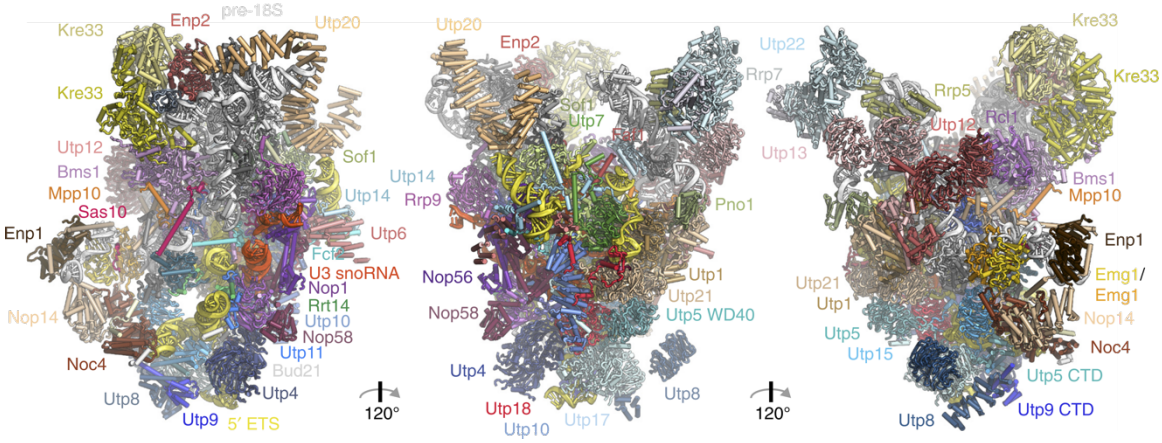

Figure 16: Cryo-EM reconstruction of SSU processome from *S. cerevisiae.* Cartoon illustration of the atomic model of the SSU processome with three perspectives with embedded structures of NOP14 (skin-colored), NOC4(brown), Enp1 (dark brown) and EMG1 (yellow/orange). Figure reprinted with permission from *Barandun et al.*[159]

1.2.3.2.2. Inhibition of proliferation and rRNA synthesis

In order to elucidate, if anti-proliferative effects of **VioA** could arise from NOP14 activity inhibition, effects of NOP14 on cell growth were examined using HeLa NOP14 knockdown cells. Therefore, HeLa cells were transfected with either NOP14 siRNA (small interfering RNA) or nt siRNA (non-targeted small interfering RNA) as control, respectively. Subsequently, proliferation was measured in real-time using a XCELLigence proliferation assay. For this assay, cells are seeded on plates containing electronic sensors. Cells interact with these sensors by attaching to the surface, resulting in an impedance response. As this impedance response - converted to a relative cell index - directly correlates to the cell number, proliferation can be measured over time.[165]

As illustrated in Figure 17, cells treated with nt siRNA proliferate in a normal manner with a calculated doubling time of approximately 26 hours. In contrast, NOP14 knockdown revealed a significant effect on proliferation. Whereas in case of nt siRNA treatment, the cell number is increasing starting at 40 h incubation time, NOP14 knockout cells show poor proliferation behavior and the cell number almost remained static until the end of measurement after an initial slight increase. This decreased proliferation is also reflected in a significantly higher calculated doubling time of approximately 60 hours.

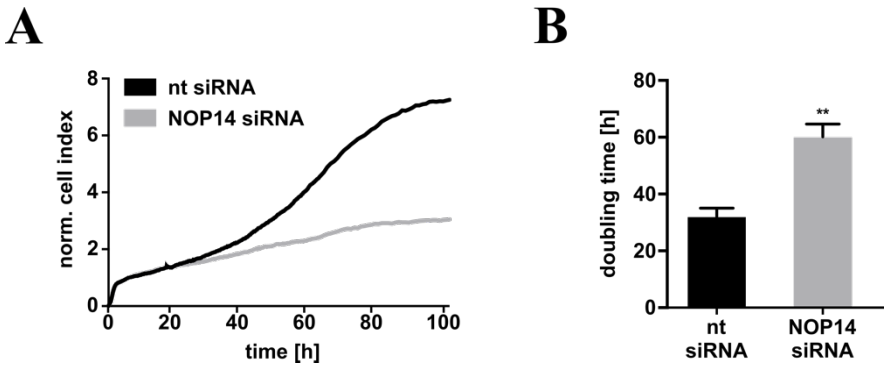

Figure 17: A) xCELLigence real-time proliferation measurement of HeLa cells transfected with nt or NOP14 siRNA for 24 h before seeding into E-plates. Proliferation was monitored for the following 72 h. Visualized curve is representative for all three independent experiments. **B)** Respective doubling time values were calculated using xCELLigence RTCA software. Bars represent the mean ± SEM of three independent experiments performed in triplicates, two-tailed unpaired Student's t-test, **<0.002. Experiment was carried out by Christina Orgler.

As outlined in chapter 1.2.1., **VioA** exerts potent anti-proliferative effects. Comparable effects are observed for NOP14 knockdown cells. As **VioA** targets NOP14, this compound-target interaction putatively leads to impaired NOP14 function and thus results in compound-induced reduction of proliferation. However, a direct evidence for this putative explanation is missing so far.

VioA treatment and NOP14 knockdown revealed a comparable phenotype in terms of anti-proliferation. As NOP14 is known to exhibit an essential function in ribosome biogenesis, both, **VioA** treatment and NOP14 knockdown were tested for their potential to influence the initial step of ribosome biogenesis – the transcription of rRNA.

The process of rRNA transcription from genes encoding for ribosomal RNAs (rRNAs) occurs in the nucleoli (Chapter 1.1.2.2.). These rRNAs depict the nucleic acid backbone of the ribosome and therefore are of crucial importance for proper ribosome generation.[62] The synthesis of rRNA can be tracked by feeding 5-FU as this uracil derivate is subsequently incorporated into freshly synthesized rRNA, which can be detected by immunostaining and confocal microscopy.

In a first target validation experiment, the influence of NOP14 on rRNA production was investigated. Therefore, HeLa cells were transfected with NOP14 siRNA or nt siRNA as control for 48 h, respectively. Subsequently, cells with nucleolar rRNA foci were considered as rRNA producing cells (Figure 18A) in a nuclear run on assay. Analog to this experiment, HeLa cells were incubated (37°C, 24 h) with **VioA** (5 nM or 10 nM) or DMSO, respectively. Cells incubated with actinomycin D – a known rRNA synthesis inhibitor - served as positive control (Figure 18B).

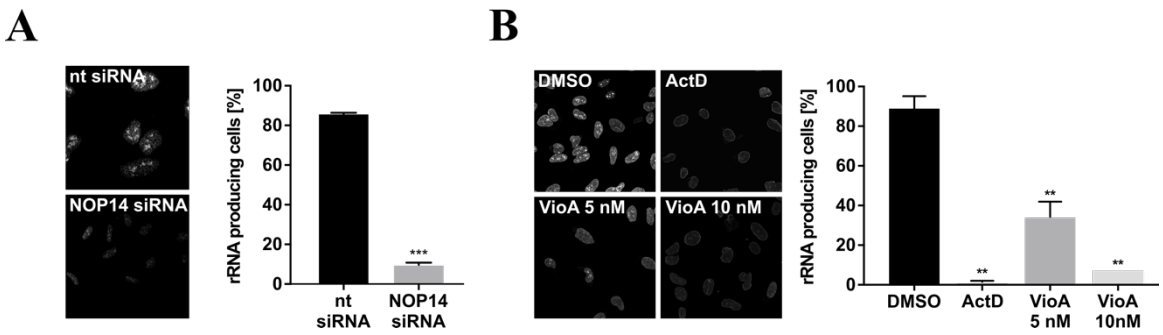

Figure 18: A) HeLa cells were transfected with nt or NOP14 siRNA for 48 h prior to nuclear run on assay. Cells with nucleolar rRNA foci were as rRNA producing cells. Bar diagram visualizing the mean ± SEM of three independent experiments performed in duplicates, two-tailed unpaired Student's t-test, ***P<0.001. **B)** Nuclear run on assay with HeLa cells treated with **VioA** for 24 h or 6 µM Actinomycin D (ActD) for 2 h. Experiment was carried out by Christina Orgler.

In contrast to nt siRNA treated cells, the incorporation of 5-FU into freshly synthesized rRNA was significantly reduced in NOP14 knockdown cells, indicating that decrease in NOP14 expression levels lead to a diminished rDNA transcription rate. In literature, linkage between NOP14 and transcription levels of rRNA are so far unknown. As a consequence, it can only be assumed, that impaired NOP14 levels lead to an negative regulation of initial ribosome biogenesis processes in a feedback loop. Presumably, the complex process of ribosome biogenesis is thwarted at initial stage if downstream processes are altered.

Interestingly, in line with NOP14 knockdown experiments, a decrease of rRNA synthesis rate was observed by **VioA** treatment. Incubation of HeLa cells with 5 nM **VioA** led to a decrease of freshly synthesized rRNA of more than 50%, and was further reduced by 10 nM **VioA**, showing a high potency of **VioA** in reduction of rRNA synthesis. As both, knockdown of NOP14 and incubation of the cells with **VioA** lead to decreased rRNA levels in the nucleoli, these findings could deliver a hint that **VioA** leads to an impaired function of NOP14 upon binding and thereby to decreased rRNA levels.

As already mentioned, ActD was utilized as positive control leading to decreased rRNA transcription levels as known Pol I inhibitor. By intercalating into GC-rich regions of rDNA, actinomycin D (ActD) inhibits Pol I dependent transcription. As proper interaction of rDNA and Pol I is imperative for nucleoli arrangement, disruption of this transcriptional machinery *via* ActD treatment results in nucleoli disassembly. As **VioA** also led to diminished rRNA production levels, it was investigated whether **VioA** acts via a comparable mechanism as **ActD**. Therefore, cells were treated with **VioA** (10 nM final concentration) or **ActD** (6 µM final concentration) for 2 hours. DMSO treated cells functioned as negative control. After incubation time, cells were immunostained for NOP14 , and nuclei stained with Hoechst.(Figure 19).

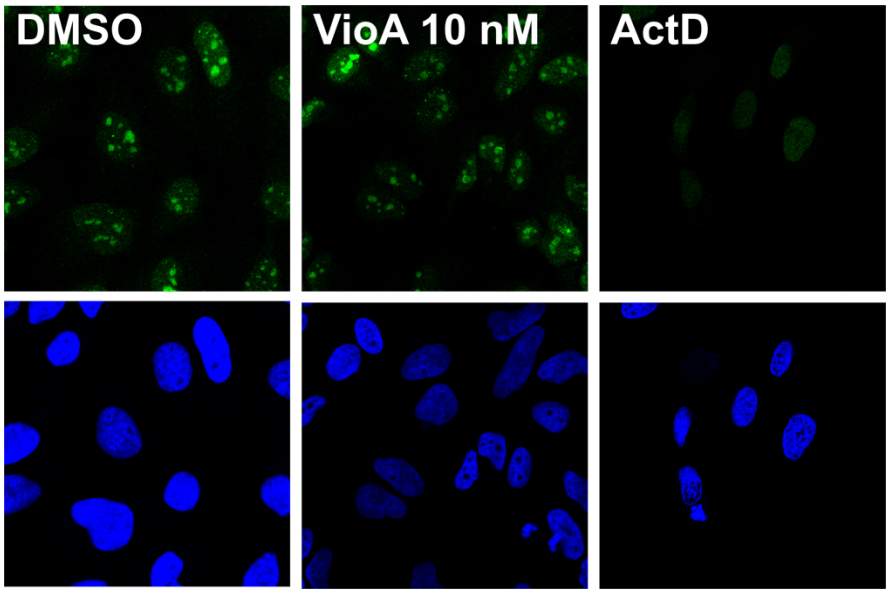

Figure 19: HeLa cells were treated with 10 nM **VioA** or 6 µM **ActD** 2 h and immunostained for NOP14. Nuclei were stained with Hoechst (blue). Experiment was carried out in triplicates an representative immune fluorescence images are shown. Experiment was carried out by Christina Orgler.

As ActD leads to disassembly of the nucleoli, NOP14 was distributed in the whole nucleolus due to nucleolar disruption. In contrast to actinomycin D treated cells, and in line with DMSO cells, nucleoli remained intact upon **VioA** treatment, as NOP14 retained its

nucleolar localization. Nucleolar assembly was not perturbed by **VioA**. Therefore, it can be concluded, that VioA does not action *via* inhibition of rDNA transcription.

As **VioA** does not interfere with rDNA – Pol I interaction, the compound apparently exerts its inhibitory effect on rRNA production via a different, unknown mechanism.

1.2.3.2.3. Whole proteome analysis

To elucidate the influence of **VioA** treatment on global protein expression and to investigate if **VioA** causes decreased expression levels of NOP14, EMG1 and NOC4L, full proteome analysis was performed. Therefore, Jurkat cells were incubated with **VioA** (10 nM final concentration) or DMSO, respectively. Cells were washed with PBS followed by lysis with a detergent-based buffer. Protein concentration was adjusted to equal amounts in all samples using a BCA assay. Subsequently, proteins were precipitated with acetone (-20°C, overnight), centrifuged, reconstituted in buffer, tryptically digested and resulting peptides analyzed by LC-MS/MS. Resulting raw data were analyzed with MaxQuant and Perseus. A two-sided student's *t*-test was applied to calculate fold change of protein expression and statistical significance (*p*-value) for each protein and visualized in a volcano plot. Proteins exhibiting a $\log_2$ fold change of >1 or <-1, respectively and a $-\log_{10}$ p-value of >1.3 were considered as significantly dysregulated.

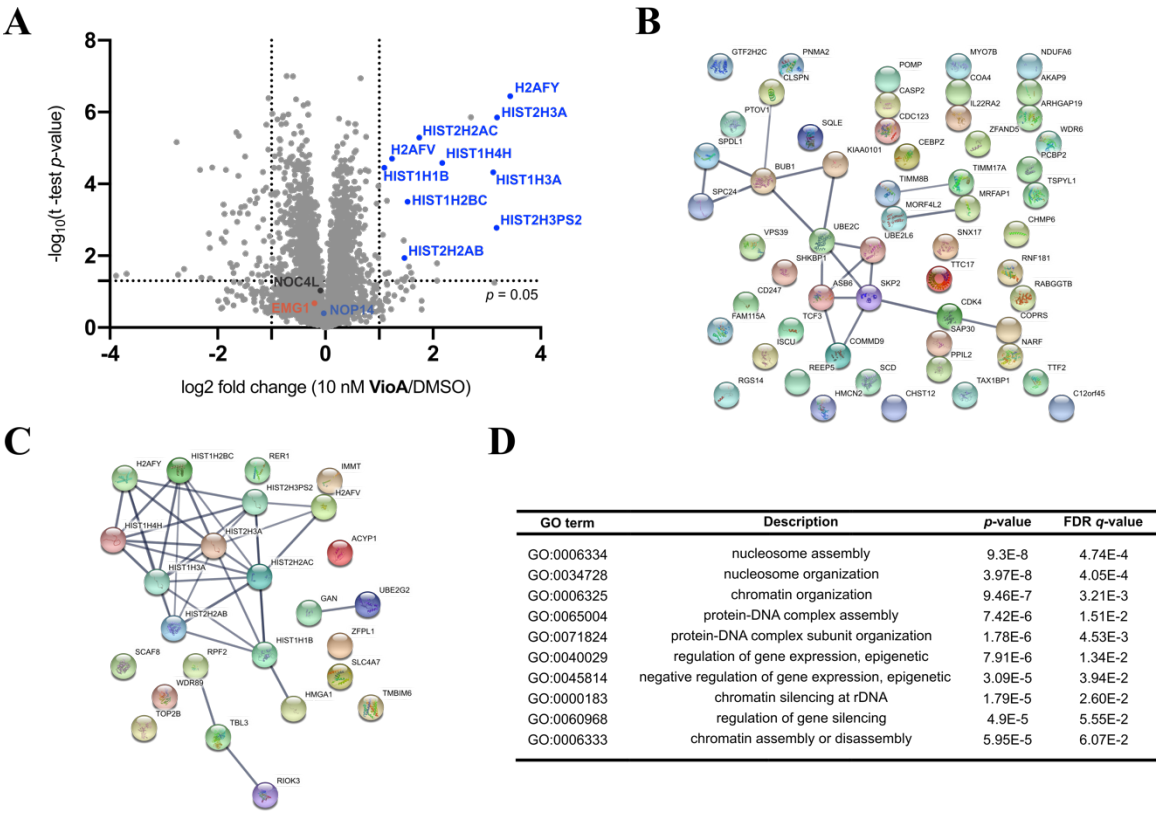

GO term	Description	*p*-value	FDR *q*-value
GO:0006334	nucleosome assembly	9.3E-8	4.74E-4
GO:0034728	nucleosome organization	3.97E-8	4.05E-4
GO:0006325	chromatin organization	9.46E-7	3.21E-3
GO:0065004	protein-DNA complex assembly	7.42E-6	1.51E-2
GO:0071824	protein-DNA complex subunit organization	1.78E-6	4.53E-3
GO:0040029	regulation of gene expression, epigenetic	7.91E-6	1.34E-2
GO:0045814	negative regulation of gene expression, epigenetic	3.09E-5	3.94E-2
GO:0000183	chromatin silencing at rDNA	1.79E-5	2.60E-2
GO:0060968	regulation of gene silencing	4.9E-5	5.55E-2
GO:0006333	chromatin assembly or disassembly	5.95E-5	6.07E-2

Figure 20: Whole proteome analysis of Jurkat cells treated with **VioA** (10 nM, 24 h) in comparison to DMSO treated cells. **A)** Volcano plot represents two-sample *t*-test results of VioA treated cell in comparison to DMSO control (n=4). Cutoff criteria were defined as $\log_2 = \pm 1$ ratio factor and $-\log_{10}$(t-test *p*-value) = 1.3 (dotted lines). NOP 14 (purple), NOC4L (dark grey), EMG1 (orange) and histone proteins (blue) are highlighted in the plot Interaction network of significantly **B)** depleted proteins and **C)** proteins with increased occurrence as analyzed using STRING v11 database[166]. Parameters applied for correlation network creation are described in the experimental part. **D)** GO term enrichment analysis was carried out for upregulated proteins using GOrilla.[167]

Interestingly, expression levels of NOP14 as target of **VioA** as well as NOC4L and EMG1 were not dysregulated upon compound treatment. Non-altered protein abundance indicated that **VioA** binding to NOP14 does not lead to depletion or augmented protein synthesis of these proteins (Figure 20A). The majority of significant dysregulated proteins is downregulated (56 proteins against 28 upregulated proteins) upon treatment with **VioA**, which could stem from the general anti-proliferative effect of **VioA**. Another explanation for reduced protein synthesis is impaired ribosome biogenesis, leading to a decreased protein synthesis. Dysregulated proteins were analyzed using the STRING v11 database[168,169] separately for up- and downregulated proteins to identify interacting proteins within each group. In case of downregulation, one predominant interaction network was revealed (Figure 20B) and a preponderant number of the proteins in this network are assigned to play a role in cell cycle progression (67% of the central network, 25% of all downregulated proteins, GO term 0007049: cell cycle, GO term 0022402: cell cycle process, GO 0000278: mitotic cell cycle). Remarkably, the majority of proteins showing increased expression upon **VioA** treatment are histones, as indicated in the volcano plot (Figure 20A: blue dots and gene names). Consequently, these proteins depict a strong interaction network pattern among upregulated proteins (Figure 20C).

However, rather than utilizing the entire measured proteome as background, the STRING DB algorithm utilizes three different background sets to assess statistically significant enriched GO terms: whole genome, druggable genome and kinases. However, depending on the employed buffers utilized during the workflow, the profile of extracted proteins is biased and does not reflect the whole proteome. Thereby, background gene sets as utilized by STRING DB algorithm are not suitable for the whole proteome analysis.
Therefore, in order to assess statistically significant enriched GO terms over all dysregulated proteins, a gene set enrichment analysis using GOrilla[167] was performed. Here, the GO term enrichment of the dysregulated proteins was calculated against the background of all measured proteins (Figure 20D). Whereas an isolated analysis of all depleted proteins against the measured proteome did not reveal any significantly enriched GO terms, the analysis of all dysregulated proteins showed a clear overrepresentation of nucleosome associated biological processes.

The distinct overrepresentation of histones in **VioA** treated samples might stem from increased presence of chromatin, histones and nucleosomes in the utilized aqueous buffer as the cells are treated with an apoptosis-inducing agent. DNA fragmentation is regarded as a hallmark of apoptotic cell death, leading to release of nucleosome particles.[170]

As this fragmentation increases the solubility of these nucleosomal parts, *e.g.* histones, their abundance increases. Therefore, elevated levels of histones in **VioA** treated samples might arise from apoptosis induction. Even though, exerted IC_{50} of **VioA** in the conducted apoptosis assay was significantly higher (approx. 3-fold), apoptosis induction effects apparently are detectable at lower concentrations on a whole proteome level.

1.2.3.2.4. Whole proteome analysis of NOP14 knockdown cells

In order to further elucidate the effect of NOP14 depletion on a whole proteome level, a full proteome analysis was performed using NOP14 siRNA transfected HeLa cells compared to nt siRNA treated cells. In line with previous described transfection experiments, cells were treated with siRNA for 48 hours, prior to execution of whole proteome analysis workflow as described above.

Knockdown of NOP14 revealed few proteins significantly dysregulated (Figure 21), thus indicating that influence of NOP14 silencing on whole proteome expression levels is limited. Of note, NOP14 was not tracked in MS-samples even though presence of the protein in the samples and an efficient knockdown could be verified by Western Blot in the samples.

NOP14 knockdown led to decreased levels of NOC4L. Even though a direct link between expression levels of NOC4L and NOP14 has not been shown yet, co-expression of both proteins stands to reason as they form a heterodimer, essential for SSU processome formation and maturation of pre-40S subunit.[159]

Besides, NOC4L, a second protein involved in 40S subunit maturation, was identified as significantly downregulated – serine/threonine-protein kinase RIO2 (RIOK2). Comparable to NOP14 and NOC4L, RIOK2 is involved in pre-40S subunit export to the cytoplasm. In contrast to the other mentioned proteins its function thereby is not essential. Furthermore, RIOK2 is responsible for the cleavage of essential nuclear protein 1 (Enp1) from exported 40S precursor by physical interplay but not its catalytic activity.[171] Interestingly, Enp1 is located in close proximity to NOP14 in the SSU processome in yeast.[159] However, besides a local closeness between these proteins a further link between RIOK2 and NOP14 is not known which could explain the decreased expression of RIOK2

upon NOP14 knockdown. Further conclusions involving Enp1 are not possible, as the protein was missing in the data set.

Interestingly, EMG1 expression levels were not affected by NOP14 knockdown, indicating that NOP14 presence conducts EMG1 to the nucleolus but does influence EMG1 expression. In contrast to increased abundance upon **VioA** treatment as revealed by whole proteome analysis, HIST2H2AC was downregulated by NOP14 knockdown. A direct link between NOP14 and HIST2H2AC is missing in literature. However, a post-translational modification of histone H2A *via* glutamine methylation is proven to exclusively occur in yeast over the 35S rDNA transcriptional unit, thus enabling rDNA transcription via Pol I[172]. Thereby, NOP14 and HIST2H2AC are loosely connected by playing a role in the same biological process of ribosome biogenesis. However, a detailed connection between both proteins is unknown so far.

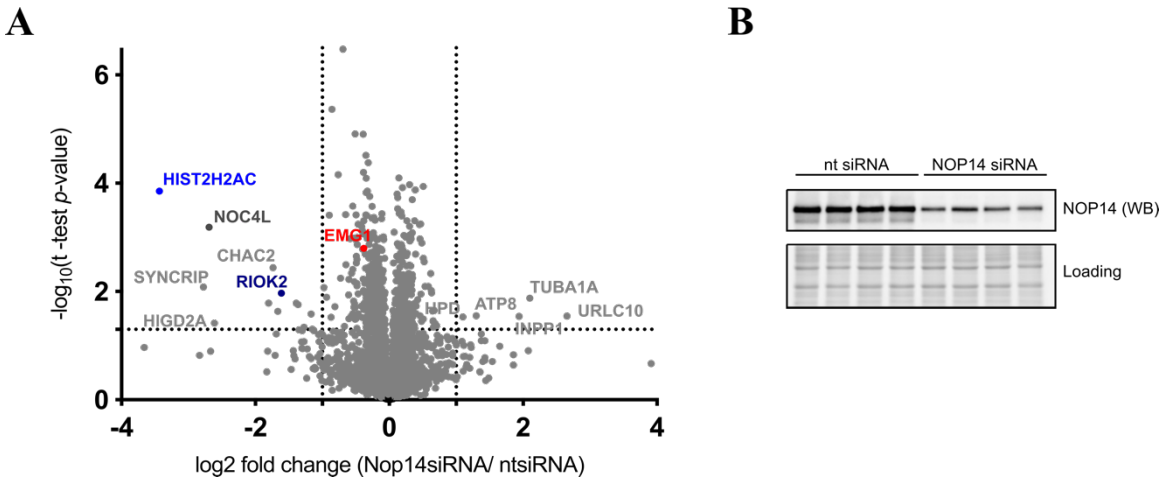

Figure 21: Whole proteome analysis after NOP14 knockdown in HeLa cancer cells. Cells were transfected with NOP14 siRNA or nt siRNA, respectively for 24 h. **A)** Volcano plot represents two-sample *t*-test results of NOP14 siRNA treated cells compared to nt siRNA treated cells (n=4). Cutoff criteria were defined as $\log_2 = \pm 1$ ratio factor and $-\log_{10}$(t-test *p*-value) = 1.3 (dotted lines). HIST2H2AC (blue), NOC4L (dark grey), RIOK2 (dark blue) and EMG1 (red) are colored in the plot. Remaining significant dysregulated proteins are additionally labeled. Even though not detected via mass spectrometry, NOP14 was present in the samples as shown by western blot analysis. **B)** Western blot analysis confirmed successful knockdown of NOP14 despite the absence of the protein in the MS-derived dataset.

1.2.3.2.5. Interactome studies on the influence of VioA on NOP14 and its binding partners

As outlined above, NOP14 functions as a scaffold protein in the SSU processome complex without known enzymatic activity. As the interactions with EMG1 and NOC4L in this ribonucleoprotein complex are essential for ribosome biogenesis, the interactome of NOP14 was studied using MS-based co-immunoprecipitation (co-IP).

Intact Jurkat cancer cells were incubated with DSSO-crosslinker, to ensure covalent attachment of intracellular binding partners as described previously.[173] Subsequently, cells were lysed and co-IP was carried out using an immobilized anti-NOP14 antibody. Isotype control treated samples served as control to identify unspecific binding events. Finally, pulled-down proteins were analyzed *via* LC-MS/MS, raw data preprocessed using MaxQuant[140] and statistically evaluated using two-sample students *t*-test (Perseus[151]) (Figure 22A).

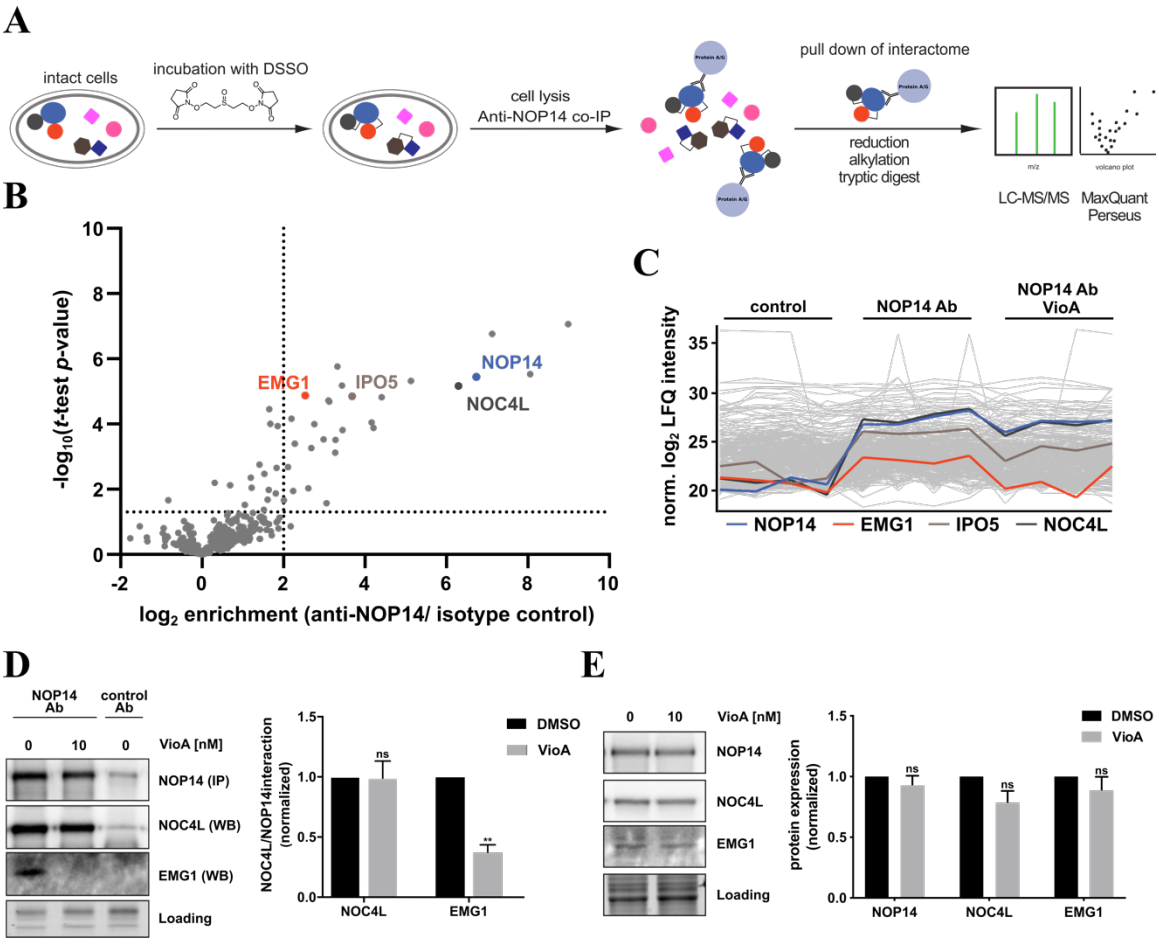

Figure 22: Co-Immunoprecipitation with anti-NOP14 antibody. **A)** Schematic workflow of MS-based co-IP. Live cells were treated with **VioA** (10 nM) or DMSO for 24 h, respectively. Subsequently, DSSO crosslinker was added to covalently link protein complexes within cells. NOP14 and linked proteins were enriched using an anti-NOP14 antibody and immobilized on protein A/G beads. Tryptic peptides were measured via LC-MS/MS, and analyzed using MaxQuant

and Perseus. **B)** Volcano plot represents two-sample t-test results of anti-NOP14 coIP compared to isotype control coIP (n=4). Cutoff criteria were defined as $\log_2$= 2 enrichment factor and -$\log_{10}$(t-test *p*-value) = 1.3 (dotted lines). NOP 14 (blue), NOC4L (dark grey), EMG1 (orange) and IPO5 (green) highlighted in the plot. **C)** Comparison of normalized LFQ intensities of NOP14, NOC4L, EMG1 and IPO5 in isotype control and anti-NOP14 co-IP samples, treated with 10 nM VioA prior to co-IP after missing value imputation. **D)** Co-IP of NOP14 in Jurkat cells and detection of NOP14 and interactors NOC4L/ EMG1 by western blot analysis. A representative experiment out of three independent experiments is shown. Bars represent mean ± SEM of three independent experiments, two-tailed unpaired Student's *t*-test, *** P<0.001. **E)** Western Blot of analysis of NOP14, NOC4L and EMG1 expression levels of Jurkat cells either treated with **VioA** (10 nM) or DMSO, respectively for 24 h comparable to whole proteome analysis. Bars represent the mean ± SEM of three independent experiments, two-tailed unpaired Student's *t*-test, ns P>0.05.

Comparison of pulled-down proteins to isotype control co-IP samples revealed several highly significantly enriched proteins (Figure 22B, Table 5), amongst others, EMG1 and NOC4L as known interaction partners of NOP14. Comparable to the location of NOP14, the majority of these proteins are located in the nucleus (57%, GO term 0005635: nucleus[174]).

Another interaction partner of interest is Importin-5 (IPO5), as this protein is known to be involved in nuclear import of several ribosomal proteins (RPL37A, RPS7 and RPL5) comparable to other members of the importin beta family[175]. As IPO5 is part of the cargo complex importin, responsible for the import of RPS7 from the cytoplasm, an interaction might occur during the incorporation of RPS7 into the 40S subunit. However, this hypothesis requires further validation experiments and is so far only an assumption. Furthermore, EMG1 is known to be imported into the nucleolus by the importin α/ importin β (Impα/β) and importin β/ importin 7 (Impβ/7) heterodimer.[162] IPO5 as part of the importin complex might interact with EMG1 thereby being also enriched in the interactome study.

Nucleoprotein TPR (TPR), having a function in shuttling proteins into and out of the nucleus, depicts another protein significantly enriched. This protein has a scaffold function in the nuclear pore complex (NPC) and was shown to influence the number of NPCs per nucleus.[176] Interestingly, NPCs were recently shown to possess translocation activity of pre-ribosomes in yeast.[177] As NOP14 is known to be involved in pre-40S export into the cytoplasm, TPR might interact with NOP14 in this process, or at least is located in close proximity to NOP14, thereby enabling a covalent crosslink upon DSSO crosslinker application.

Except for EMG1 and NOC4L, an interaction with NOP14 is experimentally not validated and unknown for the remaining enriched proteins. It has to be mentioned, that some of the enriched proteins might interact with each other and are crosslinked to each other without interacting with NOP14. These proteins could depict false-positive interaction partners of NOP14 in the co-IP data presented here. This would be an explanation for proteins located in the mitochondrion or the endoplasmic reticulum.

Another explanation for the enrichment of non-nuclear proteins might be that the utilized NOP14 antibody is not entirely specific for NOP14 but also binds to other proteins non-specifically.

Table 5: Significantly enriched proteins (log_2 enrichment > 2, $-log_{10}$ *t*-test *p*-value > 1.3) in MS-based co-IP experiments. Cells were incubated with 2 mM DSSO crosslinker for chemical cross-linking of protein-protein interactions and subsequent pull down using via anti-NOP14 antibody relatively to isotype control treated samples (n=4).

Log_2 enrichment	-log10 (t-test p-value)	Gene name	Protein name
8.99	7.06	TFG; TFG/ALK fusion	Protein TFG; Tyrosine-protein kinase receptor
8.06	5.53	SNAP29	Synaptosomal-associated protein 29
7.12	6.76	NANS	Sialic acid synthase
6.75	5.46	NOP14	Nucleolar protein 14
6.30	5.18	NOC4L	Nucleolar complex protein 4 homolog
5.13	5.32	DECR	2,4-dienoyl-CoA reductase, mitochondrial
4.41	4.82	MTCL1	Microtubule cross-linking factor 1
4.21	3.88	DTWD2	DTW domain-containing protein 2
4.16	4.05	NACC1	Nucleus accumbens-associated protein 1
3.70	4.86	IPO5	Importin-5
3.45	3.82	SEPT6	Septin 6
3.44	5.18	SEPT7	Septin 7
3.32	5.76	TPR	Nucleoprotein TPR
3.27	3.51	CIZ1	Cip1-interacting zinc finger protein
3.27	3.11	GFPT1	Glutamine-fructose-6-phosphate aminotransferase 1
3.12	4.68	PRKCA	Protein kinase C alpha type
3.10	4.72	SEPT2	Septin 2
3.06	1.57	SUB1	Activated RNA polymerase II transcriptional coactivator p15
2.98	3.53	HNRNPA2B1;HNRPA2B1	Heterogeneous nuclear ribonucleoproteins A2/B1
2.75	4.00	NAPA	Alpha-soluble NSF attachment protein
2.69	3.27	IST1	IST1 homolog
2.61	2.03	PPP2R1A	Serine/threonine-protein phosphatase 2A 65 kDa regulatory subunit A alpha isoform
2.48	4.89	EMG1	Ribosomal RNA small subunit methyltransferase NEP1
2.28	3.39	HSD17B10	3-hydroxyacyl-CoA dehydrogenase type-2
2.24	1.95	PPA1	Inorganic pyrophosphatase
2.20	4.17	ATAD3A/B	ATPase family AAA domain-containing protein 3A/B
2.11	2.68	EEF1D	Elongation factor 1-delta
2.01	1.66	PCBP2	Poly(rC)-binding protein 2

In order to identify proteinogenic interactions of NOP14, which are sensitive to **VioA** treatment, intact Jurkat cells were incubated with **VioA** (10 nM, 24 h) prior to the co-IP workflow. Treatment with **VioA** led to loss of several proteins (see Appendix). Furthermore, intensities of proteins in samples treated with anti-NOP14 antibody, isotype control or anti-NOP14 antibody treatment and additional VioA incubation were compared to identify **VioA** dependent depletion of proteins.

Interestingly, while NOP14-NOC4L interaction remained unperturbed upon **VioA** incubation, the interaction between NOP14 and EMG1 was disrupted (Figure 22C). Of note, interaction with IPO-5 was also shown to be influenced by **VioA** treatment, however not to the same extent as for EMG1. As interactions between NOP14 and IPO-5 are unknown so far, and decrease in signal intensity upon **VioA** treatment depicted to be less crucial, following experiments concentrated on the interaction of NOP14 to EMG1 and NOC4L.

The findings for EMG1 and NOC4L could be verified in independent co-IP experiments with western blot readout, showing a loss of signal intensity for EMG1 after **VioA** incubation, while signal intensity for NOC4L remained constant (Figure 22D). In order to verify that loss of interaction between NOP14 and NOC4L did not stem from decreased expression levels caused by compound incubation, Western Blot analysis against NOP14, NOC4L and EMG1 was conducted. Thereby, it could be shown, that **VioA** treatment does not have a significant impact on expression of these proteins, but leads to selective loss of interaction between NOP14 and EMG1. **VioA**-independent expression levels were additionally verified in whole proteome analysis (Figure 19A) as discussed above.

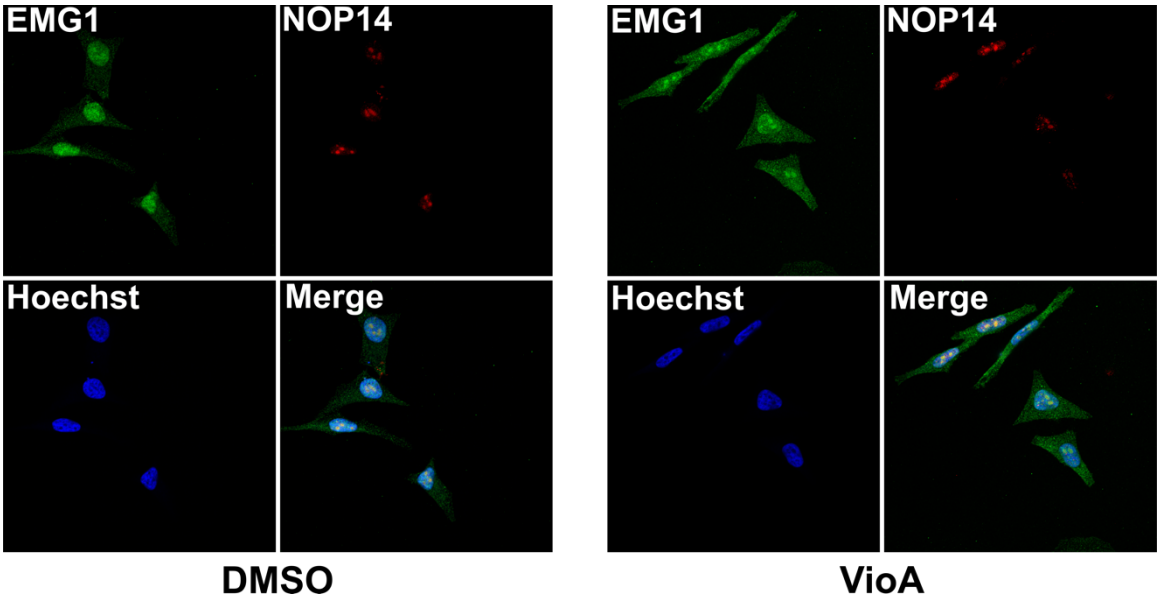

Figure 23: Immunofluorescence microscopy images of HeLa cells treated with **VioA** (10 nM, 24 h) and co-stained for NOP14 (red) and EMG1 (green). Nulcei were stained with Hoechst 33342. Representative images out of three independent experiments performed in duplicates are visualized. Experiments were carried out by Christina Orgler.

As mentioned in Chapter 1.2.3.2.1. the localization of EMG1 and NOP14 in the nucleolus heavily depends on unperturbed interactions to respective binding partners. As indicated by the results of the interactome studies, the NOP14-EMG1 interaction is selectively disrupted by **VioA** treatment, whereas the NOP14-NOC4L interaction remains

unaffected. According to the literature, EMG1 should consequently loose its nucleolar localization whereas NOP14 should maintain it, as its interaction to NOC4L is maintained.[153,164]

To investigate this assumption, HeLa cells were incubated with **VioA** (10 nM) or DMSO respectively for 24 h, co-stained for NOP14 (red) and EMG1 (green) and visualized using fluorescence microscopy.

In line with interactome study results, NOP14 maintained its localization in the nucleolus, upon **VioA** treatment, whereas a clear distribution of EMG1 in the entire cell is observed in comparison to DMSO treated samples.

Thereby, it could be shown that **VioA** targets NOP14 leading to a selective loss of interaction with EMG1, while interaction to NOC4L remained intact.

1.3. Summary and Outlook

In conclusion, the myxobacterial natural products vioprolides A-D were investigated towards their biological activity against a panel of cancer cell lines. In line with reports in literature, **VioA** illustrated the most active representative of this compound class. Whereas the compound exhibited comparable potent anti-proliferative activity against all tested cell lines, ALL cell lines were shown to be particularly sensitive towards apoptosis induction upon **VioA** treatment. To investigate the therapeutic potential of **VioA**, the compound was tested in ALL patient derived xenograft (PDX) cells. Whereas control PBMCs barely responded to **VioA** treatment, ALL patient cells displayed an increasing apoptosis rate, giving reasons to consider the vioprolide scaffold as a potential lead structure in anticancer drug development.

Even though target identification results using a **VioA** derived probe (**VioA-P**) remained inconclusive due to outlined reasons (suggestions for 2nd generation probes see 1.2.2.1.6.), cellular targets of **VioA** were identified using thermal proteome profiling (TPP). NOP14 and U2SURP showed significant stabilization upon compound treatment, with NOP14 exhibiting highest stabilization. Whereas U2SURP could not be validated as target of **VioA**, NOP14 was extensively studied using diverse biochemical and proteomics methods.

MS- and western blot based co-IP experiments revealed that **VioA** treatment leads to a selective loss of interaction between NOP14 and EMG1, while the interaction between NOP14 and NOC4L remained unperturbed. Additional whole proteome analysis and Western Blot experiments indicated that this loss of interaction did not stem from dysregulated expression levels of the affected proteins. Finally, fluorescence imaging experiments revealed that **VioA**-dependent loss of interaction between NOP14 and EMG1 led to delocalization of EMG1 in the cell.

Even though detailed mechanistic insights into the mode of action of **VioA** in cancer cells have been obtained, numerous scientific questions remain unanswered. First of all, even though a stabilizing effect of NOP14 by **VioA** engagement was discovered, the specific site of interaction is still unknown. Putatively, **VioA** binds into the region of NOP14, which is known to interact with EMG1[153]. An option to obtain unambiguous evidence of the binding site of **VioA** could be the application of 2nd generation **VioA** probes in binding site identification experiments.

In literature, a link between EMG1 delocalization and impaired biogenesis of the 40S subunit are known.[162] Even though a **VioA** dependent delocalization of EMG1 could be shown, a clear evidence for resulting impaired ribosome biogenesis is missing so far. Therefore, analytical ultracentrifugation experiments could be carried out to quantify altered expression levels of 40S subunit upon **VioA** treatment.[178] As dysregulated ribosome biogenesis leads to p53-dependent apoptosis[179], these experiments could bridge between the interaction of NOP14 with **VioA** and apoptotic effects exhibited by **VioA**. Finally, experiments (target identification, interactome analysis, etc.) could be conducted to reveal reasons for the cell type specific apoptotic effects of **VioA**.

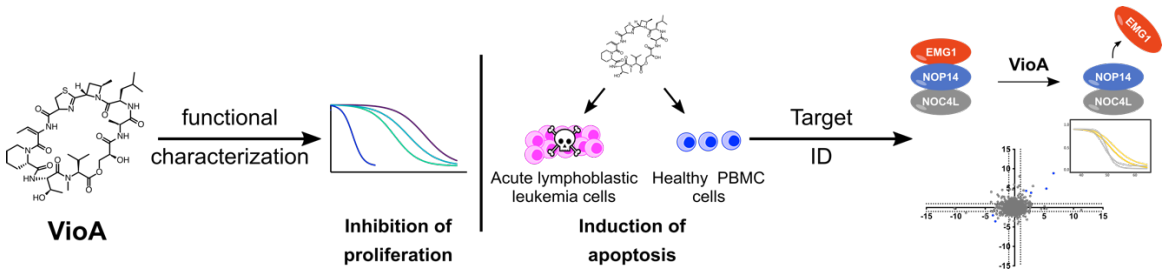

Figure 24: Graphical summary of the project.

Chapter II – -omics insights into the ClpXP machinery of *Staphylococcus aureus*

2. -omics insights into the ClpXP machinery of *Staphylococcus aureus*

2.1 Introduction

2.1.1. *Staphylococcus aureus* – a major bacterial human pathogen

Gram-positive round-shaped *Staphylococcus aureus* (*S. aureus*) populates a high percentage of humans and colonizes, as a commensal bacterium of the microbiota different parts of the human body, *e.g.* the nasal area, respiratory tract and the skin.[180-183] However, apart from its symbiotic behavior, *S. aureus* additionally depicts a severe opportunistic human pathogen, causing severe infections, *e.g.* infective endocarditis, meningitis, toxic shock syndrome and pneumonia, often developed from surgical wound and skin infections as well as food poisoning.[184,185]

The severity of staphylococcal infections is reflected by the fact that *S. aureus* derived bacteremia led to a mortality rate of 80% until tackled by the use of penicillin G in the 1940s.[186,187] The introduction of antibiotics in general greatly improved modern medicine and significantly expanded life expectancy.[188] However, resistant *S. aureus* strains were shortly discovered after and today wide spread resistance to penicillin in *S. aureus* isolates almost entirely prevents its applicability in clinics. The introduction of methicillin to the market for the treatment of penicillin resistant strains solely provided short-termed relief, as first methicillin-resistant *S. aureus* strains (MRSA) were discovered shortly after.[186,187] The fast development of resistances to antibiotics introduced to the market due to inappropriate use as well as their frequent application in animal farming resulted in the antibiotic resistance crisis human mankind is facing today, narrowing down therapeutic options for the treatment of bacterial infections. This antibiotic resistance crisis represents one of the greatest health threats, resulting in a race between development of new antibiotics and the occurrence of new bacterial resistances against these new drugs.[189-191]

Today, hospital- and community-acquired MRSA (HA-MRSA and CA-MRSA, respectively) are globally spread and MRSA depicts a preeminent cause of infections in hospitals worldwide, with more than 150,000 patients per year in the European Union and

approx. 11,000 deaths per year in the USA.[192-195] Vancomycin, an antibiotic glycopeptide discovered in the 1950s, illustrates the most frequent utilized antibiotic to treat invasive MRSA infections.[187,196,197] However, *S. aureus* strains developing vancomycin resistance (VRSA) were discovered in the 1990s and to date 15 cases of VRSA infections are reported in the U.S.[187,198]

Even though VRSA reported cases are rare, MRSA represents a leading cause of bacterial infections today. Therefore, *S. aureus* belongs to the multiresistant ESKAPE organisms (*Enterococcus faecium, Staphylococcus aureus, Klebsiella pneumoniae, Acinetobacter baumanii, Pseudomonas aeruginosa* and *Enterobacter spp.*), which are of particular interest for antibacterial drug discovery.[199,200]

2.1.2. Virulence factors of *Staphylococcus aureus*

For the successful colonization of its host (*e.g.* humans) *S. aureus* expresses its pathogenesis utilizing various virulence factors. These virulence factors can roughly be classified in two sub-categories: secreted and cell-surface-associated virulence factors.[201] In order to colonize host tissue *S. aureus* produces surface proteins, termed adhesins, which have the ability to agglutinate with collagen, fibronectin and fibrinogen present in the bloodstream once bacteria overcome the epithelial barrier.[202,203] Examples for these adhesion proteins are protein A (spa)[204], cell wall-anchored collagen adhesin (CNA)[205], fibrinogen binding proteins clumping factors ClfA and ClfB[206] as well as fibronectin binding proteins FnBPA and FnBPB[207]. The listed proteins solely depict examples among a vast plethora of known virulence factors.[203,207,208]

After entering the blood stream, *S. aureus* is faced by the initial line of defense of the immune system such as neutrophils and human leukocytes. Neutrophils attempt to combat infection, *e.g.* by ingesting pathogenic invaders, utilizing reactive oxygen species and antibacterial peptides. In consequence, *S. aureus* is equipped with several mechanisms to evade the immune system and establish a stable infection.[201,203,209,210] In order to evade the immune system (*e.g.* by killing of neutrophils) and invade the host organism *S. aureus* utilizes a variety of virulence factors which can be grouped in pore-forming toxins, superantigens and other toxins and extracted enzymes.[202,211] An example for these pore-forming toxins are the leukocidins, e.g. Leukotoxin AB (LukAB)[212] which are excreted by *S. aureus* biofilms.[195,213] α-hemolysin and γ-hemolysin depict further prominent representatives of secreted pore-forming exo-toxins responsible for lysis of red blood cells in order to obtain nutrients.[214,215]

Another category of toxins are superantigens. These antigens are capable of extremely upregulating T-cells by binding to MHC class II protein, leading to an uncontrolled and unspecific immune response by the body. The excretion of elevated levels of cytokines can lead to symptoms *e.g.* fever and shock.[201] Prominent examples of theses toxin are staphylococcal enterotoxins (SEs) and staphylococcal enterotoxin-*like* (Se*l*s) proteins as well as the toxic shock syndrome toxin 1 (TSST-1).[216,217]

Examples for excreted proteins with functions other than pore-forming toxins and superantigens are: staphylokinase (*sak*), capable of overcoming antibacterial peptides[218], and hyaluronidase (HysA) [219]

As mentioned above the named virulence factors solely depict examples as *S. aureus* utilizes an arsenal of virulence factors, and the reader is referred to reviews covering toxins[211,220], adhesion factors[207,208] and extacellular enzymes[221] in more detail.

S. aureus is able to control the production of virulence factors according to growth phase, environmental conditions (*e.g.* pH) and host response utilizing several regulatory mechanisms. Amongst others, these mechanisms include alternative sigma factor σ^B, proteins binding to DNA (*e.g.* SarA) four two-component systems (AgrAC, ArlRS, SrrAB and SaeRS).[222-224] In general two-component systems contain a histidine kinase required for extracellular signal sensing, and downstream response regulators.[225]

The most prominent two-component system in *S. aureus* is the so called accessory gene regulator (*agr*), which is also considered as the "global regulator of staphylococcal virulence"[222] as it controls the expression of a great number of virulence factors.[226] The Agr two-component system functions as a quorum sensing system, enabling *S. aureus* to communicate intercellularly and coordinate protein expression in the cell composite during infection.[227,228] The Agr two-component system contains four genes *agrA-D* with all four genes taking over specific functions. Whereas *agrA-C* depict genes for the translation of the histidine kinase and respective response regulators, *agrD* encodes for the autoinducing peptide (AIP).[229] This quorum sensing signal is translated from *agrD* and matured by membrane protease AgrB prior to excretion into the extracellular lumen. Excreted AIP binds to the surface located sensor region of histidine kinase AgrC which in turn phosphorylates response regulator AgrA. Therefore, AgrA interacts with transcriptional regulator SarA, leading to an increased transcription of the transcript RNAII (agr operon) and RNAIII (regulator RNA). Transcription of RNAIII in turn leads to enhanced secretion of virulence factors (*e.g.* hemolysins) and additionally to an impaired expression of cell-surface binding proteins (*e.g.* protein A).[230]

Interestingly, Agr activity has been shown affected by the ClpXP degradation system formed by caseinolytic protease P (ClpP) and its associated chaperone ClpX.[231-234]

2.1.3. The ClpXP complex in *S. aureus*

2.1.3.1. Architecture and function of ClpP proteases

In order to maintain cellular function and proper protein homeostasis, cells are capable of degrading misfolded or aggregated proteins, which lost their functionality due to exceeding their life-span or environmental stress, *e.g.* UV radiation or heat-shock. While in eukaryotic cells the proteasome represents the predominant degradation machinery *Staphylococcus aureus* is equipped with different proteases for protein degradation: Lon, FtsH, ClpYQ[235], ClpXP and ClpCP.[236]

The tetradecameric ClpP complex is composed of two homo heptameric ring structures of ClpP monomers stacked together, forming a barrel-shaped complex, with homologues found in all organisms. In line with other bacterial energy-dependent AAA+ (ATPase associated with diverse cellular activities) proteases, ClpP subunits contains a peptidase domain. The peptidase domain contains a catalytic tirad (Asp-His-Ser) in its active site. The active sites of the fourteen subunits point to the inside of the barrel, forming a catalytic chamber. The access to this catalytic chamber is limited by narrow axial pores, allowing entrance only to small peptides which are digested inside the barrel. Therefore, the ClpP complex alone depicts solely a peptidase function. However, by the interaction with hexameric rings of AAA+ ATPases (*e.g.* ClpC, ClpE and ClpX in *gram*-positive bacteria and ClpA and ClpX in *gram*-negative bacteria) the function of ClpP is extended to full protease function. The hexameric ATPases function as chaperones, unfolding proteinogenic substrates under ATP consumption, thereby enabling the entrance of the unfolded protein into the catalytic chamber.[237-239]

In *S. aureus* ClpP tetradecamers form fully functional proteolytic degradation machineries by associating with ClpC and ClpX, thus forming the two proteolytic complexes ClpCP and ClpXP. Hexameric rings of ClpC or ClpX, respectively, are stacked on top of both heptameric ClpP rings. Of note, published data indicate that the proteolytic activity of ClpCP is more important for *S. aureus* than the activity of ClpXP.[240]

2.1.3.2. The role of the Clp machinery in *S. aureus*

The phenotypic influence of ClpP and ClpX regarding cell physiology, response to environmental stress conditions and virulence has been studied by utilizing *clpP*/*clpX* deletion and point mutants.

In order to evaluate the impact of ClpP and ClpX on cellular growth under oxidative stress respective deletion mutants were incubated with hydrogen peroxide and their growth behavior studied on Agar plates. The impaired growth of both deletion mutant indicate that both – ClpP and ClpX – exhibit different yet substantial roles in oxidative stress response.[234]

In the same publication it was shown that Δ*clpP* and Δ*clpX* mutant strains displayed an altered growth behavior under heat shock or low temperature conditions. Interestingly, *clpP* deletion was tolerated significantly better at low temperatures, whereas *clpX* absence was more tolerated at elevated temperatures.[234]

Moreover, ClpP and ClpX were not only shown to contribute to the adaption to unfavorable environmental conditions, but also were shown in several mouse models to play a significant part in the phenotype of virulence of diverse pathogenic bacteria.[234,241,242]

The phenotypic correlation of *clpP* and its correlation to bacterial pathogenesis in mouse models was further studied on a more molecular level, by investigating the impact of ClpP on the expression of virulence factors.[231,233,234,243] It was shown, that *clpP* and *clpX* deletion mutation led to significantly reduced expression of agr genes.[234,243] These findings led the authors to the conclusion that in turn *agr* is controlled by ClpP via an indirect mechanism, *e.g.* by degrading negative regulators of *agr*.[243]

Putatively as a consequence of altered expression of Agr two-component system, various virulence factors are described as being dysregulated in *clpP* and *clpX* mutant strains, indicating that the Clp machinery impacts virulence in *S. aureus*.

The chemical manipulation of the ClpXP protease in order to suppress the virulence of pathogenic bacteria has been investigated in numerous studies, revealing multiple ClpP modulating chemical tools with promising potencies.[239,244,245]

Additionally to studies focusing on the impact of ClpP and ClpX on virulence factors, transcriptome analysis of *clpP* and *clpX* mutant strains providing a global unbiased view on dysregulated gene expression are reported.[233,240,246] Published results revealed that additional pathways, *e.g.* iron homeostasis and DNA damage repair mechanisms are influenced by ClpP and ClpX. Even though proteomics studies focusing on *S. aureus*

virulence can be found in literature[247], no unbiased evaluation of the influence neither ClpP nor ClpX *via* global proteome analysis has been published yet.

2.1.4. Scope of this work

In this work the impact of ClpP and ClpX on the global intra- and extracellular proteome as well as the metabolome of *S.aureus* was investigated using label-free MS-based whole proteome and secretome analysis and an untargeted metabolomics approach.

In order to uncover ClpP and ClpX dependent dysregulations, *S. aureus* Δ*clpP*, *S. aureus* clpP S98A and *S. aureus* Δ*clpX* mutants were compared to a *S. aureus* NCTC 8325 wildtype control group.

For the investigation of ClpP-dependent proteinogenic dysregulation wildtype cells were compared to a markerless *clpP* deletion mutant constructed by *Christian Fetzer*[122]. The markerless Δ*clpP* mutant, in comparison to other deletion mutants owing an antibiotic resistance as replacement on the gene loci, has the advantage that putative and unknown changes of the proteome and metabolome based on the implemented antibiotic resistance gene are ruled out. In addition to the deletion mutant a clpP S98A point mutant strain, constructed by *Christian Fetzer*[122], was utilized in this work. In line with the knockout mutant, the active site point mutant lacks ClpP peptidase activity, however protein-protein interactions with ClpP could be still facilitated.

In order to decipher ClpX-dependent proteomic changes, a markerless *clpX* deletion mutant was constructed following the same procedure as already accomplished for the generation of the Δ*clpP* mutant.[122]

2.2. Results and discussion

2.2.1. Generation of *S. aureus* ΔclpX mutant strain

2.2.1.1. Construction of pMAD vector for *clpX* deletion

In 2004 *Arnaud et. al.* published the shuttle pMAD, originating from pE194^{ts}::pBR322 for the allelic replacement in gram-positive bacteria.[248] Utilizing this plasmid, the authors were able to successfully construct *Listeria monocytogenes* Δ*clpB* mutant strains. Besides antibiotic resistance genes (*bla* and *ermC*) for antibiotic based selection procedures, pMAD is also equipped with a multiple cloning site, the thermosensitive pE194 replication origin and the gene *bgaB* encoding for a β-galactosidase from *B. stearothermophilus*. Cells carrying the pMAD plasmid are colored in blue when plated on X-Gal (5-bromo-4-chloro-3-indolyl-β-galactopyranoside) containing plates, as the plasmid encoded galactosidase enables the cells to cleave X-Gal leading to the release of a blue indigo dye. Thereby, cells containing the plasmid can be easily identified in a blue/white screen.

In order to eliminate the *clpX* gene from *S. aureus*, the genome section located directly up- and downstream of the target gene were amplified separately via PCR. Therefore, four primers A-D were designed, with comparable melting point temperatures. Primer A and B encoding for the DNA region upstream of *clpX* and primer C and D encoding for the respective downstream section. Primer B and C were located at the beginning or end of the clpX gene segment, overlapping solely in the start or stop codon, respectively. Isolated genomic DNA of S. aureus NCTC 8324 functioned as template for initial PCRs leading to the separate amplification of the upstream (Fragment AB) and downstream (Fragment CD) gene section of *clpX* which were subsequently purified. Primers B and C were additionally equipped with a complementary sequence to the start/stop codon of *clpX*. Thereby, using overlap extension PCR (OE-PCR)[249] the fragments AB and CD were fused resulting in the *clpX* upstream-downstream fusion product (1627 bp) containing the merged start/stop codon of *clpX* and the surrounding DNA section. For the fusion of fragment AB with fragment CD, both fragments were combined in a first PCR and fusion of both fragments conducted in 15 PCR cycles. The resulting upstream/downstream fusion product was amplified in a second PCR step. Successful product formation was confirmed by agarose gel electrophoresis. Primer A and D as well as pMAD vector contain *BamHI* restriction sites. Therefore, the PCR fragment

and pMAD vector were digested with *BamHI* prior to ligation reaction. In order to avoid recirculation of the linearized plasmid it was additionally dephosphorylated prior to ligation. The ligated pMAD *ΔclpX* construct was transformed into chemically competent *E. coli* NEB® 10-beta cells (*New England BioLabs*) for amplification. Successful construction of pMAD *ΔclpX* plasmid was confirmed by analytical restriction digest using BamHI and BsrDI restriction enzymes prior to agarose gel electrophoresis as well as sequencing following colony PCR.

2.2.1.2. *clpX* deletion in *Staphylococcus aureus*

E. coli strains contain DNA-methlytransferase *dam* and *dcm* in their genome, which are utilized to methylate adenosine and cytosine in the DNA for the regulation of gene expression, chromosome replication and various other cellular processes.[250,251] Consequently, NEB® 10-beta *E. coli*, cover the introduced pMAD Δ*clpX* with a strain specific methylation pattern.

In line with other bacterial strains, *S. aureus* is equipped with several restriction modification (R-M) systems, which recognize foreign DNA due to the methylation pattern, thereby refusing the incorporation thereof.[252] In order to circumvent this problem restriction-defective *S. aureus* RN4220 mutant is often utilized as an intermediate host prior to the introduction of the plasmid of interest into a *S. aureus* wildtype strain as *S. aureus* RN4220 is capable of accepting the *E. coli* specific methylation pattern and covering the plasmid with an *S. aureus* methylation pattern during replication.[252-254]

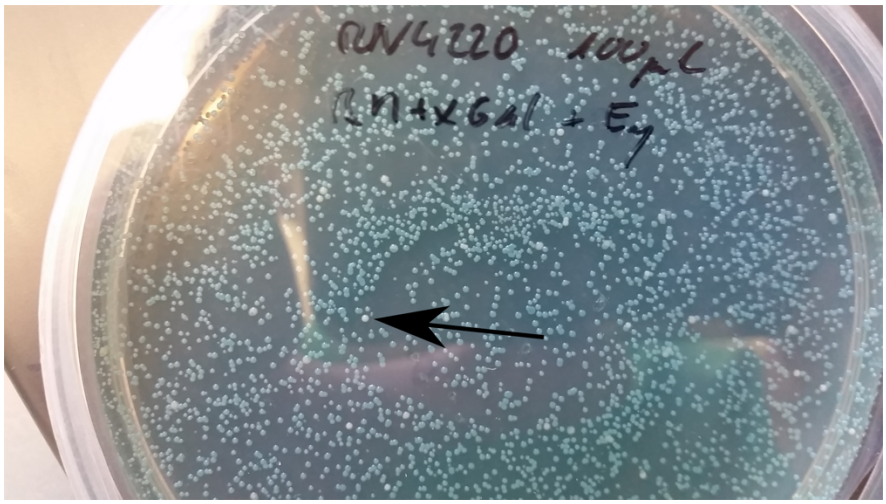

Figure 25: Colonies containing the pMAD plasmid are colored blue as they are capable of cleaving X-Gal included in BM-agar plates due to the β-galactosidase encoded in the plasmid. Missing coloration (arrow) indicate failed incorporation of the plasmid.

Therefore, the plasmid was isolated from NEB® 10-beta *E. coli* cells, purified, incubated with electrocompetent *S. aureus* RN4220 and transformed via electroporation. Subsequently, cells were inoculated with BM medium and plated on agar plates containing erythromycin and X-Gal. Plates were incubated (37 °C) until colony formation was observed. Blue colored colonies, indicating a successful incorporation of the plasmid, were utilized for liquid cultures for subsequent plasmid extraction. Electrocompetent *S. aureus* NCTC 8325 cells were incubated with isolated and purified plasmid and transformed via electroporation. In line with the electroporation of *S. aureus* RN4220 cells, *S. aureus*

NCTC 8325 cells were streaked onto agar plates containing erythromycin and X-Gal and blue colonies subjected to further workflow steps.

Single crossover step via homologous sequences leading to the incorporation of the pMAD plasmid into the genome of *S. aureus* NCTC 8325 are temperature driven. Integration of the plasmid into genomic DNA is favored at 30 °C. Subsequently applied elevated temperatures (42 °C) only allow the replication of plasmid incorporated into genomic DNA, whereas episomal vectors cannot be replicated. A further incubation step at 30 °C leads to an additional recombination occurance resulting in the reformation of the pMAD plasmid. Depending on the site of recombination of two homologous sequences, the second crossover step leads to the generation of the desired mutation and free episomal plasmid inside the cell, or again wildtype. If the cells are now incubated at 42 °C again, the resulting episomal plasmid is lost as only genomic DNA can be amplified. Cells containing episomal pMAD plasmid are colored in blue, whereas cells having incorporated the plasmid-derived DNA into their genome are colored in light blue.[248]

Successful single crossover events, result in a light blue coloring of the respective colonies. Light blue colored colonies were utilized for subsequent workflow. The final double crossover was achieved by the incubation at varying temperatures in another selection step. Successful incorporation of the gene is accompanied by plasmid loss, leading to the formation of white colonies on X-Gal agar plates and the loss of erythromycin resistance.

In order to validate successful generation of *S. aureus* ΔclpX mutant, colony PCR was carried out and the product sequenced.

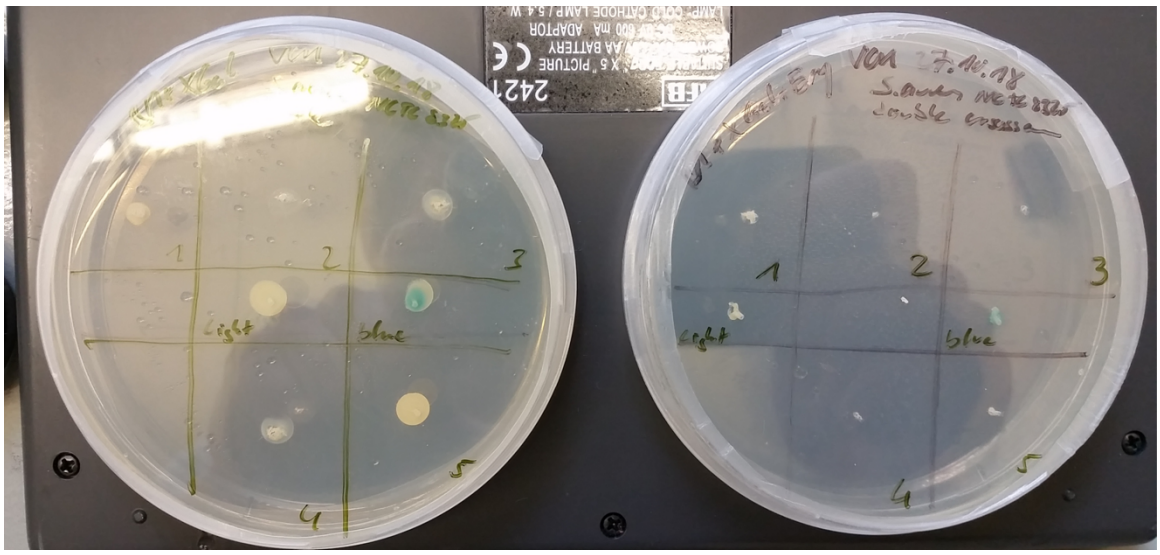

Figure 26: Selection of generated *S. aureus* NCTC 8325 Δ*clpX* mutants. Single colonies were screened simultaneously on agar plates containing X-Gal in without (left) and with (right) erythromycin. Colonies which lost the pMAD plasmid

do not show blue coloration and do not grow on plates containing the antibiotic. This was the case for colonies 2, 3 and 4. Colony 5 showed a slight growth.

2.2.2. Growth behavior of genetic *S. aureus* mutants

As ClpP effects virulence of *S. aureus* on its full potential in the late stationary phase[255], this growth state was chosen for sampling of cells for all following experiments. Growth curves were recorded for all genetic *S. aureus* mutants and the wildtype strain to estimate the required incubation time for all strains to reach similar post-exponential growth phase states.

Overnight cultures of all strains were diluted to an optical density at a wavelength of 600 nm (OD_{600}) of 0.03 and bacterial growth monitored by measuring OD_{600} every 30-60 min and data visualized (Figure 27).

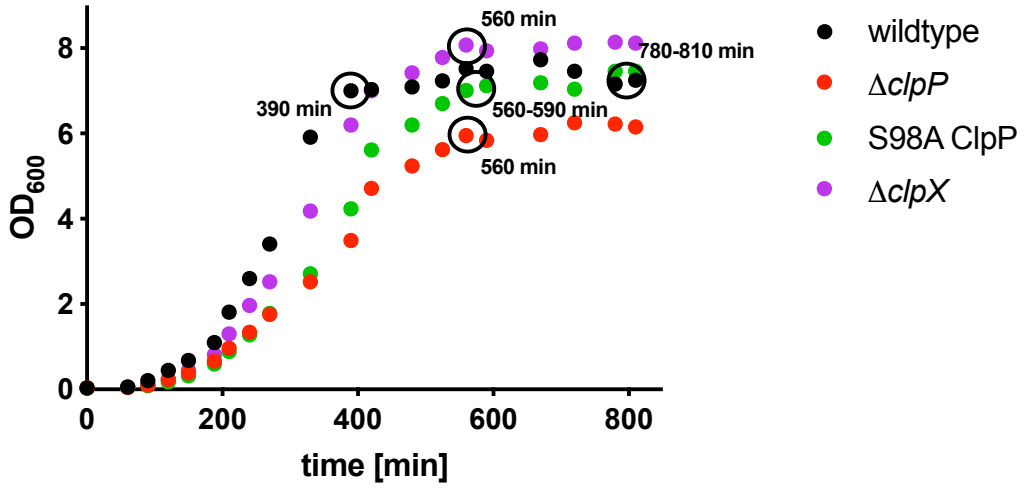

Figure 27: Growth curves of *S. aureus* NCTC8325 and genetic mutant strains. OD_{600} of a day culture was measured every 30-60 min. to monitor bacterial growth. Growth curves of wildtype (black), *ΔclpP* (red), S98A ClpP point mutant (green) and *ΔclpX* (purple) are shown. Transition from exponential growth to stationary phase was determined for all strains and marked (black circles) and incubation time (stated in plot) determined, which is necessary for each strain to reach stationary phase from the starting point of the day culture. Additionally, the end point for the stationary phase for *S. aureus* wildtype is highlighted.

As expected, wildtype cultures reached the transition point from exponential growth to the stationary phase first after 6.5 h (390 min.), followed by both deletion mutants *ΔclpP* and *ΔclpX* (9.3 h = 560 min) and S98A point mutant (9.3-9.8 h, 560-590 min.). Wildtype cells were observed residing in late stationary phase 13.5 h (810 min) after the inoculation of the day culture, indicating that the stationary phase lasts at least 7 h (420 min), and a comparable growth behavior was expected for genetic mutant strains. Therefore, cultures of all strains were sampled 7 h after entering the stationary phase in subsequent experiments, resulting in the following incubation times: 13.5 h for wildtype, 16.5 h for *ΔclpP* and *ΔclpX* mutants and 17 h for S98A ClpP point mutant strain.

2.2.3. Whole proteome analysis

To decipher the influence of genetic manipulations of the ClpXP machinery a label-free whole proteome analysis was carried out and global protein expression levels in the mutants compared among each other and referenced to the *S. aureus* NCTC 8325 wildtype. All *S. aureus* strains were grown in 7 biological replicates distributed over several days and sampled as stated in the previous chapter. Cells were washed several times with PBS to remove extracellular proteins, prior to lysis and tryptic digest of soluble proteins. LC-MS/MS analysis of resulting peptides was followed by raw data preprocessing using MaxQuant[125] and statistical data analysis revealing significantly altered proteins was carried out using Perseus[151].

2.2.3.1. Estimation of global differences in protein expression

For a first approximate assessment of sampling reproducibility among all biological replicates as well as a first estimation of global differences between groups of samples a principal component analysis (PCA) was carried out (Figure 28A). Therefore, data was filtered with the requirement of five out of seven valid values in one sample group for each quantified protein. The great deviation in signal intensity for ClpP and ClpX (due to the respective genetic depletion) alone might be sufficient to provoke group separation in the principal component analysis. However, as it was intended to study if changes upon these mutations affect the proteome globally and lead to group separation, signal intensities for ClpP and ClpX were removed prior to analysis.

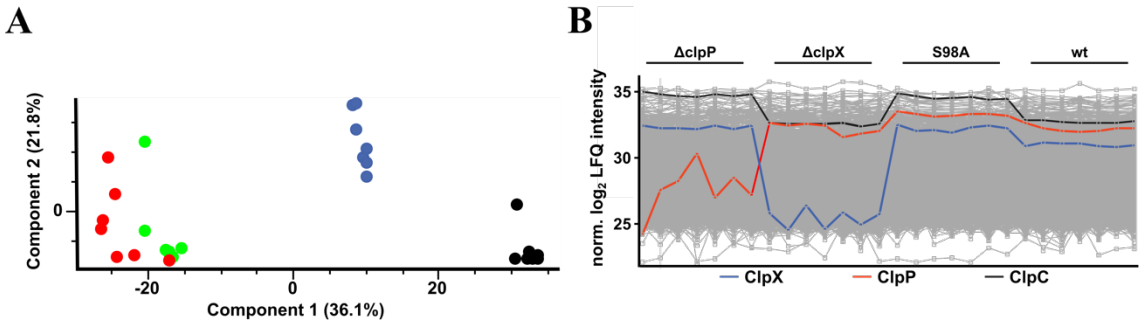

Figure 28: Global assessment of changes in the proteome of *S. aureus* due to conducted genetic modifications. **A)** Principal component analysis (PCA) of genetic *S. aureus* mutants in comparison to the wildtype. Whereas wildtype

(black) and Δ*clpX* (blue) cluster among each other separated from Δ*clpP* (red) and S98A ClpP point mutant (green), the both *clpP* mutants do not exhibit separation from each other, indicating that a majority of proteins display comparable altered expression levels in both mutants in comparison to the wildtype. **B)** Normalized LFQ intensities after missing value imputation for ClpC (black), ClpP (red) and ClpX (blue) across all measured samples.

The analysis revealed a close clustering of the samples within each of the groups, indicating a high reproducibility of the applied workflow. As expected, genetic manipulation of *clpP* and *clpX* led to global changes in the expressed proteome, reflected in a clear separation of the mutant sample groups from the wildtype. Additionally, the deletion of *clpX* seems to globally affect the protein expression less than both tested genetic manipulations of *clpP*. Interestingly, Δ*clpP* mutant samples and S98A point mutant samples cluster undistinguishable together. These observations give rise to the assumption, that class dependent differences between these two groups might be marginal, *e.g.* solely reflected in altered expression of specific proteins or pathways, rather than on a global level.

As already mentioned, ClpP interacts with ClpC and ClpX in *S. aureus* to form the proteolytic complexes ClpCP and ClpXP, respectively. For a first rough investigation of the influence of genetic manipulations of *clpP* and *clpX* on the expression levels of ClpC, ClpP and ClpX, the LFQ intensities of all three proteins were plotted after missing value imputation (Figure 28B) across all measured samples.

Indicated in Figure 28B, knockout of *clpX* led to an expected, nearly entire, depletion of ClpX in the respective samples after quantification using MaxQuant. However, in case of the Δ*clpP* mutant samples a quite distinct residual intensity of ClpP could be detected. To confirm the purity of the bacterial stocks, an overnight culture was streaked on agar plates and ten colonies separately subjected to colony PCR to amplify the respective gene section. As control a colony PCR using *S. aureus* NCTC 8325 wildtype was carried out. In comparison to control samples, the amplified gene section was significantly shorter indicating missing *clpP* gene in that section (see Appendix). Additionally, the amplified gene section was subjected to sequencing. As these experiments independently confirmed that the strain was not contaminated by ClpP containing parent strain, it remains unclear why residual ClpP intensity was detected in these samples. MaxQuant peptide tables revealed unique peptides of ClpP detected in the Δ*clpP* samples. Carry over of the liquid chromatography column from an adjacent sample might be a reason for these findings. However, absent ClpX peptides in Δ*clpX* samples speak against the theory of carry over during LC-MS/MS analysis. In conclusion, a reason for the detected ClpP peptides could not be elucidated, but authenticity of the respective clpP deletion strain could be confirmed via independent experiments.

Strikingly, genetic manipulations of *clpP* provoked a slight but reproducible overexpression of ClpX in comparison to the wildtype (blue line, Figure 27B, enrichment $\log_2 = 1.73$ for Δ*clpP* and 1.63 for S98A) in comparison to wildtype samples, evaluated by two-sample student's *t*-test. As a response to the functionally impaired ClpXP machinery in *clpP* mutant strains, the cells likely initiate an increased expression of ClpX for compensation of the impaired proteolytic complex. Following this argumentation, translation of ClpP in S98A mutants should also be elevated in order to compensate for the present, but impaired peptidase. Indeed, slight upregulation of ClpP ($\log_2$ enrichment = 1.41 in comparison to the wildtype) has been detected. Interestingly, ClpP levels in Δ*clpX* samples are comparable to wildtype samples. These findings might indicate that the cells, even though lacking ClpX, still can accomplish a majority of the tasks of ClpP, eventually by the ClpCP complex. This conclusion would be in line with reported findings, that a majority of proteins are degraded by ClpCP rather than by ClpXP.[234,240,256,257]

This might also explain the dysregulation of ClpC in the studied genetic mutants. In *clpP* genetic mutants, ClpC is significantly upregulated (black line, Figure 28B, enrichment $\log_2 = 2.64$ for Δ*clpP* and 2.38 for S98A) in comparison to the wildtype. In contrast, ClpC levels in Δ*clpX* samples remain unaffected by the genetic manipulation. The ClpCP complex is of importance in *S. aureus* for degrading proteins aggregated under environmental stress.[240]

As ClpP expression is altered or its function impaired (in case of S98A point mutant) respectively, an increased expression of ClpC might depict the cellular response to overcome the lack of intact ClpCP. The increased levels of ClpC, might also stem from its functional properties as chaperone, utilized to regain the function of aggregated or misfolded proteins as they cannot be degraded due to the absence of functional ClpP proteolytic complexes. However, the stated reasons for the increased levels of ClpC in *clpP* deficient strains might not explain the phenotype entirely. Additionally to its function as chaperone, ClpC is known to influence several metabolic pathways in *S. aureus* independently from its interaction with ClpP*, e.g.* pyruvate and phosphate metabolism.[258] Therefore, lack of functional ClpP might also have a so far unknown influence in metabolic pathways the cell attempts to balance by increasing levels of ClpC.

2.2.3.2. Influence of *clpP* deletion on global protein expression

Statistical analysis of protein expression levels in *clpP* knockout strains in comparison to wildtype expression levels were evaluated using a two-sample student's *t*-test. Cut off criteria for significant dysregulated proteins were defined as follows: $\log_2 = 1$ or -1 (2-fold enrichment or depletion) respectively and $-\log_{10}$ *t*-test *p*-value = 1.3 (Figure 29A). Numerous proteins exhibited altered expression levels, with 240 significantly down- and 273 significantly upregulated proteins. In order to classify the dysregulated proteins and identify altered pathways, significant proteins were subjected to network analysis using the STRING v11 database[166] (Figure 29B and C). Network analysis revealed several interaction patterns among downregulated proteins: virulence associated proteins, proteins involved in amino acid metabolism, purine metabolism, UMP *de novo* biosynthesis and succinate dehydrogenase complex (Figure 29B).

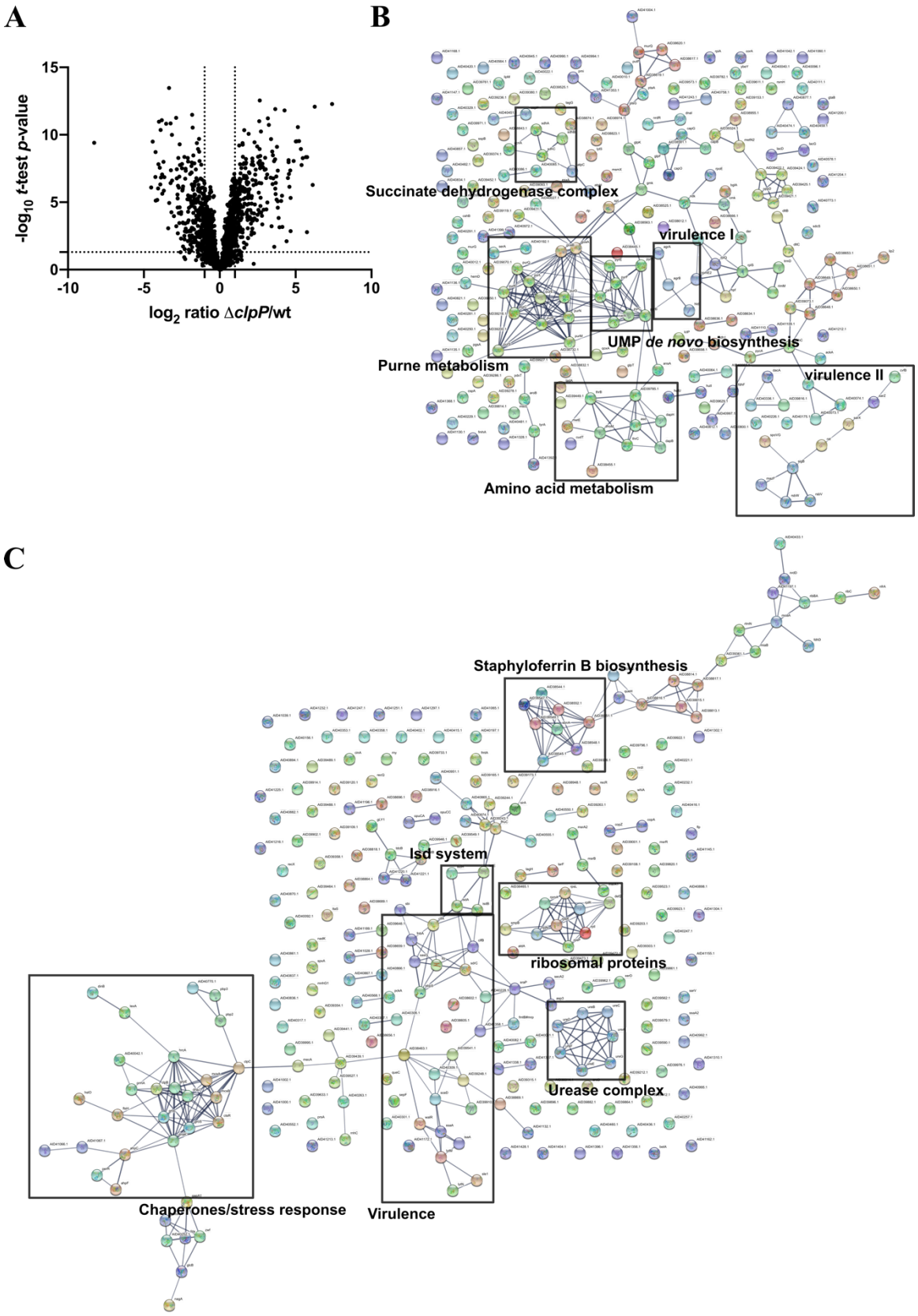

Figure 29: Whole proteome analysis of *S. aureus ΔclpP* compared to *S. aureus* wildtype. A) Volcano plot represents two-sample t-test results of *S. aureus ΔclpP* compared to *S. aureus* wildtype control (n=7). Cutoff criteria were defined as $\log_2 = \pm 1$ (2-fold change in protein expression) and $-\log_{10}$ (*t*-test *p*-value) = 1.3 (dotted lines). **B)** Proteins with significantly reduced expression levels were subjected to network analysis using STRING v11 database[166] applying "confidence" as meaning of network edges and a minimum required interaction score of 0.7 (high confidence). **C)** Proteins with significantly elevated expression levels were also subjected to network analysis using STRING v11 database[166] with same parameters as for downregulated proteins. Assignments of clusters was cluster was performed using GO annotations, KEGG assignments and literature known interactions between proteins.

2.2.3.2.1. Down regulated pathways in *ΔclpP* mutant strain in comparison to the wildtype

Virulence associated proteins

Various studies investigated the relation between ClpP and the two component system Agr, revealing decreased activity and transcription of this global transcription regulator and in particular decreased expression levels of AgrA in *clpP* mutant strains.[233,234,243] In line with these reports two proteins of the *agrBDCA* operon, namely AgrA and AgrB could be identified as downregulated in comparison to wildtype samples. As AgrA in its phosphorylated state initiates the transcription of RNAII (containing the *agrBDCA* operon) and RNAIII (containing *hld*) simultaneously[259], the observed downregulation of δ-hemolysin could be explained thereby. Additionally, Conserved virulence factor B (*clfB*), involved in *agr*-dependent pathogenesis[260] was downregulated. The downregulation of these two proteins further reflects the extended influence of *clpP* knockout onto Agr controlled downstream virulence factors.

Transcription of the global transcription regulator *mgrA* is regulated by RNAIII.[261] As RNAIII gene expression is downregulated, also MgrA is found to be downregulated in *clpP* knockout strains, in line with previous reports.[257] MgrA is involved in virulence, as it negatively controls Glycyl-glycine endopeptidase LytM and probable cell wall hydrolase LytN as well as HTH-type transcriptional regulator SarV.[262,263] Interestingly, these proteins were found upregulated in Δ*clpP* in comparison to the wildtype strain in the whole proteome analysis here, and increased levels might stem from missing regulation by MgrA.

In order to identify other known global transcription regulators besides the *agr* operon[264] and MgrA, the data set was screened for dysregulated proteins belonging to the regulators expressed by the operons *arlRS*, *saePQRS*, *srrAB*, *vraSR*, *graSR*, *hssRS* and the *sarA* family.

Even though proteins belonging to the respective global transcription regulators have been found, only the *sarA* family revealed members to be influenced by *clpP* depletion. SarX and SarZ have been observed down regulated whereas SarV was upregulated as already mentioned. Additionally RNA polymerase sigma factor (*sigB*), involved in virulence factor control, as well as proteins of the contranscripted $mazEF_{SA}$ TA module[265] (RsBV, RsBW and MazF) exhibited decreased expression levels.

In summary, *clpP* deletion led to the downregulation of major transcription regulators involved in virulence, namely proteins of the *agr* operon, of the *sarA* family and

RNA polymerase sigma factor. Furthermore, several downstream proteins of the Agr system and RNA polymerase sigma factor have been observed downregulated, indicating a comprehensive impact on these pathways.

However, *clpP* deletion did not affect virulence associated protein exclusively but also altered major metabolic pathways.

Purine and UMP *de novo* biosynthesis

Strikingly, *clpP* deletion led to a significant decreased expression of a high number of proteins involved in the purine and pyrimidine (especially UMP biosynthesis) metabolism.

In *S. aureus* proteins responsible for purine biosynthesis are encoded by the *purEKCSQLFMNHD* purine biosynthetic operon. Transcription of the entire operon is mediated by *purR*.[266] The purine biosynthetic pathway yields IMP, which can be further converted into AMP or by an alternative route over XMP to GMP, which can either be converted into GTP as energy source or to as building block for RNA synthesis. The conversion to GMP is mediated by two proteins IMP dehydrogenase (*guaB*) and GMP synthetase (*guaA*).[267,268] Interestingly, all enzymes translated from the purine biosynthetic operon except Bifunctional purine biosynthesis protein PurH (*purH*) are downregulated. Solely bifunctional purine biosynthesis protein PurH (*purH*), present in the data set, was not affected. PurH should be downregulated as well, if the entire operon is affected by a regulatory mechanism. The reasons for this remarkable finding remain elusive. The regulator of the entire operon, Pur operon repressor PurR (*purR)*, was not detected. Additionally, proteins encoded by the *gua* operon leading to biosynthesis of GMP were observed as downregulated as well.

The downregulation of proteins of two downstream operons is quite remarkable. Experiments in *Streptococcus mutans* revealed that ClpP indirectly modulates the purine biosynthesis pathway by regulating dihydrofolate reductase (*folA*), which is required for the *de novo* synthesis of purines.[269] Therefore, the dataset was searched for *folA* but the encoded protein was not present. Even though not identified in the dataset, the link between ClpP and purine biosynthesis *via folA* could also be valid for *S. aureus* and explain the dysregulation of the purine biosynthesis pathway and downstream GMP synthesis.

Suppression of purine metabolism has been observed in literature, and the authors suspected a correlation thereof with reduced growth rate of *clpP* deletion strains.[257]

The UMP *de novo* biosynthesis leads to the formation of UMP, which depicts a major building block for the synthesis of other pyrimidine derivatives. The gene cluster

encoding for enzymes involved in pyrimidine biosynthesis is called *pyr* operon and its transcription is negatively controlled by bifunctional protein PyrR (*pyrR*). Besides the *carAB* operon encoding for Carbamoyl-phosphate synthase small chain (*carA*) and Carbamoyl-phosphate synthetase large chain (*carB*), which initiate the synthesis of pyrimidines originating from glutamine, the genes *pyrB, pyrC, pyrE* and *pyrF* belong to this operon. The encoded proteins convert carbamoyl-phosphate to UMP.[270] In Δ*clpP* knockout strains, expression levels of proteins including PyrR, encoded by the entire operon were found to be downregulated. This is interesting, as previously an inactivation of PyrR was shown to upregulate *carA* and *carB* transcription.[270] MgrA was shown to govern the expression of genes encoding for enzymes involved in purine and pyrimidine biosynthesis.[271] However, as the direction of regulation of the individual protein expression in the whole proteome analysis conducted here is partly contrary to the transcriptome analysis of *mgrA* deletion mutants, it can be concluded, that purine/pyrimidine pathways are not exclusively influenced by a ClpP-mediated mechanism affecting MgrA.

The mechanisms leading to a Clp machinery dependent dysregulation of these pathways is so far unknown. However, it has been shown, that purR activity is decreased upon heat stress.[266] As ClpP absence is known to induce stress, the purine/pyrimidine pathway upregulation could depict a stress induced response to the genetic deletion.

Besides nucleotide biosynthesis pathways other metabolic pathways have been affected by *clpP* deletion, *e.g.* enzymes of the amino acid metabolism (list of proteins and respective fold changes see Appendix) and the succinate dehydrogenase complex. The operon *sdhCAB* encodes for the succinate dehydrogenase complex (Succinate dehydrogenase, flavoprotein subunit SdhA, Succinate dehydrogenase, iron-sulfur protein SdhB and Succinate dehydrogenase cytochrome b-558 SdhC) and depicts an essential metabolic pathway in the tricarboxylic acid (TCA) cycle. Additionally, this protein complex could be identified having an important role in persister cell formation.[272]

In mitochondria an interaction between ClpXP and the succinate dehydrogenase complex has been shown[273], however for bacteria a link is missing.

2.3.2.2.2. Upregulated pathways in *ΔclpP* mutant strain in comparison to the wildtype

Virulence and cell wall biosynthesis associated proteins

Several virulence-associated proteins being responsible to establish host-pathogen interactions, *e.g.* by binding to fibrinogen, fibronectin, elastin and immunoglobulin (list of proteins see Appendix) have been identified as upregulated. Strikingly, additional to these proteins proteins controlled by the WalKR system have been observed with elevated expression levels.

The essential WalKR two-component system mediates, amongst other tasks, peptidoglycan synthesis in *S. aureus* and other mechanisms in cell division. WalK depicts a transmembrane sensor histidine kinase, while WalR functions as a downstream response regulator.[274,275]

The WalKR system is known to control LytM expression, an endopeptidase which might be responsible for the release of protein A from the staphylococcal surface. The peptidoglycan composition of protein A is mediated by cross-wall murein hydrolases LytN, N-acetylmuamoyl-L-alanine amidase Sle1 and bifunctional autolysin Atl.[276] Furthermore, the WalKR system was shown to control transcription of Staphylococcal secretory antigen SsaA (*ssaA*) and Probable transglycosylase SceD (*sceD*).[277]

Interestingly, WalR and downstream controlled enzymes LytN, LytM, SceD as well as Sle1 were oberved upregulated, implicating an influence of ClpP on the entire pathway. Besides WalKR controlled proteins associated with virulence, also other protein with distinct function in virulence have been identified as upregulated.

Influence of ClpP on iron acquisition of *S. aureus*

Iron plays an important role in diverse biological pathways in bacteria, *e.g.* cell growth. In the human body iron is concentrated within cell, thus evading from access of *S. aureus*. The only access facilities for *S. aureus* to acquire iron in the human body is to capture iron from extracellular host-derived transporting proteins, *e.g.* hemoglobin, transferrin and lactoferrin. To this end the pathogen has developed several mechanisms, *e.g.* the iron-responsive determinant system (Isd system) and siderophores.[278]

IsD system

In order to ensure proper iron supply during infection of hosts, *S. aureus* utilizes amongst others the iron-responsive surface determinant (Isd) system.[279] The regulation of hemoglobin binding derived from hosts by the IsD system has been linked to the ClpP proteolytic machinery. Via Western Blot analysis a decreased expression of IsdB could be confirmed in Δ*clpP* mutants.[280] In contrast, the whole proteome analysis carried out here revealed an increase of protein expression for IsdA, IsdB, IsdE and IsdH. So far, reasons for these contrary results and the systematic increased expression levels of a majority of the Isd family proteins remains unclear.

Biosynthesis of staphyloferrin B

The siderophore staphyloferrin B and its analogue staphyloferrin A are excreted into the extracellular lumen to heist iron from host iron transporter proteins, *e.g.* transferrin and lactoferrin, due to their high affinity towards iron. Thereby, the siderophores depict an additional mechanism in iron homeostasis besides the already mentioned Isd system.[278] Strikingly, seven (SbnA, SbnB, SbnC, SbnE, SbnF, SbnG and SbnH) out of nine proteins of the staphyloferrin B biosynthesis have been observed strongly upregulated (log_2 ratio of 3 to 6, exact number see table in Appendix) in Δ*clpP* strain in comparison to the wildtype. However annotation for all of these proteins except SbnA are putative.Taken together, two mechanisms for iron acquisition of *S. aureus* are upregulated in the *clpP* deletion mutant, rising the assumption that the cells lacking ClpP are in higher need for iron.

Upregulation of the staphyloferrin B biosynthesis pathway in ClpP mutants is not new, as respective increased gene expression has been reported upregulated in *clpP* mutant strains in comparison to a I265E ClpX mutant before.[240] The same study reported an increase in gene expression of staphyloferrin A transport and synthesis and the Ferric Uptake Regulator Fur, which controls transcription of siderophores. The authors postulated, that *clpP* deletion interferes with Fur activity, thus leading to an enhanced expression of the respective genes. However, in the data set presented here, Fur was present but not regulated, indicating that another mechanism might be responsible for the monitored upregulation of iron acquiring proteins.

S. aureus utilizes iron containing proteins in its oxidative stress sensing, and subsequent response.[281] Despite heat stress also oxidative stress leads to the aggregation of proteins. Mostly derived from metabolic conversions, *e.g.* NADH production, hydrogen peroxide can react in a Fenton reaction with Fe(II) leading to hydroxide radicals, one of

the most commonly occurring reactive oxygen species (ROS), cells are exposed to.[282] To face these severe threats, cells are equipped with several mechanisms to defuse generated ROS. These ROS lead to oxidation of amino acid residues, *e.g.* cysteines in proteins thereby inducing aggreagation of proteins. As cells lacking ClpCP showed a higher sensitivity for oxidative stress, and iron metabolic pathways have been observed upregulated in these mutants, it was postulated, that staphylococcal cells increase the biosynthesis of siderophores in order to trap Fe(II) ions and reduce ROS to prevent damaged proteins from ultimate aggregation.[240]

Putatively, ClpP deletion and thereby the absence of the most important proteolytic degradation machinery leads to stress signaling, *S. aureus* compensates with oxidative stress response.

Chaperones

Another hint, *S. aureus* is forced to adapt to increased stress condition upon *clpP* deletion is an observed upregulation of chaperones and other proteins involved in stress response. In line with previous reports[257], the proteins encoded by the *clpC* operon (*ctsR-mcsA-mcsB-clpC*), as well as the chaperones ClpB, DnaK, GroEL and GroES have been observed upregulated. As misfolded proteins cannot be degraded due to the absence of ClpP, these chaperones might be upregulated in response to stabilize labile proteins.

Influence of ClpP on the Urease complex

Urease, degrading urea into NH_3 and CO_2, is transcriptionally controlled by Agr and is required in virulence in *S. aureus*.[283] The enzyme is encoded by the *ureABCDERGD* operon, and additionally Agr has been shown to be regulated by MgrA. The upregulation of Urease in *clpP* knockout strains has been reported earlier, and it was hypothesized that the upregulation of urease expression stems from downregulation of MgrA.[284] These findings are in accordance to the data presented here, as MgrA was also found to be downregulated, whereas proteins encoded by *ureA-G* were observed as upregulated.

2.2.3.3. Whole proteome comparison of *ΔclpP* deletion mutant and S98A ClpP point mutant

As mentioned above (Chapter 2.3.1.), PCA analysis revealed no global difference in the phenotype of Δ*clpP* and S98A ClpP point mutant strains. The comparable phenotype is also reflected by a high number of shared up- and downregulated proteins in comparison to the wildtype control (Figure 30A).

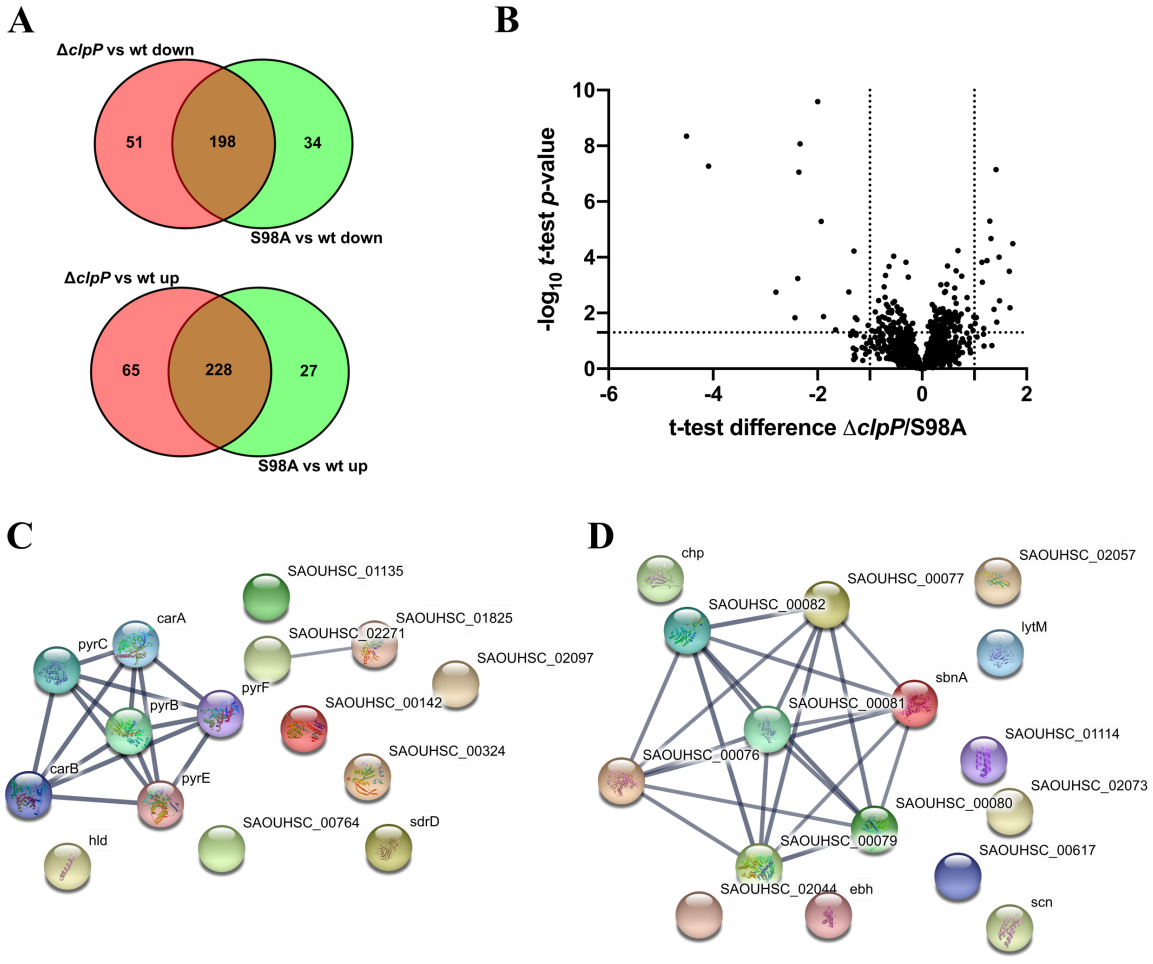

Figure 30: Whole proteome analysis of *S. aureus ΔclpP* compared to *S. aureus* S98A ClpP point mutant. A) Quantity of equally altered proteins in both genetic *clpP* mutants in comparison to the wildtype, respectively illustrated in separate Venn diagrams for up- and downregulated proteins. **B)** Volcano plot represents two-sample t-test results of *S. aureus* ΔclpP compared to *S. aureus* S98A ClpP point mutant (n=7). Cutoff criteria were defined as $\log_2 = \pm 1$ (2-fold change in protein expression) and $-\log_{10}$ (*t*-test *p*-value) = 1.3 (dotted lines). **C)** Proteins with significantly reduced expression levels were subjected to network analysis using STRING v11 using "confidence" as meaning of network edges and a minimum required interaction score of 0.7 (high confidence). **D)** Proteins with significantly elevated expression levels were also subjected to network analysis using STRING v11[166] with same parameters as for downregulated proteins.

The direct comparison of protein expression levels in Δ*clpP* knockout and S98A ClpP point mutants is of particular interest, as the analysis potentially reveals proteins which depend on the sole presence of ClpP for interactions rather than its functionality. The comparison

of protein expression levels between both mutants has been carried out previously[285] but has been repeated here using label-free quantification and a slightly modified workflow.

The conducted comparison of protein expression levels in ClpP and ClpX mutants relatively to the wildtpe include one major drawback: The distinction between accumulated protein substrates of the ClpP machinery and proteins upregulated due to secondary effects of absent ClpP degradation activity is very challenging.

This hindrance in data analysis is ruled out in the comparison of both ClpP mutant strains. To identify proteins, which depend on the physical interplay with ClpP regardless of its proper function, expression levels of proteins in Δ*clpP* deletion and S98A ClpP point mutants were compared and statistically evaluated (Figure 30B). 1660 proteins met the filtering criteria and – as visible in the volcano plot – solely a few proteins showed significant dysregulation. 17 proteins revealed a significantly decreased expression levels in the knockout mutant in comparison to the S98A ClpP point mutant, whereas 16 proteins were significantly upregulated.

2.2.3.3.1. Downregulated proteins in *ΔclpP* mutant in comparison to S98A ClpP point mutant

Depletion of ClpP led to a decrease of expression levels of δ-hemolysin (*hld*) and Serine aspartate repeat containing protein D SdrD (*sdrD*). Particularly striking is the downregulation of the entire UMP *de novo* biosynthesis cluster, as revealed by STRING analysis. UMP *de novo* biosynthesis proteins have also been observed downregulated in S98A ClpP point mutant samples in comparison to the wildtype, however to a lower extent than in the Δ*clpP* mutant. Reasons for the decreased protein levels of this entire pathway and their apparent dependency on the physical presence of ClpP are so far unknown.

Table 6: Significantly downregulated proteins (log_2 ratio ≤ -1.0, $-log_{10}$ t-test p-value > 1.3) in Δ*clpP* deletion mutant in comparison to S98A ClpP point mutant.

Gene name	Uniprot ID	log_2 ratio *ΔclpP*/S98A	$-log_{10}$ *t*-test *p*-value
Pyrimidine metabolism			
carA	Q2FZ73	-2.38	3.23
carB	Q2FZ72	-2.00	9.59

pyrB	Q2FZ75	-2.36	7.05
pyrC	Q2FZ74	-2.34	8.07
pyrE	Q2FZ70	-1.88	1.87
pyrF	Q2FZ71	-1.92	5.28
Virulence associated proteins			
hld	Q2FWM8	-1.40	2.76
sdrD	Q2G0L4	-4.51	8.34
psmA1	P0C7Y1	-2.43	1.83
Unknown function			
SAOUHSC_00142	Q2G1I1	-4.09	7.27
SAOUHSC_00324	Q2G132	-1.65	1.40
SAOUHSC_00764	Q2G058	-1.28	1.83
SAOUHSC_01135	Q2FZA4	-2.80	2.75
SAOUHSC_01825	Q2FXL0	-1.03	1.55
SAOUHSC_02097	Q2FX10	-1.25	1.76
SAOUHSC_02271	Q2FWL8	-1.33	1.35

2.2.3.3.2. Upregulated proteins in *ΔclpP* mutant in comparison to S98A ClpP point mutant

Due to their GO molecular function, the upregulated enzymes can be categorized in enzymes involved in virulence associated proteins, proteins involved in staphyloferrin B biosynthesis and proteins with no confirmed function.

Table 7: Significantly upregulated proteins (log_2 ratio ≥ 1.0, $-log_{10}$ t-test p-value > 1.3) in Δ*clpP* deletion mutant in comparison to S98A ClpP point mutant.

Gene name	Uniprot ID	log_2 ratio Δ*clpP*/S98A	$-log_{10}$ *t*-test *p*-value
Virulence associated proteins			
chp	Q2FWV5	1.43	1.67
ebh	Q2FYJ6	1.73	4.49
lytM	O33599	1.67	3.50
scn	Q2FWV6	1.18	1.44
SAOHSC_01114	Q2FZB8	1.47	4.00
Staphyloferrin B biosynthesis			
sbnA	Q2G1N3	1.29	5.29
SAOUHSC_00076 (putative: sbnB)	Q2G1N2	1.14	3.82
SAOUHSC_00077 (putative: sbnC)	Q2G1N1	1.24	3.88
SAOUHSC_00079 (putative: sbnE)	Q2G1M9	1.32	4.67
SAOUHSC_00080 (putative: sbnF)	Q2G1M8	1.42	7.15

SAOUHSC_00082 (putative: sbnH)	Q2G1M6	1.68	2.19
Unknown function			
SAOUHSC_00081	Q2G1M7	1.38	2.13
SAOUHSC_02073	Q2FX32	1.15	3.11
SAOUHSC_02044	Q2FX55	1.48	2.44
SAOUHSC_02057	Q2FX43	1.04	1.84
SAOUHSC_00617	Q2G0F2	1.02	1.62

The upregulated virulence associated proteins can be subdivided into two groups. The first group depicts proteins involved in adhesion, namely Fibrinogen-binding protein (*SAOUHSC_01114*)[286] and Extracellular matrix-binding protein ebh (*ebh*). As LytM is involved in protein A release it is also assigned to this category. Members of the second group are Chemotaxis inhibitory protein (*chp*) and Staphylococcal complement inhibitor (*scn*). Both proteins are utilized by *S. aureus* to overcome the first line of immune defense.[287]

Strikingly, six out of nine proteins of the staphyloferrin B biosynthesis have been examined as upregulated in Δ*clpP* strain in comparison to S98A ClpP point mutant. As mentioned above, the siderophore Staphyloferrin B and its analogue Staphyloferrin A are excreted into the extracellular lumen to heist iron from host iron transporter proteins, *e.g.* transferrin and lactoferrin, due to their high affinity towards iron.[278]

Based on the upregulation of this pathway, the Δ*clpP* mutant seems to display a higher iron deficiency compared to the S98A point mutant. As already mentioned, upregulation of staphyloferrin B biosynthetic protein as already been observed in *clpP* mutants in comparison to I265E ClpX point mutants.[240] However, these findings have so far have not been reported in a comparison of expression levels between *clpP* knockout and ClpP point mutants.

Conclusion

Based on the comparable protein expression profiles of Δ*clpP* and S98A ClpP mutant strains, it can be concluded that most proteins display altered expression levels compared to wt due to the lack of proteolytic activity exhibited by ClpP. However, the comparison of expression profiles of both ClpP mutant strains revealed purine/pyrimidine as well as staphyloferrin B biosynthesis pathways as significantly altered depending on the presence/ absence of ClpP regardless of its proteolytic activity.

2.2.3.4. Influence of *clpX* deletion on the whole proteome of *S. aureus*

In line with the comparison of protein expression levels in Δ*clpP* mutant and wildtype *S. aureus* strain, the influence of ClpX on the global proteome was evaluated by a comparison of protein levels in Δ*clpX* strain versus wildtype.
Similar to the deletion of *clpP*, a deletion of *clpX* exhibited a significant influence on the protein expression patterns, causing a dysregulation of a distinct number of proteins (Figure 31A). Out of 1665 proteins which passed filtering criteria, 190 proteins showed significant up and 227 proteins significant down regulation.

2.2.3.4.1. Down regulated pathways in *ΔclpX* mutant strain in comparison to the wildtype

In line with deletion of *clpP*, a deletion of *clpX* led to decreased expression levels of amino acid metabolism, succinate dehydrogenase complex proteins and pyrimidine metabolism (Figure 31B). As downregulated in both deletion strains, it can be concluded that these pathways are generally controlled by the ClpXP proteolytic machinery. However, as more proteins of the pyrimidine and purine metabolism are significantly decreased in *clpP* deletion strain, ClpP seems to affect the pathway more significantly than ClpX. A reason therefore might depict retained ClpCP activity in the *clpX* mutant.

As outlined above, *Stahlhut et al.*[240] identified ClpXP substrates in a transcriptome analysis by comparing gene expression levels of a constructed I265E ClpX point mutant, impaired in proteolytic function, to a wildtype control. In line with the mentioned transcriptome analysis results, cross-membrane ABC transporters are among the significantly downregulated proteins in the whole proteome analysis. Strikingly, an ABC transporter was reported to exhibit the most reduced gene expression upon impaired ClpX function in the mentioned paper, and in line therewith an ABC transporter domain-containing protein (*SAOUHSC_02820*, $\log_2$ ratio Δ*clpX*/wt = -7.13) represents the protein with the highest fold change of protein levels.

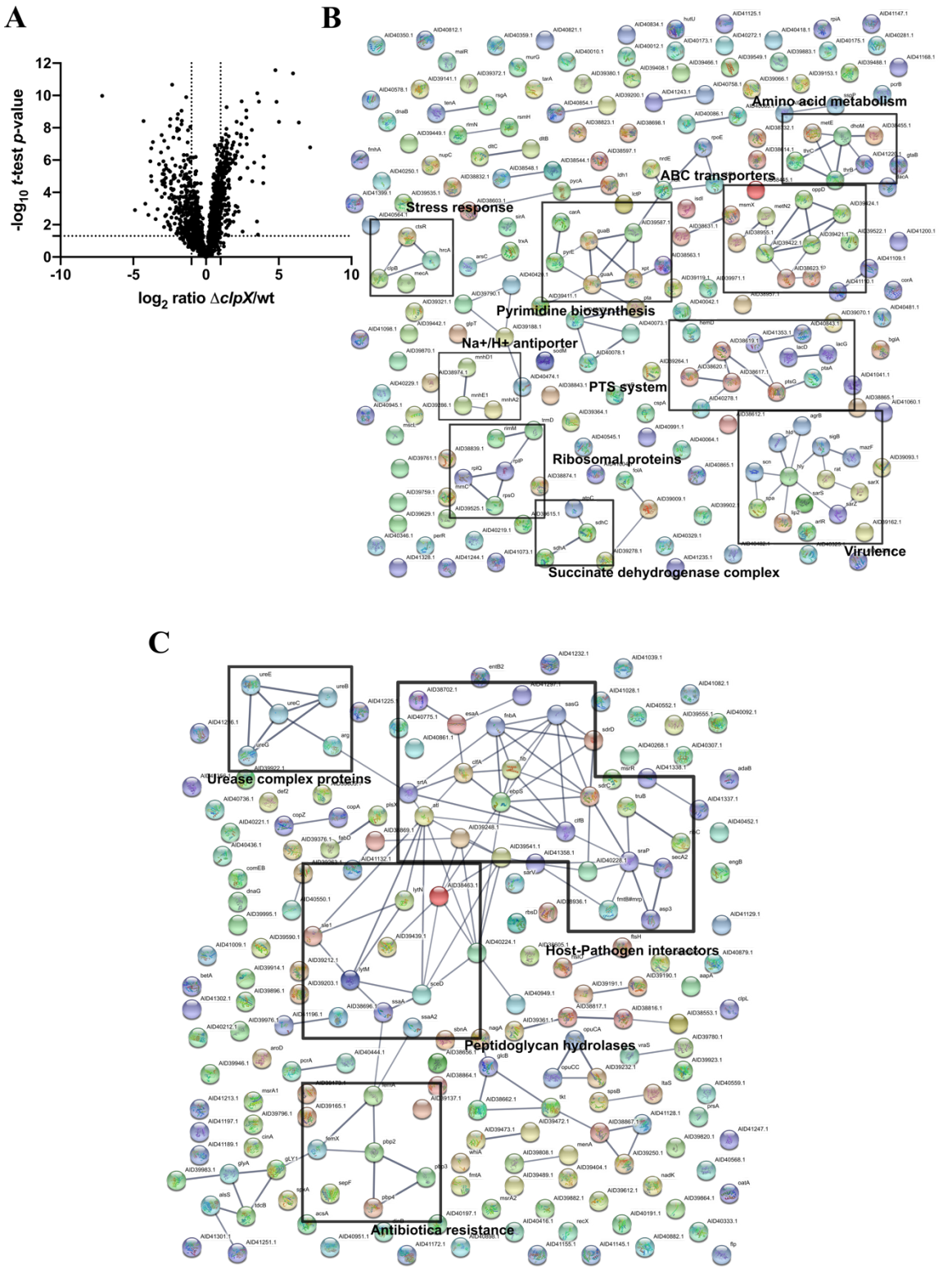

Figure 31: Whole proteome analysis of *S. aureus ΔclpX* compared to *S. aureus* wildtype. A) Volcano plot represents two-sample t-test results of *S. aureus ΔclpX* compared to *S. aureus* wildtype control (n=7). Cutoff criteria were defined as $\log_2 = \pm 1$ (2-fold change in protein expression) and $-\log_{10}$ (*t*-test *p*-value) = 1.3 (dotted lines). **B)** Proteins with significantly reduced expression levels were subjected to network analysis using STRING v11 using "confidence" as meaning of network edges and a minimum required interaction score of 0.7 (high confidence). **C)** Proteins with significantly elevated expression levels were also subjected to network analysis using STRING v11 with same parameters as for downregulated proteins. Assignments of clusters was cluster was performed using GO annotations, KEGG assignments and literature known interactions between proteins.

Various other ABC transporters have been found downregulated. As this group of proteins has not been dysregulated in *clpP* deletion mutant, the expression of ABC transporters is mediated by ClpX *via* a ClpP-independent mechanism. In addition to the ABC transmembrane transporters, another kind of transmembrane transporters, proteins of the MnH Na+/H+ antiporters complex (*mnhA2, mnhD1, mnhE1*), have been observed as downregulated.

Phosphotransferase system (PTS)

The phosphoenolpyruvate: sugar phosphotransferase system (PTS) is employed by bacteria for the supply with carbohydrates and the subsequent phosphorylation of the sugars after their intake by the cells.[288] One member of the PTS system, Phosphotransferase system glucose -specific II ABC component PtsG has been identified as upregulated in experiments comparing the gene expression levels in Δ*clpX* mutants relatively to I265E ClpX point mutant.[232] The reason therefore is yet unknown.

Virulence

As already mentioned in chapter 2.1. and stated in literature, ClpX has a substantial role in the regulation of transcription of numerous virulence factors.[231,234,240] These virulence associated proteins are controlled by transcription regulators listed above. Interestingly, numerous transcription regulators with distinct function in virulence are found downregulated, *e.g.* sigB, MgrA, AgrB (AgrA not present in the data set) as well as ArlR. In case or the two-component ArlRS system, only ArlR was downregulated, whereas ArlS remained unperturbed by the mutation. In Δ*clpP* vs. wildtype comparison both proteins ArlR and ArlS were found but were not affected by the mutation. In addition to transcriptional regulators, downstream virulence factors such as hemolysins (alpha- and delta-hemolysin), toxin Endoribonuclease MazF, and host-immune interacting proteins Staphopain A and Staphylococcal complement inhibitor (*scn*) were observed as downregulated as well. Interestingly, ClpX has been shown to control transcription of protein A independently from ClpP.[234] In accordance, protein A and its putative transcription regulator SarS[289], was found downregulated in Δ*clpX* mutant but not in Δ*clpP* mutant. Additionally virulence associated SarZ and SarX were additionally found downregulated.

Chaperones/Stress response

In contrast to the Δ*clpP* mutant, proteins involved in stress response, *e.g.* ClpB, CtsR, HrcA and MecA were identified as slightly but significantly downregulated. The trend of elevated expression of genes encoding for chaperones and stress response proteins in *clpP* mutants in comparison to ClpX point mutant has been described before[240] and confirms data presented here. Based on the reduced expression levels of chaperones and other stress response proteins it can be concluded that ClpP but not ClpX are of crucial importance in stress response.

2.2.3.4.2. Upregulated pathways in *ΔclpX* mutant strain in comparison to the wildtype

Urease complex

As subunits of the Urease complex are not only upregulated in the Δ*clpP* mutant, but also exhibit elevated expression levels in the Δ*clpX* mutant it can be concluded that the upregulation of the Urease complex stems from impaired ClpXP proteolytic machinery activity. Enhanced gene expression levels of the Urease complex was also reported in I256 ClpX point mutant strains in comparison to wildtype control.[240]

Cell wall biosynthesis regulating proteins

Besides the Urease complex, a coherent network subdivided into three minor networks is visible in the visualized STRING analysis of upregulated (Figure 31C) proteins. All of the proteins clustering are involved in pathways associated with peptidoglycan structures.

Members of the first subnetwork are involved in cell wall biosynthesis by bridging peptidoglycan structures. To this end, *S. aureus* is equipped with penicillin-binding proteins (PBPs), which are also crucial for establishing methicillin resistances.[290] In this whole proteome data set, putative PBP2 to -4 (*SAOUHSC_01467, SAOUHSC_01468 and SAOUHSC_00646*) have been observed slightly but yet significantly upregulated. In addition, FemA and FemX, members of the FemABX family (factors essential for methicillin resistance), known to incorporate glycines into the peptidoglycan structures and crosslinking peptidoglycan branches by pentaglycine interpeptide crosslinkes[291] have been

observed upregulated. Another protein owing a peptidoglycan synthesis mediating function, FmtA[290] has been monitored upregulated as well.

Whereas proteins of the first cluster are in charge of crosslinking single peptidoglycan structures via glycine interpeptides, proteins of the second cluster modify the cell surface structures by cleaving peptidoglycan crosslinks or functioning as transpeptidases.

Proteins downregulated in Δ*clpX* mutant and responsible for the cleavage of established interpeptide bridges are Staphylococcal secretory antigen SsaA and SsaA2, autolysins LytM and LytN as well as N-acetylmuramoyl-L-alanine amidase Sle1, Probable transglycosylase SceD and bifunctional autolysin Atl and its transcription regulator SarV.[263,292-295]

Transpeptidase SrtA bridges the peptidoglycan modifying enzymes of the second cluster to the third cluster – host/pathogen interacting proteins. SrtA mediates the anchoring of virulence and host/pathogen interacting proteins to the membrane surface of *S. aureus*.[296]

Amongst these virulence associated proteins are the cell adhesion proteins Clumping factor A and B (*clfAB*), Elastin binding protein EbpS (*ebps*), Fibronectin-binding protein A precursor (*fnbA*), Surface protein F and G (*sasF* and *sasG*) as well as Serine-aspartate repeat-containing protein C and D SdrC and SdrD (*sdrC* and *sdrD*)[297]. Of note, SdrC and SdrD are among the proteins with the highest increase in protein expression in comparison to the wildtype.

In addition, serine-rich adhesin for platelets SraP (*sraP*) and two proteins of the same operon being responsible for the cellular export of SraP via the accessory SecA2/SecY2 system, namely Accessory Sec system protein Asp3 (*asp3*) and Protein translocase subunit SecA2 (*secA2*)[298] have shown increased expression levels as well.

In line with the data presented here, *Stahlhut et al.* observed an increased gene expression for virulence associated cell surface proteins FnbA, FnbB and SraP.[240]

2.2.3.5. Proteins dysregulated between *ΔclpP* and *ΔclpX* mutants

Proteins affected by the ClpXP proteolytic machinery should in theory exhibit a joint dysregulation in expression levels in mutants Δ*clpP* and Δ*clpX* when compared to the wildtype. For the identification of these proteins, the overlap of up- and downregulated proteins in both mutants in comparison to the wildtype was evaluated separately. The resulting Venn diagrams illustrate a great number of proteins commonly up- (Figure 32A) and downregulated (Figure 32B) in both mutants in comparison to the wildtype, indicating that these intersections depict proteins regulated by the ClpXP machinery.

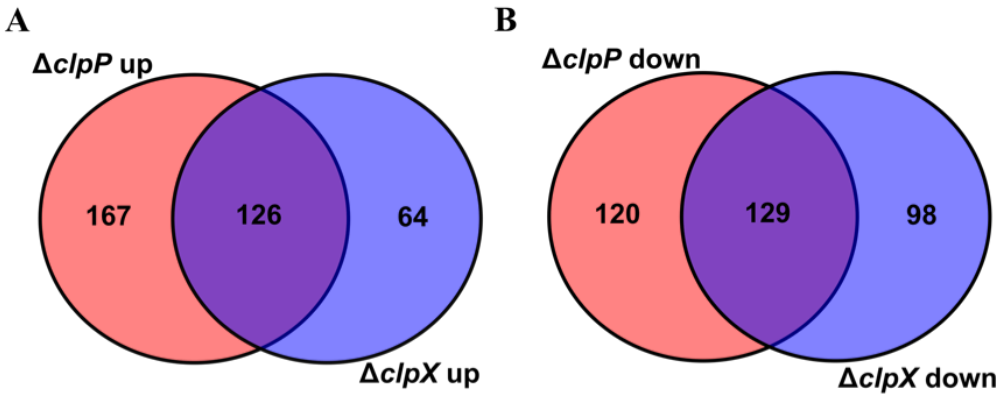

Figure 32: Comparison of dysregulated proteins in ΔclpP mutant and ΔclpX mutant relatively to the wildtype, respectively. Proteins **A)** significantly upregulated and **B)** significantly downregulated in both genetic mutants in comparison to the wildtype were compared in order to identify commonly dysregulated proteins and illustrated *via* Venn diagrams.

Consequently, proteins which display dysregulated expression patterns in a comparison of both deletion mutants potentially stem from impaired ClpCP activity. Whereas in Δ*clpX* mutant strains, ClpCP activity is retained, Δ*clpP* mutants lack both, ClpCP and ClpXP machineries. Therefore, proteins showing significantly increased expression levels might accumulate due to missing ClpCP activity in Δ*clpP* mutants. Proteins demonstrating significantly decreased expression levels contingently represent ClpXP substrates or proteins upregulated due to ClpCP activity.

Following this line of argumentation, *Stahlhut et al.* compared gene expression patterns in a *clpP* mutant to the respective expression patterns in a I256E ClpX point mutant in order to identify ClpCP proteins, which should display increased expression in *clpP* mutant in comparison to the ClpX point mutant.[240]

These proteins, identified as upregulated in Δ*clpP* mutant in comparison to Δ*clpX* mutant, can include ClpCP substrates which illustrate increased abundancy due to missing

degradation processes. However, it has to be highlighted that not all proteins upregulated necessarily depict ClpCP substrates in consequence. As shown in previous chapters, deletion mutations of ClpP and ClpX not only led to the accumulation of respective substrates, but also led to dysregulation of proteins and pathways via unknown mechanisms. Therefore, dysregulated proteins have to be carefully evaluated.

For direct comparison of protein expression levels in Δ*clpP* and Δ*clpX* mutants a two-sample student's *t*-test was carried out and significantly up- and downregulated proteins identified. 1617 proteins met the filtering criteria with 95 proteins observed as significantly down- and 185 as significantly upregulated (Figure 33A).

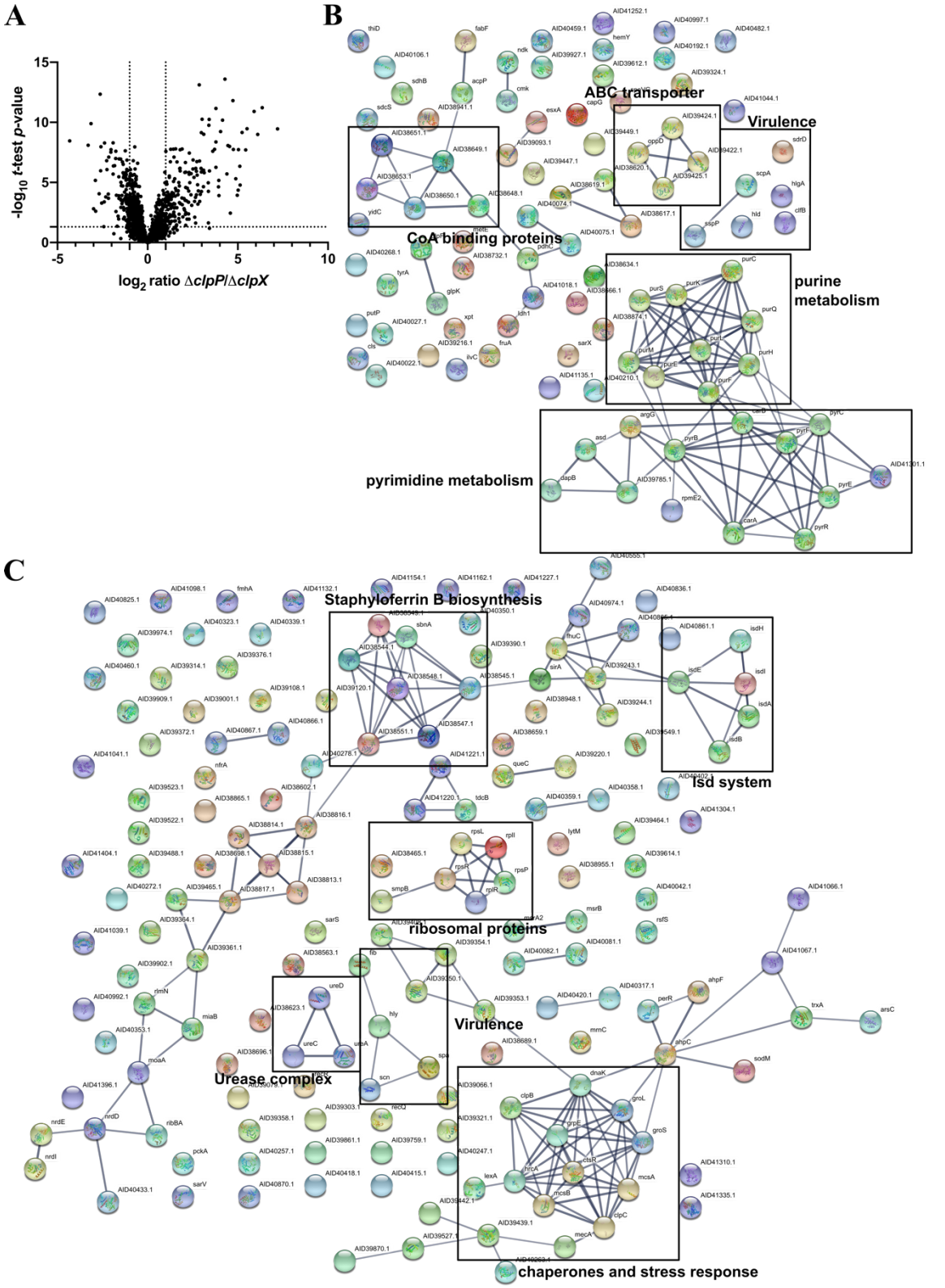

Figure 33: Whole proteome analysis of *S. aureus ΔclpP* compared to *S. aureus ΔclpX*. A) Volcano plot represents two-sample t-test results of *S. aureus ΔclpP* compared to *S. aureus ΔclpP* (n=7). Cutoff criteria were defined as $\log_2$ = ±1 (2-fold change in protein expression) and -$\log_{10}$ (*t*-test *p*-value) = 1.3 (dotted lines). Proteins assigned to the GO cellular component (GOCC) terms extracellular region (blue), intracellular region (grey), plasma membrane (red) and proteins with no assignment (black) are colored. Analysis was carried out with GO annotations[174] implemented into Perseus **B)** Proteins with significantly reduced expression levels in *clpP* deletion mutant (consequently upregulated in *clpX deletion* mutant) were subjected to network analysis using STRING v11 using "confidence" as meaning of network edges and a minimum required interaction score of 0.7 (high confidence). **C)** Proteins with significantly elevated expression levels in *clpP* deletion mutant (consequently downregulated in *clpX deletion* mutant) were also subjected to

network analysis using STRING v11 with same parameters as for downregulated proteins. Assignments of clusters was cluster was performed using GO annotations, KEGG assignments and literature known interactions between proteins.

2.2.3.5.1. Proteins downregulated in *ΔclpP* mutant relatively to *ΔclpX* mutants

Proteins with a negative ratio were subjected to STRING network analysis (Figure 33B, Table 8), revealing a dense network of purine and pyrimidine metabolizing proteins as well as virulence associated proteins, a small cluster of ABC transporters and a loose network of proteins associated with Coenzyme A (CoA) turnover. Interestingly, all virulence factors exhibiting a significantly enhanced expression in Δ*clpX* mutants in comparison to Δ*clpP*, are controlled by the Agr system.[299] *Stahlhut et al.* showed that gene expression levels of the *agrACDB* operon are significantly higher in I265E ClpX point mutant in comparison to the utilized *clpP* mutant.[240] Even though proteins encoded by the *agr* operon have not been identified in the dataset, accompanying regulation of downstream virulence proteins might explain the observed dysregulation here.

However, few of these virulence proteins (α-hemoylsin, HTH-type transcriptional regulator SarX), were also found down regulated in Δ*clpX* mutant strain relatively to the wildtype, indicating that their expression also partly dependent on ClpCP.

Table 8: Proteins with decreased expression levels (log_2 ratio ≤ -1.0, $-log_{10}$ t-test p-value > 1.3) in Δ*clpP* deletion mutant in comparison to Δ*clpX* point mutant. Proteins were categorized according to their KEGG and GO assessment as analyzed by Perseus.

Gene name	Uniprot ID	log_2 ratio *ΔclpP*/*ΔclpX*	$-log_{10}$ *t*-test *p*-value
Pyrimidine/purine metabolism			
carA	Q2FZ73	-2.40	3.38
carB	Q2FZ72	-2.63	12.35
purC	Q2FZJ3	-1.60	5.47
purE	Q2FZJ5	-1.60	3.90
purF	Q2FZI9	-1.28	4.20
purH	Q2FZI6	-1.36	5.81
purK	Q2FZJ4	-1.77	7.00
purL	Q2FZJ0	-1.91	5.70
purM	Q2FZI8	-1.23	3.69
purQ	Q2FZJ1	-2.17	3.69
purS	Q2FZJ2	-1.15	3.98
pyrB	Q2FZ75	-3.30	8.10
pyrC	Q2FZ74	-3.14	9.89
pyrE	Q2FZ70	-2.32	3.80
pyrF	Q2FZ71	-2.59	7.97
pyrR	Q2FZ77	-1.20	5.83
Virulence			
clfB	Q2FUY2	-1.36	6.50

hld	Q2FWM8	-1.48	2.92
SAOUHSC_02708 (putative hlgA)	Q2FVK3	-1.19	3.84
sarX	Q2G0D1	-1.58	6.95
scpA	Q2FY76	-1.48	3.52
sdrD	Q2G0L4	-4.32	8.46
sspP	Q2G2R8	-1.22	3.55
CoA binding proteins, putative			
SAOUHSC_00195	Q2G1D0	-1.59	3.67
SAOUHSC_00196	Q2G1C9	-1.91	8.30
SAOUHSC_00197	Q2G1C8	-2.39	8.28
SAOUHSC_00198	Q2G1C7	-1.76	7.60
SAOUHSC_00199	Q2G1C6	-2.15	7.11
ABC transporter domain-containing proteins			
SAOUHSC_00924	Q2FZR6	-2.69	4.06
SAOUHSC_00925	Q2FZR5	-2.03	7.73
SAOUHSC_00926	Q2FZR4	-1.34	2.92
SAOUHSC_00927	Q2FZR3	-2.27	6.81

Strikingly, significant upregulation befalls a dense network of purine and pyrimidine metabolizing proteins in Δ*clpX* mutant relatively to Δ*clpP*. As expression levels of proteins of the same pathway have also been decreased in Δ*clpP* mutant in comparison to the wildtype, it can be assumed that the purine/pyrimidine metabolic pathways is linked to ClpCP activity. Members of this pathways have also been confirmed as ClpCP substrates by studies utilizing a ClpC^{trap} and analyzing trapped proteins via mass spectrometry[300].
In addition, ABC transporters (also found upregulated in Δ*clpX* vs wt experiments) and CoA dependent proteins were found upregulated in Δ*clpX* mutant in comparison to Δ*clpP*.

2.2.3.5.2. Proteins upregulated in *ΔclpP* mutant relatively to *ΔclpX* mutants

Identifying ClpCP substrates by applying a ClpC^{trap} and subsequent analysis of trapped proteins with mass spectrometry *Graham et al.* confirmed known ClpCP substrates namely ClpB, DnaK, DnaJ, GroL and MecA.[300] Identifying these known substrates among the upregulated proteins in Δ*clpP* mutant in comparison to Δ*clpX* mutant here, verified the assumption that ClpCP substrates might be identifiable among the upregulated proteins in

this dataset. Chaperones involved in stress response (ClpB, ClpC, DnaK, DnaJ, GroE, GroL, GroS, GrpE) as well as respective activity and transcription controlling proteins (HrcA, CtsR, McsB and MecA) have been identified as upregulated. As concluded in previous studies, the elevated presence of chaperones as well as their upstream regulators might reflect the importance of intact ClpCP proteolytic complexes in stress response but also flag some of them as substrates of ClpCP.[300]

The increased stress due to the absence of ClpP is further reflected by the increased expression of iron acquisition systems, namely Isd system and putatively Staphyloferrin B biosynthesis.

Table 9: Proteins with elevated expression levels (log_2 ratio ≤ -1.0, $-log_{10}$ t-test p-value > 1.3) in Δ*clpP* deletion mutant in comparison to Δ*clpX* point mutant. Proteins were categorized according to their KEGG and GO assessment as analyzed by Perseus.

Gene name	Uniprot ID	log_2 ratio *ΔclpP/ΔclpX*	$-log_{10}$ *t*-test *p*-value
Chaperones/stress response			
clpB	Q2FZS8	4.28	13.60
clpC	Q2G0P5	2.86	13.12
ctsR	Q2G0P5	4.89	5.31
dnaK	Q2FXZ2	1.20	5.42
groL	Q2FWN4	1.07	4.86
groS	Q2FWN3	1.80	7.72
grpE	Q2FXZ1	1.80	5.95
hrcA	Q2FXZ0	3.61	7.60
mcsA/SAOUHSC_00503	Q2G0P7	2.31	7.44
mcsB	Q2G0P6	3.01	10.25
mecA	Q2G1U5	7.20	9.46
Isd system			
isdA	Q2FZE9	1.35	4.16
isdB	Q2FZF0	3.95	3.91
isdE	Q2FZE6	1.44	2.41
isdH	Q2FXJ2	3.37	4.26
isdI	Q2G1J2	2.96	6.16
Staphyloferrin B biosynthesis			
sbnA	Q2G1N3	4.76	7.74
SAOUHSC_00076 (putative: sbnB)	Q2G1N2	6.36	11.22
SAOUHSC_00077 (putative: sbnC)	Q2G1N1	5.24	9.15
SAOUHSC_00079 (putative: sbnE)	Q2G1M9	5.11	6.35
SAOUHSC_00080 (putative: sbnF)	Q2G1M8	5.51	9.46
SAOUHSC_00082 (putative: sbnH)	Q2G1M6	2.81	4.29
Ribosomal Proteins			
rplI	Q2G2T3	3.79	11.16

rplR	Q2FW22	2.30	5.83
rpsL	P0A0H0	4.58	2.44
rpsP	Q2FZ45	1.03	1.78
rpsR	Q2G111	1.70	4.31
Virulence			
hly	Q2G1X0	1.55	7.79
SAOUHSC_01114	Q2FZB8	2.31	5.68
scn	Q2FWV6	2.02	3.66
spa	P02976	3.79	8.37
Urease complex			
ureA	Q2FVW5	2.45	3.09
ureC	Q2G2K5	1.43	7.77
ureD	Q2G272	1.20	3.12

2.2.3.6. Conclusions and Summary from *S. aureus* whole proteome comparisons

In summary, the global expression levels of intracellular proteins in *S. aureus* have been studied using genetic mutants of *clpP* and *clpX* and compared to *S. aureus* wildtype to obtain insights into cellular pathways mediated by ClpP and ClpX.

The majority of pathways affected by the genetic manipulations have been already linked to ClpP and ClpX in previous transcriptome analysis studies, and are confirmed here on a proteome level. The protein clusters dysregulated upon genetic knockout of *clpP* and *clpX* revealed several shared pathways affected, however the profile of altered pathways did also differ significantly in other areas. Besides purine and pyrimidine metabolism, urease complex, virulence associated proteins and proteins related to stress response due to the missing degradation system (*e.g.* chaperones) were significantly altered in *clpP* deletion mutant.

Even though virulence associated proteins were affected in ClpP mutants, the dysregulation in expression of these proteins was even more explicit in *clpX* deletion mutants. The important role of ClpX and ClpP in the regulation of virulence is well known and therefore gained increased attention as favored drug target. The idea behind targeting the proteolytic complex is to disarray but not to kill the pathogenic invadors, hence aiding the immune system to overcome the bactieral infection without causing evolutionary pressure, which would lead to undesired resistance developments. To follow this strategy numerous studies focus on the development of ClpX and ClpP inhibitors.[122,238,301] Additionally the ABC transporters as well as other transmembrane transporters showed altered expression levels in comparison to the wildtype.

The method utilized here to detect changes in proteome expression could be validated as multiple validated substrates of ClpP and ClpX were found dysregulated in the same manner as reported in literature. Additionally, also ClpXP and ClpCP substrates and affected pathways and proteins were identified. However, proteins with observed dysregulation are not necessarily substrates, as absence of ClpP and ClpX eventually affects pathways via secondary mechanisms, thus making a classification of identified dysregulated proteins as novel yet unknown substrates difficult if not impossible based on the current data. Further validation experiments, *e.g.* using substrate traps, are therefore necessary.

The aim of the conducted study was to generate hypotheses on the influence of ClpP and ClpX on the whole proteome, however extracting meaningful data out of the non-targeted dataset is challenging and subsequent hypotheses testing requires further biological experiments. As metabolic pathways have been affected, especially by *clpP* knockout, a dysregulation of purine and pyrimidine intermediates could be conducted to generate complementary insights, *e.g.* by following a targeted or untargeted metabolomics approach.

Of particular interest is the marignal but striking difference in protein expression levels between *clpP* deletion and point mutant, as proteins have been revealed which partly depend on the sole presence of ClpP, regardless of its activity state. Apparently, two pathways are especially affected by the presence/absence of inactive ClpP. While numerous proteins of the pyrimidine pathways exhibited a strong depletion in protein expression in *ΔclpP* mutants in comparison to the point mutant, proteins of the staphyloferrin B biosynthesis were slightly upregulated.

So far, the analysis of protein expression was reduced to the intracellular region of *S. aureus* (including extracellular proteins prior to their excretion). However, virulence of *S. aureus* is predominantly regulated by proteins bound to the cell wall and/ or leaked into the extracellular space.[302] Therefore, the evaluation of altered secreted proteins upon genetic manipulation of the ClpP machinery is of additional interest.

2.2.4. Secretome analysis

For the comparison of secreted proteins, consumed medium of liquid cultures from the whole proteome analysis (7 biological replicates per sample group) was collected by centrifugation and subsequently filtered to remove residual bacterial cells. Filtrated medium was freeze dried, reconstituted in water and secreted proteins precipitated by Wessel-Flügge precipitation, which is especially useful to separate proteins from salt and buffer ingredients found in the media.[303] Precipitated proteins were digested and analyzed in line with conducted whole proteome analysis.

2.2.4.1. Global differences in secreted proteins

In accordance with the preceding whole proteome analysis, global differences between groups of samples and sampling reproducibility were evaluated using principal component analysis. Comparable to the conducted whole proteome analysis, the data was filtered with the requirement of five out of seven valid values in one sample group for each quantified protein.

In line with the results of the PCA analysis of the whole proteome analysis (see Chapter 2.3.1.) the biological replicates of each strain cluster together, indicating sufficient sampling reproducibility within each group (Figure 34A). In agreement with the whole proteome analysis, both genetic *clpP* mutant are indistinguishable on a global protein expression level. However, in contrast to the results of the whole proteome analysis, a global difference between the genetic *clpP* and *clpX* mutants is not observed as all genetic mutants cluster. Solely the wildtype samples cluster separately together, indicating that the global phenotype of the genetic mutants differs significantly from the parental strain but not among each other.

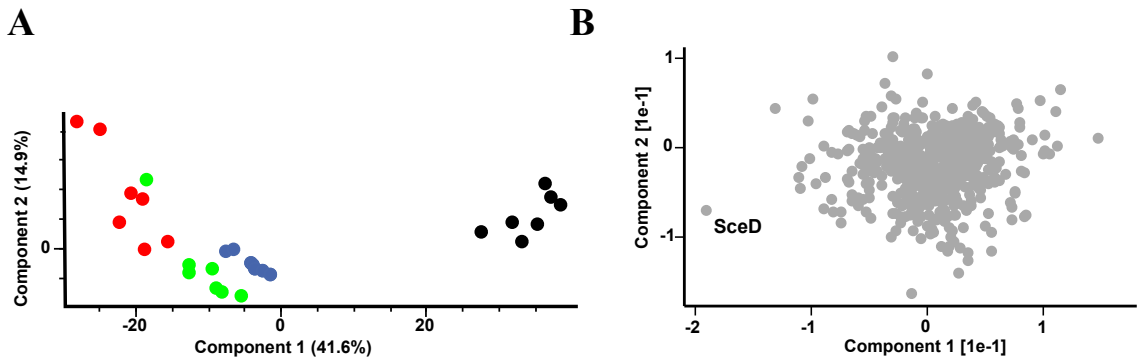

Figure 34: Global assessment of changes in the secreted proteome of *S. aureus* due to conducted genetic modifications. **A)** Principal component analysis (PCA) of genetic *S. aureus* mutants in comparison to the wildtype. Wildtype (black) samples cluster separated from Δ*clpX* (purple), Δ*clpP* (red) and S98A ClpP point mutant (green). Principal component analysis was conducted with Perseus and default settings. **B)** Loadings plot of conducted principal component analysis indicating a major influence of SceD on group separation. Loadings plot was generated using default settings in Perseus.

The corresponding loading plot (Figure 34B) revealed, that few proteins contribute to the phenotypic differences amongst the samples, *e.g.* probable transglycosylase SceD which showed to impact group separation the most. SceD is an important autolytic enzyme with distinct functions in host colonization.[295]

2.2.4.2. Comparison of secreted protein in *ΔclpP* mutant and wildtype

A two-sample student's t-test was utilized to reveal significantly altered protein expression levels in *clpP* deletion mutant in comparison to the wildtype. Cut off criteria for significant dysregulated proteins were defined as follows: $\log_2 = 1$ or -1 (2-fold enrichment or depletion) respectively and $-\log_{10}$ *t*-test *p*-value = 1.3 (Figure 35) Out of 596 proteins, 111 proteins were significantly up- and 212 proteins significantly downregulated. Hence, half of the present proteins exhibited significantly altered expression levels.

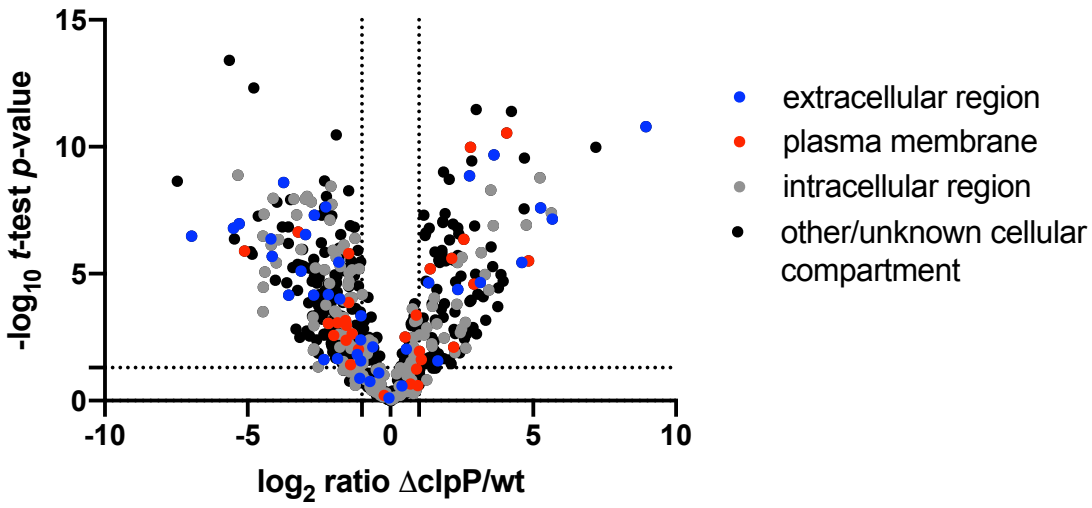

Figure 35: Secretome analysis of *S. aureus ΔclpP* compared to *S. aureus* wildtype. Volcano plot represents two-sample t-test results of *S. aureus ΔclpP* compared to *S. aureus* wildtype control (n=7). Cutoff criteria were defined as $\log_2 = \pm 1$ (2-fold change in protein expression) and $-\log_{10}$ (*t*-test *p*-value) = 1.3 (dotted lines). Proteins are highlighted in blue (extracellular region), red (plasma membrane), grey (intracellular region) or black (other/unknown cellular compartment) depending on their GO term[174] annotation for cellular component as analysed Perseus[151].

In order to distinguish between proteins originating in the intracellular part, which might hinder proper data analysis of secreted proteins, the GO annotation[174] for cellular compartment of all proteins were inspected. Proteins were categorized as extracellular (blue), plasma membrane-bound (red), intracellular (grey) and proteins with different or unknown annotation (black) depending on their GO annotation for cellular component. In theory, solely proteins from the extracellular region and membrane-bound proteins cleaved from the cell surfaces should be present in the data.

However, as is evident from Figure 35, a quite distinct amount of intracellular proteins is present in the plot. As bacterial cells were removed by centrifugation, and resulting supernatant additionally filtered, using filter with 0.22 µm pore size intact bacterial cells should not be passed through sample preparation.

One hypothesis is, that the applied pressure during filtration of the resulting supernatant led to a disruption of the cell walls of residual bacterial cells, releasing intracellular proteins into the filtrate. However, by taking the fold changes and *p*-values of these proteins into account, it can be assumed that the presence of intracellular proteins is not based on coincidental bursting of residual cells.

A second hypothesis is, that the intracellular proteins stem from dead cells, releasing proteins into the lumen when expanding their life span.

For a careful evaluation of dysregulated membrane-bound and secreted proteins, proteins assigned to “extracellular part” and “plasma membrane” dysregulated in the

volcano plot were inspected more closely, and following analysis restricted to these proteins.

2.2.4.2.1. Downregulated proteins in *ΔclpP* mutant in comparison to wildtype

Virulence associated proteins identified as significantly downregulated can be grouped into four categories: hemolysins, leukocyte targeting proteins, members of the Spl serine proteases and staphylococcus serine proteases (Table 10). Additionally, cell wall associated proteins, one transmembrane transporter and proteins which cannot be categorized into one of the mentioned groups.

Four different hemolysins (α-, β-, y-, δ-hemolysin) are known so far[215], and all of them have been identified as downregulated upon genetic deletion of *clpP* here. Whereas β-hemolysin (*hlb*) and δ-hemolysin (*hld*) showed a particular strong downregulation upon genetic knockout of *clpP*, α-hemolysin as well as two confirmed subunits of y-hemolysin, gamma hemolysin component B and C (*hlgB* and *hlgC*) and one putative gamma-hemolysin subunit (*SAOUHSC_02708*)[304] exhibited less, yet significant, altered expression levels.

As mentioned above, transcription of genes encoding for the *agr* operon and *hld* are regulated by SarA mediated transcription from RNAIII and RNAII. Members of the Agr family exhibited decreased expression levels in Δ*clpP* mutant in the whole proteome analysis compared to the wildtype. Therefore, a decreased expression and secretion of δ-hemolysin was expected.

Decreased transcription of genes encoding for hemolysins in the absence of ClpP known in literature[231,233,305] and thereby confirms the applicability of the enforced workflow.

Table 10: Significantly downregulated proteins with GO annotation "extracellular part" and "plasma membrane" in Δ*clpP* mutant relatively to the wildtype. Proteins were categorized according to their KEGG and GO assessment as analyzed by Perseus.

Gene name	Uniprot ID	$\log_2$ ratio *ΔclpP*/S98A	$-\log_{10}$ *t*-test *p*-value
Cell wall associated proteins			
atl	Q2FZK7	-1.08	3.35
ezrA	Q2FXK8	-2.17	3.04
ftsY	Q2FZ48	-1.55	2.38
Hemolysins			
hlb	Q2FWP1	-6.96	6.48
hly	Q2G1X0	-1.77	4.00
hld	Q2FWM8	-5.10	5.90
hlgB	Q2FVK1	-1.03	2.39
hlgC	Q2FVK2	-1.86	1.66
SAOUHSC_02708	Q2FVK3	-2.33	1.62
Host-Pathogen Interactions			
chp	Q2FWV5	-1.81	5.46
scn	Q2FWV6	-1.04	1.57
Leukotoxin			
lukDv	Q2FXB1	-1.16	1.82
Spl serine proteases			
splA	Q2FXC2	-4.18	6.36
splB	Q2FXC3	-3.12	5.10
splC	Q2FXC4	-4.14	5.68
splD	Q2FXC5	-2.17	4.18
splE	Q2FXC7	-3.56	4.15
splF	Q2FXC8	-2.68	4.15
Staphopain A/B			
sspB	Q2FZL3	-3.74	8.59
sspP	Q2G2R8	-5.29	6.96
Others			
hysA	Q59801	-5.50	6.80
plc	Q2G1Q2	-2.26	7.62
secA1	O06446	-1.12	2.02
SAOUHSC_02171	Q2FWV3	-2.97	6.54
SAOUHSC_02466	Q2FW51	-2.66	7.30
SAOUHSC_02650	Q2FVQ2	-1.47	5.79

The Spl serine proteases are uniquely expressed in *S. aureus* and have been identified to contribute to *S. aureus* virulence even though their specific mode of action is so far

unknown.[306] In accordance to gene expression analysis of *clpP* mutants in comparison to wildtype cells[233], all six members of the Spl serine protease family are expressed significantly less in Δ*clpP* knockout cell relatively to the wildtype. Additionally confirming the reduced gene expression observed for Staphopain in the study[233], the cysteine proteases Staphopain A (sspP) and Staphopain B (sspB) have been downregulated in the *clpP* knockout mutant in the secretome analysis here.

Besides leukotoxin LukDv (lukDv), two immune modulators staphylococcal complement inhibitor SCIN (*scn*) and chemotaxis inhibitory protein of *S. aureus* CHIPS (*chp*)[287] displayed decreased expression levels, however no correlation therefore to missing ClpP could be found in literature.

Additionally to the mentioned protein groups, three cell wall associated proteins, bifunctional autolysin AtlL (*atl*)[307], EzrA (extra Z-rings A) (*ezrA*)[308] and FtsY, which has been shown to be of crucial importance for expression of membrane proteins in *E. coli*[309],exhibited reduced expression levels.

2.2.4.2.2. Upregulated proteins in *ΔclpP* in comparison to wildtype

Upregulated proteins could be categorized into adhesion proteins, cell wall associated proteins, proteins involved in iron uptake and proteins of other categories (Table 11).

Proteins involved in adhesion exhibited a particular high upregulation in the absence of ClpP: Clumping factor A and B (*clfA, clfB*), Fibronectin-binding protein A (*fnbA*), Elastin-binding protein EbpS (*ebps*)[310], extracellular matrix binding protein Ebh (*ebh*)[311], fibrinogen-binding protein Efb[286] and Surface protein G (*sasG*). The upregulated gene expression of cell adhesion proteins, especially of fibronectin binding proteins in Δ*clpP* mutants in comparison to the parental strain has been shown before, accompanied by increased fibronectin binding of these mutants.[233] Dysregulation of the WalKR two component system due to *clpP* knockout might provide an explanation for the upregulation of adhesion proteins. At least for EbpS a dependency on WalKR is reported.[275]

Table 11: Significantly upregulated proteins with GO annotation "extracellular part" and "plasma membrane" in Δ*clpP* mutant relatively to the wildtype. Proteins were categorized according to their KEGG and GO assessment as analyzed by Perseus.

Gene name	Uniprot ID	$\log_2$ ratio *ΔclpP*/wt	$-\log_{10}$ *t*-test *p*-value
Adhesion proteins			
clfA	G0XY21	1.91	7.37
clfB	Q2FUY2	1.21	6.51
ebh	Q2FYJ6	4.84	5.51
ebpS	Q2FYF1	4.07	10.55
fnbA	P14738	2.21	5.53
SAOUHSC_01114	Q2FZB8	5.76	7.16
sasG	Q2G2B2	1.93	5.51
Cell wall associated proteins			
ftsL	Q2FZ95	1.01	1.94
isaA	Q2FV52	4.61	5.45
ltaS	Q2G093	2.57	6.35
lytM	O33599	3.63	9.68
lytN	Q9ZNI1	2.85	9.44
sceD	Q2FWF8	8.95	10.79
Iron uptake			
isdB	Q2FZF0	1.87	1.66
isdC	Q8KQR1	2.89	2.88
isdE	Q2FZE6	2.80	9.99
isdH	Q2FXJ2	7.19	9.98
Virulence			
flr	Q2FZC0	3.15	4.65
isaB	Q2FUX3	2.78	8.85
kdpC	Q2FWI1	1.08	1.62
oatA	Q2FV54	1.40	5.19
SAOUHSC_00383	Q2G0X9	1.66	1.57
SAOUHSC_00392	Q9RN32	2.36	4.39
SAOUHSC_02979	Q2G222	1.33	4.64
ssaA2	Q2G2J2	5.26	7.59
Others			
qoxA	Q2FZJ9	2.21	2.10
SAOUHSC_01676	Q2FXZ9	2.15	5.60

As outlined in chapter 2.3.2.2., the two-component system WalKR is essential for cell division. Cell wall biosynthesis associated proteins controlled by WalKR have been shown upregulated in Δ*clpP* mutants in comparison to the parental strain in the whole proteome data, amongst others: EbpS, LytM, LytN, SceD and WalR itself. Interestingly, in line with

protein expression levels in the intracellular region, SceD, LytM and LytN have been found upregulated in the extracellular space.

Of particular interest are two lytic transglycosylases probable lytic transglycosylase IsaA and lytic transglycolase SceD.[295] Of note, SceD was upregulated in all mutants in comparison to the wildtype, indicating that its expression might be linked to the ClpXP machinery via affecting WalKR. Besides the mentioned proteins other proteins involved in cell wall biosynthesis namely lipoteichoic acid synthase (*ltaS)*[312] and protein FtsL (function confirmed in *E. coli*[313]) have been found upregulated.

In accordance with elevated expression levels in the *clpP* deletion strain observed in the whole proteome dataset, excreted members of the Isd system (IsdB, IsdC, IsdE, IsdH) have been observed upregulated in the secretome as well. Reasons for elevated expression levels of iron uptake proteins have been discussed above.

Apart from proteins involved in cell wall biosynthesis other virulence associated proteins have been identified upregulated, amongst other ssaA2, shown to be loosely connected to the WaLKR system.[314]

2.2.4.3. Comparison of secreted protein in *ΔclpP* mutant and S98A ClpP point mutant

In line with the corresponding whole proteome analysis, secreted proteins with altered expression levels depending on the sole physical presence of ClpP have been identified, comparing the expression levels in clpP knockout vs S98A ClpP pointmutant in a two-sampled student's *t*-test (Figure 36A).

At a first glance, more proteins exhibit significant dysregulation in case of secreted proteins than in case of the intracellular proteins (see Chapter 2.3.3.). However, as a similarity between both comparisons – extracellular and intracellular proteins – more proteins show decreased expression levels in Δ*clpP* mutants relatively to S98A ClpP point mutant. Nevertheless, both mutants share a pronounced number of proteins commonly dysregulated in comparison to the wildtype, respectively (Figure 36B and C).

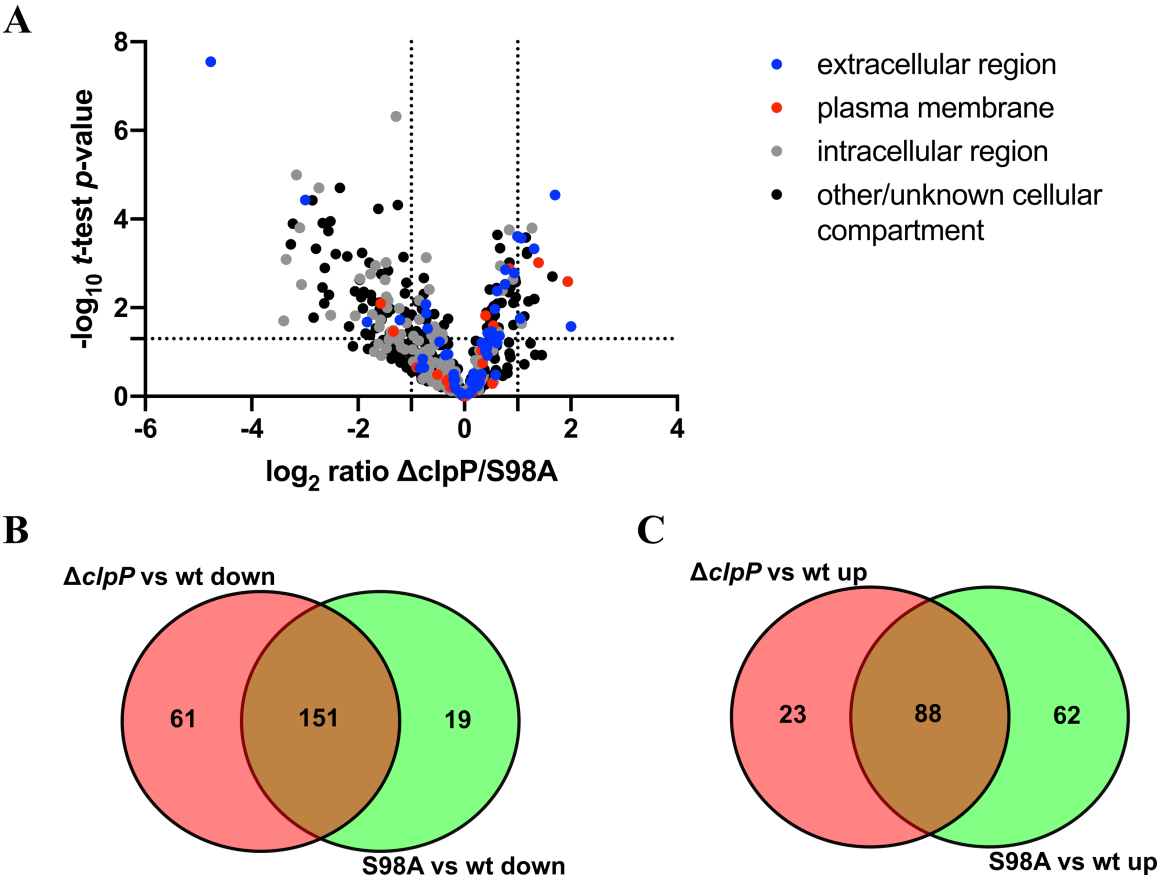

Figure 36: Secretome analysis of *S. aureus ΔclpP* compared to *S. aureus* S98A ClpP point mutant. **A)** Volcano plot represents two-sample t-test results of *S. aureus ΔclpP* compared to *S. aureus* S98A ClpP point mutant (n=7). Cutoff criteria were defined as $\log_2 = \pm 1$ (2-fold change in protein expression) and $-\log_{10}$ (*t*-test *p*-value) = 1.3 (dotted lines). Proteins are highlighted in blue (extracellular region), red (plasma membrane), grey (intracellular region) or black (other/unknown cellular compartment) depending on their GO term[174] annotation for cellular component as analysed Perseus[151]. **B)** Down- and **C)** upregulated proteins in both ClpP mutants in comparison to wildtype control were searched for similarly regulated proteins and intersections visualized in Venn diagrams.

Comparable to the data analysis in the previous chapter, significantly up- and downregulated proteins were screened for protein with a GO term assignment "extracellular region" or "plasma membrane". Six proteins with a corresponding GO term assignment showed significantly decreased expression levels, whereas five proteins were significantly upregulated.

2.2.4.3.1. Downregualted proteins in *ΔclpP* mutant in comparison to S98A ClpP point mutant

Four out of six Spl serine proteases have been detected in the data set, of which only one (SplE) exhibited significantly altered expression levels depending on the sole presence of ClpP. In Δ*clpP* mutants both, SspB and SspP have been shown downregulated relatively to the wildtype. However, SspP but not SspB displayed borderline significant reduced expression in Δ*clpP* mutants in comparison to ClpP point mutants, indicating that the expression levels of SspP are affected by the sole presence of ClpP regardless its activity state.

Additional marginal significant decreased expression levels have been observed by membrane associated FtsH and FtsY, both with distinct functions in cell wall biosynthesis. Membrane-bound FtsH depicts on of the major ATP-dependent proteases, cleaving cytosolic and membrane-bound peptides[315] and FtsY which has been shown to be of crucial importance for expression of membrane proteins in *E. coli*[309].

Interestingly, secretion of β-hemolysin (*hlb*) was strongly downregulated in Δ*clpP* mutants in comparison to point mutant samples. However, conclusions from the expression levels in whole proteome analysis cannot be drawn as the protein was not present in the respective data set. Even though impaired transcription of β-hemolysin in *clpP* knockout cells has been reported previously[233], a dependency of the pure presence of ClpP has not been reported yet.

The protein showing the strongest dysregulation in the entire data set is serine aspartate repeat containing protein D (*sdrD*), which has been shown to exhibit distinct functions in virulence and cell adhesion, especially in nasal colonization.[316] A molecular link between SdrD and ClpP has not been reported yet, but as ClpP modulates biofilm

formation in *S. aureus*[243,256] an unknown mechanism by which SdrD expression is controlled by ClpP is likely to exist.

Table 12: Significantly downregulated (log_2 ratio < -1, $-log_{10}$ t-test p-value > 1.3) proteins in Δ*clpP* mutants in comparison to the S98A ClpP point mutant.

Gene name	Uniprot ID	log_2 ratio *ΔclpP*/S98A	$-log_{10}$ *t*-test *p*-value
ftsH	Q2G0R0	-1.34	1.47
ftsY	Q2FZ48	-1.57	2.10
hlb	Q2FWP1	-3.00	4.43
sdrD	Q2G0L4	-4.77	7.55
splE	Q2FXC7	-2.65	1.68
sspP	Q2G2R8	-1.22	1.72

2.2.4.3.2. Upregulated proteins in *ΔclpP* mutant in comparison to S98A ClpP point mutant

Five proteins with desired GO-term assignment have been identified significantly upregulated in Δ*clpP* mutants over S98A ClpP point mutants (Table 13), however alteration of expression ratios was detected as less prominent compared to the observed downregulation.

Additionally to increased expression levels in Δ*clpP* mutants in comparison to the parental strain, FPRL1 inhibitory protein (*flr*) displayed also marginal elevated secretion levels in this mutant compared to the point mutant. Besides FPRIP, the proteins LytM and Fibrinogen-binding protein (*SAOUHSC_01114*)[286] have been upregulated in Δ*clpP* in comparison to the point mutant and additionally relatively to the wildtype control group.

Table 13: Significantly upregulated (log_2 ratio > 1, $-log_{10}$ t-test p-value > 1.3) proteins in Δ*clpP* mutants in comparison to the S98A ClpP point mutant. Proteins were categorized according to their KEGG and GO assessment as analyzed by Perseus.

Gene name	Uniprot ID	log_2 ratio *ΔclpP*/S98A	$-log_{10}$ *t*-test *p*-value
flr	Q2FZC0	1.05	1.78
isdC	Q8KQR1	2.00	1.58
isdH	Q2FXJ2	1.70	4.54
lytM	O33599	1.07	3.57
SAOUHSC_01114	Q2FZB8	1.31	3.33

Of note, two proteins of the Isd iron scavenging system (IsdC and IsdH) have been upregulated as well comparably to the S98A ClpP point mutant, probably indicating a higher iron demand of the knockout- in comparison to the point mutant.

2.2.4.3.3. Discussion of regulated proteins in *ΔclpP* mutants in comparison to S98A ClpP point mutant

Analogous to the whole proteome comparison of both genetic *clpP* mutants, secretome analysis of both revealed an overall comparable phenotype as revealed by PCA analysis and a striking majority of common dysregulated proteins in comparison to the wildtype.

Whole proteome comparison revealed two distinct pathways dysregulated in the whole proteome analysis. In contrast, in case of the secretome no distinct pathways are affected when focusing on proteins of the extracellular and plasma membrane. Yet, the highly significantly decreased secretion of SceD and β-hemolysin in the *ΔclpP* mutant relatively to the S98A ClpP depicts an interesting finding. Apparently, both proteins rely upon an unknown mechanism on the presence of ClpP independent from its functionality.

2.2.4.4. Comparison of secreted protein in Δ*clpX* mutant and wildtype

For the comparison of altered secreted proteins based on *clpX* knockout, expression levels of secreted proteins of the mutant in comparison to wildtype expression levels were evaluated using a two-sample student's *t*-test. Cut off criteria for significant dysregulated proteins were defined as follows: $\log_2$ = 1 or -1 (2-fold enrichment or depletion) respectively and $-\log_{10}$ *t*-test *p*-value = 1.3 (Figure 37A) Out of 608 proteins, 139 proteins were significantly up- and 173 proteins significantly downregulated. Consequently, more than half of the present proteins exhibited significantly altered expression levels.

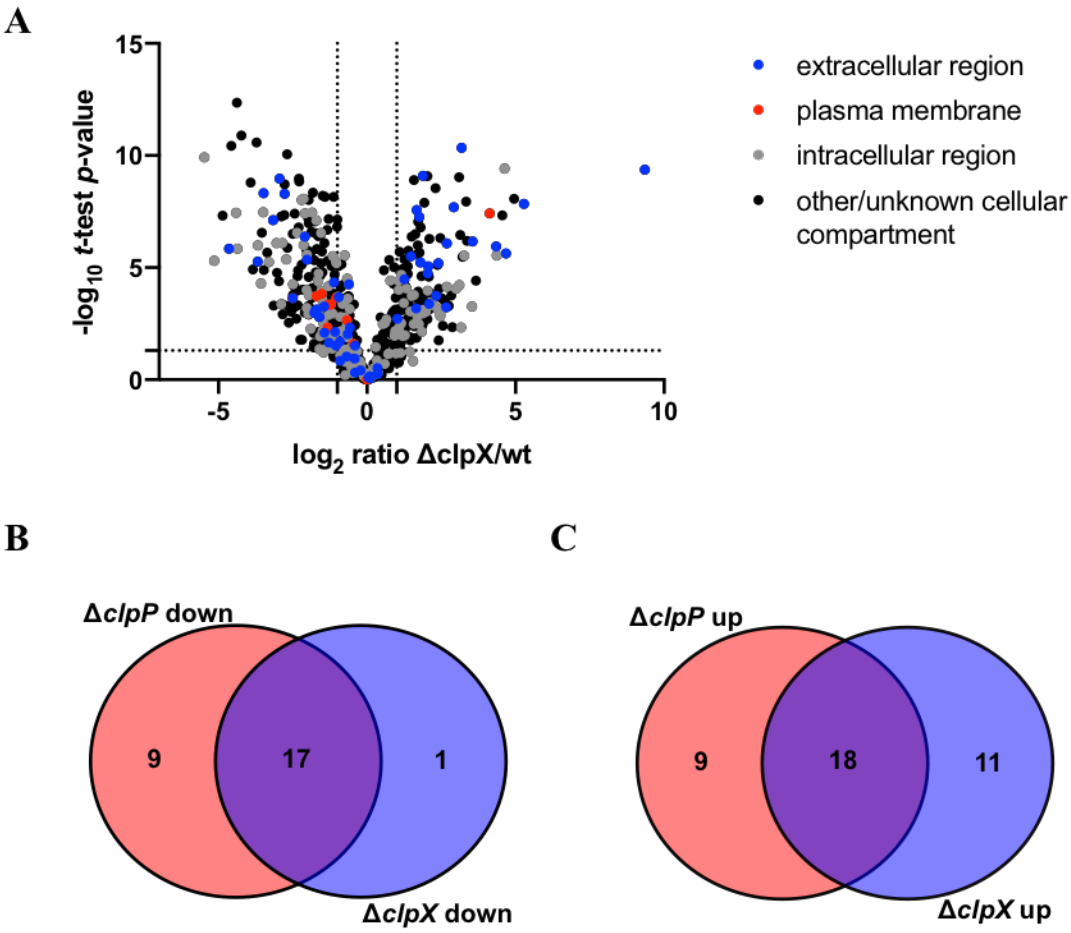

Figure 37: Secretome analysis of *S. aureus ΔclpX* compared to *S. aureus* wildtype. **A)** Volcano plot represents two-sample t-test results of *S. aureus ΔclpX* compared to *S. aureus* wildtype control (n=7). Cutoff criteria were defined as $\log_2 = \pm 1$ (2-fold change in protein expression) and $-\log_{10}$ (*t*-test *p*-value) = 1.3 (dotted lines). Proteins are highlighted in blue (extracellular region), red (plasma membrane), grey (intracellular region) or black (other/unknown cellular compartment) depending on their GO term[174] annotation for cellular component as analysed Perseus[151]. **B)** Down- and C) upregulated proteins in both genetic knockout mutants in comparison to wildtype control were searched for similarly regulated proteins with the GO annotation "extracellular region" and "plasma membrane" and intersections visualized in Venn diagrams.

According to the PCA analysis, the global differences between the genetic knockout mutants Δ*clpP* and Δ*clpX* regarding expression profiles of secreted are marginal. This is

also reflected by the large number of commonly dysregulated secreted proteins with the GO annotation "extracellular region" and "plasma membrane" (Figure 37B + C).

2.4.4.4.1. Downregulated secreted proteins in ΔclpX mutant relatively to the wildtype

As already mentioned in the previous chapter, both genetic deletion mutants share a majority of commonly downregulated proteins, giving rise to the assumption that the ClpXP machinery is necessary to express and secrete most of these proteins (Table 14), *e.g.* the Spl serine proteases, staphopain A and B as well as the hemolysins.

Exclusively protein A (*spa*) exhibited significantly decreased expression levels in the Δ*clpX* mutant, whereas its expression levels have not been altered in the *clpP* deletion mutant strain. A ClpP-independent expression of protein A solely mediated by ClpX has been suggested previously and matches with the observations found here.[317]

Table 14: Significantly downregulated (log_2 ratio < -1, $-log_{10}$ t-test p-value > 1.3) proteins in Δ*clpX* mutants in comparison to the wildtype. Proteins were categorized according to their KEGG and GO assessment as analyzed by Perseus.

Gene name	Uniprot ID	log_2 ratio *ΔclpX*/wt	$-log_{10}$ *t*-test *p*-value
Hemolysins			
hlb	Q2FWP1	-3.68	5.27
hld	Q2FWM8	-2.50	3.65
hly	Q2G1X0	-1.74	3.09
Virulence			
plc	Q2G1Q2	-2.09	6.38
SAOUHSC_02171	Q2FWV3	-2.02	5.35
Host-pathogen interactions			
chp	Q2FWV5	-2.77	8.29
SAOUHSC_02466	Q2FW51	-1.11	4.34
scn	Q2FWV6	-1.44	3.26
spa	P02976	-2.94	8.96
Staphopain A/B			
sspB	Q2FZL3	-3.16	7.11
sspP	Q2G2R8	-3.48	8.32
Spl serine proteases			

splA	Q2FXC2	-1.69	3.13
splB	Q2FXC3	-1.59	2.79
splC	Q2FXC4	-1.29	1.66
splD	Q2FXC5	-1.08	2.13
splE	Q2FXC7	-1.43	2.10
splF	Q2FXC8	-1.77	2.99
Others			
hysA	Q59801	-4.64	5.83

2.4.4.4.2. Upregulated secreted proteins in *ΔclpX* mutant relatively to the wildtype

As it was observed for upregulated proteins in the deletion mutants in comparison to the wildtype, both genetic mutants illustrate a majority of proteins commonly upregulated. For instance, both mutants led to the increased expression of adhesion proteins, cell wall associated proteins as well as numerous virulence associated proteins.

However, a distinct number of proteins have been identified exclusively upregulated in the Δ*clpX* mutant, amongst others SdrC, SdrD, LipA, as well as FtsH. Proteins SdrC and SdrD, superantigen-like protein (SSL) 7 (*SAOUHSC_00392, ssl7*)[318] have additionally been shown upregulated in the whole proteome in comparison to the wildtype.

Interestingly, among all upregulated proteins (Table 15), SceD displays an extreme upregulation in *clpX* deletion mutants, and has additionally been observed upregulated in whole proteome analysis in comparison to the wildtype.

Table 15: Significantly upregulated (log_2 ratio > 1, $-log_{10}$ t-test p-value > 1.3) proteins in Δ*clpX* mutants in comparison to the wildtype. Proteins were categorized according to their KEGG and GO assessment as analyzed by Perseus.

Gene name	Uniprot ID	log_2 ratio *ΔclpX*/wt	$-log_{10}$ *t*-test *p*-value
Adhesion proteins			
clfA	G0XY21	1.76	7.25
ebpS	Q2FYF1	3.10	9.03
fnbA	P14738	2.06	5.05
SAOUHSC_02802 (putative)	Q2G1T5	1.48	5.50
sasG	Q2G2B2	1.03	2.72
Cell wall associated proteins			
ftsL	Q2FZ95	1.23	4.07

isaA	Q2FV52	4.68	5.64
ltaS	Q2G093	2.68	6.08
lytM	O33599	2.05	4.74
lytN	Q9ZNI1	2.33	3.75
SAOUHSC_02979	Q2G222	1.80	5.23
sceD	Q2FWF8	9.36	9.37
Iron Uptake			
isdH	Q2FXJ2	1.65	3.18
Virulence			
flr	Q2FZC0	2.67	3.23
ftsH	Q2G0R0	1.48	2.61
isaB	Q2FUX3	2.92	7.69
kdpC	Q2FWI1	1.89	3.45
oatA	Q2FV54	1.37	4.72
SAOUHSC_00052	Q2G1Q1	2.03	2.70
SAOUHSC_00392 (ssl7)	Q9RN32	2.09	3.38
SAOUHSC_01855	Q2G247	1.72	3.93
sdrC	Q2G0L5	3.18	10.35
sdrD	Q2G0L4	1.88	9.09
ssaA2	Q2G2J2	5.28	7.84
Others			
lipA	Q2FUU5	1.26	4.48
qoxA	Q2FZJ9	2.12	3.87
SAOUHSC_00383	Q2G0X9	2.40	5.19
SAOUHSC_02404	Q2FW95	3.55	6.17

2.2.4.5. Proteins dysregulated between Δ*clpP* and Δ*clpX* mutants

In line with the comparative whole proteome analysis between both deletion mutants (see Chapter 2.3.5.), differences in the secreted proteome were analyzed and significantly dysregulated proteins identified using a two-sampled student's *t*-test (Figure 38). Out of 531 proteins, 87 exhibited significantly higher expression levels in Δ*clpX* mutants relatively to Δ*clpP* (negative ratio in displayed volcano plot, Figure 38), whereas 58 proteins displayed a higher expression rate in Δ*clpP* mutant in comparison to the Δ*clpX* mutant (positive ratio in shown volcano plot, Figure 38).

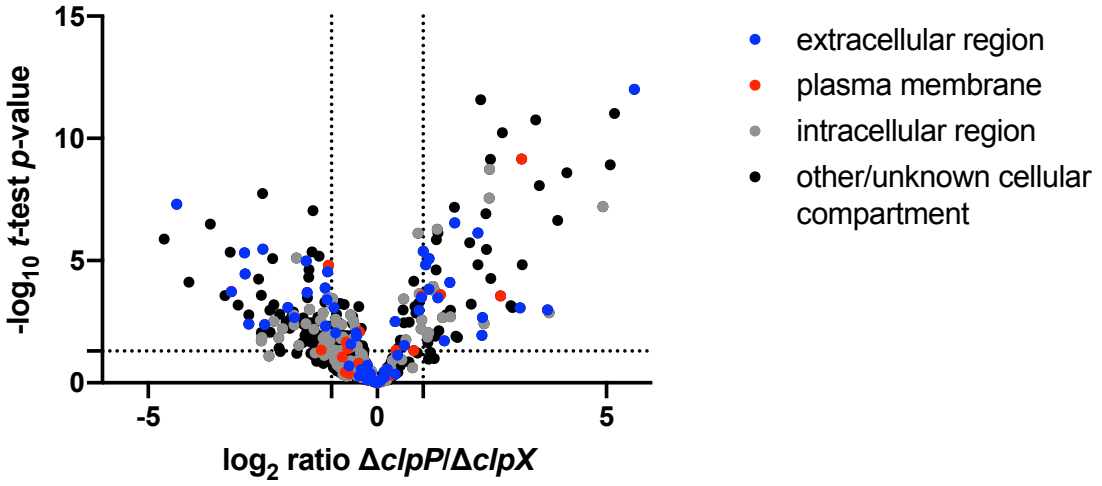

Figure 38: Secretome analysis of *S. aureus ΔclpP* compared to *S. aureus ΔclpX*. Volcano plot represents two-sample *t*-test results of *S. aureus ΔclpP* compared to *S. aureus ΔclpX* (n=7). Cutoff criteria were defined as $\log_2 = \pm 1$ (2-fold change in protein expression) and $-\log_{10}$ (*t*-test *p*-value) = 1.3 (dotted lines). Proteins are highlighted in blue (extracellular region), red (plasma membrane), grey (intracellular region) or black (other/unknown cellular compartment) depending on their GO term[174] annotation for cellular component as analysed Perseus[151].

2.2.4.5.1. Secreted proteins upregulated in *ΔclpX* mutant in comparison to *ΔclpP* mutant

As already discussed, proteins with elevated expression levels in the Δ*clpX* mutant in comparison to the Δ*clpP* mutant (Table 16) might stem from ClpX activity independent from engagement with ClpP. However, as pointed out above additional secondary effects

are likely to contribute to the elevated protein levels independent from a direct effect of ClpX.

The Spl serine proteases have been shown to experience reduced expression levels in both genetic mutants in comparison to the wildtype, respectively. However, a higher degree of reduction has been observed for *clpP* mutants additionally in a direct comparison of both mutants, indicating that the expression of the majority of the Spl serine proteases depends on a higher level on ClpP rather than on ClpX. The same observation has been made for the hemolysins.

The highest depletion in the comparison of Δ*clpP* against Δ*clpX* has been observed for SdrD. The protein has already been observed upregulated in the *clpX* deletion mutant in comparison to the wildtype and - more strikingly – highly dependent on the presence of ClpP regardless its functional state. A direct link between SdrD and the ClpP machinery could not be found, however it is known that the ArlRS-MgrA cascade is involved in SdrD expression.[319] In reverse, MgrA expression was observed downregulated in *clpP* deletion strain in whole proteome analysis here. Therefore, decreased SdrD expression might go in hand with reduced expression of MgrA. Nevertheless, the reason for altered SdrD expression levels depending on the sole physiological presence of ClpP cannot be explained therewith.

Table 16: Significantly upregulated (log_2 ratio < -1, $-log_{10}$ t-test p-value > 1.3) proteins in Δ*clpX* mutants in comparison to the Δ*clpP*. Proteins were categorized according to their KEGG and GO assessment as analyzed by Perseus.

Gene name	Uniprot ID	log_2 ratio *ΔclpP/ΔclpX*	$-log_{10}$ *t*-test *p*-value
Cell wall associated proteins			
atl	Q2FZK7	-1.08	4.54
ftsY	Q2FZ48	-1.22	1.35
Hemolysins			
hlb	Q2FWP1	-2.88	4.45
hld	Q2FWM8	-3.18	3.74
hlgC	Q2FVK2	-1.95	3.08
SAOUHSC_02708	Q2FVK3	-2.80	2.40
Host-pathogen interactions			
sdrD	Q2G0L4	-4.38	7.31
Staphopain			
sspP	Q2G2R8	-1.81	2.67
Spl serine proteases			
splA	Q2FXC2	-2.50	5.47
splB	Q2FXC3	-1.53	3.70
splC	Q2FXC4	-2.90	5.32

splD	Q2FXC5	-1.09	3.41
splE	Q2FXC7	-2.45	2.38
Others			
lip2	Q2G155	-1.13	2.32
lipA	Q2FUU5	-1.14	3.88
SAOUHSC_02466	Q2FW51	-1.55	4.98
SAOUHSC_02650	Q2FVQ2	-1.06	4.81

2.2.4.5.2. Secreted proteins upregulated in *ΔclpX* mutant in comparison to *ΔclpP* mutant

Elevated protein levels observed in Δ*clpP* mutants in comparison to Δ*clpX* (Table 17) potentially stem from impaired ClpCP activity. Furthermore, these elevated levels might derive from ClpX activity, functioning independently of ClpP in certain pathways. Therefore, and as outlined in Chapter 2.3.5., upregulated proteins in this experiment cannot necessarily be classified as ClpCP substrates or ClpCP dependent proteins, as various secondary effects can lead to an elevated expression of these proteins.

Strikingly, five proteins of the iron-regulated surface determinant system (Isd) display elevated protein levels in the medium of Δ*clpP* mutants in comparison to Δ*clpX* mutants with IsdH being strongly upregulated. IsdH additionally displayed elevated expression levels in Δ*clpX* mutants relatively to the wildtype. Controlling function of the Clp machinery over the Isd system is known, however the observations made here stand in contrast to findings reported in literature. For IsdB a decreased expression for Δ*clpP* and Δ*clpX* mutants was reported, whereas a *clpC* inactivation led to increased levels of the protein.[280] As the ClpCP machinery is impaired in Δ*clpP* mutants in contrast to Δ*clpX* mutants, an increased expression of IsdB would be in line with literature known findings. However, the general upregulation of IsdB in both genetic knockout mutants here stands in contrast to the findings reported.

Table 17: Significantly upregulated (log_2 ratio > 1, $-log_{10}$ t-test p-value > 1.3) proteins in Δ*clpP* mutants in comparison to the Δ*clpX*. Proteins were categorized according to their KEGG and GO assessment as analyzed by Perseus.

Gene name	Uniprot ID	log_2 ratio Δ*clpP*/Δ*clpX*	$-log_{10}$ *t*-test *p*-value
Adhesion proteins			
ebh	Q2FYJ6	3.72	2.98
SAOUHSC_01114	Q2FZB8	1.33	3.48
sdrC	Q2G0L5	1.06	4.83
Cell wall associated/WalKR			
lytM	O33599	1.58	4.10
lytN	Q9ZNI1	1.00	5.39
Host-pathogen interactions			
spa	P02976	2.19	6.13
Iron Uptake			
isdA	Q2FZE9	1.69	6.54
isdB	Q2FZF0	2.30	2.66
isdC	Q8KQR1	2.28	1.94
isdE	Q2FZE6	3.15	9.16
isdH	Q2FXJ2	5.61	12.00
Others			
SAOUHSC_00325	Q2G131	2.69	3.56
SAOUHSC_00399	Q2G0X4	1.13	3.84
SAOUHSC_01676	Q2FXZ9	1.38	3.61
SAOUHSC_02404	Q2FW95	1.13	5.08

Interestingly, SdrC was upregulated in Δ*clpP* mutants, whereas SdrD was upregulated in Δ*clpX* mutants. Both, SdrC and SdrD have been upregulated in *clpX* deletion mutants in comparison to the wildtype, and SdrD has been shown to depend solely on the presence of ClpP as it was strongly downregulated in Δ*clpP* mutants in comparison to S98A point mutants. However, reasons for these inconclusive regulation patterns are unknown.

The regulatory effect of ClpX on protein A has already been discussed earlier and it was shown that *clpX* deletion leads to decreased levels of protein A (*spa*). Elevated levels of protein A in *clpP* deletion mutant in comparison to the *clpX* deletion mutant indicate, that solely ClpX might be in control of protein A expression via a ClpP-independent mechanism.

2.2.4.6. Summary of the Secretome analysis

In summary, altered expression levels of secreted proteins depending on genetic mutations of ClpP and ClpX have been studied.

Data analysis of the identified and quantified proteins in the medium of liquid cultures used for whole proteome analysis revealed a significant number of altered intracellular proteins. Several reasons therefore have been discussed and it can be concluded that the workflow has to be further optimized to reduce the number of intracellular proteins during sample preparation. Nevertheless, proteins with a GO annotation "extracellular region" and "plasma membrane" have been studied to identify ClpX and ClpP dependent changes in secreted proteins and cell-surface mediating proteins.

In contrast to the conducted whole proteome analysis, PCA analysis revealed clustering of all genetic mutants apart from the wildtype. Therefore indicating that in case of the proteins measured in the secretome analysis, all mutants exhibit a comparable expression pattern with slight modulations. As revealed by the loading plot of the conducted principal component analysis and in direct comparison of the mutants to wildtype, SceD was extremely upregulated in all mutants in comparison to the wildtype.

The impact of ClpP on biofilm formation is well known and in line therewith, deletion of *clpP* led to a significant dysregulation of cell adhesion proteins besides the regulation of hemolysins and secreted serine proteases. ClpP is also known to regulate iron acquiring systems[280,320], *e.g.* Isd system, and in line therewith altered expression levels in the secreted proteome have been detected. However in case of IsdB, results were contrary to reported findings.[280]

ClpX and *clpP* deletion share a majority of up- and downregulated proteins in comparison to the wildtype, indicating that ClpX holds an important role in virulence processes in cooperation with ClpP but also *via* ClpP-independent pathways. One example for a ClpP-independent regulation is the control of protein A translation.

Of particular interest are the changes in expression levels revealed in a comparison of Δ*clpP* mutant and S98A ClpP point mutant. In line with the whole proteome analysis, several proteins have been identified with altered expression levels solely depending on the presence of ClpP independently from its proteolytic function. Protein SdrD and β-hemolysin displayed the highest dependency on the presence of ClpP. However, the reasons for these findings are ambiguous and could be further investigated in further experiments.

In general, the applied secretome analysis delivered a comprehensive comparison of dysregulated secreted proteins depending on ClpP and ClpX in *S. aureus*. A large majority of altered proteins have already been described in literature, therefore confirming the applicability of the performed experiments to identify ClpP and ClpX dependent proteomic changes. The findings presented here might provide a starting point for further molecular biological studies to decipher the unknown - potentially ClpP/X dependent – pathways which lead to these dysregulations.

2.2.5 Metabolomics studies on Clp genetic mutants

As already mentioned, numerous enzymes, participating in metabolic pathways, *e.g.* purine and pyrimidine biosynthesis, have been identified dysregulated in the studied genetic mutants in comparison to the wildtype control strain. Therefore, an untargeted metabolomics experiment has been conducted to measure metabolic changes among the genetic Clp mutants relatively to the wildtype control.

Metabolomics belongs to the -omics disciplines namely genomics, transcriptomics, proteomics and metabolomics and focusses on the characterization and quantification of small molecular compounds, *e.g.* metabolites and metabolic intermediates, within diverse biological matrices [*e.g.* entire cells, tissue and biofluids (urine, blood, etc.)]. Even though depicting a relatively new discipline within the -omics field, metabolomics is widely applied in diverse fields, *e.g.* biomarker discovery[321,322], doping control[323], drug development (tracking of metabolic conversion of drug under study)[322], as well as the characterization of enzymes of unkown function in reduced settings, *e.g.* bacterial and mammalian cell culture[324] .

Most commonly used analytical techniques in metabolomics are nuclear magnetic resonance (NMR), gas chromatography coupled mass spectrometry (GC-MS) and liquid chromatography coupled to mass spectrometry (LC-MS). In part due to its high sensitivity and reduced sample preparation need, LC-MS depicts the most widely applied analytical method in metabolomics today.[325-327]

Workflows carried out in metabolomics can be divided into targeted and non-targeted approaches Targeted metabolomics focuses on the quantification of a single metabolite or a subset of metabolites, which are often linked to a certain phenotype. As the compounds of interest are known, the utilized method can be optimized regarding source parameters (*e.g.* spray voltage, lenses and quadrupoles) to enhance the selectivity for these specific metabolites using authentic chemical standards. With tailored compound-specific methods in hand, phenotype-based changes of these small molecules can be quantified in an absolute manner.[328]

In contrast, non-targeted metabolomics depicts an unbiased method to measure a maximum possible number of metabolic features (ions characterized by a pair of unique *m/z* values and unique retention times) within a single measurement, and global changes in the metabolic profile based on a phenotype are elucidated. If identified, significantly

changing metabolic features can be linked to a database entry. The retention time and MS/MS spectra of the metabolic feature and an authentic chemical standard are compared and thereby the metabolic feature characterized. If no database entry matches the identified metabolic feature, further structure elucidation experiments, *e.g.* MS^n fragmentation experiments, have to be conducted in subsequent analytical runs.[328]

Great advancements have been made in the recent years, increasing the sensitivity and speed of applied mass spectrometers as well as the resolving power of utilized HPLC and UPLC systems. Additionally, bioinformatic tools, *e.g.* XCMS, MetAlign, MetaboAnalyst, Progenisis IQ and Compound Discoverer opened doors also for scientists with a non-bioinformatic background to analyze untargeted data. However, non-targeted metabolomic studies still face high hurdles to overcome in order to decipher phenotype-relevant metabolic profiles and changes.

Metabolites are often isolated from respective biological matrices applying liquid-liquid extraction (LLE) or solid-phase extraction (SPE) methods. Both methods have their advantages and disadvantages, however their common drawback is a certain degree of bias introduced into sample preparation. Solvents applied in liquid-liquid extractions are more suitable for a certain subset of metabolites, while discriminating other compound classes. The problem occurs in SPE as the utilized solid phases retain certain compound classes better than others.[329]

The next step after sample preparation, sample measurement, adds diverse possibilities to the workflow. Numerous columns with different retention mechanisms, *e.g.* C18, C8, HILIC and ZIC-HILIC can be utilized for the chromatographic separation of extracted metabolites exhibiting better separation for non-polar (C18, C8) or polar substances (HIILC, ZIC-HILIC).

Finally, selected source parameters and general MS-parameters are not able to deliver optimal ionization, fragmentation and isolation conditions for all extracted substances. Therefore, certain compound classes might be favored during the ionization process, discriminating other compound classes therefore making a comprehensive measurement of all metabolites at the same time impossible.

Additional pitfalls are present in the data analysis process. Data analysis pipelines are more and more convenient to utilize, also for users with limited bioinformatic background, and related data bases with compound entities such as METLIN[330] and HMDB[331] are continuously increasing. However, their entities do by far not cover the entire human metabolome. Metabolome coverage is even less extended for other organisms such as yeast

(YMDB[332]) and *E. coli* (ECMDB[333]). For other organisms, *e.g. Staphylococcus aureus*, databases do not exist at all, hindering an efficient metabolite identification.

2.2.5.1. Global changes observed in the metabolome due to introduced mutations

For the untargeted metabolic comparison of *S. aureus* genetic mutant strains relatively to the wildtype, samples were collected simultaneously to the conducted whole proteome data, enabling a direct correlation of both datasets. As mainly primary metabolic pathways, involved in the biosynthesis of polar metabolites have been affected by the genetic mutations, a polar extraction solvent (80% MeOH (aq.) was utilized for the extraction procedure. Extracted metabolites were separated on a HILIC column prior to MS measurements, as these columns are especially suitable for the retention of polar compounds.

Pelleted bacterial samples were washed with cold 0.9% NaCl solution to remove residual medium, and were subsequently lysed in 80% MeOH (aq.), followed by incubation at -20 °C overnight to ensure complete protein precipitation. Aggregated proteins were removed by centrifugation and resulting supernatants dried *in vacuo*. Samples were reconstituted in H_2O/ACN 1:1, centrifuged and resulting supernatant transferred into LC-MS vials. A pooled sample was prepared, serving for data-dependent acquisition MS^2 (DDA MS^2) fragmentation experiments and as quality control to check for measurement reproducibility across all runs. Samples were measured in positive and negative mode.

As already mentioned, various bioanalytical pipelines are available for the data analysis of untargeted metabolomics data. In this study, Compound Discoverer™ (Version 3.0.0.294) was utilized for quantification and identification of metabolic features as well as statistical analysis.

As a tailored database for *Staphylococcus aureus* is not available, the databases for the organisms human (HMDB), *E. coli* (ECMDB), yeast (YMDB) as well as BioCyc and ChemSpace have been utilized for identification steps.

Compared to the conducted unbiased whole proteome and secretome studies, a principal component analysis was carried out in an initial data analysis step to check for reproducibility across biological replicates and to observe first global differences between compared genetic modified strains and the wildtype control (Figure 39).

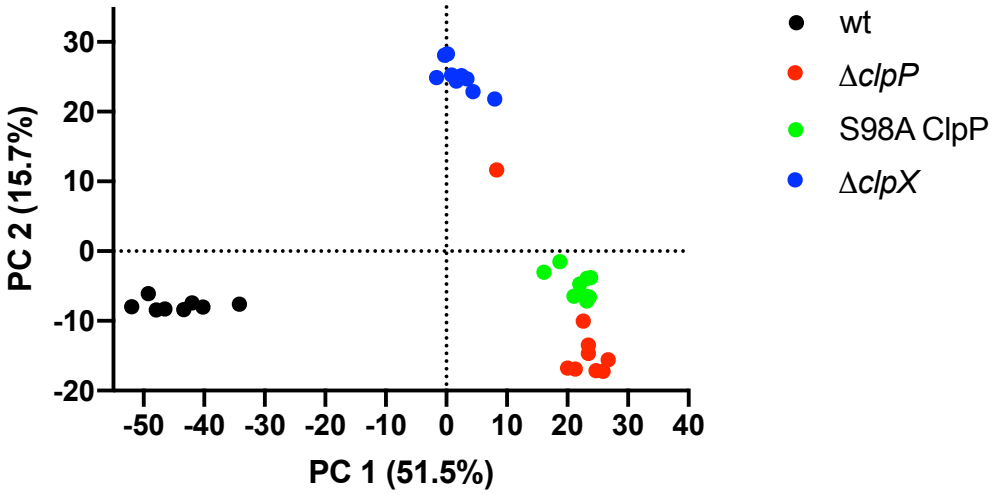

Figure 39: Principal component analysis (PCA) of genetic *S. aureus* mutants in comparison to the wildtype was conducted for a global assessment of changes in the metabolome of *S. aureus* due to conducted genetic modifications. Wildtype (black) samples cluster separated from Δ*clpX* (purple), Δ*clpP* (red) and S98A ClpP point mutant (green). Principal component analysis was conducted with Compound Discoverer and default settings.

PCA analysis revealed a dense clustering of biological replicates within each sample group (except for one outlier identified for *ΔclpP* samples), indicating a relatively high reproducibility. Samples of S98A ClpP point mutant and *ΔclpP* mutant cluster close together, in short distance to *ΔclpX* mutant and in further distance to wildtype control samples.

Therefore, the results indicate that – in line with presented proteomics data – the global difference between *clpP* deletion mutant and active site ClpP point mutant is marginal on the metabolome level. As *ΔclpX* mutant samples cluster in close yet distinct distance, it can be concluded that the global metabolic difference between genetic ClpP and ClpX mutants is present but not as significant as the difference to wildtype control. Hence, ClpP and ClpX have a significant influence on the metabolome of *S. aureus*, as expected from the observed altered metabolic enzyme in both mutants.

Strikingly, PCA analysis of the metabolome data revealed comparable results to PCA analysis results of the whole proteome and secretome analysis, indicating that genetic ClpP and ClpX mutants affect both, proteome and metabolome levels, globally in a comparable manner.

2.2.5.2 Metabolic comparison of *ΔclpP* and S98A ClpP point mutant

A student's *t*-test was carried out to identify significant changes in the measured metabolome caused by the sole presence/absence of ClpP, and results visualized in a volcano plot (Figure 40). 14 features were identified as significantly upregulated and 19 features as significantly downregulated. The identification of a reduced number of metabolic features, significantly altered in the comparison of both ClpP mutants, is in accordance with the conducted whole proteome analysis of both strains, which also revealed solely a few altered proteins.

As the conducted whole proteome analysis revealed several proteins of the pyrimidine pathways dysregulated, altered levels of the respective metabolites were also expected. The metabolic intermediates of this pathway are also shared by humans. Therefore, an identification should in theory be possible even a *Staphylococcus aureus* database was not available for the metabolomics experiments.

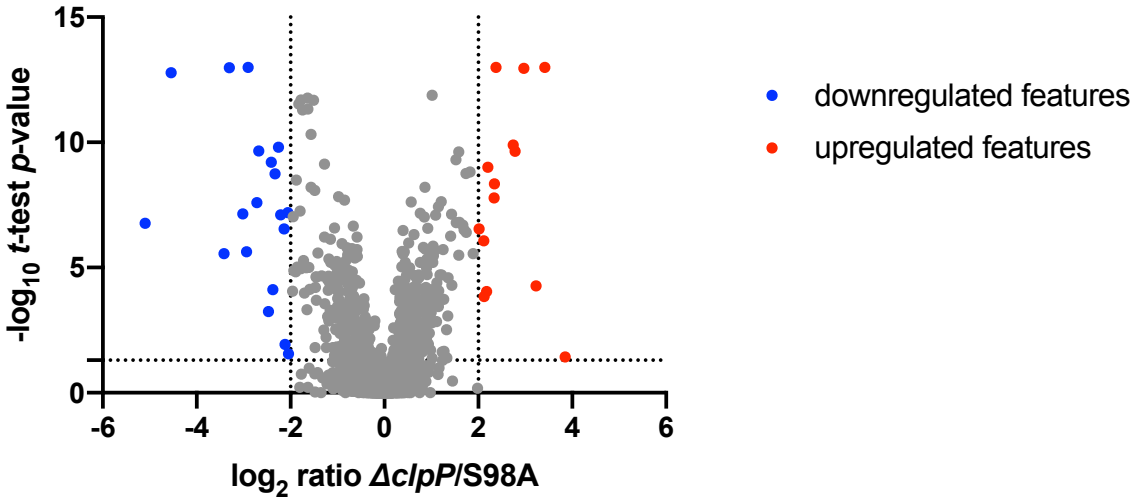

Figure 40: Untargeted metabolomics results of *S. aureus ΔclpP* compared to *S. aureus* S98A ClpP point mutant. Volcano plot represents two-sample *t*-test results of *S. aureus ΔclpP* compared to *S. aureus S98A* ClpP point mutant (n=9). Cutoff criteria were defined as $\log_2 = \pm 2$ (4-fold change in feature intensity) and $-\log_{10}$ (*t*-test *p*-value) = 1.3 (dotted lines). Features highlighted in blue were observed downregulated in the knockout mutant in comparison to the point mutant. Features highlighted in red were identified as upregulated.

Data analysis revealed significantly dysregulated features (Table 18) and respective chemical formulas could be predicted for these dysregulated features. However, MS/MS spectra could only be found in the QC samples utilized for DDA-MS/MS identification runs for three out of 33 metabolite features (marked in Table 17, MS/MS spectra in the appendix). As the spectra could not be matched to MS/MS spectra in the used databases and for most features MS/MS spectra were not provided by DDA fragmentation

experiments, an identification process at this stage of these features is impossible. In-depth MS/MS fragmentation spectra obtained in additional targeted experiments for these dysregulated features would be required to extract biological meaningful information.

Table 18: Significantly dysregulated metabolic features in *ΔclpP* deletion mutant in comparison to S98A ClpP point mutant. Statistical analysis of significantly altered metabolic features, as well as the prediction of chemical composition, was carried out using Compound Discoverer.

Feature $[M+H]^+$	Predicted chemical formula	log_2 ratio Δ*clpP*/S98A	$-log_{10}$ *t*-test *p*-value
Upregulated			
362.17087	$C_{19}H_{19}N_7O$	2.20	9.00
430.30240	$C_{20}H_{39}N_5O_5$	3.85	1.43
326.17139	$C_{15}H_{23}N_3O_5$	2.12	3.85
473.15054	$C_{18}H_{24}N_4O_{11}$	2.34	8.34
315.16580	$C_{12}H_{26}O_9$	2.38	13.00
491.16110	$C_{12}H_{27}N_8O_{11}P$	2.34	7.80
*271.07254**	$C_7H_{10}N_8O_2S$	2.02	6.54
398.14938	$C_{15}H_{27}NO_9S$	2.18	4.04
279.06467	$C_9H_{14}N_2O_6S$	2.97	12.96
445.16107	$C_{17}H_{31}N_6P_3S$	3.23	4.27
495.13229	$C_{16}H_{33}O_{11}P_3$	2.74	9.89
249.09061	$C_9H_{16}N_2O_4S$	2.12	6.07
455.13989	$C_{20}H_{29}N_2O_4P_3$	2.79	9.64
290.17123	$C_{13}H_{19}N_7O$	3.42	13.00
Downregulated			
257.07452	$C_6H_8N_8O_4$	-3.42	5.55
677.27478	$C_{24}H_{41}N_{10}O_{11}P$	-2.72	7.59
430.22351	$C_{24}H_{31}NO_6$	-5.10	3.39
546.27661	$C_{25}H_{46}N_3O_4P_3$	-2.38	6.77
217.11795	$C_9H_{16}N_2O_4$	-2.47	3.27
324.19116	$C_{16}H_{25}N_3O_4$	-2.33	8.74
267.09747	$C_{12}H_{14}N_2O_5$	-2.91	13.00
*330.12967**	$C_7H_{20}N_7O_6P$	-2.68	9.66
554.31812	$C_{24}H_{48}N_3O_9P$	-2.12	1.92
422.15881	$C_{14}H_{30}N_7P_3S$	-2.41	9.21
204.04402	$C_6H_9N_3O_3S$	-2.05	7.19
290.17120	$C_{12}H_{23}N_3O_5$	-2.21	7.11
298.99039	$C_6H_7N_2O_{10}P$	-3.02	7.15
*347.01410**	$C_6H_{12}N_4O_9P_2$	-2.94	5.64
329.17099	$C_9H_{25}N_6O_5P$	-2.14	6.54
311.16052	$C_{10}H_{19}N_{10}P$	-2.04	1.57
120.04420	C_7H_5NO	-3.30	13.00

2.2.5.3. Putatively identified metabolites dysregulated across genetic Clp mutants

Statistical analysis using a student's *t*-test revealed hundreds of metabolic features up- and downregulated in the comparisons of the genetic mutants relatively to the wildtype. However, due to missing databases and low numbers of MS/MS spectra assignments, mapping of detected metabolic features to known metabolites has been hindered greatly.

In order to extract meaningful biological data from the untargeted metabolomics experiment despite mentioned hurdles, the obtained data was filtered for metabolic features with an assigned MS/MS spectrum and a full match for mzCloud search. 34 metabolic features met the filtering requirements and fold change as well as significance have been evaluated using a student's *t*-test for reported comparisons (Table 19). Intensities of the putatively identified metabolites across sample groups have been analyzed and visualized using Box-Whisker plots (Figure 41).

It should be noted, that mapping of metabolic features to an actual metabolite is only valid, if high-resolution *m/z* values, corresponding MS/MS spectra and the chromatographic retention time match to an authentic chemical standard, measured on the very same system. Therefore, assignments based exclusively on high-resolution MS-data and corresponding MS^2 fragment patterns are not sufficient to identify a metabolite for certain. Nevertheless, the acquired data provides important information on the putative metabolite for biological interpretation, but have to be validated in further comparative measurements with the respective chemical standard.

The majority of the 35 putatively identified metabolic features, meeting all mentioned requirements, correspond to amino acids as well as nucleotides. Notably, these findings are in line with the identified dysregulated metabolic pathways in genetic Clp machinery mutants (purine/pyrimidine as well as amino acid metabolism).

Some of the identified metabolites are listed multiple times (Table 18). The reason is, that two metabolic features with different retention times have very similar high-resolution *m/z* values as well as MS/MS spectra, matching to the same database entry. In order to identify which of these metabolic features actually represents the assigned metabolite, authentic chemical standards have to be measured with the same analytical method.

Most of the putatively identified amino acids and nucleotides exhibit decreased levels in all mutants relatively to the wildtype. Strikingly, in most cases metabolite levels

exhibited a stronger dysregulation upon genetic ClpP mutation than in case of ClpX relatively to the wildtype control.

As already mentioned, the assignment of metabolic features is of putative nature, and therefore further MS-based validation experiments have to be conducted. In a first approach *m/z* values, MS^2 fragmentation patterns and retention times of authentic chemical standards have to be mapped to the mentioned dysregulated putative metabolites for valid validation. Furthermore, these authentic standards could be used to develop a targeted method tailored for the sensitive detection of amino acids and nucleotides in order to confirm the findings of the untargeted approach in an independent experimental setting. A method specified for the detection of amino acids and nucleotides might enhance the coverage of these compound classes, leading to the identification of further metabolites of these compound classes with altered levels.

Table 19: Metabolites putatively identified using Compound Discoverer (Version 3.0.094) by searching for high-resolution m/z value and MS/MS spectra match in stated databases. Metabolites were tested for significant change in two sample comparison via student's test in Compound Discoverer for stated two sample comparisons.

	Δ *clpP* vs wt		Δ *clpX* vs wt		S98A vs wt		Δ *clpP* vs S98A		Δ *clpP* vs Δ *clpX*	
Metabolite	**Log_2 ratio Δ *clpP*/wt**	**$-\log_{10}$ *t*-test *p*-value**	**Log_2 ratio Δ *clpX*/wt**	**$-\log_{10}$ *t*-test *p*-value**	**$\log_2$ ratio S98A/wt**	**$-\log_{10}$ *t*-test *p*-value**	**$\log_2$ ratio Δ *clpP*/S98A**	**$-\log_{10}$ *t*-test *p*-value**	**$\log_2$ ratio Δ *clpP* /Δ *clpX***	**$-\log_{10}$ *t*-test *p*-value**
Amino acids										
α-Aspartylphenylalanine	-4.31	7.98	-1.28	3.98	-2.42	6.06	-1.89	-0.17	-3.02	4.79
1-Aminocyclohexanecarboxylic acid	-1.28	8.00	-1.00	6.87	-1.61	8.00	0.33	1.75	-0.28	2.96
Arginine	-1.62	3.83	-1.29	1.23	-1.7	4.76	0.08	0.08	-0.33	0.85
Aspartic acid	-2.37	1.93	-0.95	1.21	-2.37	2.04	0	0.00	-1.42	3.68
Carnitine	-0.42	0.35	0.19	0.48	-0.38	0.42	-0.04	0.00	-0.61	1.84
Glutamic acid	-0.71	0.53	0.16	0.24	-0.58	0.46	-0.14	0.00	-0.87	1.68
Histidine	-0.82	7.17	-0.28	0.06	-0.62	5.73	-0.2	0.37	-0.54	1.79
Isoleucine	-1.68	8.00	-0.7	2.13	-1.57	8.00	-0.11	0.36	-0.98	6.29
Methionine	-1.5	7.78	-0.9	1.59	-1.2	5.95	-0.3	1.01	-0.61	0.60
Methionine	-0.78	0.82	0.12	0.02	-0.51	1.31	-0.27	0.02	-0.9	0.42
N-α-Acetyl-arginine	-1.47	7.29	-1.26	5.56	-1.44	7.47	-0.03	0.00	-0.21	0.58
N-Acetylornithine	-1.72	8.00	-0.7	1.79	-1.67	8.00	-0.05	0.12	-1.01	5.96
Norleucine	-3.58	7.28	-2.4	2.03	-3.08	4.44	-0.5	1.53	-1.17	4.00
Norleucine	-4.08	7.97	-2.85	4.95	-3	5.31	-1.08	3.16	-1.22	3.57
Phenylalanine	-1.63	2.28	-0.9	2.88	-1.44	1.98	-0.19	0.00	-0.73	2.22
Phenylalanine	-3.38	8.00	-1.2	3.29	-3.34	8.00	-0.03	0.00	-2.17	7.97
Phenylalanine	-0.74	7.10	-0.41	0.15	-0.68	3.92	-0.06	1.77	-0.33	0.62
Pipecolic acid	0.07	0.12	-0.06	0.04	-0.13	0.60	0.19	1.45	0.13	0.44
Pipecolic acid	-2.32	1.13	-1.44	3.84	-2.82	2.94	0.5	0.35	-0.88	0.56
Threonine	-1.01	1.32	-0.69	3.94	-1.02	2.03	0	0.03	-0.33	0.61

Nucleotides											
2'-Deoxyadenosine	-0.63	4.74	-1.64	5.85	-1.16	1.93	0.53	0.52	1.01	-0.66	
5'-S-Methyl-5'-thioadenosine	0.7	0.87	0.36	2.02	-0.07	0.15	0.77	3.17	0.34	1.75	
Adenine	-0.85	2.09	-0.98	3.45	-0.76	0.55	-0.09	0.22	0.13	0.19	
Adenine	0.68	2.27	0.34	0.92	0.06	0.00	0.62	2.47	0.34	0.25	
Adenosine	-0.89	2.00	-0.86	2.75	-0.78	0.59	-0.11	0.18	-0.03	0.04	
Cytidine	-1.86	0.00	-0.63	1.05	-0.98	2.50	-0.87	0.70	-1.23	2.02	
Cytidine 5'-monophosphate	-1.38	0.09	-0.06	0.07	-0.55	0.51	-0.83	2.89	-1.32	1.10	
Guanine	-1.85	8.00	-0.96	3.68	-1.57	7.98	-0.28	0.45	-0.88	2.34	
Indole-3-acrylic acid	-3.22	6.58	-2.45	4.06	-3.95	7.96	0.73	1.35	-0.77	1.96	
Others											
1-Aminocyclohexanecarboxylic acid	-1.28	8.00	-1	6.87	-1.61	8.00	0.33	1.75	-0.28	2.96	
2-Hydroxycinnamic acid	-2.22	6.77	-1.11	-0.54	-2.73	7.98	0.51	1.47	-1.11	0.83	
Acetylcholine	-1.7	3.46	-1	0.02	-2.11	4.66	0.4	0.16	-0.71	2.32	
Choline	-2.87	8.00	-1.94	5.55	-2.68	8.97	-0.19	0.32	-0.93	0.61	
N-Acetyl-D-penicillamine	-0.86	3.34	-0.15	0.42	-0.59	0.27	-0.26	1.15	-0.71	1.43	
Thiamine	-0.35	0.26	-1.35	-0.68	-1.22	3.35	0.87	1.78	1.01	2.67	

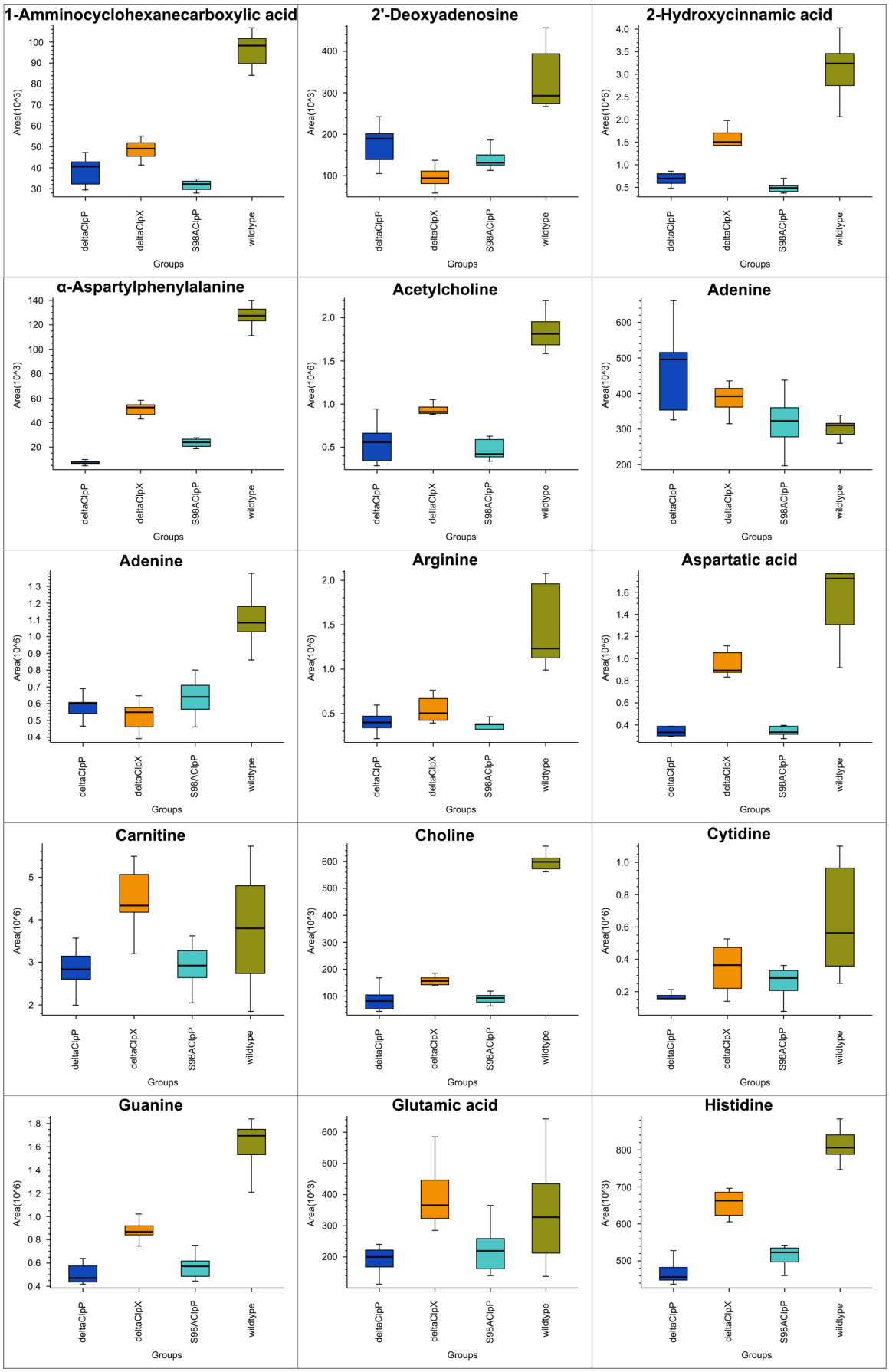

Figure 41: Box-Whisker plots of putatively identified metabolites, visualizing measured intensities across all samples per group, as calculated using Compound Discoverer. Figure is continued on the next page.

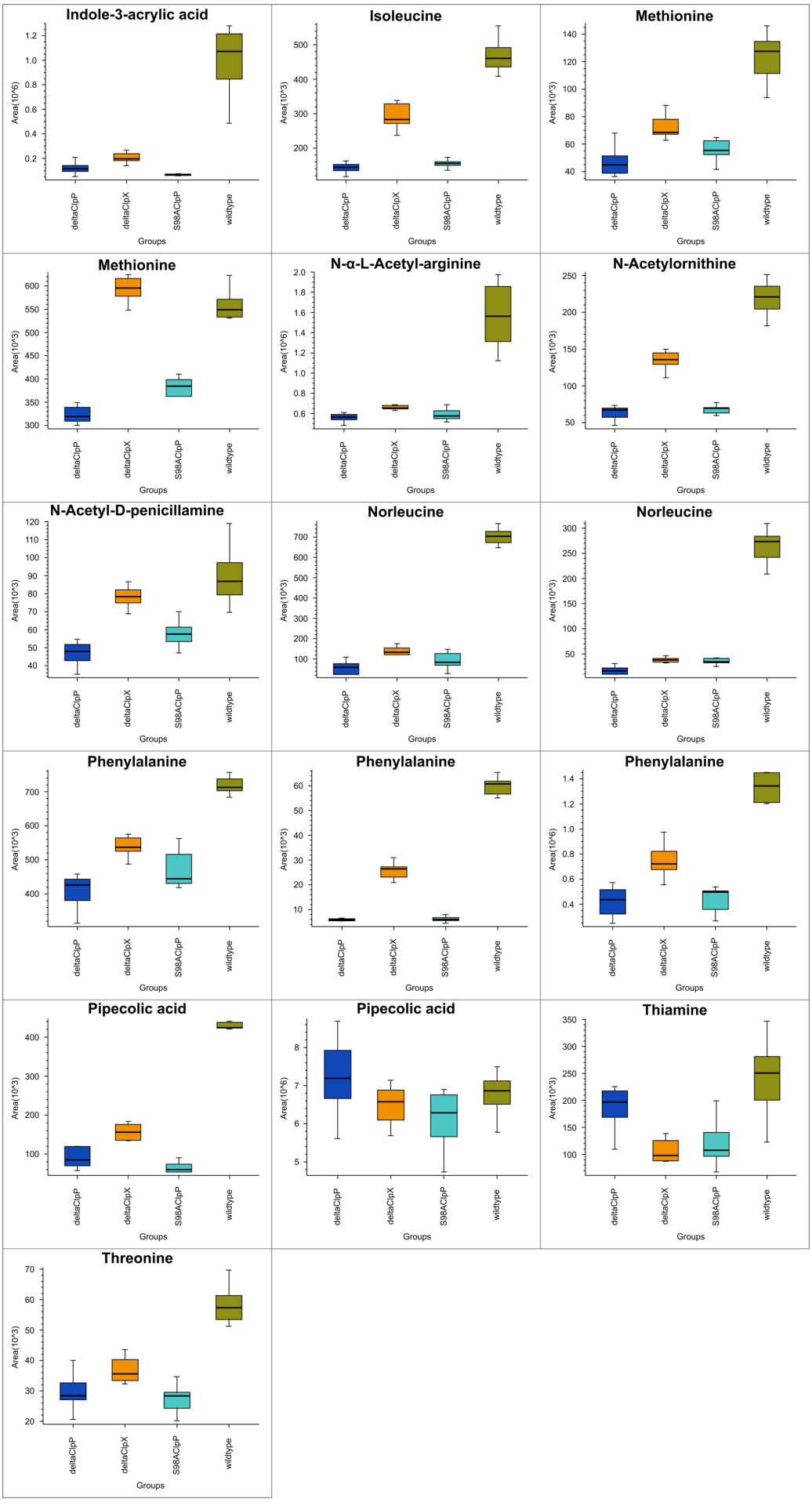
Indole-3-acrylic acid
Area(10^6)
Isoleucine
Area(10^3)
Methionine
Area(10^3)
Methionine
Area(10^3)
N-α-L-Acetyl-arginine
Area(10^6)
N-Acetylornithine
Area(10^3)
N-Acetyl-D-penicillamine
Area(10^3)
Norleucine
Area(10^3)
Norleucine
Area(10^3)
Phenylalanine
Area(10^3)
Phenylalanine
Area(10^3)
Phenylalanine
Area(10^6)
Pipecolic acid
Area(10^3)
Pipecolic acid
Area(10^6)
Thiamine
Area(10^3)
Threonine
Area(10^3)
deltaClpP
deltaClpX
S98AClpP
wildtype
Groups

2.3. Summary and Outlook

In summary, proteomics and metabolomics approaches were applied to impartially investigate the influence of genetic mutations of the ClpXP machinery on the intracellular proteome, the excreted secretome as well as intracellular metabolites. Therefore, a markerless *S. aureus clpX* deletion mutant was generated, and utilized in a comparative setting with a markerless clpP deletion mutant and an active site S98A ClpP mutant in comparison to *S. aureus* wildtype control.

Unbiased studies using *S. aureus* ClpP and ClpP mutant strains to decipher the global impact of these proteins on cellular pathways and specific proteins have already been reported in literature, comparing gene expression levels relatively to the wildtype. In the study presented here, a comparable analysis on the proteome level has been conducted. A strong correlation between literature reported altered pathways and the results of the proteomics experiments presented here validated the conducted workflow.

Deletion of *clpP* and *clpX* genes revealed an extensive influence on protein expression levels in the intracellular and extracellular region, leading to altered protein levels of several hundred proteins. The complexity of the observed dysregulation has been conducted by generating correlation networks of these dysregulated proteins using STRING, GO terms as well as KEGG pathways assignments. Observed protein clusters have been discussed in the whole proteome and secretome section. Strikingly, analysis of proteins with altered expression levels depending on the sole presence/absence of ClpP by comparison of expression levels of *clpP* deletion mutants with S98A ClpP point mutants exhibited two distinct pathways affected, namely iron homeostasis and purine/pyrimidine biosynthesis. In addition to metabolic pathways, proteins involved in virulence and cell wall biosynthesis have been observed dysregulated in whole proteome and secretome analysis.

In addition to conducted proteomics experiments, an untargeted metabolomics study has been carried out. Identified, dysregulated metabolites could be linked to altered metabolic pathways identified in the whole proteome analysis. Even though these findings have to be validated in further experiments, the results provide a promising starting point for in-depth metabolic studies. Here, putatively identified metabolites could be verified using authentic chemical standards. In addition, metabolic features displaying significant altered concentration levels in *ΔclpP* mutant relatively to the S98A ClpP point mutant

could be subjected to in-depth structure analysis using MS^n fragmentation experiments to illuminate respective chemical structures. Finally, application of other extraction solvents and columns might uncover additional metabolites significantly altered in the utilized *S. aureus* mutant strains and therefore provide more insights into the metabolome affected by these genetic mutations.

The comparative analysis was carried out with planktonic *S. aureus* cultures in the early stationary phase. However, as expression of virulence factors greatly differs between *S. aureus* in planktonic state and colonized in biofilms, an evaluation of the whole proteome and secretome of *S. aureus* isolated from biofilms would depict an interesting complementary approach, and new insight into the influence of ClpP and ClpX could be gained thereby.

3. Experimental part

3.1. Experimental part for Chapter I

3.1.1. Chemical synthesis

General remarks

Chemical reagents and solvents used for chemical synthesis were purchased in reagent grade or higher purity from *Alfa-Aesar, AppliChem, Acros Organics, Sigma-Aldrich, TCI Europe* or *Merck* and were used without further purification. 2-(3-But-3-ynyl-3H-diazirin-3-yl)-ethanol was purchased from *Ark Pharm Inc*.

Flash column chromatography as performed on silica gel (Geduran Si 60, 40-63 µm, *Merck*), and elution solvents distilled pior to use. Analytical thin-layer chromatography was performed on aluminium-baked TLC Silica gel 60 F254 plates (*Merck*) and analytes visualized by UV detection at 254 nm or stained via aq. $KMNO_4$. Synthesized compounds were dissolved in $CDCl_3$ (*Sigma-Aldrich*) for NMR measurements.

LC-ESI-HR-MS analysis of the compounds was carried out using an Thermo Finnigan LTQ FT-ICR (*Thermo Finnigan*) mass spectrometer (R = 100,000, profile mode), equipped with a Dionex Ultimate 3000 HPLC (*Dionex*). HPLC separation was accomplished with a XBridge C18 column (3.5 µm, 4.6 x 100 mm, *Waters*) at a column temperature set to 30°C. Mobile phases used for separation were 0.1% (v/v) formic acid in H_2O (*Sigma-Aldrich*, HPLC-grade) (A) and 90:10 MeCN:H_2O (*Sigma-Aldrich*, HPLC-grade) and 0.1% (v/v) formic acid (B). Gradient (flowrate 1.1 mL/min) applied: in 10 min from 20 to 98% B, kept for 4 min at 98% prior to column equilibration at 20% B for 4 min.
Fragmentation spectra of **VioA** and **VioA-P** were recorded on an LTQ Orbitrap XL (R = 30,000) in positive mode. Molecules were fragmented using normalized collision energy (NCE) = 35 with wideband activation switched on.

3.1.1.1. Synthesis of 2-(3-(but-3-yn-1-yl)-3H-diazirin-3-yl)acetic acid

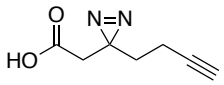

$C_7H_8N_2O_2$

152.15 g/mol

To a stirred solution of 2-(3-But-3-ynyl-3H-diazirin-3-yl)-ethanol (99 mg, 0.73 mmol, 1 eq.) in acetone (6 mL) at 0°C Jones reagent (2 M CrO_3 in H_2SO_4 (aq), 1.43 mL, 2.9 mmol , 4 eq.)was added dropwise. The reaction solution was allowed to gain room temperature and stirred for 2 h. Subsequently, the reaction was quenched with 70% isopropanol (10 mL) and filtrated over kieselgur. The filter cake was washed with acetone (3x10 mL) and the filtrate dried over $MgSO_4$, concentrated *in vacuo* and purified using flash chromatography on silica gel (hexane/ethyl acetate 4:1 + 2% acetic acid) to give minimalist photocrosslinker acid (88 mg, 0.57 mmol, 79%) as a yellowish oil.
Spectral data are consistent with those published previously.[145]

TLC (Hex/EtOAc = 4/1 + 2% acetic acid): R_f = 0.32 [UV | KMnO4]. **^{1}H NMR** (400 MHz, $CDCl_3$): δ [ppm] = 10.94 (s, 1H), 2.40 (s, 2H), 2.05 (td, *J* = 7.3, 2.6 Hz, 2H), 2.00 (t, *J* = 2.6 Hz, 1H), 1. (t, *J* = 7.3 Hz, 2H). **^{13}C NMR** (100 MHz, $CDCl_3$): δ [ppm] = 175.9, 82.5, 69.7, 39.6, 32.0, 25.3, 13.3. **ESI-HR-MS** (m/z): 303.10979 $[2M-H]^-$ calc. 303.11320

3.1.1.2. Synthesis VioA-P

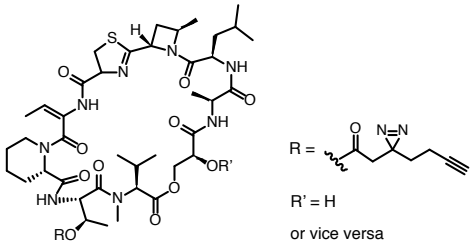

$C_{47}H_{68}N_{10}O_{12}S$

997.18 g/mol

A solution of minimalist photocrosslinker acid (7.76 mg, 51.02 µmol, 2 eq.), DMAP (156.1 µg, 1.28 µmol, 5 mol%.), and DCC (10.53 mg, 51.02 µmol, 2 eq.) in DCM (160 µL) was cooled to 0°C. **VioA** (22 mg, 25.51 µmol, 1 eq.) was dissolved in dichloromethane (200 µL) and added slowly to the solution. The reaction mixture was stirred for 4 h at 0°C and was allowed to gain room temperature overnight. Next, the solution was concentrated *in vacuo* and purified by silica gel chromatography using EtOAc/MeOH 9:1 to give **VioA-P** (7.6 mg, 7.62 µmol, 30%) as a colorless solid.

TLC (EtOAc/MeOH = 9/1): R_f = 0.37 [UV | KMnO4]. **ESI-HR-MS** positive mode (m/z): 997.48034 $[M+H]^+$ (calc. 997.48116) **HPLC analysis** A = 100% H_2O 0.1% FA; B = 90% MeCN 10% H_2O 0.1% FA, Gradient: T_0 : B = 20% T_{10} = 98% Retention time: 8.05 min.

3.1.2. Biochemistry

3.1.2.1. Cell culture

Cell lines for biological assays

Cells for biochemical assays were handeled by Christina Orgler in the laboratory of Prof. Dr. Angelika M. Vollmar (Ludwig-Maximilian Universität München)

Jurkat cells were provided by P.H. Krammer (*Heidelberg, Germany*) and cultured in RPMI 1640 (*PAN Biotech*) containing FBS 10% (*Sigma Aldrich*), pyruvate 1mM (*Merck*) and penicillin/streptomycin (P/S) (*PAN Biotech*) for biochemical assays conducted by Christina Orgler in the laboratories of Prof. Angelika M. Vollmar (Ludwig-Maximilian Universität München). in CCRF-CEM cells were obtained from M. Kavallaris (*Sydney, Australia*) and cultured in RPMI 1640 containing (*PAN Biotech*) FCS 10% (*Sigma Aldrich*) and P/S (*PAN Biotech*). HeLa and T24 cells were provided by the DSMZ (Braunschweig, Germany) and cultured in DMEM (*PAN Biotech*) containing FCS 10% and P/S. HL-60 cells from ATCC (Manassas, VA, USA) were maintained in IMDM medium (*Thermo Fisher*) supplemented with FCS 20% and P/S. All cells were incubated at 37°C with 5% CO_2 at constant humidity.

Cell lines for proteomics, MTT assays and analytical AfBPP experiments.

Jurkat cells were cultured in RPMI 1640 (*Sigma Life Science*) containing 10% (v/v) fetal bovine serum (FBS) (*Sigma Aldrich*), pyruvate (1 mM final concentration, *Merck*) and L-glutamine (2 mM final concentration, *PAA*). HeLa cells were grown in Dulbecco's Modified Eagle Medium (DMEM high glucose, 4.5 g/; *Sigma Life Science*) additionally supplemented with 10% FBS and L-glutamine (2 mM final concentration, *PAA*). HeLa cells were detached with Accutase (*Thermo Fisher Scientific*). Determination of cell numbers was accomplished by mixing cell suspension with trypan blue [1:1 (v/v)], followed by counting live cells in a *Neugebauer* improved cell counting chamber. All cells were incubated at 37°C with 5% CO_2 at constant humidity. Pre-warmed sterile PBS (136.9 mM NaCl, 10.1 mM Na_2HPO_4, 2.7 mM KCl, 1.8 mM KH_2PO_4 in ddH_2O, pH 7.4) was used to wash cell between passages.

Patient-derived xenograft cells and peripheral blood mononuclear cells

Cells were exclusively handeled by Christina Orgler in the laboratory of Prof. Dr. Angelika M. Vollmar (Ludwig-Maximilian Universität München)

The preclinical mouse model for acute leukemia using patients' cells has already been described previously.[334] PDX cells were freshly isolated from the bone marrow or spleen of NOD.Cg-*Prkdc*^{scid} *Il2rg*^{tm1Wjl}/SzJ (NSG) mice and cultured in RPMI 1640 (*PAN Biotech*) containing FCS 20%, pyruvate 1mM (*Merck*) and P/S (*PAN Biotech*). Patients clinical characteristics are listed in appendix. Written informed consent was obtained from all patients. The study was performed in accordance with the ethical standards of the responsible committee on human experimentation (written approval by the Research Ethics Boards of the medical faculty of Ludwig-Maximilians-University, Munich, numbers 068-08 and 222-10) and with the Helsinki Declaration of 1975, as revised in 2000. Peripheral blood mononuclear cells were freshly isolated from EDTA- anticoagulated blood of healthy donors by gradient centrifugation using Ficoll-Paque PLUS (GE Healthcare, Chicago, IL, USA) according to manufacturer's protocol. The cells were maintained in RPMI 1640 with 2 mM glutamine and 1mM pyruvate and supplemented with 20% (v/v) FCS.

3.1.2.2. Cell viability, proliferation assays and apoptosis assays

3.1.2.2.1. Cell titer blue assay

Cells were exclusively handeled by Christina Orgler in the laboratory of Prof. Dr. Angelika M. Vollmar (Ludwig-Maximilian Universität München)

Cells were seeded into 96- well plates (5000 cells/well) and incubated for 3h. Subsequently, cells were treated with indicated compounds for 72 h. After incubation with compound, cell titer blue® (CTB) agent (*Promega*) was added to each well (volume ration 2:5) and incubated (4 h, 37°C, 5% CO_2). Fluorescence readout at 595 nm was accomplished using a SpectraFluor Plus^{TM} microplate reader (*Tecan*). As a reference value for cell number at the first day of the experiment, cells were seeded in triplicates on a separate plate and incubated with CTB. Fluorescence intensity of control samples was subtracted from recorded fluorescence of compound stimulated cells, and viable cells [%] were determined relatively to DMSO control.

3.1.2.2.2. Crystal violet assay

Cells were exclusively handeled by Christina Orgler in the laboratory of Prof. Dr. Angelika M. Vollmar (Ludwig-Maximilian Universität München).

To monitor proliferation of adherent cells, cells were seeded into 96-well plates (2500 cells/ well) and incubated for 24 h prior to treatment (72 h, 37°C, 5% CO_2) with compound or DMSO, respectively. After incubation, media was removed by suction, cells washed with PBS stained and fixed using aq. crystal violet solution (0.5% (w/v) crystal violet, 20% (v/v) MeOH) for 10 min. Stained cells were rinsed with ddH_2O and dried. Subsequently, crystal violet was reconstituted in aq. sodium citrate solution (0.1 M sodium citrate , 50% (v/v) EtOH) and absorbance measured at 540 nm using a Tecan Sunrise™ microplate reader (*Tecan*). As a reference value for cell number at the first day of the experiment, cells were seeded in triplicates on a separate plate and incubated with sodium citrate solution for 10 min. Absorbance intensity of control samples was subtracted from recorded fluorescence of compound stimulated cells, and viable cells [%] were determined relatively to DMSO control.

3.1.2.2.3. MTT assay

50 µL/well Jurkat cell suspension were seeded (16,000 cells/well) in 96-well plates (transparent Nunc round-bottomed, *Thermo Fisher Scientific*). Compound (50 µL/well, 0.1% final DMSO concentration) in varying concentrations or DMSO respectively was added in RPMI-1640 medium containing 10% (v/v) FBS in triplicates and cells incubated (37°C, 5% CO_2, 24 h). Subsequently, cells were supplemented with 3-(4,5-dimethyl-2-thiazolyl)-2,5-diphenyl-2*H*-tetrazolium bromide solution (MTT) (20 µL/well, 5 mg/mL in PBS, *Sigma Aldrich*) and incubated (37°C, 5% CO_2, 2 h). For cell lysis, triplex lysis buffer (50 µL; 10% (w/v) SDS, 0.012 M HCl, 2% (v/v) Isobutanol) was added to each well, pipetted up and down and incubated (37°C, 5% CO_2, o.n.). Absorbance at 570 nm was measured and background at 630 nm subtracted using a Tecan Infinite M200 Pro (*Tecan*). Absorbance values were normalized to absorbance of DMSO-treated samples. Sigmoidal curve fit and IC_{50} determination was achieved by using GraphPadPrism 8 (*Graphpad*)

using the "log (inhibitor) vs. response --variable slope four parameters" function. Experiments were carried out in three biological replicates in triplicates each.

3.1.2.2.4. xCELLigence assay

Experiment was conducted by Christina Orgler in the laboratory of Prof. Dr. Angelika M. Vollmar (Ludwig-Maximilians-Universität München).

Transfected HeLa cells were seeded (5000 cells/well) in equilibrated E-plates 16 (*ACEA Biosciences*). After attachment, cell response was monitored in real-time for subsequent 72 h at 37°C. Increase in impedance was measured using xCELLigence system (*Roche*) and the cell index (proportional to cell number) evaluated by the internal software. Subsequently, cell index was normalized to cell index at the time point of treatment and data further analyses using the RTCA software 2.0 (*ACEA Biosciences*).

3.1.2.2.5. Apoptosis and cell cycle analysis

Experiment was conducted by Christina Orgler in the laboratory of Prof. Dr. Angelika M. Vollmar (Ludwig-Maximilians-Universität München)

Apoptosis rate was determined by propidium iodide (PI) staining and flow cytometry as described by *Nicoletti et al.*[335,336] Cells were seeded (100,000 cells/well) into 24 well plates and incubated for 24 h. Subsequently, cells were incubated (24 h or 48 h) with compound or DMSO, respectively. After incubation time, cells were detached (Trypsin?), washed with ice cold PBS, and finally permeabilized and stained using fluorochrome solution (50µg/ ml propidium iodide, 0.1% (w/v) sodium citrate, 0.1% (v/v) Triton X-100 in PBS). Incubation (30 min., 4°C, in the dark) was followed by analysis flow cytometry analysis using FACS Canto II device (*BD Biosciences*) using 10,000 events recorded at Ex488 nm/ Em585 nm per sample. Cell cycle analysis and apoptotic cells were determined with FlowJo 7.6 analysis software (*Tree Star*).

3.1.2.2.6. Evaluation of specific apoptosis in PBMCs and PDX cells

Experiment was conducted by Christina Orgler in the laboratory of Prof. Dr. Angelika M. Vollmar (Ludwig-Maximilians-Universität München)

PDX cells and PBMCs were stimulated with test compounds for 24h and subsequently transferred to FACS tubes, washed with PBS and resuspended in 250µl PBS. Next, cells were analyzed on a FACS Canto II and the percentage of viable and apoptotic cells was determined by forward/ side scatter gating as described previously [337]. Specific apoptosis rate was calculated according to the following formula:

$$Specific\ apoptosis\ [\%] = \frac{apoptotic\ cells\ VioA\ [\%] - \ apoptotic\ cells\ DMSO\ [\%]}{100\% - apoptotic\ cells\ DMSO\ [\%]}$$

3.1.3.3. Confocal microscopy assisted experiments

All confocal microscopy assisted experiments were conducted by Christina Orgler in the laboratory of Prof. Dr. Angelika M. Vollmar (Ludwig-Maximilians-Universität München).

3.1.3.3.1. Immunostaining

Cells were seeded into ibidiTreat 8-well µ-slides (*ibidi GmbH, Germany*) and incubated overnight. Next, cells were incubated (24 h, 37°C, 5% CO_2) with VioA or DMSO, respectively. Incbation was followed by a washing step with PBS and subsequently cells were fixed (10 min) with 4% para-formaldehyde (PFA) in PBS. Subsequently, cells were permeabilized (0.1% Triton X-100 in PBS, 15 min), cells washed with PBS and finally incubated with BSA solution (1% BSA (*Sigma Aldrich*) in PBS, 2 h) under gentle agitation. Subsequently, cell were incubated (overnight, 4°C)) with anti-NOP14 (rabbit, *Sigma Aldrich*) and anti-EMG1 (mouse, *Sigma Aldrich*) antibody, diluted 1:400 (v/v) in 1% BSA in PBS. After incubation, cells were washed with PBS + 0.2% Tx-100 (three times) and corresponding Alexa 488 anti-mouse lgG (H+L) (goat *Invitrogen*) or Alexa 674 anti-rabbit lgG (H+L) (chicken, *Invitrogen*) secondary antibody (diluted 1:500 in PBS) added (2 h, rt, in the dark). Nuclei staining was accomplished by incubation (30 min, rt) of cells with Hoechst 33342 (5 µg/mL final concentration) and cells washed with PBS (3x 10 min).

FluorSave™ reagent (*Merck*) containing medium was added to each well and wells sealed with a cover slip. Confocal microscopy was performed using a Leica SP8 LSM system (*Leica Microsystems*), and pictures analysed with the Leica LAS X (*Leica*) or ImageJ (*LIH*) software.

3.1.3.3.2. Nuclear run on assay

Experiments were conducted by Christina Orgler in the laboratory of Prof. Dr. Angelika M. Vollmar (Ludwig-Maximilians-Universität München).

Cells were seeded into ibidiTreat 8-well µ-slides (*ibidi GmbH*) and incubated with 5-FU (5 mM final concentration, *Sigma Aldrich*) for a minimum incubation time of 1 h. Fixation and permeabilization was accomplished as described in Chapter 4.1.2.3.1. Subsequently, cells were stained with anti-BrdU antibody (B8434, *Sigma-Aldrich*) as primary antibody and Alexa Fluor 488 goat anti mouse (*Invitrogen, Carlsbad, CA, USA*) as secondary antibody. Percentages of positive cells were calculated. Treatment with actinomycin D (6 µM) served as positive control for transcriptional inhibition.

3.1.3.3.3. Procedure for western blot analysis

Experiments were conducted by Christina Orgler in the laboratory of Prof. Dr. Angelika M. Vollmar (Ludwig-Maximilians-Universität München).

Proteins were separated by SDS-PAGE and transferred onto PVDF membranes by tank blotting. The following primary antibodies were used: CASP3 (sc-7148, *Santa Cruz*), CASP8 (#9746, *Cell Signaling*), EMG1 (SAB1406991, *Sigma-Aldrich*), NOC4L (HPA053424, Sigma Aldrich) NOP14 (HPA039596, *Sigma-Aldrich*), PARP (#9542, *Cell Signaling*). Proteins were detected by chemiluminescence detection using ECL solution and developing membranes on the ChemiDoc Touch (*Bio-Rad, Hercules, CA, USA*) imaging system. Loading control was either performed by adding 0.5% TCE (2,2,2-Trichloroethanol, Sigma-Aldrich) to the PAGE gels according to the TGX Stain-Free Gels system (*Bio-Rad, Hercules, CA, USA*) or expression levels of Actin (A2066, *Sigma-Aldrich*) were used .

3.1.3.4. Procedure for western blotting

Experiments were conducted by Christina Orgler in the laboratory of Prof. Dr. Angelika M. Vollmar (Ludwig-Maximilians-Universität München).

In case of adherent cell types, medium was removed by suction, cells washed with ice-cold PBS and lysis buffer added [stock solution: 2 mM EDTA, 137 mM NaCl, 10% (v/v) glycerol, 2 mM $Na_4P_2O_7$ x 10 H_2O, 20 mM TRIS-base, 1% (v/v) Triton-X 100, 20 mM $C_3H_7Na_2O_6Px$ 5 H_2O, 10 mM NaF; utilized lysis buffer: 920 µL lysis buffer stock solution, 20 µL Na_3VO_4 (100 mM stock solution), 20 µL PMSF (50 mM stock solution), 40 µL 25x Complete®]. Cells were frozen at -80°C overnight followed by detachement using a cell scraper. Cell suspension was transferred into tube (Eppendorf) and centrifuged (14,000 rpm, 10 min, 4°C). In case of suspension cells, cell suspension was washed with ice-cold PBS, resuspended in lysis buffer and incubated at -80°C overnight. In line with processing of adherent cells, samples were centrifuged, and whole cell lysate stored at -20°C until further use. For protein loading adjustment, protein concentration was determined by Bradford assay. Subsequently 5x SDS sample buffer [5x stock solution: 3.125 M Tris-HCl, 50% (v/v) glycerol, 5% (v/v) SDS, 2% (w/v) DTT, 0.015% (w/v) Pyronin Y in ddH_2O, utilized sample buffer: 20% (v/v) 5x SDS sample buffer] was added to the samples and protein concentration was adjusted by adding 1x SDS sample buffer. Afterwards the samples were heated at 95°C for 5 min and stored at -20°C before gel electrophoresis. For separation of proteins, discontinuous SDS- polyacrylamide gel electrophoresis (SDS PAGE) was performed. Equal amounts of protein samples were loaded on polyacrylamide (PAA) gels consisting of a separation and a stacking gel. The PAA concentration used was typically 12%, but was adjusted depending on the molecular weight of the analyzed proteins. The Mini Protean 3 system chamber (*Bio-Rad*) was filled with electrophoresis buffer [4.9 mM Tris, 38 mM glycine, 0.1% (w/v) SDS in ddH_2O)] and gels were loaded with samples. Electrophoresis was performed at a current of 100 V for 21 min and at 200 V for 45 min for protein stacking and separation, respectively. To determine the molecular weight of the proteins detected, a pre-stained protein ladder PageRuler™ or PageRuler Plus™ was subjected to gel electrophoresis in parallel.

3.1.3.5. Dual-luciferase splicing assay

Experiments were conducted by Christina Orgler in the laboratory of Prof. Dr. Angelika M. Vollmar (Ludwig-Maximilians-Universität München).

HeLa cells were seeded into 6-well plates and allowed to adhere overnight. Attached cells were either transfected with an intron-containing (Luc-I, #62858, Addgene) or intronless (Luc, #62857, *Addgene*) firefly luciferase reporter and an empty vector Renilla-Luc control plasmid (pGL4.74, *Promega*). FuGene HD served as transfection reagent and was used according to manufacturer's instructions and cells were transfected for 16h. Next, transfection reagent containing medium was removed and fresh growth medium was added before stimulation with **VioA** or the general splicing inhibitor isoginkgetin for 24h. Subsequently luciferase assay was performed using Dual-Luciferase Reporter Assay System (*Promega* E1960) following the manufacturer's instructions.

3.1.3.6. Western blot based co-Immunoprecipitation

Experiments were conducted by Christina Orgler in the laboratory of Prof. Dr. Angelika M. Vollmar (Ludwig-Maximilians-Universität München).

Jurkat cells were seeded at a density of 1 x 10^5 cells/ ml and treated as indicated. Next, cells were pelleted, washed with ice-cold PBS and cell lysis was performed by incubating cells with Triton-X 100 lysis buffer for 30 min on ice. After removal of cell debris by centrifugation, protein concentration was determined and 500 µg protein per sample was mixed with 10µl precipitation antibody (NOP14: HPA039596, *Sigma-Aldrich*) and 50 µl µMACS Protein G magnetic beads. The mixture was incubated under gentle agitation at 4°C for 4h. In parallel 500 µg protein, mixed with 5 µl normal rabbit IgG1 control antibody (#2729, *Cell Signaling*) and 50 µl magnetic beads was prepared as negative control. For co-IP, the magnetic labeled NOP14 and its interacting proteins were retained on Miltenyi µColumns that were placed into the µMACS separator magnetic field and equilibrated with Triton-X 100 buffer before sample loading. After four washing steps with Triton-X 100 buffer the proteins were eluted with 1x SDS sample buffer pre-heated to 95°C and subjected to western blot.

3.1.3.7. Western blot based transfection experiment

Experiments were conducted by Christina Orgler in the laboratory of Prof. Dr. Angelika M. Vollmar (Ludwig-Maximilians-Universität München).

For gene silencing, cells were transfected according to the DharmaFECT™ Transfection Reagents- siRNA transfection protocol. Cells were seeded in antibiotic free medium at a density of 0.15 x 10^6 cells / ml the day before transfection. For one 6-well, 10µl siRNA (c=5µM] was diluted in 190µl serum-free medium and 4µl DharmaFECT I reagent was diluted in 196µl serum-free medium and incubated for 5 min at RT. The content of the two tubes was gently mixed by carefully pipetting up and down, incubated for 20 min at RT and subsequently transferred to the culture plate.

3.1.3. Proteomics sample preparation

3.1.3.1. Analytical Affinity-based protein profiling

For concentration dependent labeling, Jurkat cells were seeded ($3x10^6$ cells/well) in Nunc 6-well plates (*Thermo Fisher Scientific*) in 1 mL RPMI-1940 medium (*Sigma Aldrich*) w/o FBS, supplemented with 1 µL of **VioA-P** in varying concentrations (stock solution in DMSO, 0.1% final DMSO concentration) or DMSO respectively and incubated (37°C, 1 h, 5% CO_2). Subsequently, samples were subjected to UV irradiation (*Philips* TL-D BLB UV lamps, 365 nm) for 20 min while cooling on ice. In case of the varying UV-irradiation durations, HeLa cells were seeded ($3x10^6$ cells/well) in Nunc 6-well plates (*Thermo Fisher Scientific*) and grown to 90% confluency. Subsequently, cells were washed with warm PBS (2 mL) and incubated with 1 mL DMEM medium supplemented with **VioA-P** (5µM final concentration, stock solution in DMSO, 0.1% final DMSO concentration) or DMSO, respectively. Next, samples were subjected to UV irradiation (*Philips* TL-D BLB UV lamps, 365 nm) for varying time durations while cooling on ice. In case of both experiments, cells were detached using a cell scraper, washed with PBS (1 mL) and lysed using pre-cooled lysis buffer (100 µL, 1% (v/v) NP40, 1% (w/v) sodium deoxycholate in PBS) for 30 min on ice. Cell debris was removed by centrifugation (21,000 g, 30 min, 4°C) and resulting supernatants transferred into new tubes. Samples were supplemented with 100 µM TAMRA-azide (10 mM stock in DMSO, *Base Click*), 1 mM $CuSO_4$ (50 mM stock in ddH_2O), 500 µM BTTAA ligand (10 mM in DMSO, *Jena Bioscience*). Samples were shortly vortexed and click reaction initiated by the addition of 2 mM sodium ascorbate (100 mM stock in ddH_2O, *Merck*). Samples were incubated (rt, 1 h, in the dark) and click reaction subsequently quenched by the addition of 2x SDS Laemmli buffer [100 µL, 1:1 (v/v), 63 mM Tris-HCl, 10% (v/v) Glycerol, 2% (w/v) SDS, 0.0025% (w/v) Bromphenol blue, 5% (v/v) β-Mercaptoethanol]. For SDS-PAGE analysis, 30 µL per sample were applied per gel lane on a NuPAGE™ SDS-PAGE gel (4-12% acrylamide). One lane was supplemented with BenchMark™ fluorescent protein standard (*Thermo Fisher Scientific*). Fluorescence was subsequently recorded using a LAS 4000 luminescent image analyzer (*Fujifilm*), equipped with a VRF43LMD3 lens (*Fujinon*) and a 575DF20 filter. Gels were stained using Coomassie staining solution [0.25% (w/v) Coomassie Brilliant Blue R250, 9.2% (v/v) acetic acid, 45.5% (v/v) ethanol], and destained subsequently using Coomassie Destaining Solution [10% (v/v) acetic acid, 20% (v/v) ethanol] and gels inspected for equal protein load.

3.1.3.2. Preparative Affinity-based protein profiling

For preparative labelling experiments, $6x10^6$ Jurkat cells were resuspended in 6 mL RPMI-1940 medium (*Sigma Aldrich*) w/o FBS and supplemented with 6 µL of **VioA-P** in varying concentrations (stock solution in DMSO, 0.1% final DMSO concentration) or DMSO respectively and seeded into 15 cm dishes (*Sarstedt*). After incubation (37°C, 5% CO_2, 1 h), samples were subjected to UV irradiation (*Philips* TL-D BLB UV lamps, 365 nm) for 20 min while cooling on ice. Cells were detached using a cell scraper, washed with PBS (10 mL) and lysed using pre-cooled lysis buffer (1 mL, 1% (v/v) NP40, 1% (w/v) sodium deoxycholate in PBS) for 30 min on ice. Cell debris was removed by centrifugation (21,000 g, 30 min, 4°C), resulting supernatants transferred into new falcons, and protein concentration determined using the Roti®-Quant universal kit (*Carl Roth*) for BCA assay. Equal amounts of protein (360 µg) were adjusted to a final volume of 280 µL. For copper (I)-catalyzed azide-alkyne cycloaddition, samples were supplemented with trifunctional linker (100 µM, 10 mM stock solution in DMSO), THPTA ligand (500 µM, 10 mM stock solution in DMSO, *Sigma-Aldrich*) and $CuSO_4$ (1 mM, 50 mM stock solution in H_2O). Reaction was initiated by the addition of sodium ascorbate (2 mM, 100 mM stock solution in H_2O). Samples were briefly vortexed and incubated for 1h in the dark at room temperature. Cycloaddition was quenched and proteins precipitated by the addition of 4-fold excess of acetone (1.3 mL) and incubated overnight at -20°C. Next, precipitated proteins were pelleted (21,000 g, 20 min, 4°C) and supernatant discarded. For detergent removal, protein pellet was resuspended in cold methanol (500 µL) using ultrasonication (10% intensity, 10 sec, Sonopuls HD 2070 ultrasonic rod, *BANDELIN electronic GmbH & Co. KG*). Procedure was carried out twice. 0.4% (w/v) SDS in PBS (1 mL) was added to the samples, and protein pellets dissolved by sonication (10% intensity, 10 sec, Sonopuls HD 2070 ultrasonic rod, *BANDELIN electronic GmbH & Co. KG*) at room temperature. Prior to enrichment, avidin-agarose beads (50 µL, *Sigma-Aldrich*) were equilibrated by washing with 0.4% (w/v) SDS in PBS (3x1 mL). Subsequently, samples were added to equilibrated avidin-agarose beads and incubated under continuous inverting for 1 h at room temperature. Removal of unspecific binding proteins was accomplished by washing the beads with 0.4% (w/v) SDS in PBS (3x 1 mL, 400 g, 2 min) and PBS (5x 1 mL, 400 g, 2 min). Next, beads were resuspended in X-buffer (200 µL, 7 M urea, 2 M thiourea in 20 mM HEPES buffer pH 7.5) and proteins reduced by the addition of DTT (1 mM, 1 M stock in ddH_2O) and incubated under gentle mixing (25°C, 45 min, 450 rpm). Alkylation

of proteins was achieved by the addition of IAA (5.5 mM, 550 mM stock in ddH_2O) and incubated under gentle mixing (25°C, 30 min, 450 rpm). Alkylation reaction was stopped by the addition of DTT (4 mM, 1 M stock in ddH_2O) and incubated under gentle mixing (25°C, 30 min, 450 rpm). Proteins were predigested with LysC (3.33 µg/mL, 0.5 mg/mL stock in ddH_20; *Wacko*) under gentle mixing (25°C, 2 h, 450 rpm). TEAB buffer (600 µL, 50mM, *Sigma-Aldrich*) was added, and samples further digested with trypsin (2 µL, 0.5 mg/mL stock, sequencing grade, modified; *Promega*) overnight under mixing (37°C, 800 rpm). Digest was stopped the following day by the addition of formic acid (0.1% final concentration; *Sigma-Aldrich*) and peptides desalted using Sep-Pak C18 1 cc Vac cartridges (*Waters*) and the following procedure: Resin was washed with MeCN (1 mL) and elution buffer (80% MeCN, 0.5% FA) prior to equilibration with 0.1% TFA (3 mL). Peptide solutions were loaded to the cartridges and bound peptides washed with 0.1% TFA (3 mL) and 0.5% FA (0.5 mL) and finally eluted with elution buffer (0.75 mL). Peptides were dried using a centrifugal vacuum concentrator (*Eppendorf*) and stored at -80°C. Prior to LC-MS/MS analysis dried peptide samples were reconstituted in 1% FA in ddH_2O (40 µL), sonicated for 10 min and filtered using 0.22 µm Ultrafree-MC® centrifugal filters (*Merck*, UFC30GVNB), preequilibrated with 300 µL 1% FA in ddH_2O and transferred into LC-MS vials. Experiments were carried out in triplicates.

3.1.3.3. Thermal protein profiling (TPP)

In situ thermal proteome profiling experiments were carried out as reported previously[137] with minor modifications. $6x10^7$ Jurkat cells were washed with PBS, resuspended in medium w/o FBS (15 mL) and supplemented with **VioA** (1µM; 1 mM stock solution in DMSO, 0.1% final concentration of DMSO) or DMSO respectively and transferred into T75-flasks (*Sarstedt*). After incubation (37°C, 5% CO_2, 1 h) cells were pelleted (800 g, 6 min, rt), supernatant discarded, cells resuspended in PBS (15 mL) and centrifuged again. Resulting cell pellets were taken up in PBS (1 mL) and cell suspension distributed into 0.2-mL PCR tubes (*Kisker Biotech*, $6x10^6$ Mio cells per tube) and kept at room temperature prior to heat treatment. **VioA** and DMSO treated samples were heated in parallel for 3 min. to the respective temperature (37°C, 41.2°C, 44°C, 48°C, 53.1°C, 56.3°C, 59.3°C, 62.5°C and 67.1°C) in a PCR cycler (*Techne*), incubated for 3 min. at room temperature, and subsequently snap-frozen in liquid nitrogen and stored at -80°C. Cell lysis was

accomplished using four freeze-thaw cycles (incubation for 30 seconds at 25°C, followed by snap-freezing in liquid nitrogen). Subsequently, PBS (50 µL) was added and the samples subjected to ultracentrifugation (100,000 g, 20 min, 4°C). 100 µL of the resulting supernatant was transferred into new 1.5 mL LoBind tubes (*Eppendorf*). For protein amount normalization, protein concentration of the two lowest temperature point samples (37°C and 41°C) were determined with a sample aliquot (10 µL) using Roti®-Quant universal kit (*Carl Roth*). Proteins were precipitated by adding acetone (400 µL) and incubated overnight (-20°C). Next, precipitated proteins were pelleted (21,000 g, 20 min., 4°C), supernatant discarded and protein pellet resuspended by sonication (10% intensity, 10 sec, Sonopuls HD 2070 ultrasonic rod, *BANDELIN electronic GmbH & Co. KG*) in pre-chilled methanol (500 µL). Protein pellet washing step was carried out twice. Subsequently, proteins were resuspended in X-buffer (300 µL, 7 M urea, 2 M thiourea in 20 mM Hepes buffer pH 7.5) by sonication (procedure as described above). Proteins were reduced with DTT (1 mM, 1 M stock in ddH_2O) and incubated under gentle mixing (25°C, 45 min, 450 rpm). Alkylation of proteins was achieved by the addition of iodoacetamide (5.5 mM, 550 mM stock in ddH_2O) and incubated under gentle mixing (25°C, 30 min, 450 rpm). Alkylation reaction was stopped by the addition of DTT (4 mM, 1 M stock in ddH_2O) and incubated under gentle mixing (25°C, 30 min, 450 rpm). Proteins were predigested with LysC (3.33 µg/mL, 0.5 mg/mL stock in ddH_2O; *Wacko*) under gentle mixing (25°C, 2 h, 450 rpm). TEAB buffer (900 µL, 50 mM, *Sigma-Aldrich*) was added, and samples further digested with trypsin (4 µL, 0.5 mg/mL stock, sequencing grade, modified; *Promega*) overnight under mixing (37°C, 800 rpm). Digest was stopped the following day by the addition of formic acid (0.1% final concentration; *Sigma-Aldrich*) and peptides desalted using Sep-Pak C18 1 cc Vac cartridges (*Waters*) and the following procedure: Resin was washed with MeCN (1 mL) and elution buffer (80% MeCN, 0.5% FA) prior to equilibration with 0.1% TFA (3 mL). Peptide solutions were loaded to the cartridges and bound peptides washed with 0.1% TFA (3 mL) and 0.5% FA (0.5 mL) and finally eluted with elution buffer (0.75 mL). Peptides were dried using a centrifugal vacuum concentrator (*Eppendorf*) and stored at -80°C. Peptides were reconstituted in elution buffer and a volume of each sample corresponding to 25 µg protein in the two lowest temperature points transferred into new 1.5 mL LoBind tubes. Samples were dried and taken up in TMT buffer 1 (10 µL, 10% MeCN 90% 200 mM TEAB buffer) and incubated under gentle mixing (25°C, 15 min, 400 rpm)**.** Additional TMT buffer 1 (25 µL) was added to each sample. TMT isobaric labels (TMT10plex™ isobaric Labels Reagent

Set 1x 0.8 mg, *Thermo Fisher Scientific*) were allowed to gain room temperature and taken up in MeCN (41 µL). 10 µL of each label solution was added to a sample according to applied temperature point (see Table 22) and incubated under gentle mixing (25°C, 1 h, 400 rpm). Reaction was stopped by the addition of 5% (v/v) hydroxylamine solution (5 µL, *Sigma-Aldrich*) and incubated under gentle mixing (25°C, 15 min, 400 rpm). Labeled peptides were combined into a single sample per experiment, TMT solution 2 (100 µL, 60% (v/v) 200 mM TEAB buffer 40% (v/v) MeCN) added and samples dried using a centrifugal vacuum concentrator. Dried labeled peptides were reconstituted in 0.5% formic acid (200 µL) and desalted using C18 StageTips (eight layers; Empore disk-C18; 47 mm; *Agilent Technologies*) and the following procedure: layers were washed with MeOH (90 µL), elution buffer (200 µL) and 0.5% FA (600 µL). Samples were loaded on stage tips (500g, 2 min) and bound peptides washed with 0.5% formic acid (600 µL) and eluted with elution buffer (300 µL). Eluted peptides were dried in a centrifugal vacuum concentrator. For HILIC fractionation, samples were reconstituted in HILIC buffer A (110 µL, 95% MeCN 5% H_2O and 0.1% TFA), sonicated, vortexed and centrifuged (21,000 x g, 10 min, 4°C). Peptide fractionation was carried out using an UltiMate 3000 HPLC system (*Dionex*) equipped with an YMC-Pack PVA-Sil column (5 µm, 150 x 2.1 mm, 120 Å, *YMC Europe GmbH*). Gradient elution was carried out with 95% MeCN 5% H_2O and 0.1% TFA (A) and 95% H_2O 5% MeCN and 0.1% TFA (B). 100 µL sample were injected and separated using a 62.5 min gradient (7.5 min 0% B, 50 min to 30% B, 3.5 min to 50% B and 2.5 min to 100% B) at a flow rate of 0.2 mL/min, followed by a washing and column re-equilibration step (12.5 min 100% B, 0.5 min to 0% B and 22.5 min 0% B). During separation, an on-line UV detector set at 215 nm was utilized to monitor peptide mixture elution. Fractions were collected into a 96-well plate (*Eppendorf*) and resulting fractions were pooled into 10 greater fractions. Fractions were dried in a centrifugal vacuum concentrator and fractions 2-9 subjected to LC-MS/MS analysis. Prior to LC-MS/MS analysis dried peptide samples were reconstituted in 1% FA in ddH_2O (10 µL), sonicated for 10 min and filtered using 0.22 µm Ultrafree-MC® centrifugal filters (*Merck*, UFC30GVNB), preequilibrated with 300 µL 1% FA in ddH_2O and transferred into LC-MS vials. The experiment was carried out in duplicates.

3.1.3.4. Whole proteome analysis

Jurkat cells ($2.9x10^6$ cells/ dish) were seeded in RPMI-1640 medium (8 mL) w/ FBS, supplemented with with VioA (10 nM; 10 µM stock solution in DMSO, 0.1% final DMSO concentration) or DMSO respectively and incubated (24 h, 37°C, 5% CO_2). Subsequently, cells were pelleted (800 g, 5 min, rt), resuspended in PBS (10 mL) and centrifuged again. $6x10^7$ Jurkat cells were washed with PBS, resuspended in medium w/o FBS (15 mL) and supplemented with **VioA** (1µM; 1 mM stock solution in DMSO, 0.1% final concentration of DMSO) or DMSO respectively and transferred into T75-flasks (*Sarstedt*). After incubation (37°C, 5% CO_2, 1 h) cells were pelleted (800 g, 6 min, rt), supernatant discarded, cells resuspended in ice-cold PBS (15 mL) and centrifuged again. Cell pellets were resuspended in ice-cold PBS (1 mL), centrifuged, supernatant discarded and cell pellets snap-frozen in liquid N_2 and stored at -80°C until further use. For cell lysis, pellets were resuspended in pre-cooled lysis buffer (1 mL, 1% (v/v) NP40, 1% (w/v) sodium deoxycholate in PBS) and incubated for 30 min on ice. Cell debris was removed by centrifugation (21,000 g, 30 min, 4°C), resulting supernatants transferred into new falcons, and protein concentration determined using the Roti®-Quant universal kit (*Carl Roth*) for BCA assay. Per sample, a volume corresponding to 250 µg was transferred into LoBind tubes (*Eppendorf*) and proteins precipitated by the addition of -80°C cold acetone (4-fold excess). Protein precipitation was completed overnight at -20°C. Next, precipitated proteins were pelleted (21,000 g, 20 min, 4°C) and supernatant discarded. For detergent removal, protein pellets were resuspended in cold methanol (500 µL) using ultrasonication (10% intensity, 10 sec, Sonopuls HD 2070 ultrasonic rod, *BANDELIN electronic GmbH & Co. KG*). Procedure was carried out twice. Subsequently, samples were resuspended in X-buffer (300 µL, 7 M urea, 2 M thiourea in 20 mM HEPES buffer pH 7.5) and proteins reduced by the addition of DTT (1 mM, 1 M stock in ddH_2O) and incubated under gentle mixing (25°C, 45 min, 450 rpm). Alkylation of proteins was achieved by the addition of IAA (5.5 mM, 550 mM stock in ddH_2O) and incubated under gentle mixing (25°C, 30 min, 450 rpm). Alkylation reaction was stopped by the addition of DTT (4 mM, 1 M stock in ddH_2O) and incubated under gentle mixing (25°C, 30 min, 450 rpm). Proteins were predigested with LysC (3.33 µg/mL, 0.5 mg/mL stock in ddH_20; *Wacko*) under gentle mixing (25°C, 2 h, 450 rpm). TEAB buffer (900 µL, 50mM, *Sigma-Aldrich*) was added, and samples further digested with trypsin (4 µL, 0.5 mg/mL stock, sequencing grade, modified; *Promega*) overnight under mixing (37°C, 800 rpm). Digest was stopped the

following day by the addition of formic acid (0.1% final concentration; *Sigma-Aldrich*) and peptides desalted using Sep-Pak C18 1 cc Vac cartridges (*Waters*) and the following procedure: Resin was washed with MeCN (1 mL) and elution buffer (80% MeCN, 0.5% FA) prior to equilibration with 0.1% TFA (3 mL). Peptide solutions were loaded to the cartridges and bound peptides washed with 0.1% TFA (3 mL) and 0.5% FA (0.5 mL) and finally eluted with elution buffer (0.75 mL). Peptides were dried using a centrifugal vacuum concentrator (*Eppendorf*) and stored at -80°C. Prior to LC-MS/MS analysis dried peptide samples were reconstituted in 1% FA in ddH_2O (120 µL), sonicated for 10 min and filtered using 0.22 µm Ultrafree-MC® centrifugal filters (*Merck*, UFC30GVNB), preequilibrated with 1% FA in ddH_2O (125 µL) and transferred into LC-MS vials. 4 µL sample volume were injected for LC-MS/MS analysis. Experiments were carried out in quadruplicates.

3.1.3.5. Whole proteome analysis of transfection experiments

For gene silencing experiments, HeLa cells ($2.9x10^6$ cells/ dish) were seeded on 6 cm dishes (*Sarstedt*) in DMEM medium (8 mL) w/ FBS, and incubated overnight (24 h, 37°C, 5% CO_2). Next, medium was removed by suction, cells washed with pre-warmed PBS (8 mL) and Cells were transfected following the DharmaFECT™ Transfection Reagents-siRNA transfection protocol. ON-TARGETplus SMARTpool siRNA reagent against human NOP14 (*Dharmacon*), as well as ON-TARGETplus non-targeting control siRNA, which served as control, were reconstituted in 1x siRNA buffer (diluted from 5x siRNA buffer, *Dharmacon*) and adjusted to 5 µM final concentration. For both types of treatment (NOP14 siRNA and nt siRNA), respective siRNA (96 µL) was diluted in OPTI-MEM® reduced-serum medium (7296 µL, *Gibco*) and inverted several times. Additionally for both treatments, transfection reagent Dharmafect 1 (153.6 µL, *Dharmacon*) was diluted in OPTI-MEM® reduced-serum medium (7296 µL, *Gibco*) and inverted several times. All prepared solutions were incubated (rt, 5 min), and one prepared transfection reagent solution combined with one siRNA solution, respectively. Solutions were mixed by pipetting and incubated (rt, 20 min) and transferred (1.6 mL per dish and treatment) to the cells. Samples were incubated (37°C, 5% CO_2, 30 h). Subsequently, medium was exchanged for DMEM medium /w FBS (6 mL) and cells incubated (37°C, 5% CO_2) for additional 24 h. Cells were harvested using a cell scraper, centrifuged (800 g, 5 min, rt)

resuspended in ice-cold PBS (15 mL) and centrifuged again. Resulting cell pellet was resuspended pre-cooled lysis buffer (500 µL, 1% (v/v) NP40, 1% (w/v) sodium deoxycholate in PBS) and incubated for 30 min on ice. Cell debris was removed by centrifugation (21,000 g, 30 min, 4°C), resulting supernatants transferred into new falcons, and protein concentration determined using the Roti®-Quant universal kit (*Carl Roth*) for BCA assay. Per sample, a volume corresponding to 250 µg was transferred into LoBind tubes (*Eppendorf*) and proteins precipitated by the addition of -80°C cold acetone (4-fold excess). Protein precipitation was completed overnight at -20°C. Next, precipitated proteins were pelleted (21,000 g, 20 min, 4°C) and supernatant discarded. For detergent removal, protein pellets were resuspended in cold methanol (500 µL) using ultrasonication (10% intensity, 10 sec, Sonopuls HD 2070 ultrasonic rod, *BANDELIN electronic GmbH & Co. KG*). Procedure was carried out twice. Subsequently, samples were resuspended in X-buffer (300 µL, 7 M urea, 2 M thiourea in 20 mM HEPES buffer pH 7.5) and proteins reduced by the addition of DTT (1 mM, 1 M stock in ddH_2O) and incubated under gentle mixing (25°C, 45 min, 450 rpm). Alkylation of proteins was achieved by the addition of IAA (5.5 mM, 550 mM stock in ddH_2O) and incubated under gentle mixing (25°C, 30 min, 450 rpm). Alkylation reaction was stopped by the addition of DTT (4 mM, 1 M stock in ddH_2O) and incubated under gentle mixing (25°C, 30 min, 450 rpm). Proteins were predigested with LysC (3.33 µg/mL, 0.5 mg/mL stock in ddH_20; *Wacko*) under gentle mixing (25°C, 2 h, 450 rpm). TEAB buffer (900 µL, 50mM, *Sigma-Aldrich*) was added, and samples further digested with trypsin (4 µL, 0.5 mg/mL stock, sequencing grade, modified; *Promega*) overnight under mixing (37°C, 800 rpm). Digest was stopped the following day by the addition of formic acid (0.1% final concentration; *Sigma-Aldrich*) and peptides desalted using Sep-Pak C18 1 cc Vac cartridges (*Waters*) and the following procedure: Resin was washed with MeCN (1 mL) and elution buffer (80% MeCN, 0.5% FA) prior to equilibration with 0.1% TFA (3 mL). Peptide solutions were loaded to the cartridges and bound peptides washed with 0.1% TFA (3 mL) and 0.5% FA (0.5 mL) and finally eluted with elution buffer (0.75 mL). Peptides were dried using a centrifugal vacuum concentrator (*Eppendorf*) and stored at -80°C. Prior to LC-MS/MS analysis dried peptide samples were reconstituted in 1% FA in ddH_2O (120 µL), sonicated for 10 min and filtered using 0.22 µm Ultrafree-MC® centrifugal filters (*Merck*, UFC30GVNB), preequilibrated with 1% FA in ddH_2O (125 µL) and transferred into LC-MS vials. 4 µL sample volume were injected for LC-MS/MS analysis. Experiments were carried out in quadruplicates.

3.1.3.6. MS-based co-Immunoprecipitation

For MS-based co-Immunoprecipitation experiments $4x10^6$ cells were plated out on 6 cm dishes (*Sarstedt*) in 8 mL media supplemented with **VioA** (10 nM, 10 µM stock solution in DMSO, 0.1% final concentration of DMSO) or DMSO respectively. After incubation (37°C, 5% CO_2, 24 h) 37°C, 5% CO_2, cells were counted and readjusted to a number of $4x10^6$ cells per dish. Cells were subsequently, pelleted (800 x g, 6 min, rt), supernatant discarded, and cells washed in PBS (2 mL) twice. For *in situ* cellular cross-linking cells were resuspended in PBS (1 mL) supplemented with DSSO crosslinker (2 mM, 100 mM stock solution in DMSO, 2% final concentration of DMSO, synthesized as described previously[173]). After incubation (37°C, 5% CO_2, 1 h) cells were pelleted (600 g, 5 min, 4°C), supernatant discarded, and remaining DSSO crosslinker quenched by resuspending cells in cold tris buffer (1 mL, 50 mM Tris-HCl, pH = 8.0). Cells were pelleted (600 g, 5 min, 4°C), resuspended in cold PBS (1 mL), pelleted and supernatant discarded. For cell lysis, cells were taken up in IP lysis buffer (500 µL, 50 mM Tris-HCl, 150 mM NaCl, 1 mM $MgCl_2$, 5% (v/v) glycerol, 1% (v/v) NP-40, pH = 7.4) and incubated for 30 min on ice. Cell lysate was cleared from debris (21,000 g, 20 min, 4°C), protein concentrations determined using Roti®-Quant universal kit (*Carl Roth*) and samples normalized to a total protein amount of 500 µg per sample (protein concentration 1 µg/µL). 30 µL Protein A/G Agarose beads (*Pierce Biotechnology, Thermo Fisher Scientific*) were equilibrated with cold IP wash buffer (1 mL, 50 mM Tris-HCl, pH = 7.4, 150 mM NaCl, 1 mM $MgCl_2$, 5% (v/v) glycerol, 0.05% NP-40), centrifuged (1,000 g, 1 min, 4°C), supernatant discarded and 500 µL of sample added directly to the beads. Additionally, 10 µL of the polyclonal rabbit anti-NOP14 antibody (stock concentration 0.1 mg/mL, *Sigma-Aldrich*), was added. For determination of unspecific background binding to the beads and the antibody constant regions, 0.4 µL of isotype control rabbit mAb IgG (stock concentration 2.5 mg/mL, *Cell Signaling Technology*) was added to control samples, and all samples incubated at 4°C under constant rotation overnight. Subsequently, samples were centrifuged (1,000 g, 1 min, 4°C) and supernatant discarded. For removal of unspecific bound proteins, pelleted beads were resuspended in IP wash buffer (1 mL), centrifuged (500 g, 30 sec, 4°C), and supernatant discarded. The procedure was carried out twice, and twice again with IP basic buffer (50 mM Tris-HCl, pH = 7.4, 150 mM NaCl, 5% (v/v) glycerol) for detergent removal. Samples were reduced and digested by the addition of IP elution buffer I (25 µL, 50 mM Tris-HCl, pH = 8.0; 5 ng/µL Trypsin (500 ng/µL stock solution, sequencing grade,

modified, *Promega*), 2 M Urea, 1 mM DTT (500 mM stock solution in H_2O)). Samples were incubated (30 min, 600 rpm, rt) prior to addition of IP elution buffer II (100 µL; 50 mM Tris-HCl; pH = 8.0; 2 M Urea; 5 mM IAA (500 mM stock solution in H_2O)), followed by incubation at 37°C and 600 rpm overnight. Tryptic digest was stopped by the addition of FA (1% final concentration). Samples were desalted using C18-stage tips (double layer; Empore disk-C18; 47 mm; *Agilent Technologies*) using the following procedure: Equilibration with MeOH (70 µL), followed by washing with 0.5% FA (3x 70 µL), sample load and a washing step (3x 70 µL, 0.5% FA). Finally, peptides were eluted with elution buffer (3x 30 µL; 80% MeCN, 0.5% FA). Samples were dried using a centrifugal vacuum concentrator (*Eppendorf*). Prior to LC-MS/MS analysis dried peptide samples were reconstituted in 1% FA in ddH_2O (26 µL), sonicated for 10 min and filtered using 0.22 µm Ultrafree-MC® centrifugal filters (*Merck*, UFC30GVNB), preequilibrated with 300 µL 1% FA in ddH_2O and transferred into LC-MS vials. The experiment was carried out in quadruplicates.

3.1.4. Targeted metabolic assay sample preparation

Several flasks of cultured Jurkat cells were pooled and centrifuged (800g, 10 min, rt). Resulting cell pellet was washed with cold PBS (80 mL) and pelleted again. Cells were lysed by resuspending cell pellet in cold lysis buffer (1 mL, 1% (v/v) NP40, 1% (w/v) sodium deoxycholate in PBS) and incubation for 30 min on ice. Subsequently, cell debris was removed by centrifugation (21,000 g, 15 min, 4°C) and resulting supernatants transferred into new falcons and protein concentration determined using the Roti®-Quant universal kit (*Carl Roth*) for BCA assay. Protein concentration was adjusted to 1 mg/mL by diluting samples with lysis buffer and stored at -80°C until further use. For time-dependent degradation analysis of **VioA-P**, cell lysate (400 µL) was incubated with **VioA-P** (50 µM, 50 mM stock in DMSO, 0.1% final concentration of DMSO) under gentle mixing (800 rpm, 37°C). At the respective time points (0, 1, 2, 4, 6, 8 and 24 h) an aliquot (50 µL) of the solution was transferred into a new Lobind tube and proteins precipitated by adding MeCN (200 µL) and incubated overnight (-20°). Next, precipitated proteins were

pelleted (21,000 g, 30 min, 4°C) and supernatants transferred into LC-MS vials. Experiment was carried out in triplicates.

3.1.5. Mass spectrometry

3.1.5.1. Mass spectrometry for AfBPP

Samples were separated and analyzed with an Ultimate 3000 Nano HPLC system (*Thermo Fisher Scientific*) equipped with an Acclaim C18 PepMap100 75µm ID x 2 cm trap column and an Acclaim PepMap C18 RSLC 75 µm ID x 50 cm separation column in an EASY-Spray™ setting, coupled to an Q Exactive Plus (*Thermo Fisher Scientific*). For peptide separation, samples were loaded on the trap column and washed for 10 min with 0.1% TFA in ddH_2O at a flow rate of 5 µL/min. Subsequently, peptides were transferred to the analytical column for peptide separation and separated using the following 132 min gradient (Buffer A: H_2O + 0.1% FA; B: MeCN + 0.1% FA) with a flow rate of 300 nL/min.: in 7 min to 5% B, in 105 min from 5% to 22%, in 10 min from 22 to 35% and in another 10 min to 90% B. Separation gradient was followed by a column washing step using 90% B for 10 min and subsequent column re-equilibration with 5% B for 5 min. Peptides were ionized using an EASY-Spray™ source with variable voltage and a capillary temperature of 275°C. Q Exactive Plus was operated in a TopN data dependent mode of 12. MS full scans (scan range 375 – 1,500 m/z) was performed in the orbitrap at a resolution of R = 140,000 (at 200 m/z) and an automatic gain control (AGC) ion target of 3.0e6 with a maximum injection time of 80 ms and RF Lens amplitude set to 60%. Peptides with charge states of 2 – 7 and an intensity higher than 1e4 were isolated in the quadrupole using a window of 1.6 m/z and subjected to higher-energy collisional dissociation (HCD; HCD collision Energy set to 27%). Dynamic exclusion was set to 60s. MS^2 scans were recorded in the orbitrap at a resolution of R = 17,500, with an AGC target set to 1e3 and a maximum injection time of 100 ms.

3.1.5.2. Mass spectrometry for MS-based co-Immunoprecipitation

Samples were separated and analyzed with an Ultimate 3000 Nano HPLC system (Thermo Scientific) equipped with an Acclaim C18 PepMap100 75 µm ID x 2 cm trap column and an Acclaim PepMap C18 RSLC 75 µm ID x 50 cm separation column in an EASY-Spray™ setting, coupled to an LTQ Orbitrap Fusion (Thermo Scientific).

For peptide separation, samples were loaded on the trap column and washed for 10 min with 0.1% TFA in ddH_2O at a flow rate of 5 µL/min. Subsequently, peptides were transferred to the analytical column for peptide separation and separated using the following 132 min gradient (Buffer A: H2O + 0.1% FA; B: MeCN + 0.1% FA) with a flowrate of 300 nL/min.: 7 min at 5%B, in 105 min from 5% to 22%, in 10 min from 22 to 35% and in another 10 min to 90% B. Separation gradient was followed by a column washing step using 90% B for 10 min and subsequent column re-equilibration with 5% B for 5 min. Peptides were ionized using an EASY-Spray^{TM} source with variable voltage and a capillary temperature of 275°C. Orbitrap Fusion was operated in top speed mode with 3 s cycle time. Internal calibration was performed by using the ion signal of fluoranthene cations (EASY-ETD/IC source). MS full scans (300 – 1500 m/z) were performed in the orbitrap at a resolution of R = 120,000 (at 200 m/z) with an automatic gain control (AGC) ion target of 2e5 and a maximum injection time of 80 ms and RF Lens amplitude set to 60%. Monoisotopic precursor selection was enabeled and dynamic exclusion set to 60 s. Most intense peptides with charge states of 2 – 7 and an intensity higher than 5e3 were isolated in the quadrupole using a window of 1.6 m/z and subjected to higher-energy collisional dissociation (HCD; HCD collision energy set to 30%). MS^2 ions were collected in the iontrap to a target of 1e4 for maximum injection time of 100 ms with "inject ions for all available parallelizable time" enabeled.

3.1.5.3. Mass spectrometry for thermal proteome profiling

Samples were analyzed by LC-MS/MS using an Ultimate 3000 Nano HPLC system (*Thermo Fisher Scientific*) equipped with an Acclaim C18 PepMap100 75µm ID x 2 cm trap column and an Acclaim PepMap C18 RSLC 75 µm ID x 50 cm separation column in an EASY-Spray^{TM} setting, coupled to an LTQ Orbitrap Fusion (*Thermo Fisher Scientific*). Prior to separation, samples (3 µL) were loaded on the trap column and washed for 10 min with 0.1% TFA in ddH_2O at a flow rate of 5 µL/min. Subsequently, peptides were transferred to the analytical column for peptide separation and separated using the following 120 min gradient (Buffer A: H_2O + 0.1% FA; B: MeCN + 0.1% FA) with a flow rate of 300 nL/min.: 10 min 5% B, in 50 min from 5% to 22%, in 60 min from 22 to 35% B. Separation gradient was followed by a column washing step using 90% B for 10 min and subsequent column re-equilibration with 5% B for 5 min. Peptides were ionized using

an EASY-Spray™ source (Spray Voltage = 2.2 kV) and a capillary temperature of 275°C. LTQ Orbitrap Fusion was operated in a top speed data-dependent mode with 3 s cycle time. Internal calibration was performed by using the ion signal of fluoranthene cations (EASY-ETD/IC source). MS full scans (scan range 375 – 1,500 m/z) were performed in the orbitrap at a resolution of R = 120,000 (at 200 m/z) with an automatic gain control (AGC) ion target of 4.0e5 with a maximum injection time of 50 ms and RF Lens amplitude set to 60%. Dynamic exclusion was set to 60 s.
Most intense peptides with charge states of 2 – 7 and an intensity higher than 5e4 were isolated in the quadrupole using a window of 1.0 m/z and subjected to higher-energy collisional dissociation (HCD; HCD collision energy set to 35%). MS^2 ions were collected in the iontrap to a target of 1e5 for maximum injection time of 105 ms.

3.1.5.4. Mass spectrometry for whole proteome experiments

Samples were separated and analyzed with an Ultimate 3000 Nano HPLC system (Thermo Scientific) equipped with an Acclaim C18 PepMap100 75 µm ID x 2 cm trap column and an Acclaim PepMap C18 RSLC 75 µm ID x 50 cm separation column in an EASY-Spray™ setting, coupled to an LTQ Orbitrap Fusion (Thermo Scientific).
For peptide separation, samples were loaded on the trap column and washed for 10 min with 0.1% TFA in ddH_2O at a flow rate of 5 µL/min. Subsequently, peptides were transferred to the analytical column for peptide separation and separated using the following 132 min gradient (Buffer A: H2O + 0.1% FA; B: MeCN + 0.1% FA) with a flowrate of 300 nL/min.: 7 min at 5%B, in 105 min from 5% to 22%, in 10 min from 22 to 35% and in another 10 min to 90% B. Separation gradient was followed by a column washing step using 90% B for 10 min and subsequent column re-equilibration with 5% B for 5 min. Peptides were ionized using an EASY-Spray™ source with variable voltage and a capillary temperature of 275°C. Orbitrap Fusion was operated in top speed mode with 3 s cycle time. Internal calibration was performed by using the ion signal of fluoranthene cations (EASY-ETD/IC source). MS full scans (300 – 1500 m/z) were performed in the orbitrap at a resolution of R = 120,000 (at 200 m/z) with an automatic gain control (AGC) ion target of 2e5 and a maximum injection time of 50 ms and RF Lens amplitude set to 60%. Monoisotopic precursor selection was enabeled and dynamic exclusion set to 60 s. Most intense peptides with charge states of 2 – 7 and an intensity higher than 5e3 were

isolated in the quadrupole using a window of 1.6 m/z and subjected to higher-energy collisional dissociation (HCD; HCD collision energy set to 30%). MS^2 ions were collected in the ion trap to a target of 1e4 for maximum injection time of 35 ms with "inject ions for all available parallelizable time" enabeled.

3.1.5.5. Mass spectrometry for targeted metabolic assay

Metabolic profiling and MS/MS analysis was carried out on a Ultimate™ 3000 RSLC system (*Thermo Scientific*) coupled to an LTQ Orbitrap XL mass spectrometer (*Thermo Scientific*). Chromatographic separation was carried out using an Accucore C18 aQ (150 x 2.1 mm, 2.6 µm, *Thermo Scientific*) column at 40°C and H_2O + 0.1% FA (A) and MeCN + 0.1% FA (B). Following gradient was applied for sample elution (flow rate: 0.5 mL/min): 3 min pre-equilibration with 2% B, 0.5 min 2% B, in 9.5 min from 2% to 100% B, 3 min at 100% B, in 0.5 min from 100% B to 2% B, followed by column re-equilibration at 2% B for 2.5 min. Mass spectrometric measurements were accomplished in positive ion mode (HESI-II source, *Thermo Scientific*) with following source parameters: capillary voltage 4.2 kV, tube lens 80 V, sheath gas 60 L/h, aux gas 10 L/h, capillary voltage 48 V and capillary temperature 350°C. Full scan measurements were recorded between 50 – 1500 m/z in centroid mode at 60,000 resolution in the orbitrap. Ions of interest (**VioA** m/z 863.42, **VioA-P** m/z 997.48) were isolated in single ion monitoring (SIM) profile mode and used for relative quantification (SIM width 10 m/z) at a resolution of 30,000 in the orbitrap. Prior to measurement 10 pooled QC samples were injected (injection volume for all samples 5 µL) to equilibrate the column. Sample order was randomized in order to take metabolic degradation over time into account.

3.1.6. Bioinformatics

3.1.6.1. Data analysis of Affinity-based protein profiling and MS-based co-IP experiments

MS raw data was analyzed using MaxQuant[125,140] software (version 1.6.2.10) with Andromeda[139] search engine (searches were carried out against Uniprot database for Homo sapiens (taxon identifier: 9606, downloaded on 15.10.2018, canonical). Carbamidomethlyation of cysteines (C) was set as fixed modifications and oxidation of methionines (M) and acetylation of N-termini as variable modifications. Trypsin (without N-terminal cleavage to proline) was set as proteolytic enzyme with a maximum of two allowed missed cleavages. For main search, precursor mass tolerance was set to 4.5 ppm and fragment mass tolerance to 0.5 Da. Label free quantification (LFQ) mode was activated with a LFQ minimum ratio count of 1. Second peptide identification was enabled, and false discovery rate (FDR) determination carried out by applying a decoy database and thresholds were set to 1% FDR at peptide-spectrum match and at protein levels and "match between runs" (0.7 min match and 20 min alignment time windows) option was enabled. Normalized LFQ intensities extracted from the MaxQuant result table proteinGroups.txt were further analyzed with Perseus[151] software (version 1.6.3.2). Prior to analysis, putative contaminants, reverse hits and only identified by site hits were removed. Normalized LFQ intensities were $\log_2$ transformed and proteins with two valid values for AfBPP data and three valid values for co-IP data in at least one group were used for missing value imputation from normal distribution (width 0.3, downshift 1.8, total matrix). Two-sample Students's *t*-test including Benjamini-Hochberg multiple testing correction (FDR = 0.05) was performed. Proteins with an enrichment factor of 2 ($\log_2(x) = 1$) and $-\log_{10}$ *t*-test *p*-value of 1.3 for AfBPP data and an enrichment factor of 4 ($\log_2(x) = 2$) for co-IP data and $-\log_{10}$ *t*-test *p*-value of 1.3 were considered as significantly enriched proteins.

3.1.6.2. Data analysis for thermal proteome profiling experiments

Recorded raw files were processed using MaxQuant[125,140] software (version 1.6.2.10) and MS/MS spectra were searched against the Uniprot FASTA database for *homo sapiens* (taxon identifier: 9606, downloaded on 15.10.2018, canonical). Trypsin (without proline) was set as proteolytic enzyme with a maximum of two missed cleavages allowed. Fractions were assigned according to HILIC fractionation. Group-specific parameters were set to "Reporter ion MS2" with 10plex TMT isobaric labels for N-terminal and lysine residue modification selected. Reporter mass tolerance was set to 0.003 Da and Filter by PIF activated (min. reporter PIF set to 0.75). Ion isotopic distribution was set for each TMT label (N-terminal and lysine) as stated in Table 23 for the use of isotope correction.
Cysteine carbamidomethylation was set as fixed modification and methionine oxidation as well as N-terminal protein acetylation as variable modifications with a max. number of modifications per peptide set to 5. The second peptide identification and "match between runs" (0.7 min match time window, 20 min alignment time window) was enabled. False discovery rate determination was carried out using a decoy database and thresholds were set to 1% FDR at peptide-spectrum match and at protein levels. Protein quantification was carried out with label minimum ratio count set to 2 and peptides for quantification set to "unique and razor". Remaining parameters were utilized as given in the default settings.
Downstream data analysis of corrected reporter intensities calculated by MaxQuant in the protein groups table were further used for the determination of melting curves and T_m shifts, which was performed with R (version 3.5.1 "Feather Spray") and the TPP[137] R package (version 3.0.3). Intensities of channel TMT[10]-128C were excluded from MaxQuant outputfile as TMT label was not applied prior to downstream analysis. Corrected intensities were normalized to the lowest applied temperature TMT channel. Data analysis was carried out as stated by the authors with minor changes (`fcColumn = c(6,8,9)`).

Prior to visualization of obtained output files, data were filtered using the following criteria[82,137]:

- $R^2 > 0.8$ for fitted curves for DMSO and **VioA** treatment
- Plateau of < 0.3 for DMSO curves
- Steepest slope of protein melting curves in paired set of DMSO and **VioA** treated conditions < -0.06.

- Melting point difference for each protein between both DMSO replicates < 1.5°C.

Following additional criteria were applied for hit identification[82,137]:

- One of the *p* values for the two replicate experiments is < 0.1 and the other is < 0.05
- Melting point shifts for both paired replicates (**VioA** vs DMSO) have the same direction
- Melting point difference VioA vs DMSO > DMSO 1 vs DMSO 2

Data visualization was carried out using Graphpad Prism 8.

3.1.6.3. Data analysis for whole proteome experiments

MS raw data was analyzed using MaxQuant[125,140] software (version 1.6.2.10) with Andromeda[139] search engine (searches were carried out against Uniprot database for Homo sapiens (taxon identifier: 9606, downloaded on 15.10.2018, canonical). Carbamidomethlyation of cysteines (C) was set as fixed modifications and oxidation of methionines (M) and acetylation of N-termini as variable modifications. Trypsin (without N-terminal cleavage to proline) was set as proteolytic enzyme with a maximum of two allowed missed cleavages. For main search, precursor mass tolerance was set to 4.5 ppm and fragment mass tolerance to 0.5 Da. Label free quantification (LFQ) mode was activated with a LFQ minimum ratio count of 1. Second peptide identification was enabled, and false discovery rate (FDR) determination carried out by applying a decoy database and thresholds were set to 1% FDR at peptide-spectrum match and at protein levels and "match between runs" (0.7 min match and 20 min alignment time windows) option was enabled. Normalized LFQ intensities extracted from the MaxQuant result table proteinGroups.txt were further analyzed with Perseus[151] software (version 1.6.3.2). Prior to analysis, putative contaminants, reverse hits and only identified by site hits were removed. Normalized LFQ intensities were $\log_2$ transformed and proteins with two valid values for AfBPP data and three valid values for co-IP data in at least one group were used for missing value imputation from normal distribution (width 0.3, downshift 1.8, total matrix). Two-sample Students's *t*-test including Benjamini-Hochberg multiple testing correction (FDR = 0.05) was performed. Proteins with a ratio of ±2 ($\log_2(x) = \pm 1$) and $-\log_{10}$ *t*-test *p*-value of 1.3 were considered as significantly altered proteins. Significantly up- and down-regulated

proteins (revealed by two-sample student's t-test conducted with Perseus) were subjected separately to a correlation network analysis using the STRING (search Tool for the Retrieval of Interacting Genes/Proteins) v11 database[166]. "Homo sapiens" was selected as organism. Meaning of network edges was set to "evidence" and default setting applied for creation of interaction network. However, "minimum required interaction score" was set to high confidence (0.700). Visualized correlation networks were downloaded from the online web page. Proteins are indicated as nodes, connected by lines. Thickness of lines indicates the confidence level of known or predicted protein interactions.
For GO term enrichment analysis, significantly up-regulated proteins were subjected to analysis using the GOrilla[167] web-server. All proteins present in the dataset after filtering and missing value imputation (see 3.1.6.3.) were employed as background dataset for identification of enriched GO terms.

3.1.6.4. Data analysis for targeted metabolic assay

Raw data was processed with Xcalibur Quan Browser (*Thermo Scientific*) using Genesis algorithm (Smoothing points:15; S/N threshold: 0.5, Highest peak detection mode) and manual integration mode. Intensities of the corresponding ions were extracted and visualized using Graphpad Prism 8.

3.2. Experimental part for Chapter II

3.2.1. Biochemistry and molecular biology

S. aureus NCTC 8325 wildtype strain was obtained from Institute Pasteur, France. The genetic mutants *S. aureus* NCTC *ΔclpP* and *S. aureus* NCTC clpP S98A were obtained from *Christian Fetzer*.[285]

3.2.1.1. Generation of *S. aureus* NCTC *ΔclpX* strain

3.2.1.1.1. Oligonucleotides for the generation of *S. aureus* NCTC *ΔclpX* strain

Table 20: Oligo nucleotides utilized for the generation of *S. aureus* Δ*clpX* mutant

Primer	Sequence (5' → 3')
clpX_KO_A	GCG GGA TCC GAA GAA TAC CAT GCT GAA GAA
clpX_KO_B	CAC TTT TAT AAC ACA TCA ATG ATT ACA TTC TTT TTA CAC CCC TAT TC
clpX_KO_C	GAA TAG GGG TGT AAA AAG AAT GTA ATC ATT GAT GTG TTA TAA AAG TG
clpX_KO_D	GCG GGA TCC GTT ATC AAT TGT GTA CTA ATT AAA AG
pMAD-seq-for	CCC AAT ATA ATC ATT TAT CAA CTC TTT TAC ACT TAA ATT TCC
pMAD-seq_rev	GCA ACG CGG GCA TCC CGA TG
clpP_KO_A	ATA TGG TAC CGA AGT ATT ACG TAT TTA AAA GAA GCG
clpP_KO_D	ATA TGA GCT CCT AAA TCT GGG TGG GAA CAC

3.2.1.1.2. Construction of pMAD *ΔclpX* shuttle plasmid

Upstream (clpX_KO_A and clpX_KO_B) and downstream (clpX_KO_C and clpX_KO_D) region of clpX (each fragment approx. 1000 bp in length) were amplified by PCR using extracted *S. aureus* NCTC 8325 genomic DNA as template. In case of the upstream fragment Primer A and Primer B (2.5 µL each, 100 µM stock concentration) were combined with genomic DNA template (0.61 µL, 50 ng), dNTPs (1 µL, 10 mM stock solution, *NEB*), 5x HF buffer (10 µL, *NEB*), Phusion polymerase (0.5 µL, *NEB*) and reaction solution adjusted to 50 µL total volume with DNAse free water. For downstream

fragment amplification same procedure was carried out using primer C and primer D (2.5 µL each, 100 µM stock concentration). PCR was carried out with the following temperature program: incubation at 98°C for 1 min., 35 cycles of 98 °C for 10 sec, annealing at 61 °C for 30 sec, ligation at 72 °C for 30 sec, followed by final ligation step at 72 °C for 5 min.

Resulting PCR products were purified (Cycle Pure Kit, *EZNA*, *Omega Bio-tek*) following the vendors protocol. Fusion of both fragments in a subsequent OE-PCR was carried out as described in the following: Fragment AB (3.4 µL, 72.5 µg/µL stock concentration) and fragment CD (5 µL, 49.3 µg/µL) were combined with dNTPs (1 µL 10 mM stock concentration, *Promega*), 5x HF buffer (10 µL), Phusion® High-fidelity DNA polymerase (0.5 µL, *NEB*) and reaction solution adjusted to 50 µL final volume with DNAse free water. Fusion of both fragments was carried out using the following program: initial denaturation at 98°C for 1 min, 15 cycles of 98°C for 10 sec., annealing at 60 °C for 30 sec. and ligation at 72 °C for 30 sec., after the last cycle final ligation step at 72 °C for 5 min. was carried out. Subsequently, primer clpX_KO_A and clpX_KO_D (each 2.5 µL, 100 µM) were added for amplification of fragment ABCD using additional 24 PCR cycles. The resulting fragment ABCD (1627 bp) was purified (Cycle Pure Kit, *EZNA*, *Omega Bio-tek*) following the vendors protocol.

Next, the resulting PCR product (20.51 µL, 48.75 ng/µL stock concentration) was digested (15 min., 37 °C) using 10x Cutsmart buffer (5 µL, *NEB*), *BamH1* (1 µL, *NEB*, standard protocol) and total volume adjusted to 50 µL with DNAse free water. In parallel pMAD plasmid, extracted from *E. coli* SA08B (17.27 µL, 57.9 ng/µL stock concentration) was digested following the same procedure, and additionally dephosphorylated (15 min, 37°C) by incubation with phosphatase (1 µL, TSAP, *Promega*, stated restriction digestion protocol). Fragment ABCD and linearized pMAD vector were fused by ligation using the following procedure: Plasmid (6.89 µL, 7.25 ng/µL) was combined with fragment ABCD (1.2 µL, 49.65 ng/µL, ratio vector:insert / 1:6), 2x Quick Ligation reaction buffer (10 µL, *NEB*), DNA ligase (1 µL, T4 DNA Ligase, *Promega*) and incubated overnight (8°C). The resulting ligation product was chemically transformed into NEB®-10β competent *E. coli* cells without prior purification, following the vendors protocol and transformed cell plated onto lysogeny broth (LB, 5.0 g/L yeast extract, 10.0 g/L tryptic peptone, 5.0 g/L NaCl in ddH_2O) agar plates containing ampicillin. Correct insertion of the pMAD Δ*clpX* vector was verified using colony PCR. Therefore, a small part of the colony was diluted in 50 µL water and 1 µL of this cell suspension mixed with clpX_KO_A and clpX_KO_D (2.5 µL each),

5x HF-buffer (10 µL), dNTPs (1 µL), Phusion polymerase (0.5 µL) and total volume adjusted to 50 µL with DNAse free water. Initial denaturation step was modified to 95 °C for 10 min. The resulting PCR product (clpX_KO_A and clpX_KO_D) as well as the extracted plasmid (Plasmid Mini Kit I, *ENZA, Omega Bio-tek*) (pMAD-seq-for and pMAD-seq-rev) was sequenced.

3.2.1.1.3. Preparation of electrocompetent *S. aureus* cells

1 mL of an *S. aureus* overnight culture was added to 100 mL BM-medium (10.0 g/L soy peptone, 5.0 g/L yeast extract, 5.0 g/L NaCl, 1.0 g/L K_2HPO_4 x $3H_2O$, 1.0 g/L glucose in ddH_2O, pH = 7.5) and incubated (37°C, 200 rpm) until OD_{600} = 0.5. Subsequently, cells were harvested by centrifugation (5000 g, 15 min. 4°C) and washed with cold and sterile 10% glycerol solution (three times: 1x 100 mL, 1x 50 mL, 1x 25 mL). The cell pellet obtained after the last centrifugation step was resuspended in 10% glycerol solution (400 µL), aliquoted (à 75 µL), snap-frozen in liquid nitrogen and stored at -80°C until further use.

3.2.1.1.4. Transformation of pMAD Δ*clpX* into *S. aureus*

An aliquot of electrocompetent *S. aureus* RN4220 cells was thawed on ice and incubated with pMAD *ΔclpX* plasmid (4 µg) for 10 min at room temperature in a 0.2 cm electroporation cuvette (*BioRad*). Subsequently, cells were electroporated (exponential, 25 µF, 2 kV, 100 Ω, Gene Pulser Xcell, *BioRad*) and immediately inoculated with BM-medium (1 mL, pre-warmed) and incubated (37 °C, 90 min., 200 rpm). Incubation step was followed by plating the resulting cell suspension onto BM agar plates (1 µg/mL erythromycin, 100 µg/mL X-Gal) and incubated at 37°C until colony formation was observed.

Blue *S. aureus* RN4220 colonies were inoculated with BM-medium (25 mL, containing erythromycin) over night at 30 °C. Plasmid extraction was performed (Plasmid

Plus Midi Kit, *Qiagen*) using the vendors high-yield protocol with minor modifications. For efficient cell lysis, 50 µL lysostaphin (2 mg/mL) was added after the addition of P1 buffer (4 mL) and samples incubated for 40 min at 37°C without shaking. The isolated plasmids were eluted from the cartridge with RNAse free water (200 µL), solvent evaporated (vacuum concentrator, *Eppendorf*) and isolated plasmid reconstituted in RNAse free water (30 µL).

Electroporation protocol was repeated with *S. aureus* NCTC 8325 and plasmid extracted from *S. aureus* RN4220. Blue colonies grown on BM agar plates (containing 1 µg/mL erythromycin and 100 µg/mL X-Gal) were incubated overnight at 30°C in BM medium (1 µg/mL erythromycin). For single crossover integration, overnight culture was diluted 1:1000 in BM medium (10 mL), incubated for 2 h at 30°C and 6 h at 42°C for plasmid loss. Dilution series from liquid culture (10^{-2} to 10^{-6}) were prepared and 100 µL of each dilution plated onto BM-agar plates (1 µg/mL erythromycin, 100 µg/mL X-Gal) and incubated at 42°C until blue colony formation was observed, indicating single crossover events. Five light blue colonies (dark blue would indicate plasmid presence) were combined in BM-medium (10 mL) and incubated for 8 h at 30°C. The resulting culture was diluted (1:1000) in BM-medium (10 mL) and incubated overnight at 42°C. Resulting overnight culture was again diluted (1:1000) in BM-medium (10 mL) and incubated at 30°C for 4 h. The resulting day culture was transferred to 42°C and incubated for 4 h. Dilution series from liquid culture (10^{-2} to 10^{-6}) were prepared and 100 µL respectively plated onto BM-agar plates (100 µg/mL X-Gal) and incubated at 42°C. The resulting white colonies were picked and plated respectively on BM-agar plates containing erythromycin and X-Gal (1 µg/mL erythromycin, 100 µg/mL X-Gal) and plates solely containing X-Gal. Plates were incubated at 30°C and resulting white, erythromycin sensitive colonies subjected to colony PCR (procedure see 3.2.1.1.2.) for amplification of DNA segment containing *clpX* deletion and verified by sequencing.

3.2.1.2. Recording of growth curves

Overnight cultures of all bacterial strains were diluted to OD_{600} = 0.03 in 100 mL B-medium (5.0 g/L yeast extracts, 10.0 g/L Tryptic peptone, 5.0 g/L NaCl, 1.0 g/L K_2HPO_4 in ddH_2O) and incubated (37°C, 200 rpm) in 300 mL baffled Erlenmeyer flasks. For each

time point 1 mL of the bacterial culture was transferred into cuvettes and OD_{600} determined via photometric measurement. Data was visualized using Graphpad Prism 8.

3.2.2. Sample preparation for MS-based experiments

3.2.2.1. Sample collection for all MS-based experiments

Overnight cultures of S. aureus NCTC 8325 wt, *ΔclpP, ΔclpX* and clpP S98A were diluted in 100 mL B-medium in 300 mL baffled Erlenmeyer flasks to an OD_{600} = 0.03 and incubated (37°C, 200 rpm) for 13.5 h (wt), 16.5 h (*ΔclpP, ΔclpX*) or 17 h (clpP S98A). Varying incubation times ensured similar post-exponential growth phases for all utilized strains. Optical density of all cultures was determined after incubation time and 15 mL OD_{600} = 5 harvested separately for whole proteome analysis and untargeted metabolomics studies by centrifugation (6000 g, 10 min, 4°C). 2 mL of the resulting supernatant were sterile-filtered (0.22 µm) per sample and snap-frozen in liquid N_2. Cells pellets were washed twice with cold aq. 0.9% NaCl solution and resulting bacterial cell pellet snap-frozen in liquid N_2 and stored at -80°C. The procedure was carried out on multiple days resulting in 7 biological replicates per strain for whole proteome and secretome analysis and 9 biological replicates per strain for untargeted metabolomics experiments.

3.2.2.2. Sample processing for whole proteome analysis

Cell pellets were thawed on ice, resuspended in lysis buffer I (470 µL, 100 mM Tris-HCl, 0.4% (w/v) SDS in ddH_2O, pH 7) and cells lysed by sonication using a SONOPULS sonication probe (5x 20 sec, 80% Int., *Bandelin*) with cooling breaks in between. Subsequently, lysis buffer II (188 µL, 100 mM Tris-HCl, 9.6% (w/v) SDS, 1.25% (w/v) sodium deoxycholate in in ddH_2O, pH 7) was added to all samples, followed by an additional sonication step (1x 10 sec, 10% Int.). Samples were incubated (90°C, 10 min, 400 rpm) and subsequently centrifuged (13,000 g, 10 min, 4°C). Resulting supernatant was transferred into new Eppendorf tubes and protein concentration determined using the

Roti®-Quant universal kit (*Carl Roth*) for BCA assay. Equal amounts of protein (300 µg) were transferred into Eppendorf LoBind tubes and proteins precipitated by addition of 4-fold volume excess of pre-chilled Acetone (-80°C) and incubation overnight at -20°C. Precipitated proteins were pelleted (21,000 g, 15 min, 4°C), supernatant discarded and resulting protein pellets resuspended in pre-chilled MeOH (500 µL, LC-MS grade, *VWR*) and centrifuged again. Resulting protein pellets were further processed as outlined in Chapter 3.1.3.2

3.2.2.3. Sample processing for secretome analysis

Frozen sterile-filtered supernatants were freeze-dried *in vacuo*, and resulting pellet redissolved in H_2O (150 µL, LC-MS grade, *VWR*). Debris was removed by centrifugation (21,000 g, 15 min, rt) and resulting supernatant transferred into new Eppendorf LoBind tubes. MeOH (600 µL, LC-MS grade, *VWR*) was added, samples briefly vortexed and centrifuged (13,000 rpm, 10 sec, rt). Next, Chloroform (225 µL, HPLC grade, *Sigma Aldrich*) was added and samples again vortexed and centrifuged. Subsequently H_2O (450 µL) was added, samples briefly vortexed and sonicated for 7 min in a sonication bath. Subsequently, samples were centrifuged (13,000 rpm, 10 sec, rt) and upper liquid layer discarded. MeOH (450 µL) were added and samples again briefly vortexed and centrifuged (13,000 rpm, 20 min, rt). Resulting supernatant was discarded and protein pellet dried. Further processing of protein pellets was carried out as described in Chapter 3.1.3.2.

3.2.2.4. Sample processing for untargeted metabolomics

Cell pellets were thawed on ice, resuspended in 80% MeOH (1 mL, LC-MS grade, *VWR*) and cells lysed by sonication using a SONOPULS sonication probe (2x 30 sec, 80% Int., *Bandelin*) with cooling breaks in between. Protein precipitation was completed overnight at -20°C. Subsequently, samples were centrifuged (21,000 g, 30 min, 4°C) and resulting supernatants transferred into new Eppendorf LoBind tubes. Cell extracts were dried *in*

vacuo using a centrifugal vacuum concentrator (*Eppendorf*) and stored at -80°C. Prior to LC-MS/MS analysis dried samples were reconstituted in 80 µL H_2O/MeCN 1:1, vortexed and centrifuged (21,000 g, 30 min, 4°C). Resulting supernatant were transferred into LC-MS vials.

3.2.3. Mass spectrometry

3.2.3.1. LC-MS/MS analysis of whole proteome and secretome

Whole proteome and secretome samples were analyzed via LC-MS/MS using the same parameter as described in Chapter 3.1.5.4.

3.2.3.2. LC-MS/MS analysis of metabolomics samples

Prior to analysis, pooled samples were prepared by combining an aliquot (5 µL) of each sample (QC sample name "QCall"). Resulting QC samples was utilized for monitoring measurement deviations within the entire run as well as for DDA-MS/MS fragmentations for metabolite identification.

Metabolic profiling and MS/MS analysis was carried out on a Ultimate™ 3000 RSLC system (*Thermo Scientific*) coupled to an LTQ Orbitrap XL mass spectrometer (*Thermo Scientific*). Chromatographic separation was carried out using an Accucore HILIC (150 x 2.1 mm, 2.6 µm, *Thermo Scientific*) column at 40°C and 5 mM NH_4OAc in 90% MeCN 10% H_2O (A) and 5 mM NH_4OAc in 50% MeCN 50% H_2O (B). After 5 min pre-equilibration with 100% A, samples were eluted with a linear gradient from 100% to 0% A over 25 min at a flow rate of 400 µL/min, followed by 5 min at 0% A and column reequilibration with 100% A for 5 min. Mass spectrometric measurements were accomplished in positive ion mode (HESI-II source, Thermo Scientific™) with following source parameters: capillary voltage 4.2 kV, tube lens 40 V, vaporizer temperature 350 °C, sheath gas 60 L/h, aux gas 10 L/h, capillary voltage 48 V and capillary temperature 275 °C. Full scan measurements were recorded between 50 – 1000 m/z in centroid mode at 30,000 resolution in the orbitrap. In case of fragmentation experiments, Orbitrap XL was operated in a Top3 data dependent mode. MS full scans (scan range 50 – 1000 m/z) were performed in the orbitrap at a 30,000 resolution in profile mode. MS fragmentation spectra were recorded in the ion trap in centroid mode with "Wideband activation" option activated. Prior to measurement 15 pooled QC samples were injected to equilibrate the column. In order to take metabolic degradation over time into account, sample order was

randomized and QC samples were injected after every 10th sample to check instrument performance.

3.2.4. Bioinformatics

3.2.4.1. Analysis of whole proteome data

MS raw data was analyzed using MaxQuant[125,140] software (version 1.6.5.) with Andromeda[139] search engine (searches were carried out against Uniprot database for *Staphylococcus aureus* NCTC 8325 (taxon identifier: 9606, downloaded on 07.01.2019, canonical). Carbamidomethlyation of cysteines (C) was set as fixed modifications and oxidation of methionines (M) as variable modifications. Trypsin (without N-terminal cleavage to proline) was set as proteolytic enzyme with a maximum of two allowed missed cleavages. For main search, precursor mass tolerance was set to 4.5 ppm and fragment mass tolerance to 0.5 Da. Label free quantification (LFQ) mode was activated with a LFQ minimum ratio count of 1. Second peptide identification was enabled, and false discovery rate (FDR) determination carried out by applying a decoy database and thresholds were set to 1% FDR at peptide-spectrum match and at protein levels and "match between runs" (0.7 min match and 20 min alignment time windows) option was enabled. Normalized LFQ intensities extracted from the MaxQuant result table proteinGroups.txt were further analyzed with Perseus[151] software (version 1.6.3.2). Prior to analysis, putative contaminants, reverse hits and only identified by site hits were removed, and normalized LFQ intensities were $\log_2$ transformed. Proteins with a minimum of five valid values in at least one group were used for missing value imputation from normal distribution (width 0.3, downshift 1.8, total matrix). Principle component analysis PCA was carried out using default settings.

For the comparison of expression levels of two bacterial strains, data was filtered for a minimum of five valid values in at least one group, prior to missing value imputation from normal distribution (width 0.3, downshift 1.8, total matrix). Two-sample Students's *t*-test including Benjamini-Hochberg multiple testing correction (FDR = 0.05) was performed. Proteins with a ratio of 2 [$\log_2(x) = 1$] and $-\log_{10}$ *t*-test *p*-value of 1.3 were considered as significantly dysregulated proteins.

GO terms annotation for Staphylococcus aureus were obtained from the Gene Ontology Consortium and loaded, together with KEGG pathway assignments into Perseus. Significantly up- and downregulated proteins were subjected separately to correlation network analysis using STRING v11[166] using "*Staphylococcus aureus*" as organism. Meaning of network edges was set to "evidence" and default setting applied for creation of protein interaction networks. However, "minimum required interaction score" was set to high confidence (0.700). Visualized correlation networks were downloaded from the online web page. Proteins are indicated as nodes, connected by lines. Thickness of lines indicates the confidence level of known or predicted protein interactions. Results of the student's t-test were visualized using Graphpad Prism 8. Downloaded GO terms, KEGG pathway assignments as well as stated literature of dysregulated proteins were utilized for analysis and manual clustering.

3.2.4.2. Analysis of secretome data

MS raw data was analyzed using MaxQuant[125,140] software (version 1.6.5.) with Andromeda[139] search engine (searches were carried out against Uniprot database for *Staphylococcus aureus* NCTC 8325 (taxon identifier: 93061, downloaded on 07.01.2019, canonical). Carbamidomethlyation of cysteines (C) was set as fixed modifications and oxidation of methionines (M) as variable modifications. Trypsin (without N-terminal cleavage to proline) was set as proteolytic enzyme with a maximum of two allowed missed cleavages. For main search, precursor mass tolerance was set to 4.5 ppm and fragment mass tolerance to 0.5 Da. Label free quantification (LFQ) mode was activated with a LFQ minimum ratio count of 1. Second peptide identification was enabled, and false discovery rate (FDR) determination carried out by applying a decoy database and thresholds were set to 1% FDR at peptide-spectrum match and at protein levels and "match between runs" (0.7 min match and 20 min alignment time windows) option was enabled. Contaminants list implemented in MaxQuant was modified by the addition of the *Saccharomyces cerevisiae* fasta file (taxon identifier: 4932, downloaded on 31.03.2019, canonical), as medium used for bacterial growth contained pepton from yeast. Normalized LFQ intensities extracted from the MaxQuant result table proteinGroups.txt were further analyzed with Perseus[151] software (version 1.6.3.2). Prior to analysis, putative contaminants, reverse hits and only

identified by site hits were removed, and normalized LFQ intensities were $\log_2$ transformed. Proteins with a minimum of five valid values in at least one group were used for missing value imputation from normal distribution (width 0.3, downshift 1.8, total matrix). Principle component analysis PCA was carried out using default settings.

For the comparison of expression levels of two bacterial strains, data was filtered for a minimum of five valid values in at least one group, prior to missing value imputation from normal distribution (width 0.3, downshift 1.8, total matrix). Two-sample Students's *t*-test including Benjamini-Hochberg multiple testing correction (FDR = 0.05) was performed. Proteins with a ratio of 2 [$\log_2(x) = 1$] and $-\log_{10}$ *t*-test *p*-value of 1.3 were considered as significantly dysregulated proteins.

GO terms annotation for Staphylococcus aureus were obtained from the Gene Ontology Consortium and loaded, together with KEGG pathway assignment into Perseus. Results of the student's t-test were visualized using Graphpad Prism 8, and proteins colored based on their GO cellular compartment assignment (extracellular region, plasma membrane and others). GO terms as well as KEGG pathway assignments of dysregulated proteins were utilized for analysis.

3.2.4.2. Analysis of untargeted metabolomics data

Recorded raw files were analyzed using Compound Discoverer (Version 3.0.0.294). Data was analyzed using the workflow "Untargeted Metabolomics with Statistics Detect Unknowns with ID using Online Databases and mzLogic". Settings were modified as follows: Min. Precursor Mass 100 Da, Max. Precursor Mass 1500 Da, polarity mode set to positive and Min. Peak intensity set to 1.0×10^6. Following databases were selected for metabolite identifications: BioCyc, Chemspace, E. coli Metabolome Database, Human Metabolome Database, KEGG, Yeast Metabolome Database. Results of statistical analysis (PCA and student's t-test results of comparison of *ΔclpP* vs clpP S98A) were extracted and visualized using Graphpad Prism 8. Box-Whisker plots were visualized in Compound Discoverer Software.

4. Bibliography

1 Bray, F. *et al.* Global cancer statistics 2018: GLOBOCAN estimates of incidence and mortality worldwide for 36 cancers in 185 countries. *CA Cancer J Clin* **68**, 394-424 (2018).

2 Dagenais, G. R. *et al.* Variations in common diseases, hospital admissions, and deaths in middle-aged adults in 21 countries from five continents (PURE): a prospective cohort study. *The Lancet* (2019).

3 Arnold, M. *et al.* Progress in cancer survival, mortality, and incidence in seven high-income countries 1995–2014 (ICBP SURVMARK-2): a population-based study. *The Lancet Oncology* (2019).

4 Siegel, R. L., Miller, K. D. & Jemal, A. Cancer statistics, 2019. *CA Cancer J Clin* **69**, 7-34 (2019).

5 Vafaee, F. *et al.* A data-driven, knowledge-based approach to biomarker discovery: application to circulating microRNA markers of colorectal cancer prognosis. *npj Systems Biology and Applications* **4**, 20 (2018).

6 Senapati, S., Mahanta, A. K., Kumar, S. & Maiti, P. Controlled drug delivery vehicles for cancer treatment and their performance. *Signal Transduct Target Ther* **3**, 7 (2018).

7 Savage, P., Stebbing, J., Bower, M. & Crook, T. Why does cytotoxic chemotherapy cure only some cancers? *Nature Clinical Practice Oncology* **6**, 43 (2008).

8 Escudier, B. & Gore, M. Axitinib for the management of metastatic renal cell carcinoma. *Drugs R D* **11**, 113-126 (2011).

9 Widmer, N. *et al.* Review of therapeutic drug monitoring of anticancer drugs part two--targeted therapies. *Eur J Cancer* **50**, 2020-2036 (2014).

10 Kerbel, R. S. A cancer therapy resistant to resistance. *Nature* **390**, 335-336, (1997).

11 Goossens, S. & Van Vlierberghe, P. Overcoming Steroid Resistance in T Cell Acute Lymphoblastic Leukemia. *PLoS Med* **13** (2016).

12 Rodrigues, T., Reker, D., Schneider, P. & Schneider, G. Counting on natural products for drug design. *Nat Chem* **8**, 531-541, doi:10.1038/nchem.2479 (2016).

13 Harvey, A. L., Edrada-Ebel, R. & Quinn, R. J. The re-emergence of natural products for drug discovery in the genomics era. *Nat Rev Drug Discovery* **14**, 111 (2015).

14 Newman, D. J. & Cragg, G. M. Natural Products as Sources of New Drugs from 1981 to 2014. *J Nat Prod* **79**, 629-661 (2016).

15 Amaral, R., dos Santos, S., Andrade, L., Severino, P. & Carvalho, A. Natural Products as Treatment against Cancer: A Historical and Current Vision. *Clin Oncol* **4**, 1562 (2019).

16 Dawid, W. Biology and global distribution of myxobacteria in soils. *FEMS Microbiol Rev* **24**, 403-427 (2000).

17 Herrmann, J., Fayad, A. A. & Muller, R. Natural products from myxobacteria: novel metabolites and bioactivities. *Nat Prod Rep* **34**, 135-160 (2017).

18 Weissman, K. J. & Muller, R. Myxobacterial secondary metabolites: bioactivities and modes-of-action. *Nat Prod Rep* **27**, 1276-1295 (2010).

19 Munoz-Dorado, J., Marcos-Torres, F. J., Garcia-Bravo, E., Moraleda-Munoz, A. & Perez, J. Myxobacteria: Moving, Killing, Feeding, and Surviving Together. *Front Microbiol* **7**, 781 (2016).

20 Muñoz-Dorado, J., Marcos-Torres, F. J., García-Bravo, E., Moraleda-Muñoz, A. & Pérez, J. Myxobacteria: Moving, Killing, Feeding, and Surviving Together. *Frontiers in Microbiology* **7** (2016).

21 Velicer, G. J. & Vos, M. Sociobiology of the myxobacteria. *Annu Rev Microbiol* **63**, 599-623 (2009).

22 Shimkets, L. J. Social and developmental biology of the myxobacteria. *Microbiol Rev* **54**, 473-501 (1990).

23 Reichenbach, H. Myxobacteria, producers of novel bioactive substances. *J Ind Microbiol Biotechnol* **27**, 149-156 (2001).

24 Mohr, K. I. Diversity of Myxobacteria-We Only See the Tip of the Iceberg. *Microorganisms* **6** (2018).

25 Diez, J. *et al.* Myxobacteria: natural pharmaceutical factories. *Microb Cell Fact* **11**, 52 (2012).

26 Gerth, K., Bedorf, N., Hofle, G., Irschik, H. & Reichenbach, H. Epothilons A and B: antifungal and cytotoxic compounds from Sorangium cellulosum (Myxobacteria). Production, physico-chemical and biological properties. *J Antibiot (Tokyo)* **49**, 560-563 (1996).

27 Goodin, S., Kane, M. P. & Rubin, E. H. Epothilones: mechanism of action and biologic activity. *J Clin Oncol* **22**, 2015-2025 (2004).

28 Sandmann, A., Sasse, F. & Muller, R. Identification and analysis of the core biosynthetic machinery of tubulysin, a potent cytotoxin with potential anticancer activity. *Chem Biol* **11**, 1071-1079 (2004).

29 Kaur, G. *et al.* Biological evaluation of tubulysin A: a potential anticancer and antiangiogenic natural product. *Biochem J* **396**, 235-242 (2006).

30 Khalil, M. W., Sasse, F., Lunsdorf, H., Elnakady, Y. A. & Reichenbach, H. Mechanism of action of tubulysin, an antimitotic peptide from myxobacteria. *Chembiochem* **7**, 678-683 (2006).

31 Huss, M. *et al.* Archazolid and apicularen: novel specific V-ATPase inhibitors. *BMC Biochem* **6**, 13 (2005).

32 Hassfeld, J., Fares, C., Steinmetz, H., Carlomagno, T. & Menche, D. Stereochemical determination of Archazolid A and B, highly potent vacuolar-type ATPase inhibitors from the Myxobacterium Archangium gephyra. *Org Lett* **8**, 4751-4754 (2006).

33 Nickeleit, I. *et al.* Argyrin a reveals a critical role for the tumor suppressor protein p27(kip1) in mediating antitumor activities in response to proteasome inhibition. *Cancer Cell* **14**, 23-35 (2008).

34 Allardyce, D. J., Bell, C. M. & Loizidou, E. Z. Argyrin B, a non-competitive inhibitor of the human immunoproteasome exhibiting preference for beta1i. *Chem Biol Drug Des* **94**, 1556-1567 (2019).

35 Sasse, F., Steinmetz, H., Hofle, G. & Reichenbach, H. Gephyronic acid, a novel inhibitor of eukaryotic protein synthesis from Archangium gephyra

(myxobacteria). Production, isolation, physico-chemical and biological properties, and mechanism of action. *J Antibiot (Tokyo)* **48**, 21-25 (1995).

36 Anderl, T. *et al.* Gephyronic acid, a missing link between polyketide inhibitors of eukaryotic protein synthesis (part II): Total synthesis of gephyronic acid. *Angew Chem Int Ed* **50**, 942-945 (2011).

37 Nicolas, L. *et al.* Gephyronic acid, a missing link between polyketide inhibitors of eukaryotic protein synthesis (part I): Structural revision and stereochemical assignment of gephyronic acid. *Angew Chem Int Ed* **50**, 938-941 (2011).

38 Muthukumar, Y. *et al.* Investigations on the mode of action of gephyronic acid, an inhibitor of eukaryotic protein translation from myxobacteria. *PLoS One* **13** (2018).

39 Lown, J. W. The mechanism of action of quinone antibiotics. *Mol Cell Biochem* **55**, 17-40 (1983).

40 Tan, A. R. & Toppmeyer, D. L. Ixabepilone in metastatic breast cancer: complement or alternative to taxanes? *Clin Cancer Res* **14**, 6725-6729 (2008).

41 Schummer, D. *et al.* Antibiotics from gliding bacteria, LXXVI. Vioprolides: new antifungal and cytotoxic peptolides from Cystobacter violaceus. *Liebigs Annalen* **1996**, 971-978 (1996).

42 Auerbach, D., Yan, F., Zhang, Y. & Muller, R. Characterization of an Unusual Glycerate Esterification Process in Vioprolide Biosynthesis. *ACS Chem Biol* **13**, 3123-3130 (2018).

43 Yan, F. *et al.* Biosynthesis and Heterologous Production of Vioprolides: Rational Biosynthetic Engineering and Unprecedented 4-Methylazetidinecarboxylic Acid Formation. *Angew Chem Int Ed* **57**, 8754-8759 (2018).

44 Chauhan, D. *et al.* BAX/BAK-Induced Apoptosis Results in Caspase-8-Dependent IL-1beta Maturation in Macrophages. *Cell Rep* **25**, 2354-2368 (2018).

45 Franke, R. *et al.* xCELLanalyzer: A Framework for the Analysis of Cellular Impedance Measurements for Mode of Action Discovery. *SLAS Discov* **24**, 213-223 (2019).

46 Pelletier, J., Thomas, G. & Volarevic, S. Ribosome biogenesis in cancer: new players and therapeutic avenues. *Nat Rev Cancer* **18**, 51-63 (2018).

47 Pederson, T. The nucleolus. *Cold Spring Harb Perspect Biol* **3** (2011).

48 in *Medical Cell Biology (Third Edition)* (ed Steven R. Goodman) 1-26 (Academic Press, 2008).

49 Miller, M. A. & Zachary, J. F. in *Pathologic Basis of Veterinary Disease (Sixth Edition)* (ed James F. Zachary) 2-43.e19 (Mosby, 2017).

50 Boisvert, F. M., van Koningsbruggen, S., Navascues, J. & Lamond, A. I. The multifunctional nucleolus. *Nat Rev Mol Cell Biol* **8**, 574-585 (2007).

51 Lindstrom, M. S. *et al.* Nucleolus as an emerging hub in maintenance of genome stability and cancer pathogenesis. *Oncogene* **37**, 2351-2366 (2018).

52 Klinge, S. & Woolford, J. L., Jr. Ribosome assembly coming into focus. *Nat Rev Mol Cell Biol* **20**, 116-131 (2019).

53 Catez, F. *et al.* Ribosome biogenesis: An emerging druggable pathway for cancer therapeutics. *Biochem Pharmacol* **159**, 74-81 (2019).

54 Bassler, J. & Hurt, E. Eukaryotic Ribosome Assembly. *Annu Rev Biochem* **88**, 281-306 (2019).

55 GM., C. *The Cell: A Molecular Approach*. (Sinauer Associates, 2000).
56 O'Sullivan, J. M., Pai, D. A., Cridge, A. G., Engelke, D. R. & Ganley, A. R. The nucleolus: a raft adrift in the nuclear sea or the keystone in nuclear structure? *Biomol Concepts* **4**, 277-286 (2013).
57 Ruggero, D. Revisiting the nucleolus: from marker to dynamic integrator of cancer signaling. *Sci Signal* **5** (2012).
58 Arabi, A. *et al.* c-Myc associates with ribosomal DNA and activates RNA polymerase I transcription. *Nat Cell Biol* **7**, 303-310 (2005).
59 van Riggelen, J., Yetil, A. & Felsher, D. W. MYC as a regulator of ribosome biogenesis and protein synthesis. *Nat Rev Cancer* **10**, 301-309 (2010).
60 Campbell, K. J. & White, R. J. MYC regulation of cell growth through control of transcription by RNA polymerases I and III. *Cold Spring Harb Perspect Med* **4** (2014).
61 Derenzini, M., Montanaro, L. & Trere, D. What the nucleolus says to a tumour pathologist. *Histopathology* **54**, 753-762 (2009).
62 Hein, N., Hannan, K. M., George, A. J., Sanij, E. & Hannan, R. D. The nucleolus: an emerging target for cancer therapy. *Trends Mol Med* **19**, 643-654 (2013).
63 Brighenti, E., Trere, D. & Derenzini, M. Targeted cancer therapy with ribosome biogenesis inhibitors: a real possibility? *Oncotarget* **6**, 38617-38627 (2015).
64 Burger, K. *et al.* Chemotherapeutic drugs inhibit ribosome biogenesis at various levels. *J Biol Chem* **285**, 12416-12425 (2010).
65 Quin, J. E. *et al.* Targeting the nucleolus for cancer intervention. *Biochim Biophys Acta* **1842**, 802-816 (2014).
66 Hannan, R. D., Drygin, D. & Pearson, R. B. Targeting RNA polymerase I transcription and the nucleolus for cancer therapy. *Expert Opin Ther Targets* **17**, 873-878 (2013).
67 Drygin, D. *et al.* Targeting RNA polymerase I with an oral small molecule CX-5461 inhibits ribosomal RNA synthesis and solid tumor growth. *Cancer Res* **71**, 1418-1430 (2011).
68 Bywater, M. J. *et al.* Inhibition of RNA polymerase I as a therapeutic strategy to promote cancer-specific activation of p53. *Cancer Cell* **22**, 51-65 (2012).
69 Cunningham, M. J. Genomics and proteomics: the new millennium of drug discovery and development. *J Pharmacol Toxicol Methods* **44**, 291-300 (2000).
70 Workman, P. Genomics and the second golden era of cancer drug development. *Mol Biosyst* **1**, 17-26 (2005).
71 Licitra, E. J. & Liu, J. O. A three-hybrid system for detecting small ligand–protein receptor interactions. *Proceedings of the National Academy of Sciences* **93**, 12817-12821, doi:10.1073/pnas.93.23.12817 (1996).
72 Stockwell, B. R. Chemical genetics: ligand-based discovery of gene function. *Nat Rev Genet* **1**, 116-125 (2000).
73 Frantzi, M., Latosinska, A. & Mischak, H. Proteomics in Drug Development: The Dawn of a New Era? *Proteomics Clin Appl* **13** (2019).
74 Emilien, G., Ponchon, M., Caldas, C., Isacson, O. & Maloteaux, J. M. Impact of genomics on drug discovery and clinical medicine. *QJM* **93**, 391-423 (2000).
75 Tyers, M. & Mann, M. From genomics to proteomics. *Nature* **422**, 193-197 (2003).

76 McClure, R. A. & Williams, J. D. Impact of Mass Spectrometry-Based Technologies and Strategies on Chemoproteomics as a Tool for Drug Discovery. *ACS Med Chem Lett* **9**, 785-791 (2018).

77 Mallick, P. & Kuster, B. Proteomics: a pragmatic perspective. *Nat Biotechnol* **28**, 695-709, doi:10.1038/nbt.1658 (2010).

78 Oda, Y. *et al.* Quantitative chemical proteomics for identifying candidate drug targets. *Anal Chem* **75**, 2159-2165 (2003).

79 Drewes, G. & Knapp, S. Chemoproteomics and Chemical Probes for Target Discovery. *Trends Biotechnol* **36**, 1275-1286 (2018).

80 Lee, J. & Bogyo, M. Target deconvolution techniques in modern phenotypic profiling. *Curr Opin Chem Biol* **17**, 118-126 (2013).

81 van Esbroeck, A. C. M. *et al.* Activity-based protein profiling reveals off-target proteins of the FAAH inhibitor BIA 10-2474. *Science* **356**, 1084-1087 (2017).

82 Becher, I. *et al.* Thermal profiling reveals phenylalanine hydroxylase as an off-target of panobinostat. *Nat Chem Biol* **12**, 908-910 (2016).

83 Pai, M. Y. *et al.* in *Chemical Biology: Methods and Protocols* (eds Jonathan E. Hempel, Charles H. Williams, & Charles C. Hong) 287-298 (Springer New York, 2015).

84 Kam, C. M., Abuelyaman, A. S., Li, Z., Hudig, D. & Powers, J. C. Biotinylated isocoumarins, new inhibitors and reagents for detection, localization, and isolation of serine proteases. *Bioconjugate Chemistry* **4**, 560-567 (1993).

85 Abuelyaman, A. S., Hudig, D., Woodard, S. L. & Powers, J. C. Fluorescent Derivatives of Diphenyl [1-(N-Peptidylamino)alkyl]phosphonate Esters: Synthesis and Use in the Inhibition and Cellular Localization of Serine Proteases. *Bioconjugate Chemistry* **5**, 400-405 (1994).

86 Cullen, B. M., Halliday, I. M., Kay, G., Nelson, J. & Walker, B. The application of a novel biotinylated affinity label for the detection of a cathepsin B-like precursor produced by breast-tumour cells in culture. *Biochem J* **283 (Pt 2)**, 461-465 (1992).

87 Cravatt, B. F., Wright, A. T. & Kozarich, J. W. Activity-Based Protein Profiling: From Enzyme Chemistry to Proteomic Chemistry. *Annual Review of Biochemistry* **77**, 383-414 (2008).

88 Evans, M. J. & Cravatt, B. F. Mechanism-Based Profiling of Enzyme Families. *Chemical Reviews* **106**, 3279-3301 (2006).

89 Fonovic, M. & Bogyo, M. Activity Based Probes for Proteases: Applications to Biomarker Discovery,Molecular Imaging and Drug Screening. *Current Pharmaceutical Design* **13**, 253-261 (2007).

90 Fonović, M. & Bogyo, M. Activity-based probes as a tool for functional proteomic analysis of proteases. *Expert Review of Proteomics* **5**, 721-730 (2008).

91 Böttcher, T., Pitscheider, M. & Sieber, S. A. Natural Products and Their Biological Targets: Proteomic and Metabolomic Labeling Strategies. *Angew Chem Int Ed* **49**, 2680-2698 (2010).

92 Niphakis, M. J. & Cravatt, B. F. Enzyme inhibitor discovery by activity-based protein profiling. *Annu Rev Biochem* **83**, 341-377 (2014).

93 Barglow, K. T. & Cravatt, B. F. Activity-based protein profiling for the functional annotation of enzymes. *Nature Methods* **4**, 822 (2007).

94 Rooden, E. J., Bakker, A. T., Overkleeft, H. S., Stelt, M. . in *eLS* 1-9 (2018).
95 Wright, M. H. & Sieber, S. A. Chemical proteomics approaches for identifying the cellular targets of natural products. *Natural Product Reports* **33**, 681-708 (2016).
96 Zhou, Y., Li, W. & Xiao, Y. Profiling of Multiple Targets of Artemisinin Activated by Hemin in Cancer Cell Proteome. *ACS Chem Biol* **11**, 882-888 (2016).
97 Heal, W. P., Dang, T. H. & Tate, E. W. Activity-based probes: discovering new biology and new drug targets. *Chem Soc Rev* **40**, 246-257 (2011).
98 Carlson, E. E. Natural products as chemical probes. *ACS Chem Biol* **5**, 639-653 (2010).
99 Bogyo, M., Verhelst, S., Bellingard-Dubouchaud, V., Toba, S. & Greenbaum, D. Selective targeting of lysosomal cysteine proteases with radiolabeled electrophilic substrate analogs. *Chem Biol* **7**, 27-38 (2000).
100 Kolb, H. C., Finn, M. G. & Sharpless, K. B. Click Chemistry: Diverse Chemical Function from a Few Good Reactions. *Angew Chem Int Ed* **40**, 2004-2021 (2001).
101 Tornøe, C. W., Christensen, C. & Meldal, M. Peptidotriazoles on Solid Phase: [1,2,3]-Triazoles by Regiospecific Copper(I)-Catalyzed 1,3-Dipolar Cycloadditions of Terminal Alkynes to Azides. *The Journal of Organic Chemistry* **67**, 3057-3064 (2002).
102 Meldal, M. & Tornoe, C. W. Cu-catalyzed azide-alkyne cycloaddition. *Chem Rev* **108**, 2952-3015 (2008).
103 Himo, F. *et al.* Copper(I)-catalyzed synthesis of azoles. DFT study predicts unprecedented reactivity and intermediates. *J Am Chem Soc* **127**, 210-216 (2005).
104 Saxon, E. & Bertozzi, C. R. Cell Surface Engineering by a Modified Staudinger Reaction. *Science* **287**, 2007-2010 (2000).
105 Baskin, J. M. *et al.* Copper-free click chemistry for dynamic in vivo imaging. *Proc. Natl. Acad. Sci. U.S.A.* **104**, 16793-16797 (2007).
106 Agard, N. J., Prescher, J. A. & Bertozzi, C. R. A Strain-Promoted [3 + 2] Azide−Alkyne Cycloaddition for Covalent Modification of Biomolecules in Living Systems. *J Am Chem Soc* **126**, 15046-15047 (2004).
107 Ovaa, H. *et al.* Chemistry in Living Cells: Detection of Active Proteasomes by a Two-Step Labeling Strategy. *Angew Chem Int Ed* **42**, 3626-3629 (2003).
108 Hoegl, A. *et al.* Mining the cellular inventory of pyridoxal phosphate-dependent enzymes with functionalized cofactor mimics. *Nat Chem* **10**, 1234-1245 (2018).
109 Chang, P. V. *et al.* Copper-free click chemistry in living animals. *Proc. Natl. Acad. Sci. U.S.A.* **107**, 1821-1826 (2010).
110 Martell, J. & Weerapana, E. Applications of copper-catalyzed click chemistry in activity-based protein profiling. *Molecules* **19**, 1378-1393 (2014).
111 Geurink, P. P., Prely, L. M., van der Marel, G. A., Bischoff, R. & Overkleeft, H. S. Photoaffinity labeling in activity-based protein profiling. *Top Curr Chem* **324**, 85-113 (2012).
112 A. Fleming, S. Chemical reagents in photoaffinity labeling. *Tetrahedron* **51**, 12479-12520 (1995).
113 Herner, A. *et al.* 2-Aryl-5-carboxytetrazole as a New Photoaffinity Label for Drug Target Identification. *J Am Chem Soc* **138**, 14609-14615 (2016).

114 Smith, R. A. G. & Knowles, J. R. Aryldiazirines. Potential reagents for photolabeling of biological receptor sites. *J Am Chem Soc* **95**, 5072-5073 (1973).

115 Chou, C., Uprety, R., Davis, L., Chin, J. W. & Deiters, A. Genetically encoding an aliphatic diazirine for protein photocrosslinking. *Chemical Science* **2**, 480-483 (2011).

116 Ong, S.-E. *et al.* Stable Isotope Labeling by Amino Acids in Cell Culture, SILAC, as a Simple and Accurate Approach to Expression Proteomics. *Molecular & Cellular Proteomics* **1**, 376-386 (2002).

117 Boersema, P. J., Aye, T. T., van Veen, T. A., Heck, A. J. & Mohammed, S. Triplex protein quantification based on stable isotope labeling by peptide dimethylation applied to cell and tissue lysates. *Proteomics* **8**, 4624-4632 (2008).

118 Ross, P. L. *et al.* Multiplexed Protein Quantitation in Saccharomyces cerevisiaeUsing Amine-reactive Isobaric Tagging Reagents. *Molecular & Cellular Proteomics* **3**, 1154-1169 (2004).

119 Werner, T. *et al.* Ion coalescence of neutron encoded TMT 10-plex reporter ions. *Anal Chem* **86**, 3594-3601 (2014).

120 Wang, W. *et al.* Quantification of proteins and metabolites by mass spectrometry without isotopic labeling or spiked standards. *Anal Chem* **75**, 4818-4826 (2003).

121 Gleissner, C. M. *et al.* Neocarzilin A Is a Potent Inhibitor of Cancer Cell Motility Targeting VAT-1 Controlled Pathways. *ACS Cent Sci* **5**, 1170-1178 (2019).

122 Fetzer, C. *et al.* A Chemical Disruptor of the ClpX Chaperone Complex Attenuates the Virulence of Multidrug-Resistant Staphylococcus aureus. *Angew Chem Int Ed* **56**, 15746-15750 (2017).

123 Wright, M. H. *et al.* Quantitative chemoproteomic profiling reveals multiple target interactions of spongiolactone derivatives in leukemia cells. *Chem Commun (Camb)* **53**, 12818-12821 (2017).

124 Lobo, M. D. *et al.* Label-Free Proteome Analysis of Plasma from Patients with Breast Cancer: Stage-Specific Protein Expression. *Front Oncol* **7**, 14 (2017).

125 Cox, J. & Mann, M. MaxQuant enables high peptide identification rates, individualized p.p.b.-range mass accuracies and proteome-wide protein quantification. *Nat Biotechnol* **26**, 1367-1372 (2008).

126 Cox, J. *et al.* Accurate proteome-wide label-free quantification by delayed normalization and maximal peptide ratio extraction, termed MaxLFQ. *Mol Cell Proteomics* **13**, 2513-2526 (2014).

127 Bantscheff, M., Schirle, M., Sweetman, G., Rick, J. & Kuster, B. Quantitative mass spectrometry in proteomics: a critical review. *Anal Bioanal Chem* **389**, 1017-1031 (2007).

128 Mateus, A., Maatta, T. A. & Savitski, M. M. Thermal proteome profiling: unbiased assessment of protein state through heat-induced stability changes. *Proteome Sci* **15**, 13 (2016).

129 Lo, M. C. *et al.* Evaluation of fluorescence-based thermal shift assays for hit identification in drug discovery. *Anal Biochem* **332**, 153-159 (2004).

130 Martinez Molina, D. & Nordlund, P. The Cellular Thermal Shift Assay: A Novel Biophysical Assay for In Situ Drug Target Engagement and Mechanistic Biomarker Studies. *Annu Rev Pharmacol Toxicol* **56**, 141-161 (2016).

131 Krishna, S. N. *et al.* A fluorescence-based thermal shift assay identifies inhibitors of mitogen activated protein kinase kinase 4. *PLoS One* **8** (2013).
132 Senisterra, G. A. *et al.* Screening for Ligands Using a Generic and High-Throughput Light-Scattering-Based Assay. *Journal of Biomolecular Screening* **11**, 940-948 (2006).
133 Pantoliano, M. W. *et al.* High-Density Miniaturized Thermal Shift Assays as a General Strategy for Drug Discovery. *Journal of Biomolecular Screening* **6**, 429-440 (2001).
134 Martinez Molina, D. *et al.* Monitoring drug target engagement in cells and tissues using the cellular thermal shift assay. *Science* **341**, 84-87 (2013).
135 Shaw, J. *et al.* Positioning High-Throughput CETSA in Early Drug Discovery through Screening against B-Raf and PARP1. *SLAS Discov* **24**, 121-132 (2019).
136 Savitski, M. M. *et al.* Tracking cancer drugs in living cells by thermal profiling of the proteome. *Science* **346**, 1255784 (2014).
137 Franken, H. *et al.* Thermal proteome profiling for unbiased identification of direct and indirect drug targets using multiplexed quantitative mass spectrometry. *Nat Protoc* **10**, 1567-1593 (2015).
138 Reinhard, F. B. *et al.* Thermal proteome profiling monitors ligand interactions with cellular membrane proteins. *Nat Methods* **12**, 1129-1131 (2015).
139 Cox, J. *et al.* Andromeda: a peptide search engine integrated into the MaxQuant environment. *J Proteome Res* **10**, 1794-1805 (2011).
140 Tyanova, S., Temu, T. & Cox, J. The MaxQuant computational platform for mass spectrometry-based shotgun proteomics. *Nat Protoc* **11**, 2301-2319 (2016).
141 Perkins, D. N., Pappin, D. J. C., Creasy, D. M. & Cottrell, J. S. Probability-based protein identification by searching sequence databases using mass spectrometry data. *ELECTROPHORESIS* **20**, 3551-3567 (1999).
142 Bonnard, I. *et al.* Total structure and inhibition of tumor cell proliferation of laxaphycins. *J Med Chem* **50**, 1266-1279 (2007).
143 Li, Z. *et al.* Design and synthesis of minimalist terminal alkyne-containing diazirine photo-crosslinkers and their incorporation into kinase inhibitors for cell- and tissue-based proteome profiling. *Angew Chem Int Ed* **52**, 8551-8556 (2013).
144 Penghui Wang , Z. L., Lulu Jiang , Lu Zhou , Deyong Ye. Design and Synthesis of the Diazirine-based Clickable Photo-affinity Probe Targeting Sphingomyelin Synthase 2. *Letters in Drug Design & Discovery* **16**, 678-684 (2019).
145 Kleiner, P., Heydenreuter, W., Stahl, M., Korotkov, V. S. & Sieber, S. A. A Whole Proteome Inventory of Background Photocrosslinker Binding. *Angew Chem Int Ed Engl* **56**, 1396-1401 (2017).
146 Eyermann, B., Meixner, M., Brotz-Oesterhelt, H., Antes, I. & Sieber, S. A. Acyldepsipeptide probes facilitate specific detection of caseinolytic protease P independent of its oligomeric and activity state. *Chembiochem* (2019).
147 Hill, J. R. & Robertson, A. A. B. Fishing for Drug Targets: A Focus on Diazirine Photoaffinity Probe Synthesis. *J Med Chem* **61**, 6945-6963 (2018).
148 Fukami, T. & Yokoi, T. The Emerging Role of Human Esterases. *Drug Metabolism and Pharmacokinetics* **27**, 466-477 (2012).

149 Bowden, K., Heilbron, I. M., Jones, E. R. H. & Weedon, B. C. L. 13. Researches on acetylenic compounds. Part I. The preparation of acetylenic ketones by oxidation of acetylenic carbinols and glycols. *Journal of the Chemical Society (Resumed)*, 39-45 (1946).

150 Neises, B. & Steglich, W. Einfaches Verfahren zur Veresterung von Carbonsäuren. *Angewandte Chemie* **90**, 556-557 (1978).

151 Tyanova, S. *et al.* The Perseus computational platform for comprehensive analysis of (prote)omics data. *Nat Methods* **13**, 731-740 (2016).

152 Crisci, A. *et al.* Mammalian splicing factor SF1 interacts with SURP domains of U2 snRNP-associated proteins. *Nucleic Acids Res* **43**, 10456-10473 (2015).

153 Liu, P. C. & Thiele, D. J. Novel stress-responsive genes EMG1 and NOP14 encode conserved, interacting proteins required for 40S ribosome biogenesis. *Mol Biol Cell* **12**, 3644-3657 (2001).

154 Chiu, Y. H., Macmillan, J. B. & Chen, Z. J. RNA polymerase III detects cytosolic DNA and induces type I interferons through the RIG-I pathway. *Cell* **138**, 576-591 (2009).

155 Younis, I. *et al.* Rapid-response splicing reporter screens identify differential regulators of constitutive and alternative splicing. *Mol Cell Biol* **30**, 1718-1728 (2010).

156 Lei, J. J. *et al.* NOP14 suppresses breast cancer progression by inhibiting NRIP1/Wnt/beta-catenin pathway. *Oncotarget* **6**, 25701-25714 (2015).

157 Suzuki, T. *et al.* A homozygous NOP14 variant is likely to cause recurrent pregnancy loss. *Journal of Human Genetics* **63**, 425-430 (2018).

158 Phipps, K. R., Charette, J. & Baserga, S. J. The small subunit processome in ribosome biogenesis-progress and prospects. *Wiley Interdiscip Rev RNA* **2**, 1-21 (2011).

159 Barandun, J. *et al.* The complete structure of the small-subunit processome. *Nat Struct Mol Biol* **24**, 944-953 (2017).

160 Wurm, J. P. *et al.* The ribosome assembly factor Nep1 responsible for Bowen-Conradi syndrome is a pseudouridine-N1-specific methyltransferase. *Nucleic Acids Res* **38**, 2387-2398 (2010).

161 Meyer, B. *et al.* The Bowen-Conradi syndrome protein Nep1 (Emg1) has a dual role in eukaryotic ribosome biogenesis, as an essential assembly factor and in the methylation of Psi1191 in yeast 18S rRNA. *Nucleic Acids Res* **39**, 1526-1537 (2011).

162 Warda, A. S. *et al.* Effects of the Bowen-Conradi syndrome mutation in EMG1 on its nuclear import, stability and nucleolar recruitment. *Human Molecular Genetics* **25**, 5353-5364 (2016).

163 Chaker-Margot, M., Barandun, J., Hunziker, M. & Klinge, S. Architecture of the yeast small subunit processome. *Science* **355** (2017).

164 Milkereit, P. *et al.* A Noc complex specifically involved in the formation and nuclear export of ribosomal 40 S subunits. *J Biol Chem* **278**, 4072-4081 (2003).

165 Ke, N., Wang, X., Xu, X. & Abassi, Y. A. The xCELLigence system for real-time and label-free monitoring of cell viability. *Methods Mol Biol* **740**, 33-43 (2011).

166 Szklarczyk, D. *et al.* STRING v11: protein-protein association networks with increased coverage, supporting functional discovery in genome-wide experimental datasets. *Nucleic Acids Res* **47**, 607-613 (2019).

167 Eden, E., Navon, R., Steinfeld, I., Lipson, D. & Yakhini, Z. GOrilla: a tool for discovery and visualization of enriched GO terms in ranked gene lists. *BMC Bioinformatics* **10**, 48 (2009).

168 Szklarczyk, D. *et al.* The STRING database in 2011: functional interaction networks of proteins, globally integrated and scored. *Nucleic Acids Res* **39**, D561-568 (2011).

169 Szklarczyk, D. *et al.* The STRING database in 2017: quality-controlled protein-protein association networks, made broadly accessible. *Nucleic Acids Res* **45**, 362-368 (2017).

170 Nagata, S. Apoptotic DNA fragmentation. *Exp Cell Res* **256**, 12-18, doi:10.1006/excr.2000.4834 (2000).

171 Zemp, I. *et al.* Distinct cytoplasmic maturation steps of 40S ribosomal subunit precursors require hRio2. *J Cell Biol* **185**, 1167-1180 (2009).

172 Tessarz, P. *et al.* Glutamine methylation in histone H2A is an RNA-polymerase-I-dedicated modification. *Nature* **505**, 564-568 (2014).

173 Fux, A., Korotkov, V. S., Schneider, M., Antes, I. & Sieber, S. A. Chemical Cross-Linking Enables Drafting ClpXP Proximity Maps and Taking Snapshots of In Situ Interaction Networks. *Cell Chem Biol* **26**, 48-59 (2019).

174 Ashburner, M. *et al.* Gene ontology: tool for the unification of biology. The Gene Ontology Consortium. *Nat Genet* **25**, 25-29 (2000).

175 Jäkel, S. & Görlich, D. Importin beta, transportin, RanBP5 and RanBP7 mediate nuclear import of ribosomal proteins in mammalian cells. *The EMBO journal* **17**, 4491-4502 (1998).

176 McCloskey, A., Ibarra, A. & Hetzer, M. W. Tpr regulates the total number of nuclear pore complexes per cell nucleus. *Genes & Development*, (2018).

177 Delavoie, F., Soldan, V., Rinaldi, D., Dauxois, J.-Y. & Gleizes, P.-E. The path of pre-ribosomes through the nuclear pore complex revealed by electron tomography. *Nature Communications* **10**, 497 (2019).

178 Wang, X. *et al.* Use of the novel technique of analytical ultracentrifugation with fluorescence detection system identifies a 77S monosomal translation complex. *Protein Sci* **21**, 1253-1268 (2012).

179 Bursac, S., Brdovcak, M. C., Donati, G. & Volarevic, S. Activation of the tumor suppressor p53 upon impairment of ribosome biogenesis. *Biochim Biophys Acta* **1842**, 817-830 (2014).

180 Sakr, A., Bregeon, F., Mege, J. L., Rolain, J. M. & Blin, O. Staphylococcus aureus Nasal Colonization: An Update on Mechanisms, Epidemiology, Risk Factors, and Subsequent Infections. *Front Microbiol* **9**, 2419 (2018).

181 Wertheim, H. F. L. *et al.* The role of nasal carriage in Staphylococcus aureus infections. *The Lancet Infectious Diseases* **5**, 751-762 (2005).

182 Thomer, L., Schneewind, O. & Missiakas, D. Pathogenesis of Staphylococcus aureus Bloodstream Infections. *Annu Rev Pathol* **11**, 343-364 (2016).

183 Turner, N. A. *et al.* Methicillin-resistant Staphylococcus aureus: an overview of basic and clinical research. *Nature Reviews Microbiology* **17**, 203-218 (2019).
184 Tong, S. Y., Davis, J. S., Eichenberger, E., Holland, T. L. & Fowler, V. G., Jr. Staphylococcus aureus infections: epidemiology, pathophysiology, clinical manifestations, and management. *Clin Microbiol Rev* **28**, 603-661 (2015).
185 Argudin, M. A., Mendoza, M. C. & Rodicio, M. R. Food poisoning and Staphylococcus aureus enterotoxins. *Toxins (Basel)* **2**, 1751-1773 (2010).
186 Peacock, S. J. & Paterson, G. K. Mechanisms of Methicillin Resistance in Staphylococcus aureus. *Annu Rev Biochem* **84**, 577-601 (2015).
187 McGuinness, W. A., Malachowa, N. & DeLeo, F. R. Vancomycin Resistance in Staphylococcus aureus. *Yale J Biol Med* **90**, 269-281 (2017).
188 Ribeiro da Cunha, B., Fonseca, L. P. & Calado, C. R. C. Antibiotic Discovery: Where Have We Come from, Where Do We Go? *Antibiotics (Basel)* **8** (2019).
189 Fair, R. J. & Tor, Y. Antibiotics and bacterial resistance in the 21st century. *Perspect Medicin Chem* **6**, 25-64 (2014).
190 Hede, K. Antibiotic resistance: An infectious arms race. *Nature* **509**, S2-3 (2014).
191 Alanis, A. J. Resistance to antibiotics: are we in the post-antibiotic era? *Arch Med Res* **36**, 697-705 (2005).
192 Sit, P. S. *et al.* Prevalence of methicillin-resistant Staphylococcus aureus (MRSA) infection and the molecular characteristics of MRSA bacteraemia over a two-year period in a tertiary teaching hospital in Malaysia. *BMC Infect Dis* **17**, 274 (2017).
193 Köck, R. *et al.* Vol. 15 (Robert Koch-Institut, 2010).
194 Klein, E., Smith, D. L. & Laxminarayan, R. Hospitalizations and deaths caused by methicillin-resistant Staphylococcus aureus, United States, 1999-2005. *Emerg Infect Dis* **13**, 1840-1846 (2007).
195 Bhattacharya, M. *et al.* Staphylococcus aureus biofilms release leukocidins to elicit extracellular trap formation and evade neutrophil-mediated killing. *Proc Natl Acad Sci U S A* **115**, 7416-7421 (2018).
196 Liu, C. *et al.* Clinical practice guidelines by the infectious diseases society of america for the treatment of methicillin-resistant Staphylococcus aureus infections in adults and children: executive summary. *Clin Infect Dis* **52**, 285-292 (2011).
197 Butler, M. S., Hansford, K. A., Blaskovich, M. A., Halai, R. & Cooper, M. A. Glycopeptide antibiotics: back to the future. *J Antibiot (Tokyo)* **67**, 631-644 (2014).
198 Walters M, L. D., Rasheed K, Albrecht, V, McAllister, S, Limbago B, & A., K. Investigation and Control of Vancomycin-resistant Staphylococcus aureus: A Guide for Health Departments and Infection Control Personnel. *Division of Healthcare Quality Promotion Centers for Disease Control and Prevention* (2015).
199 Lee, A. S. *et al.* Methicillin-resistant Staphylococcus aureus. *Nat Rev Dis Primers* **4**, 18033 (2018).
200 Mulani, M. S., Kamble, E. E., Kumkar, S. N., Tawre, M. S. & Pardesi, K. R. Emerging Strategies to Combat ESKAPE Pathogens in the Era of Antimicrobial Resistance: A Review. *Front Microbiol* **10**, 539 (2019).
201 Foster, T. J. Immune evasion by staphylococci. *Nat Rev Microbiol* **3**, 948-958 (2005).

202 Kong, C., Neoh, H. M. & Nathan, S. Targeting Staphylococcus aureus Toxins: A Potential form of Anti-Virulence Therapy. *Toxins (Basel)* **8** (2016).
203 Foster, T. J., Geoghegan, J. A., Ganesh, V. K. & Hook, M. Adhesion, invasion and evasion: the many functions of the surface proteins of Staphylococcus aureus. *Nat Rev Microbiol* **12**, 49-62 (2014).
204 Cole, G. W. & Silverberg, N. L. The Adherence of Staphylococcus aureus to Human Corneocytes. *JAMA Dermatology* **122**, 166-169 (1986).
205 Madani, A., Garakani, K. & Mofrad, M. R. K. Molecular mechanics of Staphylococcus aureus adhesin, CNA, and the inhibition of bacterial adhesion by stretching collagen. *PLoS One* **12** (2017).
206 Ni Eidhin, D. *et al.* Clumping factor B (ClfB), a new surface-located fibrinogen-binding adhesin of Staphylococcus aureus. *Mol Microbiol* **30**, 245-257 (1998).
207 Foster, T. J. & Höök, M. Surface protein adhesins of Staphylococcus aureus. *Trends in Microbiology* **6**, 484-488 (1998).
208 Heilmann, C. Adhesion mechanisms of staphylococci. *Adv Exp Med Biol* **715**, 105-123 (2011).
209 Guerra, F. E., Borgogna, T. R., Patel, D. M., Sward, E. W. & Voyich, J. M. Epic Immune Battles of History: Neutrophils vs. Staphylococcus aureus. *Front Cell Infect Microbiol* **7**, 286 (2017).
210 Hickey, M. J. & Kubes, P. Intravascular immunity: the host-pathogen encounter in blood vessels. *Nat Rev Immunol* **9**, 364-375 (2009).
211 Grumann, D., Nubel, U. & Broker, B. M. Staphylococcus aureus toxins--their functions and genetics. *Infect Genet Evol* **21**, 583-592 (2014).
212 Oliveira, D., Borges, A. & Simoes, M. Staphylococcus aureus Toxins and Their Molecular Activity in Infectious Diseases. *Toxins (Basel)* **10**, (2018).
213 Spaan, A. N., van Strijp, J. A. G. & Torres, V. J. Leukocidins: staphylococcal bi-component pore-forming toxins find their receptors. *Nat Rev Microbiol* **15**, 435-447 (2017).
214 Bhakdi, S. & Tranum-Jensen, J. Alpha-toxin of Staphylococcus aureus. *Microbiol Rev* **55**, 733-751 (1991).
215 Vandenesch, F., Lina, G. & Henry, T. Staphylococcus aureus hemolysins, bi-component leukocidins, and cytolytic peptides: a redundant arsenal of membrane-damaging virulence factors? *Front Cell Infect Microbiol* **2**, 12 (2012).
216 Spaulding, A. R. *et al.* Staphylococcal and streptococcal superantigen exotoxins. *Clin Microbiol Rev* **26**, 422-447 (2013).
217 Xu, S. X. & McCormick, J. K. Staphylococcal superantigens in colonization and disease. *Front Cell Infect Microbiol* **2**, 52 (2012).
218 Jin, T. *et al.* Staphylococcus aureus resists human defensins by production of staphylokinase, a novel bacterial evasion mechanism. *J Immunol* **172**, 1169-1176 (2004).
219 Ibberson, C. B. *et al.* Staphylococcus aureus hyaluronidase is a CodY-regulated virulence factor. *Infect Immun* **82**, 4253-4264 (2014).
220 Otto, M. Staphylococcus aureus toxins. *Curr Opin Microbiol* **17**, 32-37 (2014).
221 Tam, K. & Torres, V. J. Staphylococcus aureus Secreted Toxins and Extracellular Enzymes. *Microbiol Spectr* **7** (2019).

222 Novick, R. P. Autoinduction and signal transduction in the regulation of staphylococcal virulence. *Mol Microbiol* **48**, 1429-1449 (2003).
223 Liu, Q., Yeo, W. S. & Bae, T. The SaeRS Two-Component System of Staphylococcus aureus. *Genes (Basel)* **7** (2016).
224 Fournier, B. & Hooper, D. C. A new two-component regulatory system involved in adhesion, autolysis, and extracellular proteolytic activity of Staphylococcus aureus. *J Bacteriol* **182**, 3955-3964 (2000).
225 Szurmant, H., White, R. A. & Hoch, J. A. Sensor complexes regulating two-component signal transduction. *Curr Opin Struct Biol* **17**, 706-715 (2007).
226 Peng, H. L., Novick, R. P., Kreiswirth, B., Kornblum, J. & Schlievert, P. Cloning, characterization, and sequencing of an accessory gene regulator (agr) in Staphylococcus aureus. *J Bacteriol* **170**, 4365-4372 (1988).
227 Wang, B., Zhao, A., Novick, R. P. & Muir, T. W. Key driving forces in the biosynthesis of autoinducing peptides required for staphylococcal virulence. *Proc. Natl. Acad. Sci U.S.A.* **112**, 10679-10684 (2015).
228 Paulander, W. *et al.* The agr quorum sensing system in Staphylococcus aureus cells mediates death of sub-population. *BMC Research Notes* **11**, 503 (2018).
229 Choudhary, K. S. *et al.* The Staphylococcus aureus Two-Component System AgrAC Displays Four Distinct Genomic Arrangements That Delineate Genomic Virulence Factor Signatures. *Front Microbiol* **9**, 1082, (2018).
230 Quave, C. L. & Horswill, A. R. Flipping the switch: tools for detecting small molecule inhibitors of staphylococcal virulence. *Front Microbiol* **5**, 706 (2014).
231 Frees, D., Sorensen, K. & Ingmer, H. Global virulence regulation in Staphylococcus aureus: pinpointing the roles of ClpP and ClpX in the sar/agr regulatory network. *Infect Immun* **73**, 8100-8108 (2005).
232 Jensen, C., Fosberg, M. J., Thalsø-Madsen, I., Bæk, K. T. & Frees, D. Staphylococcus aureus ClpX localizes at the division septum and impacts transcription of genes involved in cell division, T7-secretion, and SaPI5-excision. *Scientific Reports* **9**, 16456 (2019).
233 Michel, A. *et al.* Global Regulatory Impact of ClpP Protease of Staphylococcus aureus on Regulons Involved in Virulence, Oxidative Stress Response, Autolysis, and DNA Repair. *Journal of Bacteriology* **188**, 5783-5796 (2006).
234 Frees, D., Qazi, S. N., Hill, P. J. & Ingmer, H. Alternative roles of ClpX and ClpP in Staphylococcus aureus stress tolerance and virulence. *Mol Microbiol* **48**, 1565-1578 (2003).
235 Frees, D., Thomsen, L. E. & Ingmer, H. Staphylococcus aureus ClpYQ plays a minor role in stress survival. *Arch Microbiol* **183**, 286-291 (2005).
236 Donegan, N. P., Marvin, J. S. & Cheung, A. L. Role of adaptor TrfA and ClpPC in controlling levels of SsrA-tagged proteins and antitoxins in Staphylococcus aureus. *J Bacteriol* **196**, 4140-4151 (2014).
237 Lupas, A., Flanagan, J. M., Tamura, T. & Baumeister, W. Self-compartmentalizing proteases. *Trends in Biochemical Sciences* **22**, 399-404 (1997).
238 Moreno-Cinos, C. *et al.* ClpP Protease, a Promising Antimicrobial Target. *Int J Mol Sci* **20** (2019).

239 Malik, I. T. & Brotz-Oesterhelt, H. Conformational control of the bacterial Clp protease by natural product antibiotics. *Nat Prod Rep* **34**, 815-831 (2017).
240 Stahlhut, S. G. *et al.* The ClpXP protease is dispensable for degradation of unfolded proteins in Staphylococcus aureus. *Sci Rep* **7**, 11739 (2017).
241 Kwon, H. Y. *et al.* The ClpP protease of Streptococcus pneumoniae modulates virulence gene expression and protects against fatal pneumococcal challenge. *Infect Immun* **72**, 5646-5653 (2004).
242 Gaillot, O., Pellegrini, E., Bregenholt, S., Nair, S. & Berche, P. The ClpP serine protease is essential for the intracellular parasitism and virulence of Listeria monocytogenes. *Mol Microbiol* **35**, 1286-1294 (2000).
243 Liu, Q. *et al.* The ATP-Dependent Protease ClpP Inhibits Biofilm Formation by Regulating Agr and Cell Wall Hydrolase Sle1 in Staphylococcus aureus. *Front Cell Infect Microbiol* **7**, 181, doi:10.3389/fcimb.2017.00181 (2017).
244 Griffith, E. C. *et al.* Ureadepsipeptides as ClpP Activators. *ACS Infectious Diseases* **5**, 1915-1925 (2019).
245 Bhandari, V. *et al.* The Role of ClpP Protease in Bacterial Pathogenesis and Human Diseases. *ACS Chemical Biology* **13**, 1413-1425 (2018).
246 Kajfasz, J. K., Abranches, J. & Lemos, J. A. Transcriptome analysis reveals that ClpXP proteolysis controls key virulence properties of Streptococcus mutans. *Microbiology* **157**, 2880-2890 (2011).
247 Bonar, E., Wojcik, I. & Wladyka, B. Proteomics in studies of Staphylococcus aureus virulence. *Acta Biochim Pol* **62**, 367-381 (2015).
248 Arnaud, M., Chastanet, A. & Debarbouille, M. New vector for efficient allelic replacement in naturally nontransformable, low-GC-content, gram-positive bacteria. *Appl Environ Microbiol* **70**, 6887-6891 (2004).
249 Higuchi, R., Krummel, B. & Saiki, R. K. A general method of in vitro preparation and specific mutagenesis of DNA fragments: study of protein and DNA interactions. *Nucleic Acids Res* **16**, 7351-7367 (1988).
250 Barras, F. & Marinus, M. G. The great GATC: DNA methylation in E. coli. *Trends in Genetics* **5**, 139-143 (1989).
251 Palmer, B. R. & Marinus, M. G. The dam and dcm strains of Escherichia coli — a review. *Gene* **143**, 1-12 (1994).
252 Jones, M. J., Donegan, N. P., Mikheyeva, I. V. & Cheung, A. L. Improving transformation of Staphylococcus aureus belonging to the CC1, CC5 and CC8 clonal complexes. *PLoS One* **10** (2015).
253 Kreiswirth, B. N. *et al.* The toxic shock syndrome exotoxin structural gene is not detectably transmitted by a prophage. *Nature* **305**, 709-712 (1983).
254 Monk, I. R., Shah, I. M., Xu, M., Tan, M. W. & Foster, T. J. Transforming the untransformable: application of direct transformation to manipulate genetically Staphylococcus aureus and Staphylococcus epidermidis. *MBio* **3**, doi:10.1128/mBio.00277-11 (2012).
255 Krysiak, J. *et al.* Quantitative Map of β-Lactone-Induced Virulence Regulation. *Journal of Proteome Research* **16**, 1180-1192 (2017).

256 Frees, D. *et al.* Clp ATPases are required for stress tolerance, intracellular replication and biofilm formation in Staphylococcus aureus. *Mol Microbiol* **54**, 1445-1462 (2004).

257 Frees, D. *et al.* New Insights into Staphylococcus aureus Stress Tolerance and Virulence Regulation from an Analysis of the Role of the ClpP Protease in the Strains Newman, COL, and SA564. *Journal of Proteome Research* **11**, 95-108 (2012).

258 Chatterjee, I. *et al.* Staphylococcus aureus ClpC ATPase is a late growth phase effector of metabolism and persistence. *Proteomics* **9**, 1152-1176 (2009).

259 Tan, L., Li, S. R., Jiang, B., Hu, X. M. & Li, S. Therapeutic Targeting of the Staphylococcus aureus Accessory Gene Regulator (agr) System. *Front Microbiol* **9**, 55 (2018).

260 Xue, T., You, Y., Shang, F. & Sun, B. Rot and Agr system modulate fibrinogen-binding ability mainly by regulating clfB expression in Staphylococcus aureus NCTC8325. *Med Microbiol Immunol* **201**, 81-92 (2012).

261 Gupta, R. K., Luong, T. T. & Lee, C. Y. RNAIII of the Staphylococcus aureus agr system activates global regulator MgrA by stabilizing mRNA. *Proc Natl Acad Sci U.S.A.* **112**, 14036-14041 (2015).

262 Ingavale, S. S., Van Wamel, W. & Cheung, A. L. Characterization of RAT, an autolysis regulator in Staphylococcus aureus. *Mol Microbiol* **48**, 1451-1466 (2003).

263 Manna, A. C., Ingavale, S. S., Maloney, M., van Wamel, W. & Cheung, A. L. Identification of sarV (SA2062), a new transcriptional regulator, is repressed by SarA and MgrA (SA0641) and involved in the regulation of autolysis in Staphylococcus aureus. *J Bacteriol* **186**, 5267-5280 (2004).

264 Sahukhal, G. S. & Elasri, M. O. Identification and characterization of an operon, msaABCR, that controls virulence and biofilm development in Staphylococcus aureus. *BMC Microbiol* **14**, 154 (2014).

265 Zhu, L. *et al.* Staphylococcus aureus MazF specifically cleaves a pentad sequence, UACAU, which is unusually abundant in the mRNA for pathogenic adhesive factor SraP. *J Bacteriol* **191**, 3248-3255 (2009).

266 Goncheva, M. I. *et al.* Stress-induced inactivation of the Staphylococcus aureus purine biosynthesis repressor leads to hypervirulence. *Nat Commun* **10**, 775 (2019).

267 Kofoed, E. M. *et al.* De Novo Guanine Biosynthesis but Not the Riboswitch-Regulated Purine Salvage Pathway Is Required for Staphylococcus aureus Infection In Vivo. *J Bacteriol* **198**, 2001-2015 (2016).

268 Baxter-Gabbard, K. L. & Pattee, P. A. Purine biosynthesis in Staphylococcus aureus. *Archiv für Mikrobiologie* **71**, 40-48 (1970).

269 Chattoraj, P., Banerjee, A., Biswas, S. & Biswas, I. ClpP of Streptococcus mutans differentially regulates expression of genomic islands, mutacin production, and antibiotic tolerance. *J Bacteriol* **192**, 1312-1323 (2010).

270 Copin, R. *et al.* Sequential evolution of virulence and resistance during clonal spread of community-acquired methicillin-resistant Staphylococcus aureus. *Proc Natl Acad Sci U S A* **116**, 1745-1754 (2019).

271 Luong, T. T., Dunman, P. M., Murphy, E., Projan, S. J. & Lee, C. Y. Transcription Profiling of the mgrA Regulon in Staphylococcus aureus. *J Bacteriol* **188**, 1899-1910 (2006).

272 Wang, W. *et al.* Transposon Mutagenesis Identifies Novel Genes Associated with Staphylococcus aureus Persister Formation. *Front Microbiol* **6**, 1437 (2015).

273 Seo, J. H. *et al.* The Mitochondrial Unfoldase-Peptidase Complex ClpXP Controls Bioenergetics Stress and Metastasis. *PLOS Biology* **14** (2016).

274 Monk, I. R. *et al.* Zinc-binding to the cytoplasmic PAS domain regulates the essential WalK histidine kinase of Staphylococcus aureus. *Nat Commun* **10**, 3067 (2019).

275 Dubrac, S., Bisicchia, P., Devine, K. M. & Msadek, T. A matter of life and death: cell wall homeostasis and the WalKR (YycGF) essential signal transduction pathway. *Mol Microbiol* **70**, 1307-1322 (2008).

276 Becker, S., Frankel, M. B., Schneewind, O. & Missiakas, D. Release of protein A from the cell wall of Staphylococcus aureus. *Proc Natl Acad Sci U.S.A.* **111**, 1574-1579 (2014).

277 Zheng, L., Yan, M., Fan, F. & Ji, Y. The Essential WalK Histidine Kinase and WalR Regulator Differentially Mediate Autolysis of Staphylococcus aureus RN4220. *Journal of nature and science* **1** (2015).

278 Hammer, N. D. & Skaar, E. P. Molecular mechanisms of Staphylococcus aureus iron acquisition. *Annu Rev Microbiol* **65**, 129-147 (2011).

279 Grigg, J. C., Ukpabi, G., Gaudin, C. F. & Murphy, M. E. Structural biology of heme binding in the Staphylococcus aureus Isd system. *J Inorg Biochem* **104**, 341-348 (2010).

280 Farrand, A. J., Reniere, M. L., Ingmer, H., Frees, D. & Skaar, E. P. Regulation of host hemoglobin binding by the Staphylococcus aureus Clp proteolytic system. *J Bacteriol* **195**, 5041-5050 (2013).

281 Gaupp, R., Ledala, N. & Somerville, G. A. Staphylococcal response to oxidative stress. *Front Cell Infect Microbiol* **2**, 33 (2012).

282 Halliwell B., G. J. M. *Free Radicals in Biology and Medicine*. 5 edn, (Oxford University Press, 2015).

283 Zhou, C. *et al.* Urease is an essential component of the acid response network of Staphylococcus aureus and is required for a persistent murine kidney infection. *PLoS Pathog* **15** (2019).

284 Frees, D. *et al.* New insights into Staphylococcus aureus stress tolerance and virulence regulation from an analysis of the role of the ClpP protease in the strains Newman, COL, and SA564. *J Proteome Res* **11**, 95-108 (2012).

285 Fetzer, C. *Virulence Attenuation through Chemical and Genetic Manipulation of the Staphylococcus aureus ClpXP Protease*, Technichal University of Munich, (2017).

286 Romero Pastrana, F. *et al.* Human antibody responses against non-covalently cell wall-bound Staphylococcus aureus proteins. *Sci Rep* **8**, 3234 (2018).

287 van Wamel, W. J., Rooijakkers, S. H., Ruyken, M., van Kessel, K. P. & van Strijp, J. A. The innate immune modulators staphylococcal complement inhibitor and

chemotaxis inhibitory protein of Staphylococcus aureus are located on beta-hemolysin-converting bacteriophages. *J Bacteriol* **188**, 1310-1315 (2006).

288 Kok, M., Bron, G., Erni, B. & Mukhija, S. Effect of enzyme I of the bacterial phosphoenolpyruvate : sugar phosphotransferase system (PTS) on virulence in a murine model. *Microbiology* **149**, 2645-2652 (2003).

289 Cheung, A. L., Schmidt, K., Bateman, B. & Manna, A. C. SarS, a SarA homolog repressible by agr, is an activator of protein A synthesis in Staphylococcus aureus. *Infect Immun* **69**, 2448-2455 (2001).

290 Fan, X. *et al.* Diversity of penicillin-binding proteins. Resistance factor FmtA of Staphylococcus aureus. *J Biol Chem* **282** (2007).

291 Rohrer, S. & Berger-Bachi, B. FemABX peptidyl transferases: a link between branched-chain cell wall peptide formation and beta-lactam resistance in gram-positive cocci. *Antimicrob Agents Chemother* **47**, 837-846 (2003).

292 Delaune, A. *et al.* Peptidoglycan crosslinking relaxation plays an important role in Staphylococcus aureus WalKR-dependent cell viability. *PLoS One* **6** (2011).

293 Oshida, T. *et al.* A Staphylococcus aureus autolysin that has an N-acetylmuramoyl-L-alanine amidase domain and an endo-beta-N-acetylglucosaminidase domain: cloning, sequence analysis, and characterization. *Proc Natl Acad Sci U S A* **92**, 285-289 (1995).

294 Frankel, M. B., Hendrickx, A. P., Missiakas, D. M. & Schneewind, O. LytN, a murein hydrolase in the cross-wall compartment of Staphylococcus aureus, is involved in proper bacterial growth and envelope assembly. *J Biol Chem* **286**, 32593-32605 (2011).

295 Stapleton, M. R. *et al.* Characterization of IsaA and SceD, two putative lytic transglycosylases of Staphylococcus aureus. *J Bacteriol* **189**, 7316-7325 (2007).

296 Frankel, B. A., Kruger, R. G., Robinson, D. E., Kelleher, N. L. & McCafferty, D. G. Staphylococcus aureus sortase transpeptidase SrtA: insight into the kinetic mechanism and evidence for a reverse protonation catalytic mechanism. *Biochemistry* **44**, 11188-11200 (2005).

297 Josefsson, E. *et al.* Three new members of the serine-aspartate repeat protein multigene family of Staphylococcus aureus. *Microbiology* **144**, 3387-3395 (1998).

298 Siboo, I. R., Chaffin, D. O., Rubens, C. E. & Sullam, P. M. Characterization of the accessory Sec system of Staphylococcus aureus. *J Bacteriol* **190**, 6188-6196 (2008).

299 Jenul, C. & Horswill, A. R. Regulation of Staphylococcus aureus Virulence. *Microbiol Spectr* **6** (2018).

300 Graham, J. W., Lei, M. G. & Lee, C. Y. Trapping and identification of cellular substrates of the Staphylococcus aureus ClpC chaperone. *J Bacteriol* **195**, 4506-4516 (2013).

301 McGillivray, S. M. *et al.* Pharmacological inhibition of the ClpXP protease increases bacterial susceptibility to host cathelicidin antimicrobial peptides and cell envelope-active antibiotics. *Antimicrob Agents Chemother* **56**, 1854-1861 (2012).

302 Bronner, S., Monteil, H. & Prevost, G. Regulation of virulence determinants in Staphylococcus aureus: complexity and applications. *FEMS Microbiol Rev* **28**, 183-200 (2004).

303 Wessel, D. & Flugge, U. I. A method for the quantitative recovery of protein in dilute solution in the presence of detergents and lipids. *Anal Biochem* **138**, 141-143 (1984).
304 Nagel, A. *et al.* Inhibition of Rho Activity Increases Expression of SaeRS-Dependent Virulence Factor Genes in Staphylococcus aureus, Showing a Link between Transcription Termination, Antibiotic Action, and Virulence. *MBio* **9** (2018).
305 Gao, P. *et al.* Suppression of Staphylococcus aureus virulence by a small-molecule compound. *Proc Natl Acad Sci U.S.A* **115**, 8003-8008 (2018).
306 Paharik, A. E. *et al.* The Spl Serine Proteases Modulate Staphylococcus aureus Protein Production and Virulence in a Rabbit Model of Pneumonia. *mSphere* **1** (2016).
307 Bourgeois, I. *et al.* Characterization of AtlL, a bifunctional autolysin of Staphylococcus lugdunensis with N-acetylglucosaminidase and N-acetylmuramoyl-l-alanine amidase activities. *FEMS Microbiol Lett* **290**, 105-113 (2009).
308 Jorge, A. M., Hoiczyk, E., Gomes, J. P. & Pinho, M. G. EzrA contributes to the regulation of cell size in Staphylococcus aureus. *PLoS One* **6** (2011).
309 Seluanov, A. & Bibi, E. FtsY, the prokaryotic signal recognition particle receptor homologue, is essential for biogenesis of membrane proteins. *J Biol Chem* **272**, 2053-2055 (1997).
310 Downer, R., Roche, F., Park, P. W., Mecham, R. P. & Foster, T. J. The elastin-binding protein of Staphylococcus aureus (EbpS) is expressed at the cell surface as an integral membrane protein and not as a cell wall-associated protein. *J Biol Chem* **277**, 243-250 (2002).
311 Clarke, S. R., Harris, L. G., Richards, R. G. & Foster, S. J. Analysis of Ebh, a 1.1-Megadalton Cell Wall-Associated Fibronectin-Binding Protein of Staphylococcus aureus. *Infection and Immunity* **70**, 6680-6687 (2002).
312 Lu, D. *et al.* Structure-based mechanism of lipoteichoic acid synthesis by Staphylococcus aureus LtaS. *Proc Natl Acad Sci U S A* **106**, 1584-1589 (2009).
313 van den Berg van Saparoea, H. B. *et al.* Fine-mapping the contact sites of the Escherichia coli cell division proteins FtsB and FtsL on the FtsQ protein. *J Biol Chem* **288**, 24340-24350 (2013).
314 Xu, T. *et al.* Identification of Genes Controlled by the Essential YycFG Two-Component System Reveals a Role for Biofilm Modulation in Staphylococcus epidermidis. *Front Microbiol* **8**, 724 (2017).
315 Liu, Q. *et al.* Rewiring of the FtsH regulatory network by a single nucleotide change in saeS of Staphylococcus aureus. *Sci Rep* **7**, 8456 (2017).
316 Askarian, F. *et al.* The interaction between Staphylococcus aureus SdrD and desmoglein 1 is important for adhesion to host cells. *Scientific Reports* **6** (2016).
317 Jelsbak, L. *et al.* The chaperone ClpX stimulates expression of Staphylococcus aureus protein A by Rot dependent and independent pathways. *PLoS One* **5** (2010).
318 Chen, J., Ram, G., Penades, J. R., Brown, S. & Novick, R. P. Pathogenicity island-directed transfer of unlinked chromosomal virulence genes. *Mol Cell* **57**, 138-149 (2015).

319 Kwiecinski, J. M. *et al.* Staphylococcus aureus adhesion in endovascular infections is controlled by the ArlRS-MgrA signaling cascade. *PLoS Pathog* **15** (2019).

320 Farrand, A. J. *et al.* Proteomic analyses of iron-responsive, Clp-dependent changes in Staphylococcus aureus. *Pathog Dis* **73** (2015).

321 Monteiro, M. S., Carvalho, M., Bastos, M. L. & Guedes de Pinho, P. Metabolomics analysis for biomarker discovery: advances and challenges. *Curr Med Chem* **20**, 257-271 (2013).

322 Wishart, D. S. Emerging applications of metabolomics in drug discovery and precision medicine. *Nature Reviews Drug Discovery* **15**, 473-484 (2016).

323 Raro, M. *et al.* Untargeted metabolomics in doping control: detection of new markers of testosterone misuse by ultrahigh performance liquid chromatography coupled to high-resolution mass spectrometry. *Anal Chem* **87**, 8373-8380 (2015).

324 Sevin, D. C., Fuhrer, T., Zamboni, N. & Sauer, U. Nontargeted in vitro metabolomics for high-throughput identification of novel enzymes in Escherichia coli. *Nat Methods* **14**, 187-194 (2017).

325 Theodoridis, G. A., Gika, H. G., Want, E. J. & Wilson, I. D. Liquid chromatography-mass spectrometry based global metabolite profiling: a review. *Anal Chim Acta* **711**, 7-16 (2012).

326 Prosser, G. A., Larrouy-Maumus, G. & de Carvalho, L. P. Metabolomic strategies for the identification of new enzyme functions and metabolic pathways. *EMBO Rep* **15**, 657-669 (2014).

327 Schrimpe-Rutledge, A. C., Codreanu, S. G., Sherrod, S. D. & McLean, J. A. Untargeted Metabolomics Strategies-Challenges and Emerging Directions. *J Am Soc Mass Spectrom* **27**, 1897-1905 (2016).

328 Patti, G. J., Yanes, O. & Siuzdak, G. Innovation: Metabolomics: the apogee of the omics trilogy. *Nat Rev Mol Cell Biol* **13**, 263-269 (2012).

329 Tsakelidou, E. *et al.* Sample Preparation Strategies for the Effective Quantitation of Hydrophilic Metabolites in Serum by Multi-Targeted HILIC-MS/MS. *Metabolites* **7** (2017).

330 Guijas, C. *et al.* METLIN: A Technology Platform for Identifying Knowns and Unknowns. *Anal Chem* **90**, 3156-3164 (2018).

331 Wishart, D. S. *et al.* HMDB 4.0: the human metabolome database for 2018. *Nucleic Acids Res* **46**, 608-617 (2018).

332 Ramirez-Gaona, M. *et al.* YMDB 2.0: a significantly expanded version of the yeast metabolome database. *Nucleic Acids Res* **45**, D440-D445 (2017).

333 Sajed, T. *et al.* ECMDB 2.0: A richer resource for understanding the biochemistry of E. coli. *Nucleic Acids Res* **44**, 495-501 (2016).

334 Ebinger, S. *et al.* Characterization of Rare, Dormant, and Therapy-Resistant Cells in Acute Lymphoblastic Leukemia. *Cancer Cell* **30**, 849-862 (2016).

335 Nicoletti, I., Migliorati, G., Pagliacci, M. C., Grignani, F. & Riccardi, C. A rapid and simple method for measuring thymocyte apoptosis by propidium iodide staining and flow cytometry. *J Immunol Methods* **139**, 271-279 (1991).

336 Riccardi, C. & Nicoletti, I. Analysis of apoptosis by propidium iodide staining and flow cytometry. *Nat Protoc* **1**, 1458-1461 (2006).

337 Koczian, F. *et al.* Targeting the endoplasmic reticulum-mitochondria interface sensitizes leukemia cells to cytostatics. *Haematologica* **104**, 546-555 (2019).

5. Appendix

Supplementary tables

Table 21: Clinical characteristics of patients from which PDX cells were derived are shown.

Sample	Disease stage	Age	Sex	Subtype	Karyotype
ALL-50	initial diagnosis	7	female	pre-B	t(1;19)
ALL-199	relapse 2	8	female	pre-B	somatic trisomy 21
ALL-707	initial diagnosis	2	male	pro-B	t(4;11)

Table 22: Reporter ion isotopic distributions as stated in product data sheet for TMT10plex™ Label reagent set (LOT number:SF239894). Reporter ion isotopic distributions were used as isotope correction factors in MaxQuant data analysis.

Mass Tag	Reporter Ion	-2	-1	Monoisotopic	+1	+2
TMT^{10}-126	126.127726	0.0%	0.0%	100%	6.9%(127C)	0.1%(128C)
TMT^{10}-127N	127.124761	0.0%	0.4%	100%	7.3%(128N)	0.2%(129N)
TMT^{10}-127C	127.131081	0.0%	0.6%(126)	100%	5.9%(128C)	0.0%(129C)
TMT^{10}-128N	128.128116	0.0%	0.4%(127N)	100%	4.1%(129N)	0.0%(130N)
TMT^{10}-128C	128.134436	0.0%(126)	1.4%(127C)	100%	5.1%(129C)	0.0%(130C)
TMT^{10}-129N	129.131471	0.0%(127N)	1.4%(128N)	100%	5.0%(130N)	0.0(131)
TMT^{10}-129C	129.137790	0.0%(127C)	2.3%(128C)	100%	4.3%(130C)	0.0%
TMT^{10}-130N	130.134825	0.0%(128N)	2.7%(129N)	100%	3.9%(131)	0.0%
TMT^{10}-130C	130.141145	0.0%(128C)	2.9%(129C)	100%	3.3%	0.0%
TMT^{10}-131	131.138180	0.0%(129N)	3.4%(130N)	100%	3.3%	0.0%

Table 23: Overview of TMT slots used for incubation with temperature dependent sample fractions.

Mass Tag	Temperature point
TMT^{10}-126	37.0°C
TMT^{10}-127N	41.2°C
TMT^{10}-127C	44.0°C
TMT^{10}-128N	48.5°C
TMT^{10}-129N	53.1°C
TMT^{10}-129C	56.3°C
TMT^{10}-130N	59.3°C
TMT^{10}-130C	62.5°C
TMT^{10}-131	67.1°C

Table 24: Proteins enriched in MS-based Co-IP experiments after treatment with VioA for 24h. Cells were treated with **VioA** (10 nM) or DMSO, respectively prior to incubation with 2 mM DSSO crosslinker for chemical cross-linking of protein-protein interactions and subsequent pull down using an anti-NOP14 antibody or isotype control (n=4). Significantly enriched proteins (log_2 enrichment > 2, $-log_{10}$ *t*-test *p*-value > 1.3) are listed.

log_2 enrichment	$-log_{10}$ (*t*-test *p*-value)	Gene	Protein
7.61	4.93	TFG; TFG/ALK fusion	Protein TFG; Tyrosine-protein kinase receptor
6.70	5.24	SNAP29	Synaptosomal-associated protein 29
6.00	5.26	NOC4L	Nucleolar complex protein 4 homolog
5.67	5.35	NOP14	Nucleolar protein 14
5.65	5.90	NANS	Sialic acid synthase
4.94	5.37	DECR	2,4-dienoyl-CoA reductase, mitochondrial

3.45	3.46	MTCL1	Microtubule cross-linking factor 1
3.26	4.25	GFPT1	Glutamine-fructose-6-phsphate aminotransferase [isomerizing] 1
3.21	3.68	DTWD2	DTW domain-containing protein 2
2.78	2.24	IPO5	Importin-5
2.76	2.75	CIZ1	Cip1-interacting zinc finger protein
2.69	3.23	TPR	Nucleoprotein TPR
2.60	4.93	SEPT7	Septin-7
2.44	4.07	HNRNPA2B1;HNRPA2B1	Heterogeneous nuclear ribonucleoproteins A2/B1
2.39	4.35	NAPA	Alpha-soluble NSF attachment protein
2.38	3.63	HSD17B10	3-hydroxyacyl-CoA dehydrogenase type-2
2.30	1.79	SEPT2	Septin-2
2.15	3.05	PPA1	Inorganic pyrophosphatase
2.11	1.88	SEC22B	Vesicle-trafficking protein SEC22b

Table 25: Significantly downregulated (log_2 ratio ≤ 1, $-log_{10}$ t-test p-value > 1.3) proteins in Δ*clpP* mutants in comparison to the wildtype control. Proteins were categorized according to their KEGG and GO assessment as analyzed by Perseus.

Gene name	Uniprot ID	log_2 ratio *ΔclpP*/wt	$-log_{10}$ *t*-test *p*-value
Virulence			
agrA/SAOUHSC_02265	Q2FWM4	-1.14	3.34
agrB	Q2FWM7	-1.61	3.49
chp	Q2FWV5	-1.83	2.53
cvfB	Q2FYP3	-1.03	5.55
hld	Q2FWM8	-2.54	4.27
mazF	Q2FWI8	-1.91	2.84
mgrA	Q2G0B1	-2.33	8.35
rbsV	P60070	-1.13	3.38
rsbW	Q2FWJ3	-1.34	4.47
SAOUHSC_02160	Q2FWW2		
sarX	Q2G0D1	-3.23	10.85
sarZ	Q2FVN3	-3.95	7.56
sigB/SAOUHSC_02298	Q2FWJ4	-1.12	2.52
sspB	Q2FZL3	-1.05	1.94
sspP	Q2G2R8	-3.70	7.99
Purine metabolism			
guaA	Q2G0Y6	-2.11	8.28
guaB	Q2G0Y7	-1.81	11.48
purC	Q2FZJ3	-1.07	3.83
purD	Q2FZI3	-1.09	6.09
purE	Q2FZJ5	-1.33	4.97
purF	Q2FZI9	-1.40	6.30

purK	Q2FZJ4	-1.04	5.48
purL	Q2FZJ0	-1.50	5.24
purM	Q2FZI8	-1.36	5.80
purN	Q2FZI7	-1.98	2.89
purQ	Q2FZJ1	-1.70	2.98
purS	Q2FZJ2	-1.10	4.45
UMP *de novo* biosynthesis			
carA	Q2FZ73	-4.22	5.11
carB	Q2FZ72	-3.34	13.47
pyrB	Q2FZ75	-4.01	10.97
pyrC	Q2FZ74	-3.81	11.08
pyrE	Q2FZ70	-3.78	5.63
pyrF	Q2FZ71	-3.65	6.86
pyrR	Q2FZ77	-1.84	7.95
Succinate dehydrogenase complex			
SAOUHSC_01104 (putative: sdhA)	Q2FZC7	-2.46	5.87
SAOUHSC_01105 (putative: sdhB)	Q2FZC8	-1.74	8.46
SAOUHSC_01103 (putative: sdhC)	Q2FZC9	-2.77	4.61
Amino acid metabolism			
asd	Q2FYP0	-1.86	7.68
dapB	Q9EZ11	-1.13	3.65
dapH	Q2FYN7	-1.69	5.13
metE	Q2G122	-4.23	8.72
thrB	Q2FYV2	-1.62	2.24
SAOUHSC_01321 (putative: thrC)	Q2FYV3	-2.08	8.02

Table 26: Significantly upregulated (log_2 ratio ≥ 1, $-log_{10}$ t-test p-value > 1.3) proteins in Δ*clpP* mutants in comparison to wildtype control. Proteins were categorized according to their KEGG and GO assessment as analyzed by Perseus.

Gene name	Uniprot ID	log_2 ratio *ΔclpP*/wt	$-log_{10}$ *t*-test *p*-value
Chaperone/stress response			
clpB	Q2FZS8	2.60	11.00
clpC	Q2G0P5	2.64	12.54
ctsR	Q2G0P8	3.53	6.77
dnaJ	Q2FXZ3	1.46	6.05
dnaK	Q2FXZ2	1.10	5.75
groL	Q2FWN4	1.61	7.90
groS	Q2FWN3	1.17	3.06
grpE	Q2FXZ1	1.33	6.48
hrcA	Q2FXZ0	1.72	7.85
mcsA/SAOUHSC_00503	Q2G0P7	2.60	6.43
mcsB	Q2G0P6	2.29	9.44
Isd system			
isdA	Q2FZE9	1.81	4.07

isdB	Q2FZF0	3.83	5.06
isdE	Q2FZE6	0.99	4.27
isdH	Q2FXJ2	4.59	6.15
Staphyloferrin B synthesis			
sbnA	Q2G1N3	6.26	12.08
SAOUHSC_00076 (putative sbnB)	Q2G1N2	1.88	5.83
SAOUHSC_00077 (putative sbnC	Q2G1N1	4.87	8.05
SAOUHSC_00079 (putative sbnE)	Q2G1M9	5.07	9.52
SAOUHSC_00080 (putative sbnF)	Q2G1M8	4.27	11.80
SAOUHSC_00081 (putative sbnG)	Q2G1M7	3.76	1.41
SAOUHSC_00082 (putative sbnH)	Q2G1M6	6.40	2.12
SAOUHSC_00083 (putative sbnI)	Q2G1M5	3.08	4.46
Ribosomal proteins			
rpmA	Q2FXT0	1.24	3.38
rplI	Q2G2T3	3.38	9.69
rplN	Q2FW16	1.00	1.89
rplR	Q2FW22	2.49	4.07
rpsL	P0A0H0	4.40	2.10
rpsP	Q2FZ45	1.35	3.13
rpsR	Q2G111	1.85	4.41
Urease complex			
ureA	Q2FVW5	4.11	5.49
ureB	Q2G2K6	4.65	7.36
ureC	Q2G2K5	7.41	12.28
ureD	Q2G272	2.11	4.89
ureE	Q2G273	3.58	8.04
ureF	Q2G2K7	2.15	3.05
ureG	Q2G273	3.46	8.76
Virulence			
asp3	Q2FUW5	1.40	3.73
clfA	G0XY21	1.90	5.79
clfB	Q2FUY2	1.08	3.82
ebpS	Q2FYF1	2.00	5.97
fnbA	P14738	3.83	4.59
ftmA	Q2FZK3	1.34	5.18
sasG	Q2G2B2	1.34	4.68
sbi	Q2FVK5	1.15	3.48
secA2	Q2FUW6	1.89	5.76
sraP	Q2FUW1	2.23	6.27
walK/walR regulated proteins			
lytM	O33599	3.70	6.43
lytN	Q9ZNI1	5.69	8.35
sceD	Q2FWF8	4.05	5.09
sle1	Q2G0U9	2.69	5.33
ssaA	Q2FV55	1.23	2.85

ssaA2	Q2G2J2	1.32	3.64
walR	Q2G2U6	1.18	4.70

Table 27: Significantly downregulated (log_2 ratio ≤ -1, $-log_{10}$ t-test p-value > 1.3) proteins in Δ*clpX* mutants in comparison to wildtype control. Proteins were categorized according to their KEGG and GO assessment as analyzed by Perseus.

Gene name	Uniprot ID	log_2 ratio *ΔclpX/wt*	$-log_{10}$ *t*-test *p*-value
ABC transporters			
metN2	Q2FZZ2	-2.33	10.67
SAOUHSC_00074	Q2G1N4	-1.04	3.76
SAOUHSC_00167	Q2G1F8	-2.24	5.01
SAOUHSC_00170	Q2G1F5	-2.37	3.84
SAOUHSC_00175	Q2G1F0	-1.20	2.99
SAOUHSC_00176	Q2G1E9	-1.29	2.56
SAOUHSC_00426	Q2G0V0	-2.24	7.40
SAOUHSC_00923	Q2FZR7	-2.79	4.35
SAOUHSC_00924	Q2FZR6	-1.30	6.30
SAOUHSC_00925	Q2FZR5	-1.12	5.25
SAOUHSC_00926	Q2FZR4	-1.49	4.93
SAOUHSC_02430	Q2FW75	-1.20	3.61
SAOUHSC_03019	Q2FUT2	-1.23	1.94
Na+/H+ Antiporter			
mnhA2	Q2G2U8	-1.10	2.12
mnhD1	Q2G2H7	-2.16	2.74
mnhE1	Q2G2H8	-1.04	1.34
Virulence			
agrB	Q2FWM7	-1.54	3.09
arlR	Q9KJN4	-1.63	2.78
hld	Q2FWM8	-1.06	2.20
hly	Q2G1X0	-1.85	7.32
lip2	Q2G155	-1.97	8.56
mazF	Q2FWI8	-1.77	3.74
mgrA	Q2G0B1	-1.47	5.53
SAOUHSC_00870	Q2FZW5	-3.40	4.15
SAOUHSC_02161	Q2FWW1	-1.23	6.05
sarS	Q2G1N7	-1.77	5.57
sarX	Q2G0D1	-1.66	8.43
sarZ	Q2FVN3	-3.76	6.72
scn	Q2FWV6	-3.03	4.70
SAOUHSC_02298 (sigB)	Q2FWJ4	-1.13	2.07

spa	P02976	-3.05	7.54
Purine/Pyrimidin metabolism			
carA	Q2FZ73	-1.54	2.60
guaA	Q2G0Y6	-1.68	9.05
guaB	Q2G0Y7	-1.36	9.89
ndk	Q2FYG7	-1.17	4.88
pyrE	Q2FZ70	-1.46	5.09
rpoE	Q2FWD0	-1.38	4.35
SAOUHSC_00742	Q2G078	-1.23	7.84
xpt	Q2G0Y9	-1.31	3.99
Succinate dehydrogenase complex			
SAOUHSC_01104 (putative sdhA)	Q2FZC8	-1.54	4.86
SAOUHSC_01103 (putative sdhC)	Q2FZC9	-2.52	3.67
PTS system			
SAOUHSC_01836 (putative ptsA)	Q2FXJ8	-1.81	2.33
ptsG	Q2G1G8	-1.07	5.89
SAOUHSC_00158	Q2G1G5	-1.33	3.47
SAOUHSC_01836	Q2FXJ8	-1.81	2.33
SAOUHSC_02402	Q2FW97	-1.40	1.40
SAOUHSC_02975	Q2FUX0	-1.38	3.67

Table 28: Significantly upregulated (log_2 ratio ≥ 1, $-log_{10}$ t-test p-value > 1.3) proteins in Δ*clpX* mutants in comparison to wildtype control. Proteins were categorized according to their KEGG and GO assessment as analyzed by Perseus.

Gene name	Uniprot ID	log_2 ratio *ΔclpX/wt*	$-log_{10}$ *t*-test *p*-value
Antibiotica resistance			
femA	Q2FYR2	1.11	7.22
femX	Q2FVZ4	1.11	5.54
fmtA	Q2FZK3	1.22	5.57
SAOUHSC_00646 (putative pbp4)	Q53613	1.30	5.40
SAOUHSC_01467 (putative pbp2)	Q2FYI0	1.40	7.21
SAOUHSC_01652 (putative pbp3)	Q2FY21	1.76	6.73
Host-pathogen interactions			
asp3	Q2FUW5	1.10	3.00
atl	Q2FZK7	1.57	7.48
clfA	G0XY21	2.41	7.44
clfB	Q2FUY2	2.43	8.25
ebpS	Q2FYF1	2.11	8.38
fnbA	P14738	3.94	4.58
lytM	O33599	2.17	3.10
lytN	Q9ZNI1	5.02	8.37
SAOUHSC_02834 (srtA)	Q2FV99	1.03	3.62
SAOUHSC_02982 (sasF)	Q2FUW9	3.14	7.86

sarV	Q2FVY9	1.89	2.62
sasG	Q2G2B2	1.66	6.08
sceD	Q2FWF8	3.32	5.84
sdrC	Q2G0L5	4.85	9.61
sdrD	Q2G0L4	3.53	10.14
secA2	Q2FUW6	1.34	4.24
sle1	Q2G0U9	2.32	4.83
sraP	Q2FUW1	1.48	4.75
ssaA	Q2FV55	1.43	5.24
ssaA2	Q2G2J2	1.90	7.10
Urease complex			
ureB	Q2G2K6	3.64	9.62
ureC	Q2G2K5	5.98	11.37
ureE	Q2G2K8	2.80	6.99
ureG	Q2G273	2.77	8.63

Analytical data VioA-P synthesis

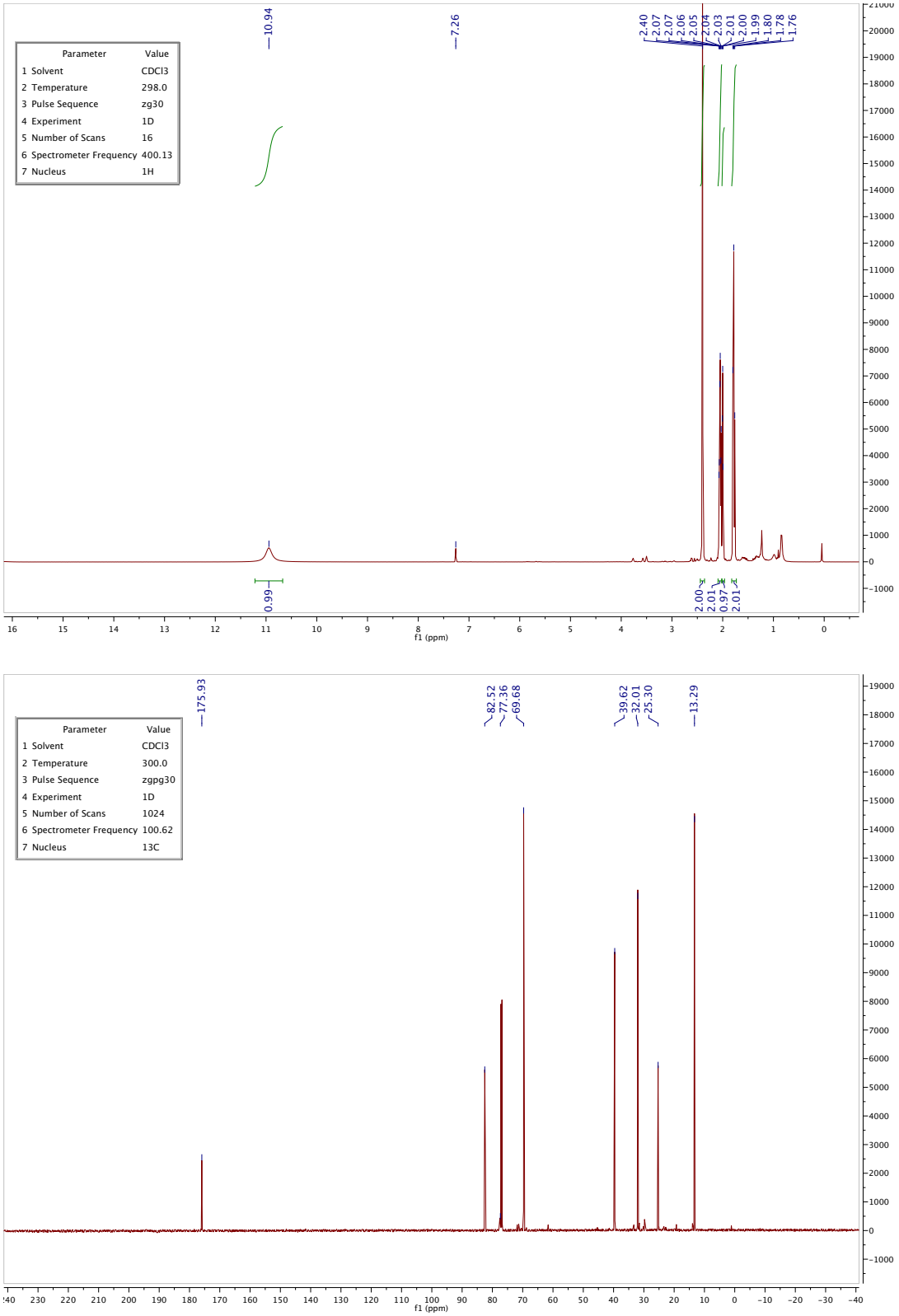

Figure 42: ^{1}H and ^{13}C NMR spectra of 2-(3-(but-3-yn-1-yl)-3H-diazirin-3-yl)acetic acid.

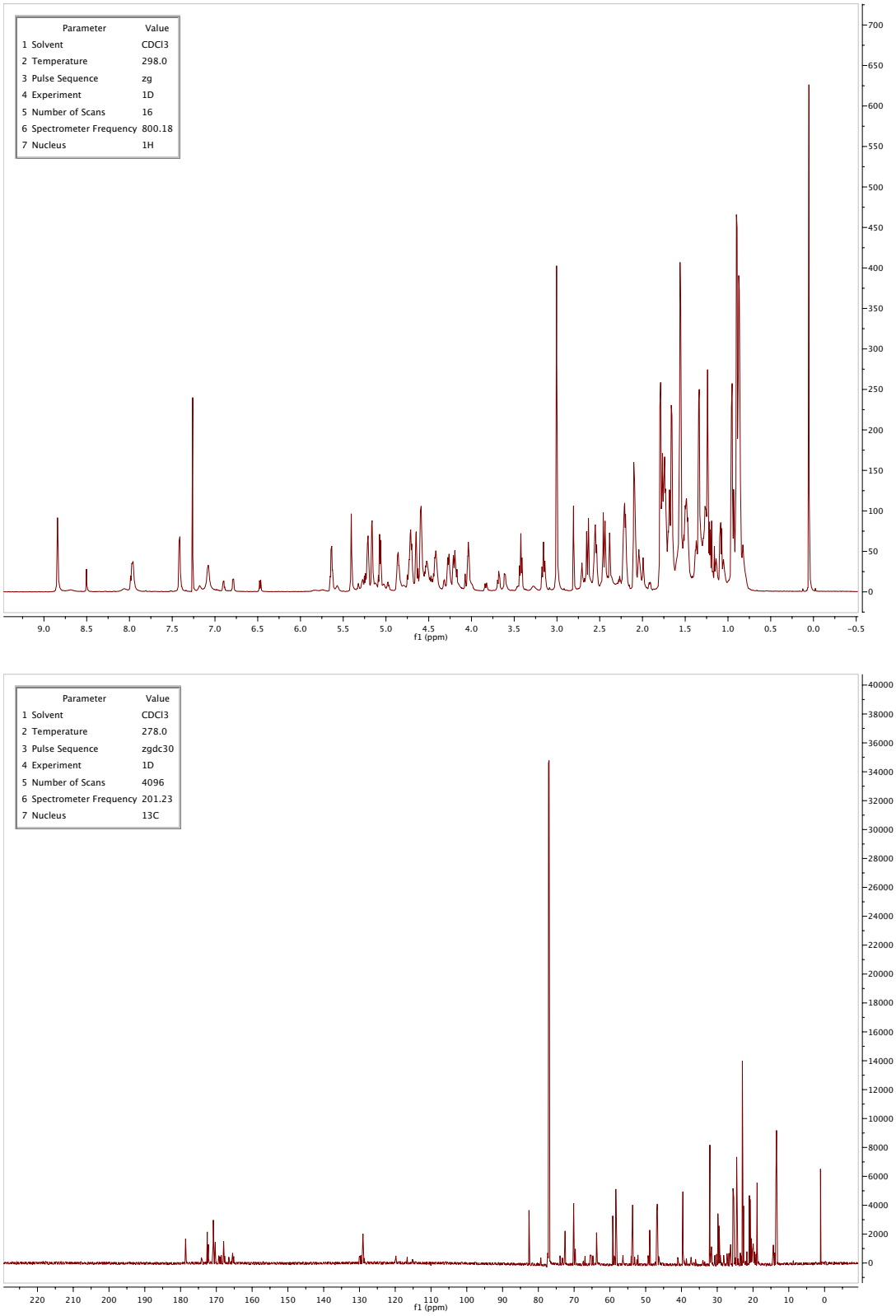

Figure 43: ^{1}H and ^{13}C NMR spectra of **VioA-P**.

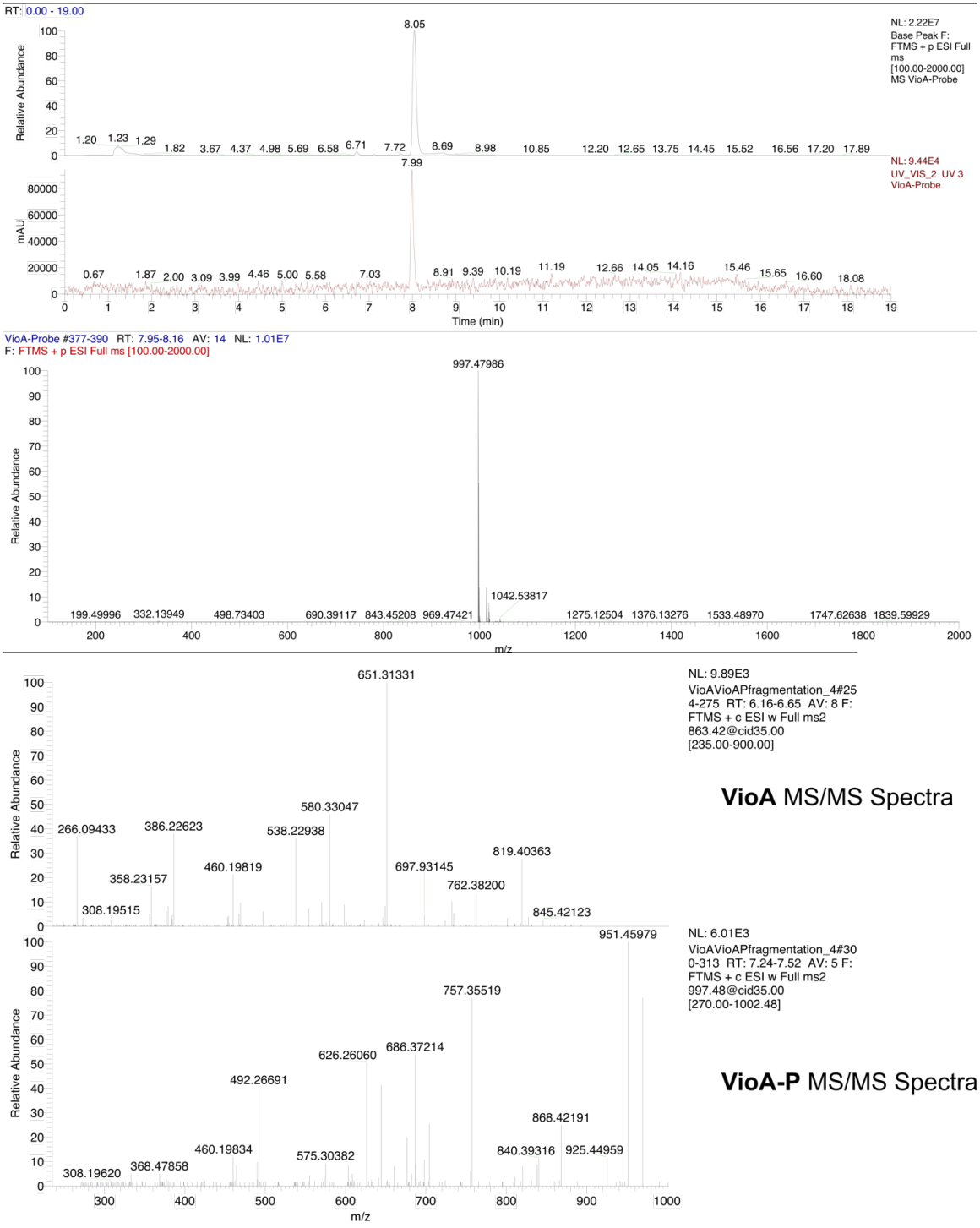

Figure 44: MS/MS fragmentation spectra of **VioA** and **VioA-P**.

Supplementary figures

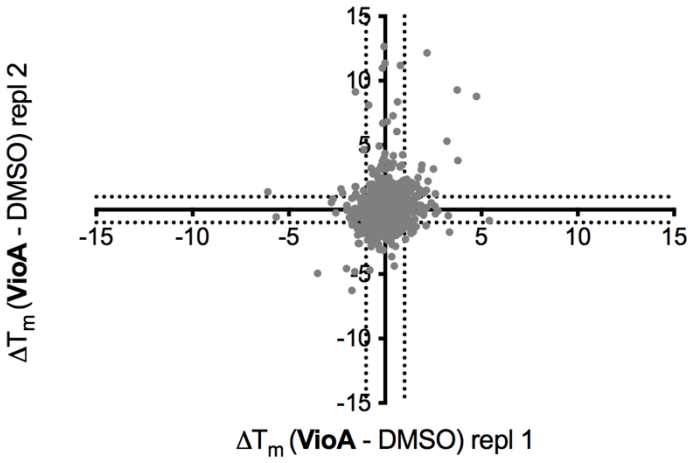

Figure 45: Scatterplot of T_m shits determined from two biological replicates of VioA vs DMSO treatment.

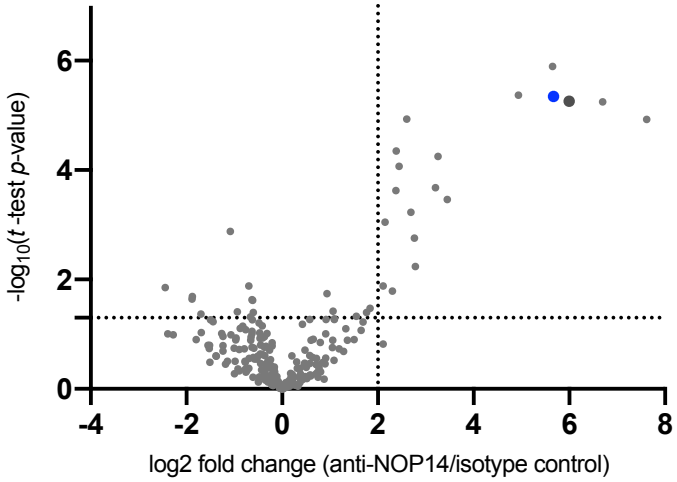

Figure 46: Volcano plot of co-IP of NOP14 against isotype control in Jurkat cells treated with VioA prior to co-IP enrichment. Cells were treated with VioA (10 nM) for 24h prior to incubation with 2 mM DSSO crosslinker for chemical cross-linking of protein-protein interactions and subsequent pull down using an anti-NOP14 antibody or isotype control. Volcano plot represents t test results of anti-NOP14 co-IP compared to isotype control co-IP (n=4 for each experiment). Cutoff criteria were defined as $\log_2$ enrichment > 2 and $-\log_{10}$ (*t*-test *p*-value) > 1.3 (dotted lines). NOP14 (blue) and NOC4L (dark grey) are highlighted in the plot. Significant enriched proteins are listed in Table S4. EMG1 is not present in the plot as it is only detected in one of four anti-NOP14 antibody pulldown samples.

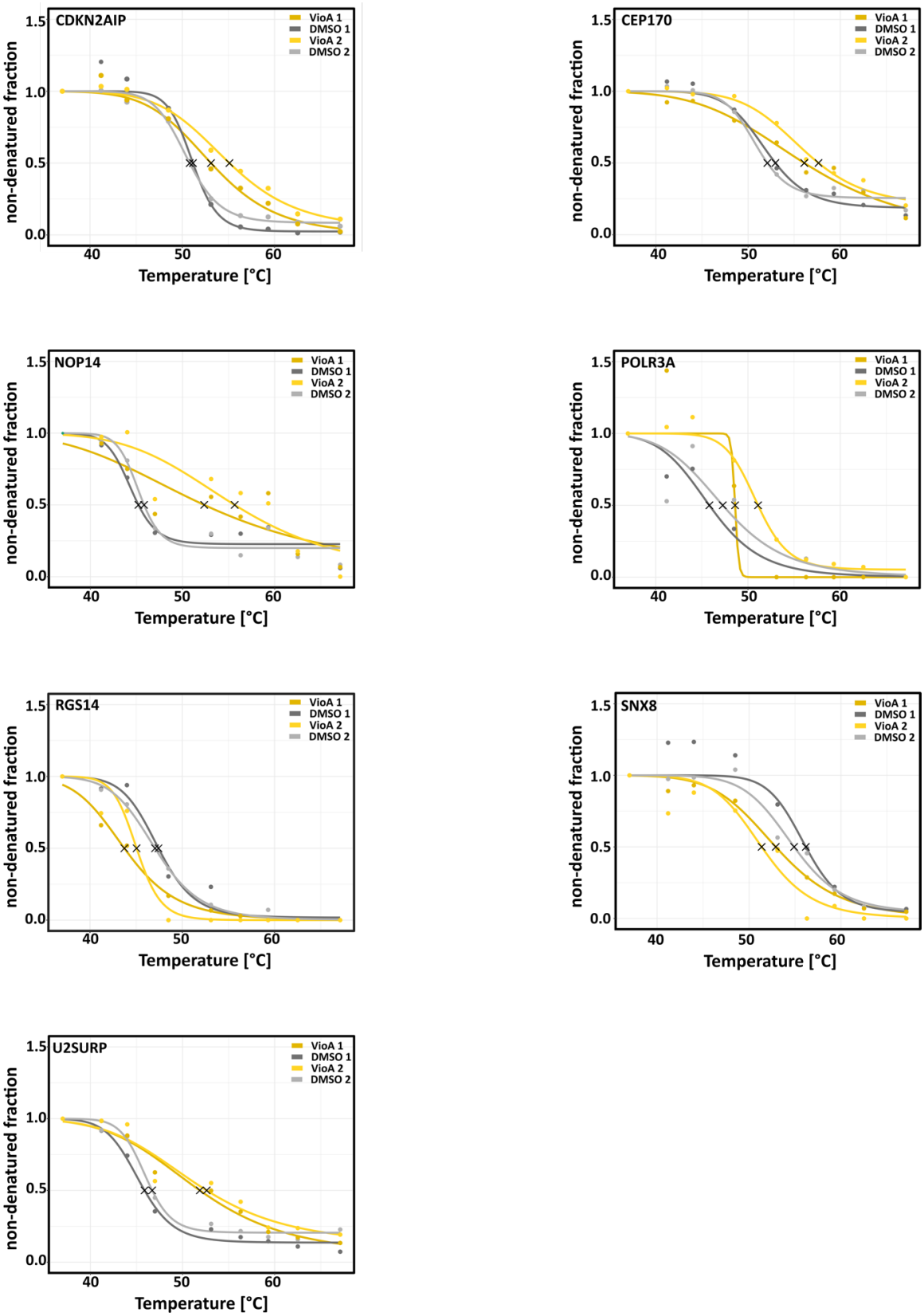

Figure 47: **Thermal melting curves of potential hits identified in thermal proteome profiling experiment.** Thermal response curves for proteins passing all filtering thresholds (see data analysis for TPP experiments) when treating cells with 1 µM **VioA** (orange) compared to DMSO controls (grey). Melting points (asterisks) and melting curve fitting was carried out and results visualized using the TPP R package[137] and Graphpad Prism 8. CEP170 met all significance criteria in one replicate but was just outside the threshold for significance in the other.

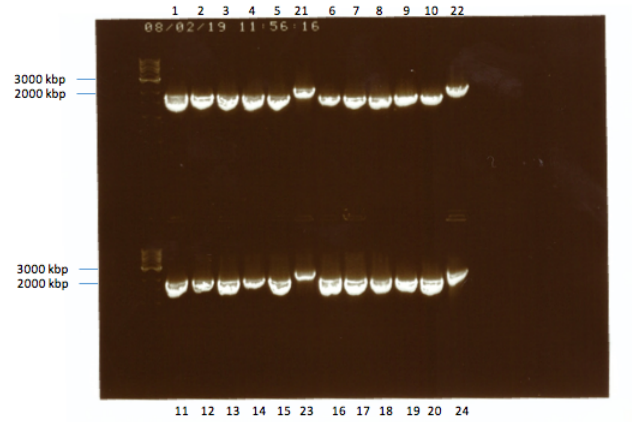

Figure 48: Colony PCR of *S. aureus* wildtype (sample 21-24) and *S. aureus ΔclpP* (samples 1-20) carried out to validate deletion of *clpP* gene. 20 colonies of *S. aureus ΔclpP* were independently subjected to colony PCR using KO_clpP_A and KO_clpP_D primers to amplify the gene with upstream and downstream flanking regions.

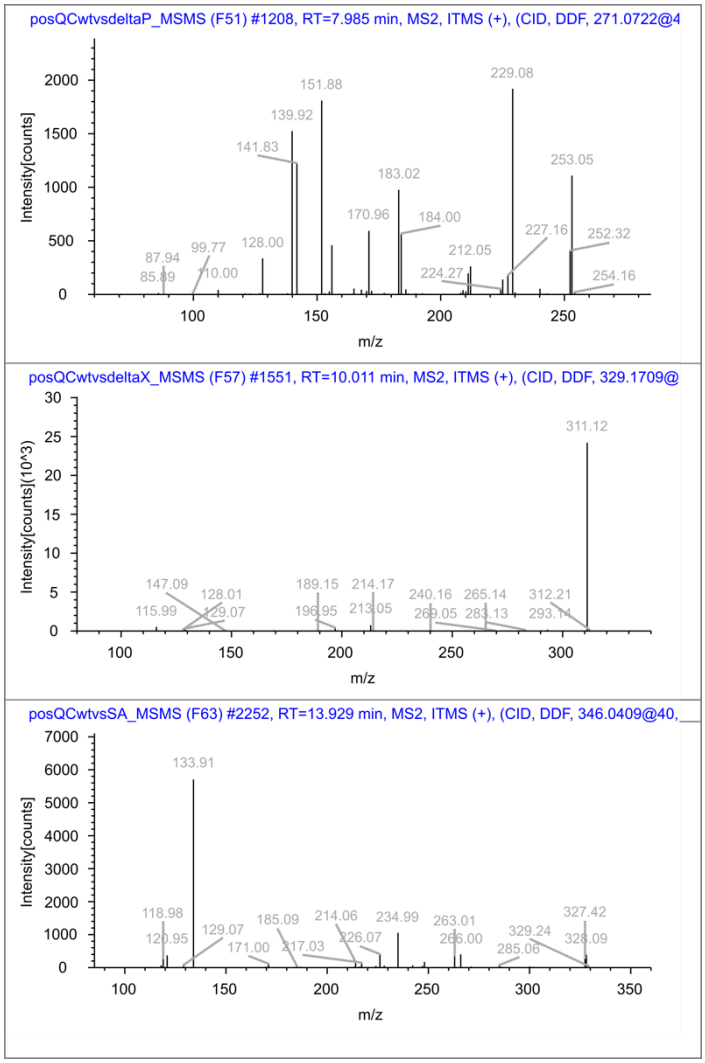

Figure 49: MS/MS spectra of metabolic features identified as dysregulated in *S. aureus* ΔclpP relatively to *S. aureus* clpP S98A. Visualization of MS/MS spectra was performed with Compound Discoverer.

6. Abbrevations

°C	Grad Celsius
5-FU	5-Fluorouracil
ABC	ATP binding casette
ABPP	Activity-based protein profiling
ACN	Acetonitrile
ActD	Actinomycin D
A*f*BP	Affinity-based probes
A*f*BPP	Affinity-based protein profiling
Agr	Accessory gene regulatory
AIP	Auto-inducing peptide
ALL	Acute lymphoblastic leukemia
AML	Acute myeloid leukemia
ATP	Adenosine triphosphate
BCA	Bicinchoninic acid
BSA	Bovine serum albumin
BTTAA	2-(4-((bis((1-(tert-butyl)-1H-1,2,3-triazol-4-yl)methyl)amino)methyl)-1H-1,2,3-triazol-1-yl)acetic acid
calc.	calculated
cDNA	Complementary DNA
CETSA	Cellular thermal shift assay
CH_2Cl_2	Dichloromethane
CTB	Cell titer blue
Da	Dalton
DCM	Dichloromethane
DDA	Data dependent aquisition
ddH_2O	Double-distilled water
DIPEA	Diisopropylethylamine
DMAP	4-Dimethylaminopyridine
DMEM	Dulbecco's Modified Eagle's Medium
DMSO	Dimethyl sulfoxide
DNA	Deoxyribonucleic acid
DSSO	Disuccinimidyl sulfoxide
e.g.	Exempli gratia
EC_{50}	half maximal effective concentration
EDC	1-ethyl-3-(3-dimethylaminopropyl)carbodiimide
eq.	equivalent
ESI	electron spray ionization
et al.	*et alli*
EtOAc	Ethyl acetate
FA	Formic acid
FBS	Fetal bovine serum
FDR	False discovery rate
GO	Gene ontology
GOCC	Gene ontology cellular component
h	Hour
HILIC	hydrophilic liquid interaction chromatography
HMDB	Human Metabolome Database
HPLC	High pressure liquid chromatography
HRMS	High resolution mass spectrometry
Hz	Hertz
IC_{50}	half maximal inhibitory concentration
iTRAQ	isobaric Tags for Relative and Absolute Quantitation
KEGG	Kyoto Encyclopedia of Genes and Genomes
LB	Lysogeny broth
LC	Liquid chromatography
LC-MS	Liquid chromatography coupled to mass spectrometry
LFQ	Label-free quantification

LFQ	Label-free quantification
LLE	Liquid liquid extraction
LysC	Endoproteinase Lys-C
m/z	Mass to charge ratio
MALDI	Matrix-assisted laser disruption ionization
MAZ	Methylazetidine
MeCN	Acetonitrile
MeOH	Methanol
METLIN	Metabolite and Chemical Entity Database
Min	Minute
MRSA	Methicilin-resistant *S. aureus*
MS	mass spectrometry
MS/MS	Tandem mass spectrometry
MTT	3-(4,5-dimethylthiazol-2-yl)-2,5-diphenyltetrazolium
MW	Molecular weight
NCE	Normalized Collision energy
nm	Nanometer
NMR	Nuclear magnetic resonance
NMR	Nuclear magnetic resonance
nt siRNA	Non-targeted small interfering RNA
OD	Optical density
on	overnight
PAL	Photoaffinity labeling
PBS	Phosphate buffered saline
PCR	Polymerase chain reaction
pH	Power of hydrogen
ppm	Parts per million
pRb	Retinoblastoma Protein
QS	Quorum sensing
rDNA	Ribosomal DNA
Rf	Reference value
RNA	Ribonucleic acid
RP	Reversed-phase
RP-HPLC	Reversed-phase High performance liquid chromatography
rpm	Rounds per minute
RPMI	Roswell Park Memorial Institute
rRNA	Ribosomal RNA
Sar	Staphylococcal accessory response
SDS	Sodium dodecylsulfate
SDS-PAGE	SDS polyacrylamide gel electrophoresis
Sec	Second
SEM	Standard error of the mean
SILAC	Stable isotope labeling with amino acids in cell culture
SIM	Single ion monitoring
siRNA	Small interfering RNA
snoRNA	Small nucleolar RNA
snRNP	Small nuclear ribonucleoprotein
SPE	Solid phase extraction
STRING	Search Tool for the Retrieval of Interacting Genes/Proteins
TAMRA	Tetramethylrhodamine
TCS	Two-component system
TFA	Trifluoroacetic acid
TFL	Trifunctional linker
T_m	Melting temperature
TMT	tandem mass tag
TOF	Time-of-Flight
TPP	Thermal proteome profiling
TPP-CCR	Thermal proteome profiling concentraction range
TPP-TR	Thermal proteome profiling thermal response
TSA	Thermal Shift Assay
TSA	Thermal Shift assay
UPLC	Ultra performance liquid chromatography

UV	Ultra Violet
Vio	vioprolide
VRSA	Vancomycin-resistant *S. aureus*
vs.	Versus
wt	Wildtype
ZIC	Zwitterionic

7. Licenses

SPRINGER NATURE LICENSE
TERMS AND CONDITIONS

Dec 17, 2019

This Agreement between TU München -- Volker Kirsch ("You") and Springer Nature ("Springer Nature") consists of your license details and the terms and conditions provided by Springer Nature and Copyright Clearance Center.

License Number	4718110806909
License date	Nov 29, 2019
Licensed Content Publisher	Springer Nature
Licensed Content Publication	Nature Reviews Cancer
Licensed Content Title	Ribosome biogenesis in cancer: new players and therapeutic avenues
Licensed Content Author	Joffrey Pelletier et al
Licensed Content Date	Dec 1, 2017
Type of Use	Thesis/Dissertation
Requestor type	academic/university or research institute
Format	print and electronic
Portion	figures/tables/illustrations
Number of figures/tables/illustrations	1
High-res required	no
Will you be translating?	no
Circulation/distribution	30 - 99
Author of this Springer Nature content	no
Title	Molecular target elucidation of vioprolide A in human cancer cells and -omics insights into the ClpXP machinery of Staphylococcus aureus
Institution name	Technische Universität München
Expected presentation date	Feb 2020
Portions	Figure 1
Requestor Location	TU München Lichtenbergstr. 4 Munich, Select One 85748 Germany Attn: Volker Kirsch
Total	0.00 EUR

Terms and Conditions

Springer Nature Customer Service Centre GmbH
Terms and Conditions

This agreement sets out the terms and conditions of the licence (the **Licence**) between you and **Springer Nature Customer Service Centre GmbH** (the **Licensor**). By clicking 'accept' and completing the transaction for the material (**Licensed Material**), you also confirm your acceptance of these terms and conditions.

1. Grant of License

1. 1. The Licensor grants you a personal, non-exclusive, non-transferable, world-wide licence to reproduce the Licensed Material for the purpose specified in your order only. Licences are granted for the specific use requested in the order and for no other use, subject to the conditions below.

1. 2. The Licensor warrants that it has, to the best of its knowledge, the rights to license reuse of the Licensed Material. However, you should ensure that the material you are requesting is original to the Licensor and does not carry the copyright of

SPRINGER NATURE LICENSE
TERMS AND CONDITIONS

Dec 17, 2019

This Agreement between TU München -- Volker Kirsch ("You") and Springer Nature ("Springer Nature") consists of your license details and the terms and conditions provided by Springer Nature and Copyright Clearance Center.

License Number	4727281075100
License date	Dec 13, 2019
Licensed Content Publisher	Springer Nature
Licensed Content Publication	Nature Structural & Molecular Biology
Licensed Content Title	The complete structure of the small-subunit processome
Licensed Content Author	Jonas Barandun et al
Licensed Content Date	Sep 25, 2017
Type of Use	Thesis/Dissertation
Requestor type	academic/university or research institute
Format	print and electronic
Portion	figures/tables/illustrations
Number of figures/tables/illustrations	1
High-res required	no
Will you be translating?	no
Circulation/distribution	50000 or greater
Author of this Springer Nature content	no
Title	Molecular target elucidation of vioprolide A in human cancer cells and -omics insights into the ClpXP machinery of Staphylococcus aureus
Institution name	Technische Universität München
Expected presentation date	Feb 2020
Portions	Figure 1
Requestor Location	TU München Lichtenbergstr. 4 Munich, Select One 85748 Germany Attn: Volker Kirsch
Total	0.00 EUR

Terms and Conditions

Springer Nature Customer Service Centre GmbH
Terms and Conditions

This agreement sets out the terms and conditions of the licence (the **Licence**) between you and **Springer Nature Customer Service Centre GmbH** (the **Licensor**). By clicking 'accept' and completing the transaction for the material (**Licensed Material**), you also confirm your acceptance of these terms and conditions.

1. Grant of License

1. 1. The Licensor grants you a personal, non-exclusive, non-transferable, world-wide licence to reproduce the Licensed Material for the purpose specified in your order only. Licences are granted for the specific use requested in the order and for no other use, subject to the conditions below.

1. 2. The Licensor warrants that it has, to the best of its knowledge, the rights to license reuse of the Licensed Material. However, you should ensure that the material you are requesting is original to the Licensor and does not carry the copyright of

8. Curriculum Vitae

Volker Christian Reinhard Kirsch

Date of Birth	September, 20 1988 Madrid, Spain

Education

03.2015 – 02.2020	Ph.D. Chemistry *Technische Universität München, Germany* Ph.D. thesis under the supervision of Prof. Dr. Stephan A. Sieber, Chair of Organic Chemistry II, *Technische Universität München, Germany* "Molecular Target elucidation of vioprolide A in human cancer cells and -omics insights into the ClpXP machinery of *Staphylococcus aureus*"
07.2014 – 02.2015	M.Sc. Chemistry *Technische Universität München, Germany* M.Sc. thesis under the supervision of Prof. Dr. Stephan A. Sieber, Chair of Organic Chemistry II, *Technische Universität München, Germany* "Synthesis and Biological Evaluation of Diketopiperazines"
03.2014 – 06.2014	M. Sc. Studies in Chemistry *Universidad Complutense de Madrid, Spain*
10.2012 – 03.2014	M. Sc. Studies in Chemistry *Technische Universität München, Germany*
10.2009 – 09.2012	B. Sc. Studies in Chemistry *Technische Universität München, Germany*

	B. Sc. Thesis under the supervision of Dr. Josue Moreno Bermudez , Isotope Technologies Garching GmbH and Prof. Dr. H. J. Wester, Chair of Pharmaceutical Radiochemistry, *Technische Universität München*, Germany "*Preliminary studies on the recycling of Yb from irradiated targets*"
11.2008 – 07-2009	Alternative Civil Service in Emergency Rescue Service Bayerisches Rotes Kreuz, Friedberg (Augsburg)
09.1999 – 07.2008	Higher education entrance level (Abitur) Wernher-von-Braun Gymnasium Friedberg